Durham E-Theses

Auger recombination in low-dimensional semiconductor structures

Taylor, R.I.

How to cite:

Taylor, R.I. (1987) *Auger recombination in low-dimensional semiconductor structures*, Durham theses, Durham University. Available at Durham E-Theses Online: http://etheses.dur.ac.uk/6699/

Use policy

The full-text may be used and/or reproduced, and given to third parties in any format or medium, without prior permission or charge, for personal research or study, educational, or not-for-profit purposes provided that:

- a full bibliographic reference is made to the original source
- a link is made to the metadata record in Durham E-Theses
- the full-text is not changed in any way

The full-text must not be sold in any format or medium without the formal permission of the copyright holders.

Please consult the full Durham E-Theses policy for further details.

Academic Support Office, The Palatine Centre, Durham University, Stockton Road, Durham, DH1 3LE
e-mail: e-theses.admin@durham.ac.uk Tel: +44 0191 334 6107
http://etheses.dur.ac.uk

AUGER RECOMBINATION IN LOW-DIMENSIONAL SEMICONDUCTOR STRUCTURES

by

R.I. Taylor, B.A.

A thesis submitted for
the Degree of Doctor of Philosophy
in the University of Durham
October 1987

The copyright of this thesis rests with the author.
No quotation from it should be published without
his prior written consent and information derived
from it should be acknowledged.

28. JAN. 1989

DECLARATION

I hereby declare that the work reported in this thesis has not previously been submitted for any degree and is not being currently submitted in candidature for any other degree.

The work reported in this thesis was carried out by the candidate.

ABSTRACT

In this thesis, calculations of Auger recombination rates in semiconductor quantum wells are presented.

Chapter One introduces Auger recombination, and the reasons for studying the Auger process are explained. Basically, Auger recombination is a non-radiative recombination mechanism that becomes more important as the carrier density increases and the bandgap decreases. In direct gap semiconductors, the Auger process has an activation energy, and the resulting highly temperature dependent Auger process is thought to be a possible cause of the high temperature sensitivity of long wavelength semiconductor lasers that are being considered for use as sources in optical fibre communications systems.

In Chapter Two, an expression is derived for the CHSH Auger recombination rate in a quantum well (QW) heterostructure. The possible Auger processes in a QW are discussed as are the differences between Auger recombination in a QW and in bulk semiconductors, and the magnitudes of QW and bulk Auger rates are compared.

In Chapter Three, the theory of Auger recombination is extended to the case of a quantum well wire (QWW), a semiconductor structure in which carriers are free to move in one direction only. It is found that there are no significant physical differences between Auger recombination in a QW and in a QWW. The ratio of QW and QWW Auger rates is evaluated.

Numerical results for Auger transition rates in 1.3μm and 1.55μm InGaAsP/InP QWs and QWWs are presented in Chapter Four, and comparison with experimental values is made. In particular, the result found in Chapter Two, that, under certain conditions, the Auger rates in the QW and the bulk are approximately the same is found to agree with experimental results from the literature.

The derivation of the CHSH Auger transition rates in QWs and QWWs that was presented in Chapters Two and Three required a number of approximations concerning the carrier statistics and the semiconductor bandstructure. In Chapter Five, these approximations are examined, and, although it is found that the use of non-degenerate carrier statistics is reasonably accurate, the assumption of parabolic energy bands can lead to overestimates of the Auger transition rates.

The first five chapters constitute the first part of the thesis, concerning Auger recombination in low-dimensional semiconductor structures. In the second part of the thesis, the realistic bandstructure of low-dimensional semiconductor structures, such as superlattices, is examined. The method used is described in Chapter Six, and is based on an empirical pseudopotential method. Results for the GaAs/AlAs superlattice are presented in Chapter Seven.

ACKNOWLEDGEMENTS

I would like to thank the members of staff and students in the Department of Applied Physics and Electronics for helping to make my time in Durham so enjoyable.

In particular, I would like to thank my supervisor, Dr. R.A. Abram for the support and advice he readily gave. Also, I would like to thank Dr S. Brand for our many interesting and useful discussions.

I would like to acknowledge the financial support that I received from the SERC and British Telecom Reseach Laboratories (via a SERC CASE award). Of the many people that I met whilst at BTRL, I would particularly like to thank Dr. Mike Burt, whose clear insight and enthusiasm for physics enabled me to learn a great deal during my visits to BTRL.

Last, but certainly not least, I would like to thank my parents for their support throughout my many years of study.

CONTENTS

	Page
Abstract	(i)
Acknowledgements	(ii)
CHAPTER ONE - Introduction	1
1.1 - Conventional long wavelength semiconductor lasers.	3
1.2 - Auger recombination in bulk semiconductors.	6
1.3 - Quantum well and quantum well wire lasers.	10
1.4 - Auger recombination in QWs and QWWs.	12
References for Chapter One.	14
CHAPTER TWO - Calculation of the quantum well CHSH Auger recombination rate.	16
2.1 - Modelling the quantum well.	17
2.2 - The QW CHSH Auger rate.	20
2.2.1 - The statistical factor.	22
2.2.2 - The matrix element for the Auger process.	25
2.3 - Use of Fermi's Golden Rule to calculate the QW CHSH Auger rate.	33
2.3.1 - Discussion of results.	43
2.4 - QW Auger rates involving one (or more) carriers in higher confined subbands.	44
2.5 - QW bound-unbound Auger processes.	46
2.6 - Summary of Chapter Two.	52
References for Chapter Two.	54
CHAPTER THREE - The CHSH Auger recombination rate in a quantum well wire.	56
3.1 - The quantum well wire.	57

3.2 - Calculation of the CHSH quantum well wire Auger rate. 59

3.3 - QWW Auger rates for general intersubband transitions. 66

3.4 - The directional dependence of the QWW Auger rate. 68

3.5 - Summary of Chapter Three. 70

References for Chapter Three. 71

CHAPTER FOUR- Numerical estimates of Auger transition rates in InGaAsP/InP quantum wells and quantum well wires. 72

4.1 - Numerical estimates of bound-bound Auger transition rates in InGaAsP/InP quantum wells. 73

4.2 - Numerical estimates of bound-unbound Auger transition rates in QWs. 83

4.3 - Comparison of theoretical and experimental results on Auger transition rates in InGaAsP/InP quantum wells. 86

4.4 - Numerical results for bound-bound Auger transitions in InGaAsP/InP QWWs. 88

4.5 - Summary of Chapter Four. 89

References for Chapter Four. 91

CHAPTER FIVE- The effects of non-parabolic bandstructure and Fermi-Dirac statistics on Auger rates. 93

5.1 - Effects of non-parabolicity on CHCC QW Auger transition rates. 94

5.2 - Effects of subband non-parabolicity on QW Auger transition rates. 98

5.3 - Numerical estimates of the effect of non-parabolicity on Auger transition rates. 104

5.4 - Effects of Fermi-Dirac statistics on QW Auger rates. 109

5.5 - The use of Fermi-Dirac statistics for calculating Auger transition rates. 111

5.6 - Summary of Chapter Five. 117

References for Chapter Five. 119

CHAPTER SIX- Electronic bandstructure calculations for semiconductor superlattices : Theory. 121

6.1 - The calculation of the bandstructure for complex wavevector for bulk semiconductors. 123

6.2 - The calculation of superlattice bandstructure. 129

References for Chapter Six. 136

CHAPTER SEVEN- The electronic structure of GaAs/AlAs superlattices. 137

7.1 - The energy-superlattice wavevector relation in a GaAs/AlAs superlattice. 139

7.2 - The energy-in plane wavevector relationship for short period GaAs/AlAs superlattices. 144

7.3 - Summary. 146

References for Chapter Seven. 147

Appendix One - Evaluation of the phase space integral appearing in the calculation of the ground state CHSH QW Auger rate. 148

Appendix Two - Calculation of $I(\underline{\kappa}_o)$. 151

Appendix Three - Erfc(x) at large values of x. 153

Appendix Four - Non-parabolicity effects on Auger rates : An example. 154

CHAPTER ONE - INTRODUCTION

The primary aim of the work reported in this thesis was the study of the important direct Auger recombination processes in low dimensional semiconductor structures such as quantum wells (QW) and quantum well wires (QWW). As will be discussed later in this chapter, Auger recombination is thought to be a major loss mechanism in long-wavelength semiconductor lasers, and so a study of Auger recombination in low-dimensional semiconductor structures will give insight into the importance of Auger processes as loss mechanisms in QW and QWW lasers. Smith [1] has undertaken a study of Auger recombination in InGaAsP/InP QWs, but the only Auger process examined was that involving conduction and heavy hole subbands. Auger processes involving other subbands of the QW (such as the spin-split off and light hole subbands) are examined in Chapter Two of this thesis, and expressions are given for Auger transition rates that are consistent with the earlier work of Smith [1]. The calculations of Auger transition rates are extended to include quantum well wires (QWW) in Chapter Three. Numerical results for Auger transition rates in QWs and QWWs for 1.3μm and 1.55μm InGaAsP/InP systems are presented in Chapter Four.

Some of the approximations used in deriving the algebraic expressions for Auger transition rates in Chapters Two and Three (such as the use of isotropic, parabolic subbands and Boltzmann statistics with quasi-Fermi levels) are examined in Chapter Five. The importance of the QW subband dispersion relations for the calculation of Auger transition rates is emphasised throughout Chapters Two to Five. To gain insight into the form of the realistic dispersion relations for QW and superlattice subbands, a method is described for the calculation of superlattice bandstructure in Chapter Six. Results that demonstrate the ability

UNIV DUNELM

of the method to calculate accurately the electronic structure of GaAs/AlAs superlattices are presented in Chapter Seven, and some of the important concepts associated with superlattice bandstructure are illustrated in that Chapter.

In the remainder of Chapter One, we explain the motivation for studying Auger transition rates in long-wavelength low dimensional semiconductor lasers.

1.1 CONVENTIONAL LONG WAVELENGTH SEMICONDUCTOR LASERS

The use of silica based optical fibres in long-haul telecommunications systems has led to the increasing importance of long-wavelength semiconductor lasers. The reasons for this are that the wavelength at which minimum attenuation through a standard silica based fibre occurs is $1.55\mu m$, and the zero of dispersion occurs at $1.3\mu m$. The quaternary alloy $In_{1-x}Ga_xAs_yP_{1-y}$ has attracted considerable interest as a material for the active region of semiconductor lasers because, when lattice matched to InP, it may be used throughout the wavelength range $1.0 - 1.7\mu m$ (see Figure (1.1)). Unfortunately, however, InGaAsP lasers have a temperature sensitivity problem. In conventional double heterostructure (DH) lasers, the temperature sensitivity of the threshold current is described by the parameter T_o, through the empirical relationship

$$J_{TH} = J_o \exp(\frac{T}{T_o}) \tag{1.1}$$

with J_{TH} being the threshold current density and T is the lattice temperature. T_o is constant over a limited temperature range, and, clearly, the larger its value, the less temperature sensitive will be the laser. For $GaAs/Ga_{0.64}Al_{0.36}As$ DH lasers $T_o \approx 160 - 200K$ [2], [3], whereas for $1.3\mu m$ and $1.55\mu m$ InGaAsP/InP DH lasers, $T_o \approx 110K$ (for $T \leq 250K$), and $T_o \approx 60 - 70K$ (for $T \geq 250K$) [2], [3]. The low room temperature value of T_o imposes limitations on the operation of InGaAsP/InP DH lasers. The temperature dependence of the optical gain can explain the T_o value of the $GaAs/Ga_{0.64}Al_{0.36}As$ DH laser [2], but not the value for the InGaAsP/InP DH lasers. For the latter system, some of the main mechanisms proposed to explain the low T_o values are Auger recombination [3],

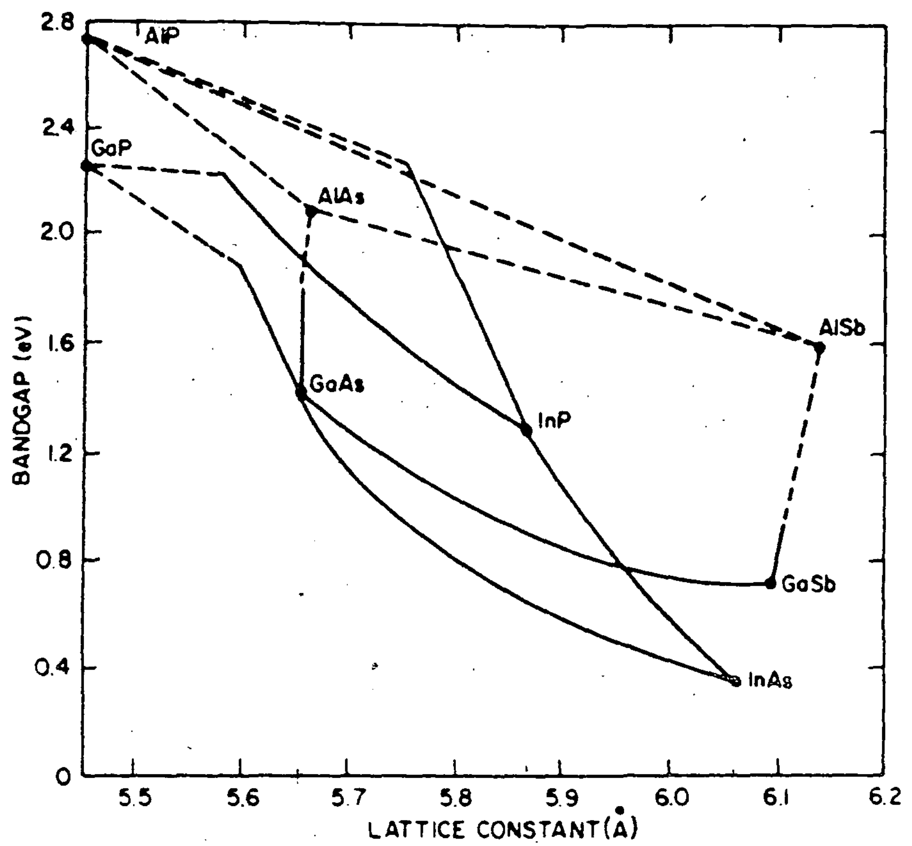

Figure 1.1 Variation of the bandgap as a function of lattice constant for III–V binary and alloy semiconductors

[4], [5], intervalence band absorption [6], and carrier leakage over the confining barriers [2], although the last mechanism is thought to be the least important [2]. Intervalence band absorption in $In_{0.72}Ga_{0.28}As_{0.6}P_{0.4}$ has recently been calculated by Childs et al [7], with the use of realistic bandstructure and the conclusion reached in that study was that intervalence band absorption was not responsible for the temperature variation of the threshold current. However, Adams [8], using results from the calculation of Childs et al [7] disagrees with the conclusion of [7], proposing that intervalence band absorption can explain the T_o values of long-wavelength semiconductor lasers. Thus, the importance of intervalence band absorption in determining T_o values of semiconductor lasers is still uncertain. Auger recombination, one of the other mechanisms proposed to explain the low T_o values in InGaAsP DH lasers is introduced and discussed in the next section. Some experimental evidence indicating the importance of Auger recombination in InGaAsP/InP DH lasers is available. Haug and Burkhard [9] have experimentally determined T_o values in InGaAsP/InP DH lasers for different alloy compositions. As the wavelength of the InGaAsP/InP DH laser increased from 1.3μm to 1.65μm, the value of T_o decreased from 75 K to 40 K. A theoretical calculation of the T_o values of the InGaAsP/InP DH lasers assuming Auger recombination alone was also presented in [8], and the theoretical values were in good agreement with experiment. Since Auger recombination becomes more important as the bandgap decreases (see next section), this experiment provides evidence for the importance of Auger recombination in determining T_o values. However, intervalence band absorption also increases with decreasing bandgap, and, given the uncertainty in some of the parameters required in theoretical estimates of Auger recombination rates (which will be discussed later in this thesis), the good agreement between theory and experiment presented in [9] may be fortuitious. Another study [10] has detected

the overflow of injected carriers from InGaAsP into the confining InP layers in 1.3μm InGaAsP/InP DH lasers. The interpretation was that energetic carriers, created by Auger recombination, flowed over the top of the confining barrier into the InP.

1.2 AUGER RECOMBINATION IN BULK SEMICONDUCTORS

Auger recombination is a non-radiative process in which a conduction band electron and a valence band hole recombine. The energy produced by the recombination is given to a third carrier, which is excited higher up its respective band. Various Auger processes are illustrated in Figure (1.2), along with the notation usually used to specify them. Quite simply, the first letters of the bands of the four states involved in the Auger transition are used to label the process. For example, an Auger process involving three carriers in the conduction band and one carrier in the heavy hole band is labelled CHCC.

Auger recombination in bulk semiconductors was first investigated by Beattie and Landsberg [11] (see also [12]). In that study, transition rates for both the CHCC and CHHH Auger process were evaluated and compared with experimental lifetimes in InSb. Since that pioneering work, transition rates for the CHLH and CHSH [3],[13],[14],[15],[16] Auger processes have also been evaluated for bulk semiconductors although the majority of these calculations, whilst giving algebraic expressions for the Auger rates, use the simplifying assumptions of isotropic, parabolic energy bands and Boltzmann statistics.

In order to calculate Auger transition rates in bulk semiconductors, first order time dependent perturbation theory is used. The difference, U, between the complete Hamiltonian of the semiconductor crystal and the Hamiltonian of the Hartree-Fock approximation is treated as the perturbation, and its matrix element between initial and final states is used in Fermi's Golden Rule [14]. If the electrons taking part in the Auger transition are labelled 1 and 2, then, as Beattie has shown explicitly [12], the only term in the perturbation operator,

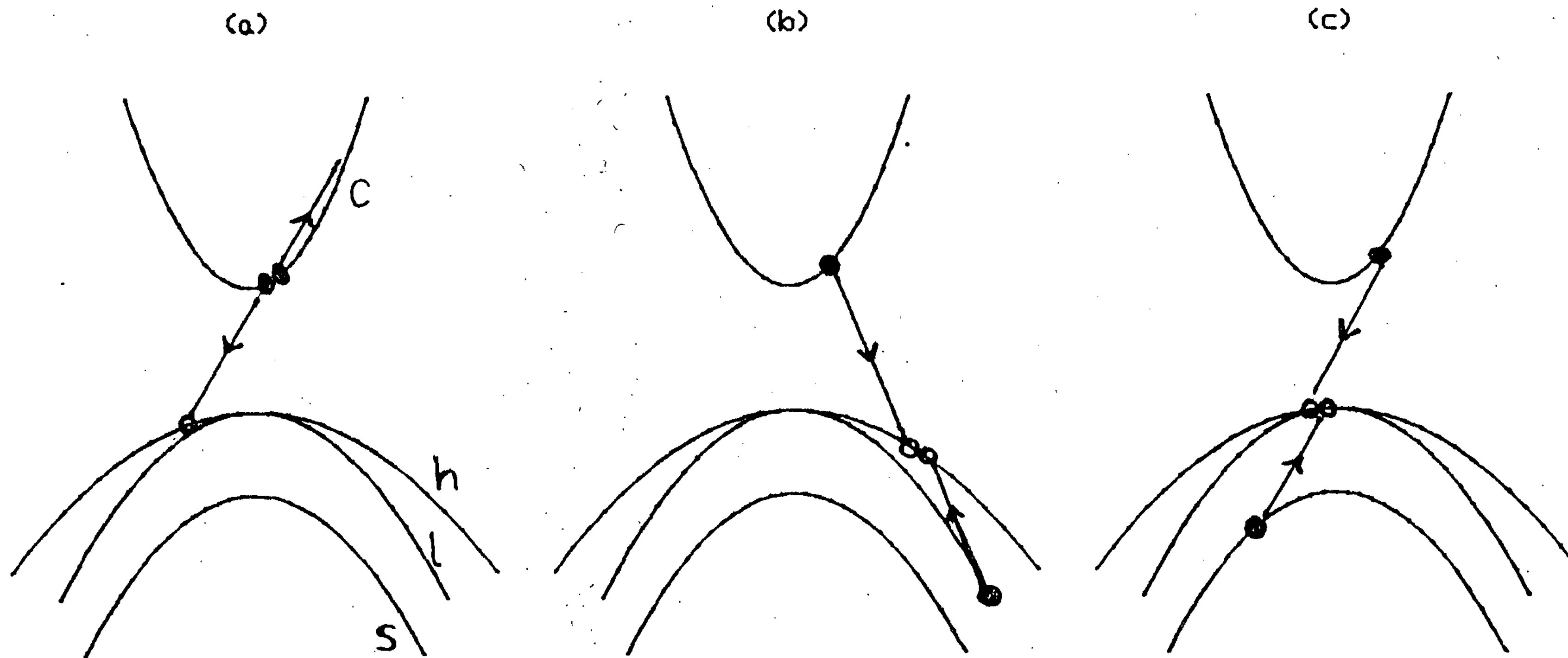

Figure (1.2) - Some Auger processes in bulk semiconductors ; (a) the CHCC process, (b) the CHLH process and (c) the CHSH process.

U, that has a non-zero matrix element is that involving $e^2/\epsilon r_{12}$ (where $r_{12} = |\underline{r}_1 - \underline{r}_2|$ and $\underline{r}_1$ is the position vector of state 1, etc.). The total recombination rate is thus obtained by carrying out the sum in Fermi's Golden Rule over all permissible initial and final states.

It is clear from an examination of references [10], [12] and [13] that the calculation is algebraically demanding, even if the simplifying assumptions of nondegeneracy and carriers occupying parabolic bands are used. However, simple physical arguments may be used to predict the form of the Auger transition rate. For the CHCC Auger process, two electrons are required in the conduction band and one hole is required in the heavy hole band. Thus, the CHCC Auger rate should depend on carrier density as n^2p (where n is the number of electrons per unit volume and p is the number of holes per unit volume). For the CHLH and CHSH Auger processes, similar arguments predict a dependence on carrier density of p^2n.

The other important feature in direct Auger processes is the conservation of both energy and momentum. The energy conservation comes from Fermi's Golden Rule, whereas the momentum conservation arises from evaluation of the matrix element, when the carrier wavefunctions are described in terms of Bloch functions. The combination of energy and momentum conservation results in direct Auger processes having an activation energy, since, for carriers to participate in an Auger process, they must lie away from the band edge, and the energy required to excite them from the band edge and place them in the configuration of the dominant Auger process is simply equal to the activation energy for that process.

Thus, the simple arguments discussed above suggest that bulk Auger transition rates should take the form

$$R_{CHCC} \propto n^2 p \exp(-\frac{E_a^{CHCC}}{k_B T}) \tag{1.2a}$$

$$R_{CHSH} \propto p^2 n \exp(-\frac{E_a^{CHSH}}{k_B T}) \tag{1.2b}$$

$$R_{CHLH} \propto p^2 n \exp(-\frac{E_a^{CHLH}}{k_B T}) \tag{1.2c}$$

where E_a is the activation energy for the Auger process given by the superscript (the activation energies for the different Auger processes will not be the same). k_B is the Boltzmann constant and T is the temperature.

Detailed calculations of the transition rate [11], [13], [14] (with the assumptions of isotropic, parabolic energy bands, and using Boltzmann statistics with quasi- Fermi levels) give results that agree with equations (1.2a,b,c), but they also predict the form of the prefactor.

Equations (1.2a,b,c) indicate that Auger recombination should be more important as :

(i) The injected carrier density increases.

(ii) The temperature increases.

(iii) The activation energy decreases.

As will be shown in Chapter Two, the activation energy of the CHCC and CHLH Auger processes are proportional to E_g, the energy gap between the conduction and valence bands. For the CHSH process, however, the activation energy is proportional to $(E_g - \Delta)$, where Δ is the spin-orbit splitting. Thus, materials that have $E_g \approx \Delta$ (e.g. GaSb) are expected to have high Auger transition rates. The fact that Auger processes are more important as the

activation energy decreases means that although Auger recombination is considered important in InGaAsP, it is thought to be unimportant in GaAs, and in the latter case, the T_o value can be explained by the temperature dependence of the carrier distribution functions.

Now that Auger recombination in bulk semiconductors has been introduced, the reasons for using quantum wells and quantum well wires as lasers will be discussed in the next section, and finally, an introduction to Auger rates in these low dimensional structures will be given.

1.3 QUANTUM WELL AND QUANTUM WELL WIRE LASERS

A quantum well (QW) laser is essentially similar to a DH laser, except that the thickness of the active layer is smaller than the de Broglie wavelength of the carriers. Thus, quantum size effects are important, and the carriers are confined in a quantum well. The carriers in the quantum well behave as a 2D electron gas (2DEG), and it is this behaviour that leads to the advantageous properties of the QW laser. A good introduction to QW heterostructure lasers has been given by Holonyak et al [18].

If parabolic subbands are assumed for the QW, then the density of confined states is step-like, whereas the assumption of parabolic bands for a bulk semiconductor leads to a parabolic density of states in conventional DH lasers (see Figure (1.3)). The step-like density of states has been predicted to lead to a narrower gain spectrum (more favourable for single mode operation) and the maximum of the gain spectrum occurs at a wavelength corresponding to the QW bandgap [19]. The high density of states at the QW band edge (compared to the vanishing density of states at the band edge in a DH laser) also leads to low threshold currents. In addition to the advantages that the form of the density of states of the 2DEG has for the threshold current of a laser, there is an added flexibility in the choice of emission wavelength of QW lasers, since altering the width of the active layer alters the QW bandgap. In addition to the above advantages, dynamic properties of QW lasers are thought to be excellent [20]. For a single QW, the optical confinement factor is likely to be small (the optical confinement factor is defined to be the fraction of radiation energy in the active layer) and in practical devices, multiple quantum wells would normally be used.

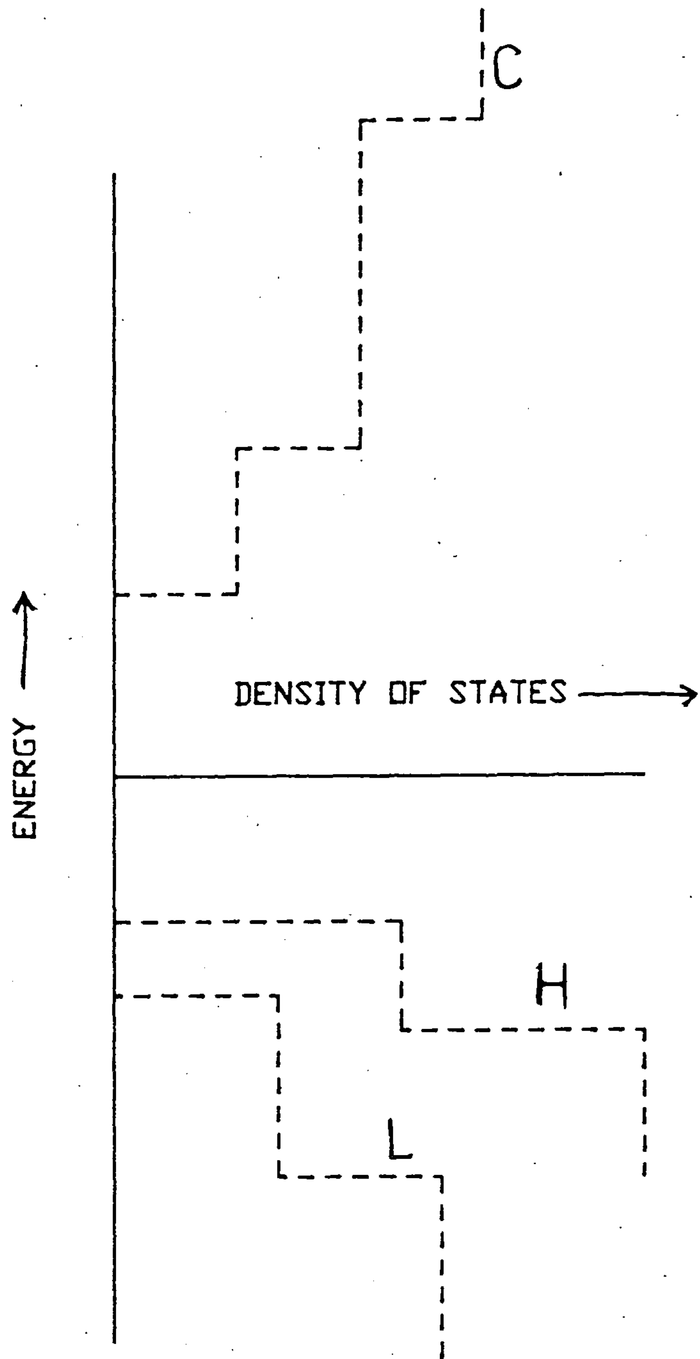

Figure (1.3) - The density of states for a 2DEG in a QW for the conduction, heavy hole, and light hole subbands (the subbands have been assumed to be parabolic).

Throughout this thesis the constituent semiconductors making up the QW have been assumed to be lattice matched. However, a recent suggestion [21] is to use a strained quantum well, and it is thought that this can reduce both intervalence band absorption and Auger recombination.

A quantum well wire (a semiconductor structure in which carriers are confined in two dimensions and free motion is possible in the third, axial direction) would also be expected to have advantageous properties as a laser, since the density of confined states for such a system would be divergent at the band edge.

In both QWs and QWWs, both the radiative and non-radiative recombination rates are expected to change from the bulk values, and it is important to examine all recombination processes in these low-dimensional structures.

Dutta [22] has calculated the threshold current of GaAs/GaAlAs quantum well lasers by evaluating the radiative recombination rate, and he concludes that the T_o value of a 200Å $GaAs/Ga_{0.48}Al_{0.52}As$ QW laser would be higher than the value in bulk GaAs, and the threshold current would be smaller. In another calculation [23], the T_o values of GaAs/GaAlAs lasers have been calculated for bulk lasers, QW lasers, QWW lasers, and, also, quantum box lasers. In that calculation, the conclusion was that T_o increased as the number of dimensions of free motion for the carriers decreased, and some experimental verification was given. In [22] and [23], non-radiative recombination was not included in the calculation (which is reasonable in GaAs), but for longer wavelength lasers, non-radiative recombination is likely to be more important.

In the next section, Auger recombination in QWs and QWWs is introduced and the differences between Auger recombination in a QW and in the bulk are emphasised.

1.4 AUGER RECOMBINATION IN QWs AND QWWs

Auger recombination in a QW differs from that in bulk semiconductors because of the different electronic structure of the QW (see Figure (1.4)). Carriers may be confined to the well, in which case they occupy a continuum of states derived from the set of subbands corresponding to the bound states of the QW, or they may have sufficient energy to propagate throughout the whole system, the so-called unbound states. Possible CHCC Auger transitions in a QW are illustrated in Figure (1.5). Figure (1.5a) illustrates a CHCC Auger process in a QW in which all the participating carriers are in ground state subbands of the QW. However, other QW Auger processes are possible for example, the excited particle could be in a higher subband (Figures (1.5b) and (1.5c)), or more than one of the carriers participating in the Auger process could be in higher subbands (Figure (1.5d)). All important combinations of CHCC Auger processes in 1.3μm and 1.55μm InGaAsP/InP QWs have been examined by Smith [1] and by Smith et al [24]. The Auger processes that were examined in this previous work [1], [24], included those in which all the participating carriers were in bound states of the QW, the so-called 'bound-bound' Auger processes. Also, Auger processes in which three of the states were bound, but the final state of the excited particle was unbound were examined. The importance of such 'bound-unbound' transitions is that processes can occur where the activation energy is zero, and so the Auger transition may have an enhanced probability. Naturally, a detailed treatment of the 'bound-unbound' processes takes account of the matrix elements of such processes, which are also important in determining the transition rates. In Chapter Two, the work

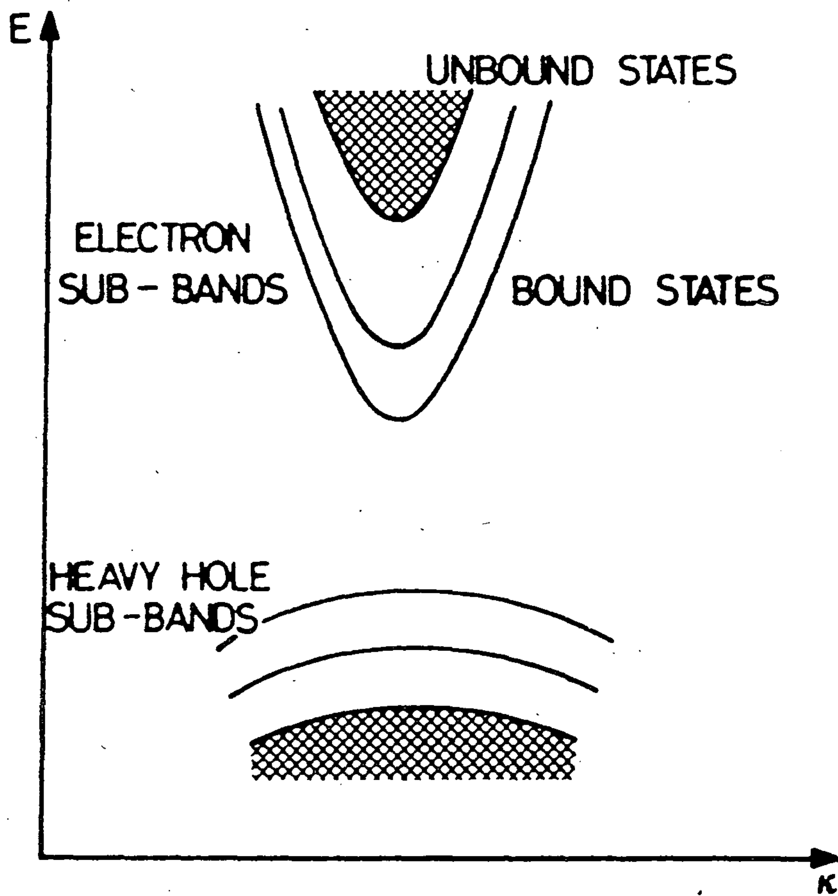

Figure 1·4 The bandstructure of the quantum well system. The discrete subbands corresponding to the bound states are shown, with only heavy holes being considered in the valence band. The continuum of subbands corresponding to the unbound states is represented by hatching. κ-in-plane wavevector.

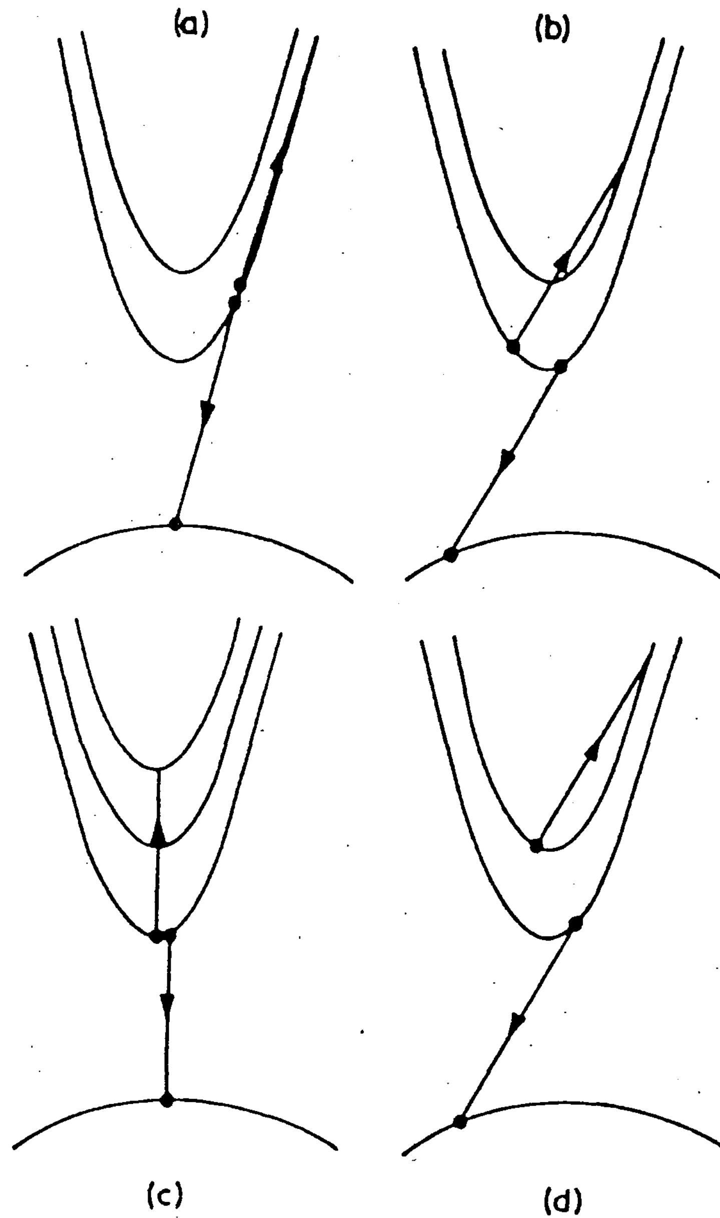

Figure (1.5) - Some typical CHCC Auger processes in a QW. See text for more explanation.

of Smith [1] and Smith et al [24] is extended to cover the possible 'bound-bound' and 'bound-unbound' CHLH and CHSH Auger processes in the QW, with numerical results for the InGaAsP/InP QW presented in Chapter Four.

Auger recombination in a quantum well wire is examined in Chapter Three. In a QWW, subbands are formed in the same way as for the QW, and so no new features are found in the QWW Auger results.

REFERENCES FOR CHAPTER ONE

[1] C. Smith, PhD Thesis, University of Durham, 1985 (unpublished).

[2] Y. Horikoshi, 'Temperature dependence of laser threshold current', in 'InGaAsP Alloy Semiconductors', edited by T.P. Pearsall, New York:Wiley, 1982, pages 379-411.

[3] N.K. Dutta and R.J. Nelson, J.Appl.Phys., 53, (1982), 74.

[4] A. Sugimura, IEEE J.Quant.Elect., QE-17, (1981), 627.

[5] A. Haug, IEEE J.Quant.Elect., QE-21, (1985), 716.

[6] A.R. Adams, M. Asada, Y. Suematsu and S. Arai, Jpn.J.Appl.Phys., 19, (1980), L621.

[7] G.N. Childs, S. Brand and R.A. Abram, Semicond. Sci. Technol., 1, (1986), 116.

[8] A.R. Adams, private communication (1987).

[9] A. Haug and H. Burkhard, IEE Proc. Part J (Optoelect.), 134, (1987), 117.

[10] W. Zhuang, B. Zheng, J. Xu, Y. Li, J. Xu and P. Chen, IEEE J.Quant.Elect., QE-21, (1985), 712.

[11] A.R. Beattie and P.T. Landsberg, Proc.Roy.Soc.,A, 249, (1958), 16.

[12] A.R. Beattie, PhD Thesis, University of Aberdeen, 1959.

[13] A.R. Beattie and G. Smith, Phys.Stat.Sol., 19, (1967), 577.

[14] A. Haug, D. Kerkhoff and W. Lochmann, Phys.Stat.Sol.(b), 89, (1978), 357.

[15] M. Takeshima, J.Appl.Phys., 43, (1972), 4114.

[16] K.H. Zschauer, Solid State Commun., 7, (1969), 1709.

[17] L.I. Schiff, 'Quantum Mechanics', Third Edition (published by McGraw Hill, 1968).

[18] N. Holonyak, Jr., R.M. Kolbas, R.D. Dupuis and P.D. Dapkus, IEEE J.Quant.Elect., QE-16, (1980), 170.

[19] M.G. Burt, Elect.Lett., 19, (1983), 210.

[20] Y. Arakawa and A. Yariv, IEEE J.Quant.Elect., QE-22, (1986), 1887.

[21] E.P. O'Reilly, K.C. Heasman, A.R. Adams and G.P. Witchlow, Superlatt.Microstruct., 3, (1987), 99.

[22] N.K. Dutta, J.Appl.Phys., 53, (1982), 7211.

[23] Y. Arakawa and H. Sakaki, Appl.Phys.Lett., 40, (1982), 939.

[24] C. Smith, R.A. Abram and M.G. Burt, Superlatt.Microstruct., 1, (1985), 119.

CHAPTER TWO

CALCULATION OF THE QUANTUM WELL CHSH AUGER RECOMBINATION RATE

INTRODUCTION

A calculation of the CHSH Auger recombination rate in a single quantum well (QW) is described. The major assumptions of the model are discussed, and an algebraic expression for the QW CHSH Auger rate is presented, for the case where all the carriers reside in their ground state subbands. Once the expression for the CHSH rate has been obtained, a change of variables immediately gives the rates of other important Auger processes such as CHCC, CHLH, CLSL, CHHH, etc.

In addition to the algebraic calculations referred to above, the evaluation of Auger transitions involving other bound or unbound states of the QW is presented and discussed.

2.1 MODELLING THE QUANTUM WELL

The QW is assumed to have abrupt interfaces between the well and barrier materials, and thus a square well potential is presented to the carriers (ignoring any charge transfer effects). For the particular well and barrier materials of interest in this thesis, the QW is as shown in Figure (2.1). The conduction and valence band discontinuities, $\triangle E_c$ and $\triangle E_v$, depend on the constituent materials of the QW structure. Throughout this thesis, unless otherwise stated, the materials making up the QW are assumed to be lattice matched, and so the heavy and light hole discontinuities are identical (in QW structures which have constituent materials of different lattice constants, the lattice constants parallel and perpendicular to the QW interfaces are unequal which breaks the original cubic symmetry of the bulk semiconductors, removing the light-hole, heavy-hole degeneracy leading to different discontinuities for the light and heavy holes).

Typical values for $\triangle E_v$ for a $GaAs/Ga_{1-x}Al_xAs$ QW are $\triangle E_v = 0.55x\ eV$ for $0 \leq x \leq 1$ [1]. In this thesis, the majority of the numerical results presented will be for the quaternary alloy $In_{1-x}Ga_xAs_yP_{1-y}$ (the well material) lattice matched to InP (the barrier material). For this system, $\triangle E_c$ is assumed to be twice that of $\triangle E_v$ [2], as was assumed by Smith [3], and Chiu and Yariv [4] in their QW Auger calculations.

The energy levels of the confined states of the quantum well have been calculated on the basis of a standard finite square well model [5]. The potential seen by the carriers is assumed to be a finite square well, and so the carrier wavefunctions are the product of a slowly varying envelope function multiplied by a rapidly varying Bloch periodic part. The envelope part of the wavefunction

Figure (2.1) - Schematic diagram of a quantum well (QW) of width L formed between semiconductors A and B (A being the well material and B being the barrier material). Semiconductor A has a bandgap of E(A), whereas B has a bandgap of E(B). The conduction and valence band offsets are ΔE_c and ΔE_v respectively.

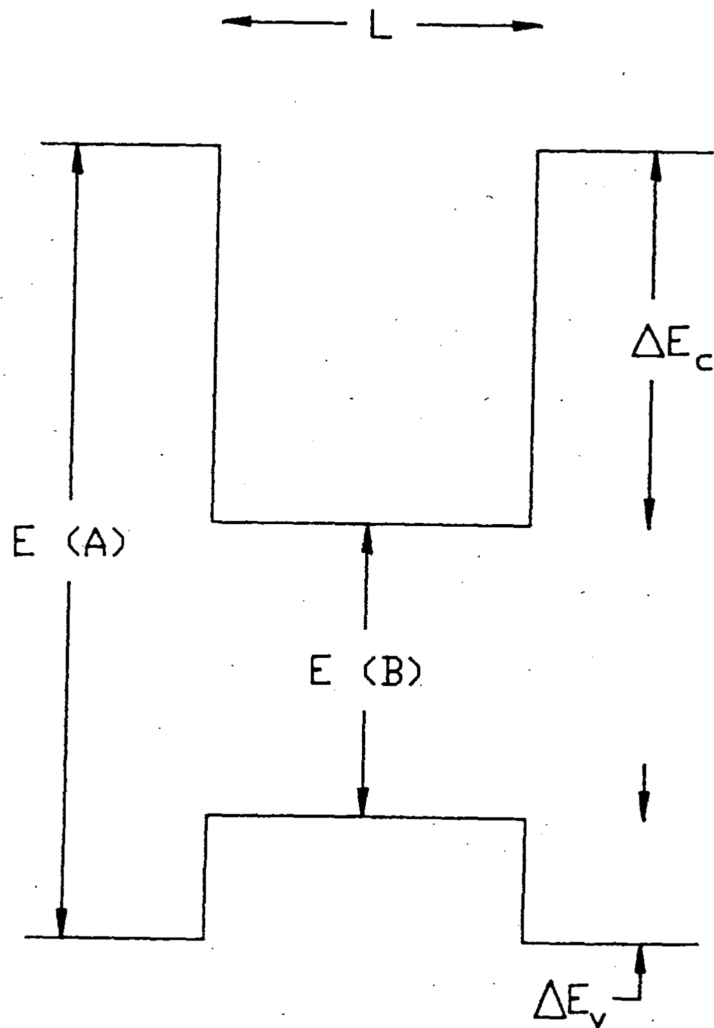

is assumed to be a simple sinusoidal function and so the calculation reduces to a 'particle in a box' problem.

If the z direction is chosen to be that direction perpendicular to the QW interfaces, then the carriers are confined in the z direction, but are free to move in the plane of the QW (the (x,y) plane), and so a subband is formed for each confined energy level (see Figure (2.2)).

For simplicity, inital calculations of the QW Auger rates are performed with the assumptions of isotropic, parabolic subbands. In addition, all subbands are assumed to have the effective mass appropriate to the material of the well region.

One of the reasons why the quantum well has been considered as useful for the active region of a semiconductor laser is that the density of states is step-like, within the parabolic subband approximation. This is due to the two-dimensional character of the motion of the carriers. The step-like density of states has been predicted to lead to an improved gain spectrum for the QW [6].

For the ground state confined level, the assumption of parabolic subbands leads to

$$E = E_1 + \frac{\hbar^2 \underline{k}^2}{2m^*} \tag{2.1}$$

where $\underline{k}$ is the in-plane wavevector, and m^* is the carrier effective mass of the subband.

The density of states of the lowest subband, $g(E)$ is given by

$$g(E) = \frac{2}{(2\pi)^2} A \int \delta(E - E_1 - \frac{\hbar^2 \underline{k}^2}{2m^*}) d\underline{k} \tag{2.2}$$

Figure (2.2) - Schematic diagram showing the energy levels of the QW and the associated in-plane dispersion relations.

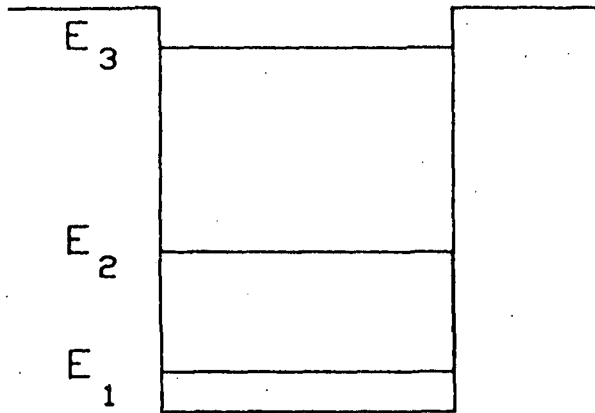

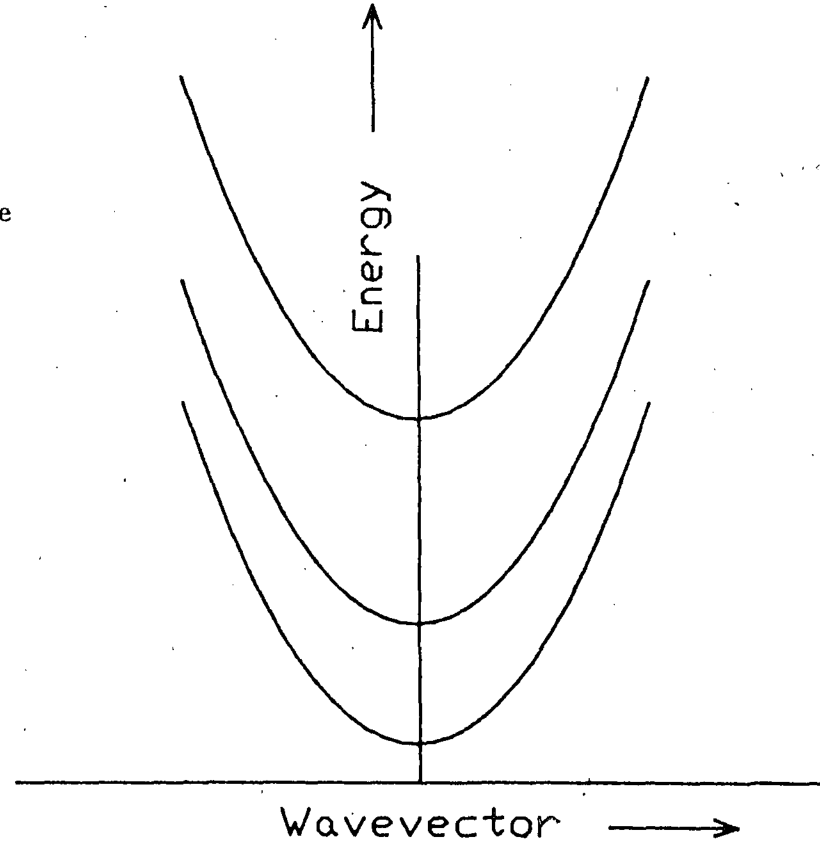

$$\Rightarrow \quad g(E) = \frac{m^* A}{\pi \hbar^2} \theta(E - E_1) \tag{2.3}$$

where A is the area in the plane of the QW, and $\theta(x)$ is the step function. A factor of two has been included to take account of the spin degeneracy. There is an obvious extension to include higher lying confined states, and the final expression for the density of confined states is

$$g(E) = \frac{m^* A}{\pi \hbar^2} \sum_{i=1}^{N} \theta(E - E_i) \tag{2.4}$$

where N is the total number of confined states in that band, and E_i is the energy level of the confined state with quantum number i. The density of states for a QW with parabolic subbands is illustrated in Figure (2.3).

In addition to Auger transitions involving bound states, there is also the possibility of transitions involving unbound states. An unbound state is one that has a kinetic energy due to motion in the z direction that exceeds the energy of the confining barrier. Smith [3] first pointed out that Auger transitions in which the final state of the excited carrier was unbound could be important, particularly at small well widths. The density of states of the unbound levels corresponds to the usual three dimensional density of states, since unbound carriers are free to move both parallel and perpendicular to the QW interfaces.

Figure (2.3) - Diagram illustrating the step like density of states of a QW (parabolic subbands have been assumed).

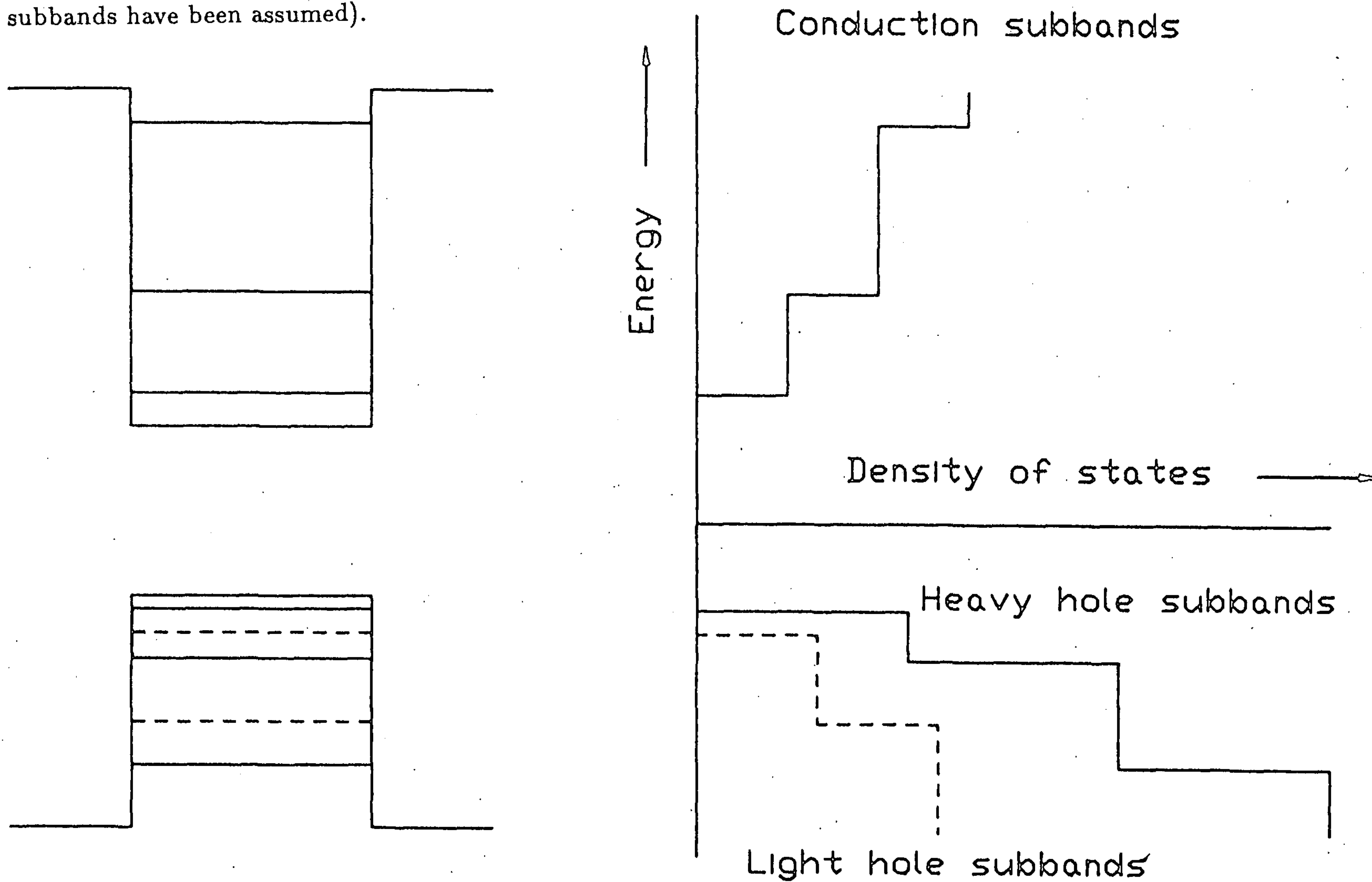

2.2 THE QW CHSH AUGER RATE

In a quantum well, the calculation of Auger transition rates is more difficult than for the bulk case, since the QW has a more complicated electronic structure. For example, the simplest CHCC process in the bulk simply involves one conduction band and one heavy-hole band. However, in a QW, there can be many conduction subbands, and many heavy-hole subbands, and to calculate the QW CHCC Auger rate, all possible Auger transitions must be taken into account. The total Auger rate in a QW can be split into two contributions, the bound-bound contribution and the bound-unbound contribution. The bound-bound contribution is the sum of the rates of all possible Auger transitions that involve bound (i.e. confined) states only. The bound-unbound contribution is the sum of the rates of all possible Auger transitions that involve bound states except for the final excited (Auger) carrier, that carrier being in an unbound state. Any unbound-unbound contribution to the total QW Auger rate is assumed to be negligible on the grounds that there will be very few carriers in unbound states initially because of the size of the band discontinuities.

Smith et al [7] have reported the most detailed Auger calculation in a QW to date, and in their calculation all possible bound-bound CHCC intersubband processes were taken into account, along with the most important bound-unbound CHCC Auger processes. However, there are many other Auger transitions in addition to the CHCC process, and simple estimates suggest that processes such as CHSH and CHLH may be as significant as the CHCC process. Hence, this chapter describes the calculation of the QW CHSH Auger transition rate, from which expressions for the transition rates of all the other important Auger processes may be obtained.

In order to calculate the Auger transition rate, the electron- electron interaction is treated as the perturbation, H_I. The transition rate per unit volume, R, of the Auger process is then given by Fermi's Golden Rule

$$R = \frac{1}{AL}\frac{2\pi}{\hbar}\sum P|\langle\Psi_i|H_I|\Psi_f\rangle|^2\delta(E) \tag{2.5}$$

where Ψ_i is the initial wavefunction for the system, Ψ_f is the final wavefunction. P is a statistical factor which is needed to weight each transition according to the probability of the states being appropriately occupied. This term will be discussed in detail in the next Section. $\delta(E)$ represents the physical fact that energy is conserved. The summation is carried out over all possible combinations of initial and final states.

2.2.1 THE STATISTICAL FACTOR

In equation (2.5), P, the so called statistical factor, gives the probability that any given set of initial and final states is occupied by carriers in such a way that an Auger transition can occur, minus the probability of occupancy for the inverse process of impact ionisation. Referring to Figure (2.4), for the CHSH Auger process to occur, states 1 and 2 need to be occupied by electrons, whereas states 3 and 4 need to be occupied by holes. The statistical factor is the probability of the above configuration occurring, minus the probability of the configuration for the inverse process occurring. Thus, we may write

$$P = P_{\text{Auger}} - P_{\text{Impact}} \tag{2.6}$$

If it is assumed that there is a single conduction band quasi-Fermi level, F_c, appropriate for all subbands, and similarly a single valence band quasi-Fermi level, F_v, the statistical factor may be written as :

$$\begin{aligned} P = & f_{c,n1}(\underline{k}_1) f_{v,n3}(\underline{k}_3) f_{v,n4}(\underline{k}_4)(1 - f_{v,n2}(\underline{k}_2)) \\ & - (1 - f_{c,n1}(\underline{k}_1))(1 - f_{v,n3}(\underline{k}_3))(1 - f_{v,n4}(\underline{k}_4)) f_{v,n2}(\underline{k}_2) \end{aligned} \tag{2.7}$$

where $n1, n2, n3, n4$ are subband indices for states 1,2,3,and 4 respectively. $f_{c,ni}(\underline{k})$ is the distribution function for the conduction band (i.e. for electron occupancy) and $f_{v,ni}(\underline{k})$ is the distribution function for the valence band (i.e. for hole occupancy). For the cases of interest in this thesis we may write

$$f_{c,ni}(\underline{k}) = \frac{1}{\lambda + \exp[\beta(E_{c,ni}(\underline{k}) - F_c)]} \tag{2.8}$$

and

Figure (2.4) - Diagram illustrating the CHSH Auger process for the QW. Other subbands of the QW have been omitted for clarity.

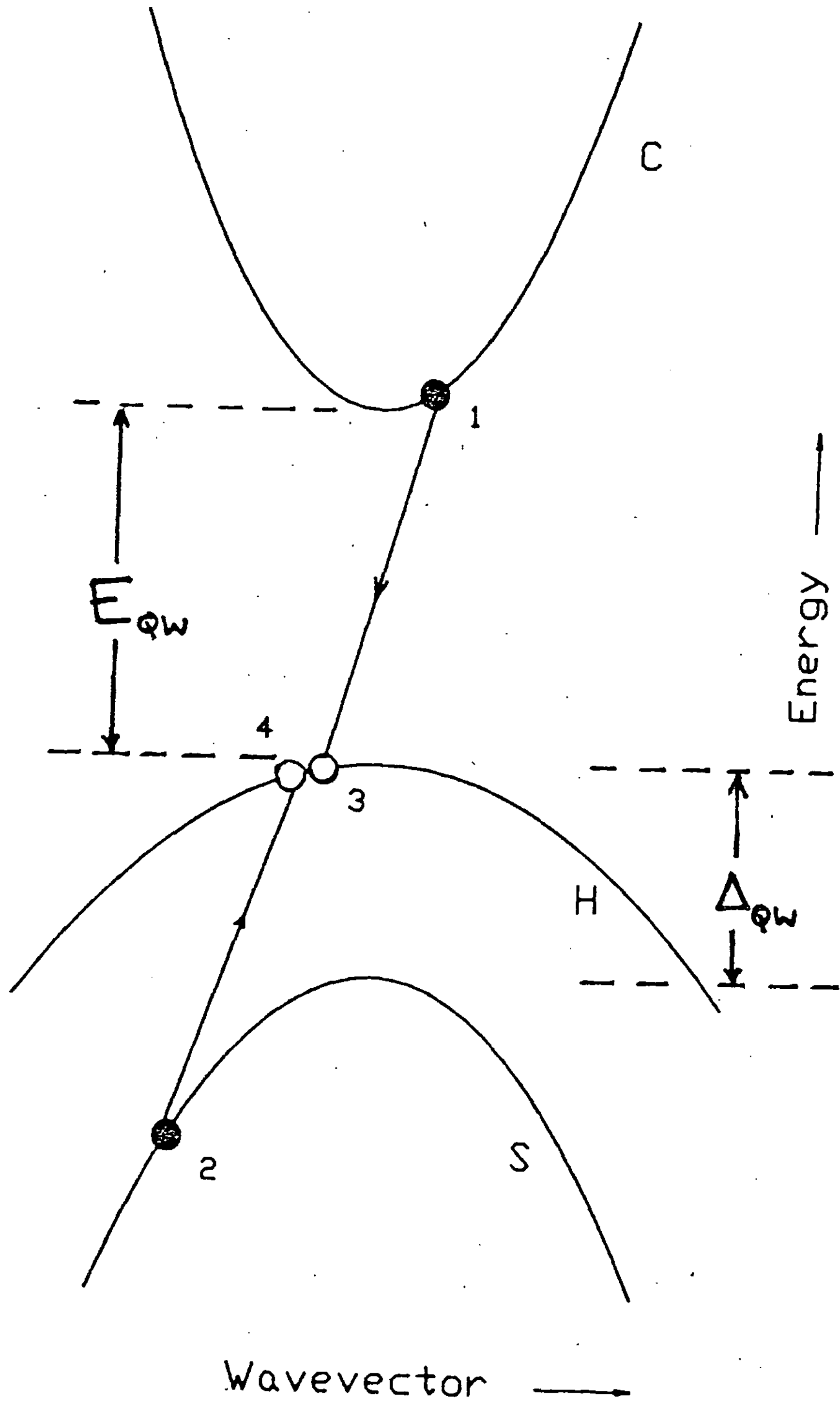

$$f_{v,ni}(\underline{k}) = \frac{1}{\lambda + \exp[\beta(F_v - E_{v,ni}(\underline{k}))]} \quad (2.9)$$

where $\beta = (1/k_B T)$, k_B is Boltzmann's constant, and T is the temperature. λ is equal to one if Fermi-Dirac statistics are used and equals zero if Boltzmann statistics are used.

Using the expressions for the distribution functions above (assuming that $\lambda = 1$), and anticipating the energy conservation, $E_1 + E_2 = E_3 + E_4$, from Fermi's Golden Rule, it is found that

$$P = \{1 - \exp[\beta(F_v - F_c)]\} f_{c,n1}(\underline{k}_1) f_{v,n3}(\underline{k}_3) f_{v,n4}(\underline{k}_4)(1 - f_{v,n2}(\underline{k}_2)) \quad (2.10)$$

Where the temperature, T, appearing in the distribution functions has been assumed to be the same for both electrons and holes.

The assumption of using one quasi-Fermi level for the electrons implies that the carriers in the conduction subbands form a gas in thermal equilibrium. Also, the holes in the valence subbands are assumed to be in thermal equilibrium. However, since we are interested in lasers, where excess electrons and holes are produced by electrical injection, the system as a whole will not be in thermal equilibrium.

Haug [8] has shown that Boltzmann statistics give an accurate prediction of Auger rates in bulk GaSb even under conditions of degeneracy until carrier densities of $n = p \approx 10^{19}\mathrm{cm}^{-3}$ are reached (at 300 K). Since typical carrier densities in semiconductor lasers are about $10^{18}\mathrm{cm}^{-3}$, the use of Boltzmann statistics is quite adequate. In this thesis we are not specifically interested in GaSb, but the conclusion reached by Haug [8] for that material will be shown (in Chapter Five) to be valid for similar materials. The use of Boltzmann statistics

in the QW can be shown to be reliable also, but in that case a correction factor must be applied at the end of the calculation. These points will be discussed in considerable detail in Chapter Five.

The use of Boltzmann statistics can simplify equation (2.10), which reduces to

$$P = \{\exp[\beta(F_c - F_v)] - 1\} \exp[\beta(E_2 - F_v)] \tag{2.11}$$

This is the expression that will be used throughout the rest of this chapter in the initial QW CHSH Auger calculations.

2.2.2 THE MATRIX ELEMENT FOR THE AUGER PROCESS

The assumption is made that the electron-electron interaction can be written as $V(\underline{r})$, where $\underline{r} = \underline{r}_2 - \underline{r}_1$, and $\underline{r}_1$, $\underline{r}_2$ are the position vectors of the initial carriers. $V(\underline{r})$ is assumed to depend on the magnitude of $\underline{r}$ only, so that $V(\underline{r}) = V(r)$. The actual form of $V(r)$ will be written down explicitly later this section.

The initial and final wavefunctions for the states involved in the Auger transition are also required. If carriers in states 1 and 2 have position vectors $\underline{r}_1$ and $\underline{r}_2$, and have spin wavefunctions σ_1 and σ_2, then the wavefunction for the initial state (assuming weak spin orbit interaction) can be written as

$$\Psi_i = \frac{1}{\sqrt{2}}\{\phi_1(\underline{r}_1)\sigma_1(1)\phi_2(\underline{r}_2)\sigma_2(2) - \phi_1(\underline{r}_2)\sigma_1(2)\phi_2(\underline{r}_1)\sigma_2(1)\} \tag{2.12}$$

and the final state wavefunction is

$$\Psi_f = \frac{1}{\sqrt{2}}\{\phi_3(\underline{r}_1)\sigma_3(1)\phi_4(\underline{r}_2)\sigma_4(2) - \phi_3(\underline{r}_2)\sigma_3(2)\phi_4(\underline{r}_1)\sigma_4(1)\} \tag{2.13}$$

where the $\phi_i(\underline{r})$ represents the spatial part of the wavefunction for the carrier in state i. In Fermi's Golden Rule, the matrix element, M, needs to be evaluated, where

$$M = \langle \Psi_f | V(r) | \Psi_i \rangle \tag{2.14}$$

Using the expressions for Ψ_i and Ψ_f, it is found by straightforward algebra, that

$$M = M_D - M_{EX} \tag{2.15}$$

with

$$M_D = \int \phi_3^*(\underline{r}_1)\phi_4^*(\underline{r}_2)V(r)\phi_1(\underline{r}_1)\phi_2(\underline{r}_2)\delta_{S1,S3}\delta_{S2,S4}d\underline{r}_1 d\underline{r}_2 \tag{2.16}$$

and

$$M_{EX} = \int \phi_3^*(\underline{r}_2)\phi_4^*(\underline{r}_1)V(r)\phi_1(\underline{r}_1)\phi_2(\underline{r}_2)\delta_{S1,S4}\delta_{S2,S3}d\underline{r}_1 d\underline{r}_2 \tag{2.17}$$

The Kronecker deltas derive from the orthonormality of the spin functions.

In terms of M_D and M_{EX} the modulus squared of M, after summing over the spin variables, can be expressed as

$$|M|^2 = 2\{|M_D|^2 + |M_{EX}|^2 + |M_D - M_{EX}|^2\} \tag{2.18}$$

The term in $|M_D|^2$ arises from Auger processes in which the initial states have opposite spins that are unchanged during the Auger transition. The term in $|M_{EX}|^2$ arises from Auger processes in which the initial states have opposite spins that are changed during the Auger transition, and the term in $|M_D - M_{EX}|^2$ arises from Auger processes in which the initial states have identical spins that are conserved during the transition. The factor of two arises since there are two ways of choosing the initial spin. Useful discussions of the possible spin configurations in Auger transitions are given in references [9] and [10]. It is clear that

$$|M_D - M_{EX}|^2 \leq |M_D|^2 + |M_{EX}|^2 \tag{2.19}$$

Thus, for any particular combination of states

$$|M|^2 = 2\eta\{|M_D|^2 + |M_{EX}|^2\} \tag{2.20}$$

Where η lies between 1 and 2. Note that the above relation is a purely numerical relation, since the various terms in equation (2.20) will have different functional forms. In equation (2.18), the term in $|M_D - M_{EX}|^2$ comes from electron collisions involving electrons with like spins. For this case, the spatial part of the initial wavefunction will be antisymmetrical, and so the Coulomb interaction will be reduced compared to the case of electrons with opposite spins, due to the average separation of the electrons being larger. It is physically reasonable to expect that $|M_D - M_{EX}|^2 \ll |M_D|^2 + |M_{EX}|^2$, the appropriate value for η is thus close to one. In fact, Beattie and Landsberg [11] note that the term in $|M_D - M_{EX}|^2$ vanishes for the most probable transitions. If a value of η of 1 is chosen, then the numerical relation of equation (2.20) may be rewritten as

$$|M|^2 = 4|M_D|^2 \tag{2.21}$$

In this approximation, Smith [3] writes the matrix element for the CHCC QW Auger process as

$$|M|^2 = \{2 + 2\delta_{n1,n2}\}|M_D|^2 \tag{2.22}$$

With n1 and n2 being the quantum numbers of the initial states involved in the QW Auger process. The above equation is derived from the fact that for initial states in subbands with different quantum numbers, the exchange process can be considered as a different intersubband transition (see Figure (2.5)), which will be counted separately. In order not to overestimate the effects of Auger processes involving initial states in different subbands, a factor $\delta_{n1,n2}$ is used.

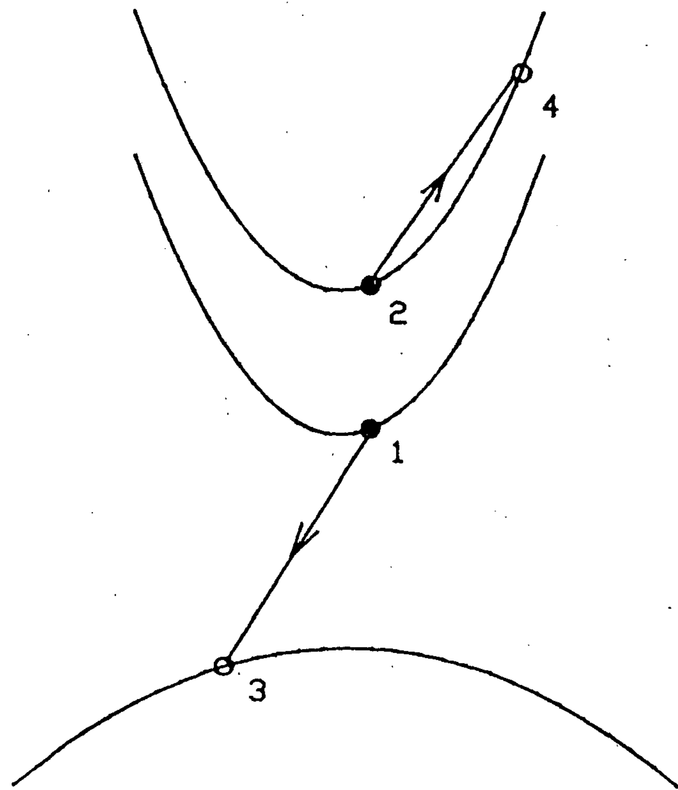

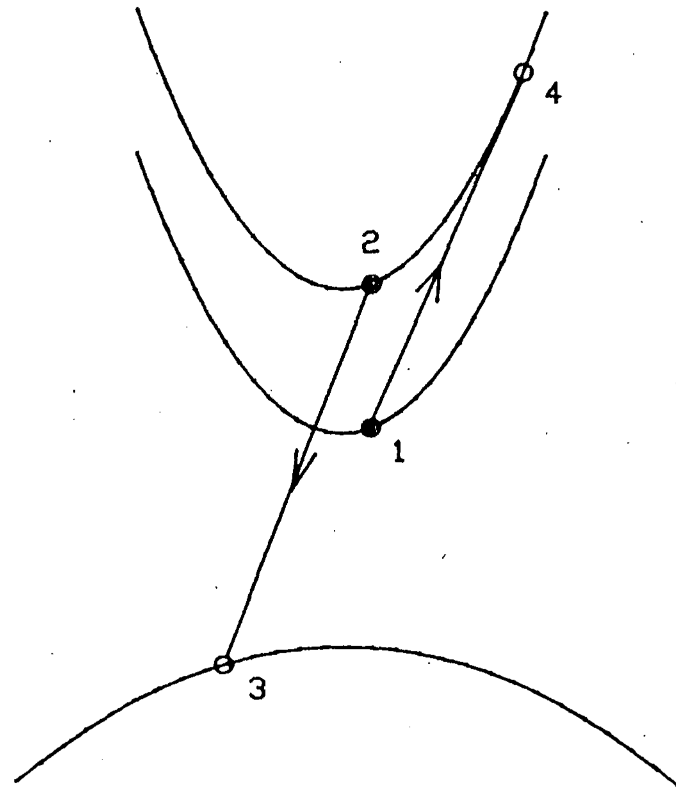

Figure (2.5) - Diagram showing how the CHCC exchange Auger process may be considered as a different, direct, intersubband transition.

For the CHSH and CHLH QW Auger processes, a factor of $(2 + 2\delta_{n3,n4})$ is required.

To proceed further with the calculation of the matrix element for the Auger process, an expression for the electron-electron interaction, $V(r)$, is required. In this thesis the expression that will be used for $V(r)$ is

$$V(r) = V(|\underline{r}_2 - \underline{r}_1|) = \frac{e^2}{4\pi\epsilon|\underline{r}_2 - \underline{r}_1|} \tag{2.23}$$

Where ϵ is the product of the relative permittivity and the free space permittivity. In recent years there has been a certain amount of controversy concerning the screening of the Coulomb interaction by free carriers. Equation (2.23) follows from a description in terms of dynamic screening [12] and the concept that the Auger transition takes place so quickly that the other carriers are unable to respond fast enough to significantly screen the interaction (in terms of energies, the transition energy is much greater than the characteristic energies in the response of the electron gas formed by the free carriers) The use of equation (2.23) is in contrast to the Thomas-Fermi screening (i.e. a static screening approximation) originally proposed by Beattie and Landsberg [11], which is

$$V(r)_{BL} = \frac{e^2}{4\pi\epsilon r}\exp(-\lambda r) \tag{2.24}$$

Where λ^{-1} is the screening radius. Rather later, Haug and Ekardt [13] proposed a screening scheme where the direct matrix element, M_D, of the Coulomb interaction, was screened dynamically, but the exchange term, M_{EX} was not screened. However, this has now been shown to be incorrect [14], [15].

By using equation (2.23) for $V(r)$, our results will be based on what is now widely accepted to be the correct description and will be directly comparable to those of Smith [3].

To evaluate the direct matrix element, M_D, the spatial part of the QW wavefunctions of the states involved in the Auger transition needs to be specified.

The QW wavefunctions will differ from those in a bulk semiconductor since the rapidly varying Bloch periodic parts of the wavefunction are modulated by a slowly varying envelope function, the period of which is of the same order of magnitude as the QW width.

For states that have energies lying in the well, the envelope function has a sinusoidal form, whereas outside the well, the envelope function will be evanescent (see Figure (2.6)). For a QW with a reasonably large potential step (e.g. about 0.3 eV), and which has a well width larger than any decay length in the barrier material, it is a good approximation to ignore the evanescent parts of the confined state wavefunctions.

Hence, the spatial parts of the QW confined state wavefunctions may be written in the following form
For $|z| \leq L/2$, (for even parity states)

$$\phi_m(\underline{r}) = B\sqrt{\frac{V_{cell}}{A}}U_m(\underline{r})\cos(k_{zm}z)\exp(i\underline{\kappa}_m.\underline{\rho}) \tag{2.25a}$$

For $|z| \leq L/2$, (for odd parity states)

$$\phi_m(\underline{r}) = B\sqrt{\frac{V_{cell}}{A}}U_m(\underline{r})\sin(k_{zm}z)\exp(i\underline{\kappa}_m.\underline{\rho}) \tag{2.25b}$$

And, for $|z| \geq L/2$

$$\phi_m(\underline{r}) = 0 \tag{2.26}$$

A is the area in the plane of the QW, B is the normalisation factor associated with the z-dependent part of the wavefunction ; m is the quantum number of

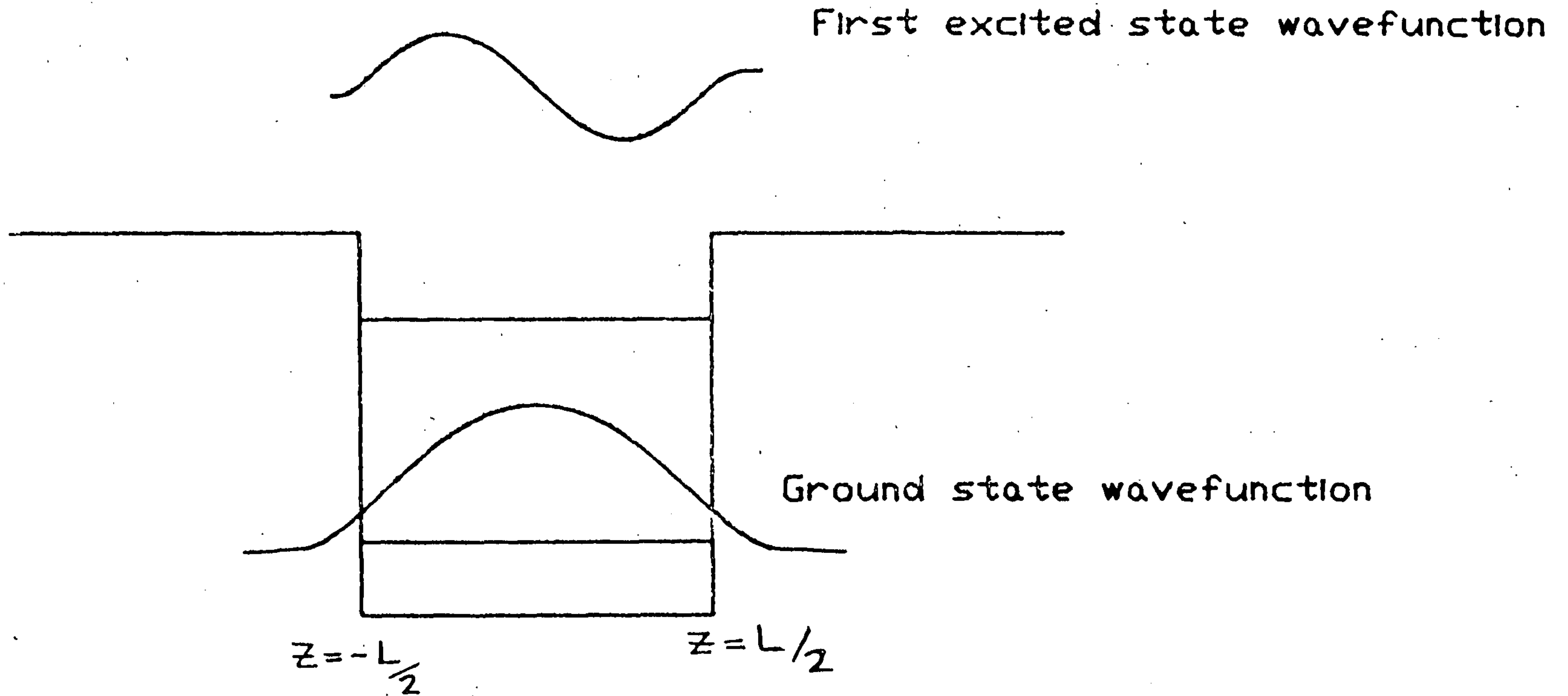

Figure (2.6) - Diagram to illustrate the form of the wavefunctions for the lowest two states of the QW, and the coordinate system used in Chapter Two is also shown.

the subband that the state occupies ; $U_m(\underline{r})$ is a Bloch periodic function ; k_{zm} is the z component of the confined state wavevector ; $\underline{\kappa}$ is the in-plane wavevector and $\underline{\rho}$ is the in-plane position vector. The expressions (2.25) and (2.26) hold for confined states, the extension to unbound states will be discussed at the end of this chapter.

For low lying energy levels in a wide, deep well, it is a good approximation to write

$$k_{zm} = \frac{m\pi}{L} \tag{2.27}$$

For algebraic convenience, the calculation of the Auger matrix element will be performed explicitly only for the case where initial and final states are in the ground state subbands. The changes in the matrix element that occur if the carriers reside in different subbands will be discussed later in the chapter. Choosing the confined state wavevectors to be integer multiples of (π/L) is convenient for algebraic work, but is not an essential assumption of the model. Realistic values of the confined state wavevectors from a finite square well calculation have been incorporated into the numerical calculations that will be discussed in Chapter Four.

From equations (2.16) and (2.23), the matrix element corresponding to the direct term in the electron-electron interaction, M_D, may be written as

$$M_D = \int\int \phi_3^*(\underline{r}_1)\phi_4^*(\underline{r}_2)\frac{e^2}{4\pi\epsilon r}\phi_1(\underline{r}_1)\phi_2(\underline{r}_2)d\underline{r}_1 d\underline{r}_2 \tag{2.28}$$

Following Smith et al [16], it is convenient to express r^{-1} in terms of its Fourier transform

$$\frac{1}{r} = \frac{1}{(2\pi)^3}\int \frac{4\pi}{q^2}\exp(i\underline{q}.\underline{r})d\underline{q} \tag{2.29}$$

From equation (2.29), the matrix element M_D, can be expressed as

$$M_D = (\frac{e^2}{\epsilon})\frac{1}{(2\pi)^3}\int \frac{I_{3,1}(\underline{q})I_{4,2}(-\underline{q})}{\underline{q}^2}d\underline{q} \tag{2.30}$$

With

$$I_{m,n}(\underline{q}) = \int \phi_m^*(\underline{r})\phi_n(\underline{r})\exp(i\underline{q}.\underline{r})d\underline{r} \tag{2.31}$$

The calculation of $I_{3,1}$ and $I_{4,2}$ is carried out using the wavefunctions in equations (2.25) and (2.26). It is convenient to expand the Bloch periodic functions in terms of reciprocal lattice vectors in an analogous way to the method employed in [11]. For a QW of well width much larger than the lattice spacing of the constituent materials making up the QW, the terms with large wavevector denominators may be neglected as discussed in [11], and $I_{m,n}$ can be approximated by $J_{m,n}$, where $J_{m,n}$ is

$$J_{m,n}(\underline{q}) = \frac{(2\pi)^2}{A}\delta(\underline{\kappa}_n - \underline{\kappa}_m + \underline{q}_{\|})\{B^2 M_{m,n}[\frac{-4\pi^2}{L^2}\frac{\sin(q_z L/2)}{q_z(q_z^2 - 4\pi^2/L^2)}]\} \tag{2.32}$$

In equation (2.32), $\underline{q}$ has been written as $(\underline{q}_{\|}, q_z)$, $\underline{q}_{\|}$ being the in-plane component of $\underline{q}$. This expression is valid for the special case where all the carriers involved in the Auger transition reside in their ground state subbands. In equation (2.32)

$$M_{m,n} = \int_{V_{cell}} U_m^*(\underline{r})U_n(\underline{r})d\underline{r} \tag{2.33}$$

It follows that M_D is given by

$$M_D = (\frac{e^2}{\epsilon})\frac{2\pi}{A^2}\delta(\underline{\kappa}_3 + \underline{\kappa}_4 - \underline{\kappa}_1 - \underline{\kappa}_2)\int_{-\infty}^{\infty} \frac{\{3,1,q\}\{4,2,-q\}}{|\underline{\kappa}_3 - \underline{\kappa}_1|^2 + q^2}dq \tag{2.34}$$

Where $\{m, n, q\}$ is the bracketed part, $\{\ldots\}$, of $J_{m,n}(\underline{q})$ in equation (2.32). To simplify the notation, the integral in equation (2.34) will henceforth be denoted by $I(\underline{\kappa}_3 - \underline{\kappa}_1)$ so that

$$M_D = (\frac{e^2}{\epsilon})\frac{2\pi}{A^2}\delta(\underline{\kappa}_1 + \underline{\kappa}_2 - \underline{\kappa}_3 - \underline{\kappa}_4)I(\underline{\kappa}_3 - \underline{\kappa}_1) \quad (2.35)$$

This is the expression for the direct matrix element, M_D, that will be used in the calculation of the QW CHSH Auger rate for the case where all the carriers involved in the Auger transition reside in their respective ground state subbands. Now that an expression for the matrix element, M_D , has been derived, it may be used, along with the statistical factor, P, (equation (2.11)) in Fermi's Golden Rule to calculate the Auger rate.

2.3 USE OF FERMI'S GOLDEN RULE TO CALCULATE THE QW CHSH AUGER RATE

An expression for the CHSH statistical factor, P, was given (equation (2.11)) in Section 2.2.1

$$P = \{\exp[\beta(F_c - F_v)] - 1\} \exp[\beta(E_2 - F_v)] \tag{2.36}$$

An expression for the direct matrix element for the QW CHSH Auger process, assuming all carriers involved in the Auger transition reside in their respective ground state subbands, was derived in Section 2.2.2 (see equation (2.35)).

$$M_D = (\frac{e^2}{\epsilon})\frac{2\pi}{A^2}\delta(\underline{\kappa}_3 + \underline{\kappa}_4 - \underline{\kappa}_1 - \underline{\kappa}_2)I(\underline{\kappa}_3 - \underline{\kappa}_1) \tag{2.37}$$

Using Fermi's Golden Rule (equation (2.5)) and converting the summation over all possible combinations of initial and final states to an integration over $\underline{\kappa}$-space, the Auger rate per unit volume, R, is given by

$$R = (\frac{2\pi}{\hbar})(\frac{e^2}{\epsilon})^2 \frac{1}{(2\pi)^8 L}\{\exp[\beta(F_c - F_v)]\}Q \tag{2.38}$$

The summation over all possible spin configurations will be included at the end of the calculation. It is also assumed that $\exp(\beta(F_c - F_v)) \gg 1$, i.e. that the recombination rate is very much greater than the impact ionisation rate. In equation (2.38) Q is defined as

$$Q = \int\int\int\int I^2(\underline{\kappa}_3 - \underline{\kappa}_1)\exp[\beta(E_2 - F_v)]\delta(\underline{\kappa})\delta(E)d\underline{\kappa}_1 d\underline{\kappa}_2 d\underline{\kappa}_3 d\underline{\kappa}_4 \tag{2.39}$$

where $\underline{\kappa} = \underline{\kappa}_1 + \underline{\kappa}_2 - \underline{\kappa}_3 - \underline{\kappa}_4$, and $E = E_3 + E_4 - E_1 - E_2$.

In order to calculate the integral in equation (2.39), the energy-wavevector dispersion relations in the QW must be known. Ideally, realistic dispersion relations from a QW bandstructure calculation should be used. A method of obtaining realistic bandstructure for a QW or superlattice will be described in Chapter Six. Unfortunately, the use of such realistic energy-wavevector dispersion relations means that algebraic expressions that illustrate the physics of the Auger processes cannot be obtained, and a fully numerical approach must be used. Therefore, in this initial work, isotropic, parabolic QW subbands are assumed. Although this is a drastic simplification, it has the advantage that the Auger rate, R, can be evaluated algebraically and it is a useful starting point for discussions of how non-parabolicity will affect the Auger results. Also it is worth noting that the parabolic subband approach only fails drastically for the excited Auger particle (state 2 in the CHSH process, and state 4 in the CHCC process). In Chapter Five, an estimate will be made of the effects of non-parabolicity on bulk CHCC Auger rates and it is shown that realistic bandstructures produce rates that deviate significantly from those calculated using a parabolic band model. This is because the excited Auger particle lies approximately a bandgap higher than the conduction band edge - and for the materials of interest in this thesis the conduction band is certainly not parabolic in the region of the excited state.

In addition to giving an insight into the physics of the Auger process, the algebraic results obtained from a parabolic band model can be compared to those obtained by other workers, and also compared to bulk rates calculated using similar assumptions.

Referring to Figure (2.7), the energy-wavevector relations for the ground state subbands of the QW may be written as

Figure (2.7) - $E-\underline{\kappa}$ relations for carriers in the ground state subbands of a QW. The zero of energy assumed in the calculations of Chapter Two is also shown.

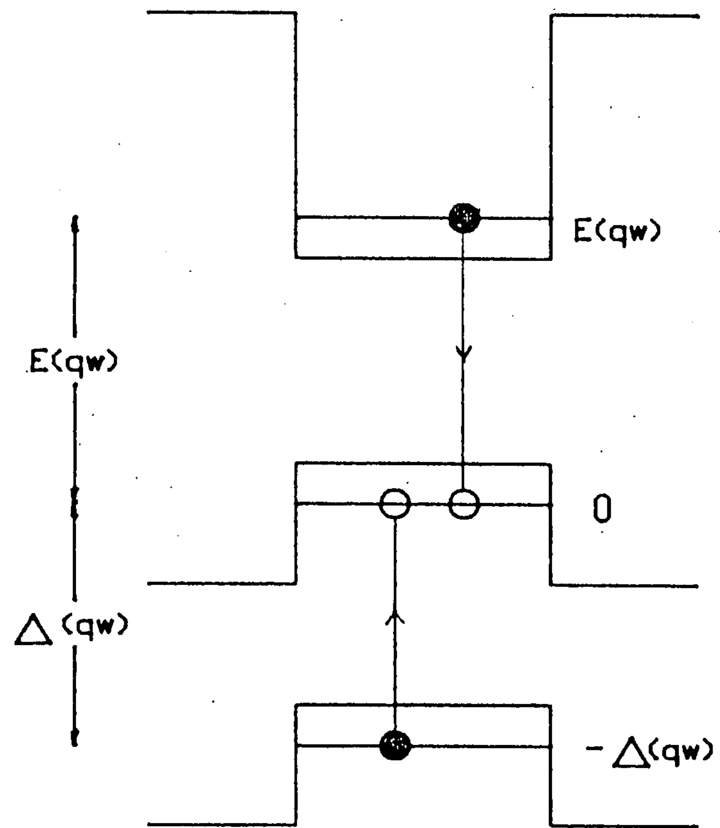

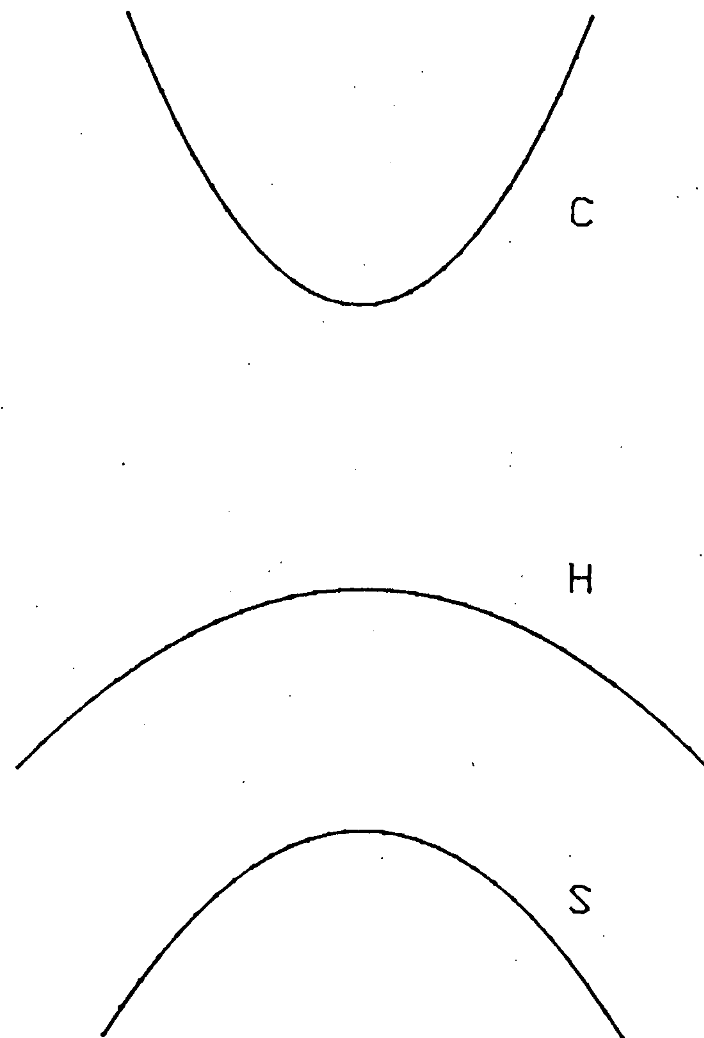

$$E_1 = E_{QW} + \frac{\hbar^2 \underline{\kappa}_1^2}{2m_C} = E_{QW} + \alpha \underline{\kappa}_1^2 \tag{2.40}$$

$$E_2 = -\Delta_{QW} - \frac{\hbar^2 \underline{\kappa}_2^2}{2m_S} = -\Delta_{QW} - \mu_S \alpha \underline{\kappa}_2^2 \tag{2.41}$$

$$E_3 = -\frac{\hbar^2 \underline{\kappa}_3^2}{2m_H} = -\mu_H \alpha \underline{\kappa}_3^2 \tag{2.42}$$

$$E_4 = -\frac{\hbar^2 \underline{\kappa}_4^2}{2m_H} = -\mu_H \alpha \underline{\kappa}_4^2 \tag{2.43}$$

where $\mu_S = m_C/m_S$ and $\mu_H = m_C/m_H$.

Thus, equation (2.39) for the $\underline{\kappa}$-space integral may be rewritten as

$$Q' = \int\int\int\int \exp(-\beta \mu_S \alpha \underline{\kappa}_2^2) I^2(\underline{\kappa}_3 - \underline{\kappa}_1) \delta(\underline{\kappa}) \delta(E) d\underline{\kappa}_1 d\underline{\kappa}_2 d\underline{\kappa}_3 d\underline{\kappa}_4 \tag{2.44}$$

with

$$E = E_{QW} - \Delta_{QW} + \alpha(\underline{\kappa}_1^2 - \mu_S \underline{\kappa}_2^2 + \mu_H(\underline{\kappa}_3^2 + \underline{\kappa}_4^2)) \tag{2.45}$$

In equation (2.44), $Q' = \exp(\beta(\Delta_{QW} + F_v))\, Q$. The integral above is intractable without the use of further approximations. The problem is that the functional form of $I^2(\underline{\kappa}_3 - \underline{\kappa}_1)$ is not known in the sense that the overlap integrals that are contained within it (as defined in equation (2.33)) do not have a known functional form.

In the calculations of Smith et al [16], for the CHCC bound-bound Auger rate in a QW, it was possible to show that the $\underline{\kappa}$ space integral for the QW CHCC process involved the relatively slowly varying $I^2(\underline{\kappa}_3 - \underline{\kappa}_1)$ and a highly peaked function, and the method of steepest descents was used to evaluate

the integral. In practice, this meant that the term $I^2(\underline{\kappa})$ was taken out of the integral and replaced by $I^2(\underline{\kappa}_o)$ - where $\underline{\kappa}_o$ is the most probable value of $(\underline{\kappa}_3 - \underline{\kappa}_1)$, the so-called threshold wavevector transfer. The method of removing $I^2(\underline{\kappa})$ from the integral and evaluating it at the threshold wavevector transfer, has been widely used (e.g. Haug [8], [17], Beattie and Landsberg [11], Sugimura [18]).

The physical reason why the term $I^2(\underline{\kappa})$ is slowly varying compared to the other terms in the $\underline{\kappa}$ space integral is that the statistical factor is highly peaked. The peak occurs because the requirement to conserve both energy and momentum means that the excited Auger particle cannot lie below a certain energy, and above this energy, the statistical factor decreases rapidly due to the exponentially decreasing nature of the distribution functions (in the Boltzmann approximation). Hence, the statistical factor is highly peaked around wavevectors corresponding to the lowest allowed energy of the excited Auger particle. This may be seen mathematically if the statistical factor (in the Boltzmann approximation) is maximised with respect to the wavevector of the excited Auger particle, with the constraints of energy and wavevector conservation [11]. Using this method, it can be shown that the wavevectors of the states involved in the most probable CHSH Auger transition (the threshold configuration) are parallel, and given by [11]

$$\underline{\kappa}_1 = -\frac{m_C}{m_H}\underline{\kappa}_3 = -\frac{m_C}{m_H}\underline{\kappa}_4 \tag{2.46}$$

Using these relations, and the fact that energy and crystal momentum are conserved, the threshold value of $\underline{\kappa}_2$ is found to be

$$|\underline{\kappa}_{2T}|^2 = \frac{m_S(2m_H + m_C)}{m_C(2m_H + m_C - m_S)}\left(\frac{E_{QW} - \Delta_{QW}}{\alpha}\right) \tag{2.47}$$

And an explicit expression for the statistical factor, P, at the threshold condition can be written as

$$P \approx C \exp(-\beta \mu_S \alpha |\kappa_{2T}|^2) \qquad (2.48)$$

Since κ_{2T} is the minimum value of wavevector for state $|2\rangle$ that can simultaneously satisfy both conservation of energy and crystal momentum, any transitions away from threshold are going to be weighted with a statistical factor that is very greatly reduced. The approximation of a highly peaked integrand is most accurate if $(E_{QW} - \Delta_{QW}) \gg k_B T$, which, fortunately, is the case of interest for bound-bound Auger transitions in the III-V materials of interest in this thesis. In passing, it is also worth noting that the relations (2.46) may also be obtained by appealing to the equal velocities criterion of Keldysh [19], and Anderson and Crowell [20]. The states involved in the most probable Auger (or impact ionisation) transition - corresponding to the threshold configuration - occur when the colliding particles have equal velocities. This leads to

$$(\underline{\kappa}_3 - \underline{\kappa}_1)_{\textbf{threshold}} = \underline{\kappa}_o \qquad (2.49)$$

where

$$|\underline{\kappa}_o|^2 = (\frac{2m_S}{\hbar^2}) \frac{(m_H + m_C)^2}{(2m_H + m_C)(2m_H + m_C - m_S)} (E_{QW} - \Delta_{QW}) \qquad (2.50)$$

The previous arguments justify taking $I^2(\underline{\kappa}_3 - \underline{\kappa}_1)$ outside the integral in equation (2.44) and evaluating it at $\underline{\kappa}_o$. Hence

$$Q' \approx I^2(\underline{\kappa}_o) \int \int \int \int \exp(-\beta \mu_S \alpha \underline{\kappa}_2^2) \delta(\underline{\kappa}) \delta(E) d\underline{\kappa}_1 d\underline{\kappa}_2 d\underline{\kappa}_3 d\underline{\kappa}_4 \qquad (2.50)$$

Evaluation of this integral gives the Auger rate per unit volume, R, of a QW for the CHSH Auger transition involving carriers in ground state subbands only.

Only the Auger process for the case of particles with opposite spins separately conserved has been considered. However, as discussed in Section 2.2.2, _all_ spin processes can be taken into account by multiplication by a factor 4η where $1 \leq \eta \leq 2$.

The evaluation of the $\underline{\kappa}$-space integral, Q', is performed in Appendix One. Using the results of Appendix One, the final result for the QW CHSH Auger rate per unit volume, for carriers residing in their ground state subbands for the case $E_{QW} \geq \Delta_{QW}$ is

$$R = \frac{1}{L}\{\exp[\beta(F_c - F_v)]\} \exp[\beta(-\Delta_{QW} - F_v)](\frac{4\eta e^4}{16\pi^4 \epsilon^2 \hbar^7}) I^2(\underline{\kappa}_o)(k_B T)^2 F \tag{2.51}$$

where $1 \leq \eta \leq 2$ and where F is a function of $E_{QW}, \Delta_{QW}, m_C, m_H, m_S$. Its explicit form is

$$F = \frac{m_C m_S m_H^2 (2m_H + m_C - m_S)}{(2m_H + m_C)^2} \exp[-\frac{(2m_H + m_C)}{(2m_H + m_C - m_S)} \frac{(E_{QW} - \Delta_{QW})}{k_B T}] \tag{2.52}$$

Equation (2.51) may be written in the following form

$$R_{QW} \propto p^2 n \exp(-\beta E_a) \tag{2.53}$$

Where $n, (p)$ are the number of electrons (holes) per unit volume in the ground state conduction (heavy hole) subbands respectively. An activation energy, E_a has been defined as

$$E_a = (\frac{m_S}{2m_H + m_C - m_S})(E_{QW} - \Delta_{QW}) \tag{2.54}$$

Equation (2.53) corresponds to the result expected from intuition. For the CHSH Auger process to occur, one electron is required in the conduction band, and two holes are required in the heavy hole band, hence the carrier dependence of the rate should be $p^2 n$. Also, direct Auger processes (i.e. those not involving phonons or traps) are expected to be activated, since the requirements of conserving both energy and crystal momentum demand that participating carriers are away from the band edge. The activation energy is simply equal to the energy required to place the participating carriers in the appropriate threshold states for an Auger transition to occur.

There is one important difference between equation (2.53) for a QW system, and the corresponding equation for a bulk semiconductor. In the bulk, a similar dependence of the CHSH Auger rate on carrier densities is found [17]

$$R_{\text{bulk}} \propto p^2 n \exp(-\beta E_a) \tag{2.55}$$

However, for a QW, the carrier densities $n, (p)$, appearing in (2.53) are _not_ the injected carrier densities, but the carrier densities of the electrons (holes) in the ground state conduction (heavy hole) subband.

Our result for the Auger rate per unit volume for the QW may be compared with previous work by Smith [3], [16] on the corresponding rate for the CHCC Auger process. The expression for the CHSH rate can be used to derive the CHCC Auger rate by a suitable change of material parameters as outlined below. If the spin-orbit splitting, Δ_{QW}, is set to zero, and m_S is set equal to m_H, then the CHSH Auger process is formally identical to the CHHH Auger process. If then m_C and m_H are permuted, and n, p (or F_c, and F_v) are also permuted, the CHCC Auger process is obtained. By doing this in equation (2.51) (noting that the value of ϵ in Smith's calculation [16] corresponds to $4\pi\epsilon$ in our calculation because of the use of SI units here), then the result

agrees exactly with the expression for the CHCC QW Auger rate (in which all the carriers reside in their ground state subbands) that was reported in [16]. By changing the material parameters in a similar way to that described above, expressions for the QW Auger rates for the CHLH, CHHH, CLSL, CLLL, CLHL, etc, processes can be found.

A comparison of the QW Auger rate with the corresponding bulk Auger rate is useful. In fact, due to uncertainties in some of the parameters which enter the expression for the Auger rate (such as the conduction-heavy hole, heavy hole-spin split off overlap integrals, as defined in equation (2.33)), a comparison of the QW and bulk Auger rates may be considered to be an improved guide compared to simple absolute estimates of the two rates.

For the purposes of comparison it is convenient to re-express equation (2.51) in the following form

$$R = \frac{36\eta}{16\pi^2}\left(\frac{e^4}{\epsilon^2\hbar}\right)\frac{\pi^3}{k_BT}\frac{|M_{CH}|^2|M_{HS}|^2}{\kappa_o^4}\left[\frac{S(\kappa_oL)}{6\pi}\right]^2 p^2n\bar{F} \tag{2.56}$$

where

$$\bar{F} = \frac{m_S(2m_H+m_C-m_S)}{(2m_H+m_C)^2}\exp\left(-\frac{m_S\beta(E_{QW}-\Delta_{QW})}{2m_H+m_C-m_S}\right) \tag{2.57}$$

and

$$M_{CH} = \int_{V_{cell}} U^*_{C,\underline{\kappa}_1}(\underline{r})U_{H,\underline{\kappa}_3}(\underline{r})d\underline{r} \tag{2.58}$$

$$M_{SH} = \int_{V_{cell}} U^*_{H,\underline{\kappa}_4}(\underline{r})U_{S,\underline{\kappa}_2}(\underline{r})d\underline{r} \tag{2.59}$$

We have also used p and n, the number of holes per unit volume and the number of electrons per unit volume of the respective ground state subbands.

$$p = \frac{m_H k_B T}{\pi L \hbar^2} \exp(-\beta F_v) \tag{2.60}$$

$$n = \frac{m_C k_B T}{\pi L \hbar^2} \exp(\beta(F_c - E_{QW})) \tag{2.61}$$

In equation (2.56) $S(\kappa_o L)$ is a dimensionless integral whose numerical value is 6π for asymptotically large values of $\kappa_o L$, and approaches zero as $\kappa_o L \rightarrow 0$ [21]. This factor arises from an explicit form for $I^2(\underline{\kappa}_o)$, and is derived in Appendix Two.

An expression for the bulk CHSH Auger rate has been reported in [17], a calculation that used isotropic, parabolic bandstructure and non-degenerate statistics - the same approximations as used in the present derivation of the CHSH QW Auger rate. Thus the expression in [17] may be used to compare the QW and bulk CHSH Auger transition rates.

In order to compare the QW and bulk rates, it would be preferable to consider systems that have identical material parameters, (e.g. the quantum well bandgap equal to the bulk bandgap, the effective masses in QW the same as those in the bulk, $\Delta = \Delta_{QW}$, etc). However, it is not immediately clear how this can be done, since the QW bandgap is necessarily larger than the corresponding bulk bandgap because of the confinement energies associated with the QW. However, if the well material is an alloy (e.g. $GaAs/Ga_{1-x}Al_xAs$ or $InP/In_{1-x}Ga_xAs_yP_{1-y}$) a change of alloy composition can cause the QW bandgap of the alloy (with the changed composition) to equal the bulk bandgap of the alloy (with the original composition) It is worth noting that changing the composition of the alloy also changes the effectives masses of carriers in the well. Thus it is possible to consider QW and bulk systems with the same material parameters if we restrict ourselves to alloys. Fortunately, the work reported

in this thesis is primarily concerned with QWs that can be used as lasers in the 1.3-1.55μm wavelength region and so concentrates on the InP/InGaAsP system QWs, with the alloy material forming the QW. Using equation (2.51) and the expression for the bulk CHSH Auger rate from [17], and assuming equal concentrations of electrons and holes in the QW and the bulk (which are much higher than the intrinsic values), it is found that

$$(\frac{R_{\mathrm{QW}}}{R_{\mathrm{bulk}}})_{\mathrm{CHSH}} = \frac{9\sqrt{\pi}}{8}(\frac{2m_H + m_C}{2m_H + m_C - m_S})[\frac{S(\kappa_o L)}{6\pi}]^2 \sqrt{\frac{k_B T}{E_a}} \tag{2.62}$$

E_a is given by

$$E_a = \frac{m_S(E_{QW} - \Delta_{QW})}{2m_H + m_C - m_S} \tag{2.63}$$

A previous calculation has been reported [22] giving the ratio of the QW and bulk Auger rates (the QW Auger rate being that for the case where all carriers reside in their ground state subbands) for the CHCC Auger process. The result was

$$(\frac{R_{\mathrm{QW}}}{R_{\mathrm{bulk}}})_{\mathrm{CHCC}} = \frac{9\sqrt{\pi}}{8}(\frac{2m_C + m_H}{m_H + m_C})\sqrt{\frac{k_B T}{E_a^{CHCC}}} \tag{2.64}$$

This result can be derived from (2.64) by assuming that the wide well limit is applicable (i.e. $\kappa_o L \to \infty$ so that $S(\kappa_o L) \to 6\pi$) and by making a change of material parameters as described earlier in the section. Simliar results may be derived for the ratio of the QW and bulk Auger rates for other Auger processes such as CHHH, CLSL, CLHL etc, for example the ratio result for the CLSL Auger process is

$$(\frac{R_{\mathrm{QW}}}{R_{\mathrm{bulk}}})_{\mathrm{CLSL}} = \frac{9\sqrt{\pi}}{8}(\frac{2m_L + m_C}{2m_L + m_C - m_S})[\frac{S(\kappa_o L)}{6\pi}]^2 \sqrt{\frac{k_B T}{E_a^{CLSL}}} \tag{2.65}$$

Results for other Auger processes are quoted in [21].

2.3.1 DISCUSSION OF RESULTS

In Section 2.3 algebraic results for QW Auger rates were presented for the case where all the carriers occupied ground state subbands. The QW Auger rates were compared to the corresponding bulk Auger rates, and relatively simply expressions were presented for the ratio of the two rates (see equation (2.64)). For typical III-V materials and reasonably wide well widths the ratio of the CHCC and CHSH Auger rates for the QW ground state case and the analogous bulk rates is of the order of $\sqrt{k_B T/E_a}$. Also, for typical III-V materials at room temperature, the activation energy, E_a, is of the same order of magnitude as $k_B T$ (i.e. a few tens of meV). Hence the ratio results suggest that, if the threshold carrier densities in the QW and the bulk lasers are the same, then the Auger rates in the QW and the bulk will not be significantly different. However, if the QW device can be optimised to allow a lower threshold carrier density, then the QW Auger rate could be decreased relative to that in the bulk. For example, if a multiple QW structure was used, the increase in the confinement factor could result in a lower threshold carrier density. The ratio results are valid for the limited range of well width where the well is narrow enough for the large majority of carriers to reside in the ground state subbands but wide enough for the wide well limit approximation to be accurate.

So far in this Chapter, only QW Auger processes in which the carriers remain in their ground state subbands have been studied. Bound-bound Auger processes can occur with some (or all) of the states involved being in higher subbands, and the expressions for the Auger rates for these transitions will differ from those for the ground state case. In the next Section, the changes that must be made to the theory, when one or more of the states involved in the Auger transition are in higher bound subbands, will be discussed.

2.4 QW AUGER RATES INVOLVING ONE (OR MORE) CARRIERS IN HIGHER CONFINED SUBBANDS

The confined states in a QW, $|1\rangle, |2\rangle, |3\rangle, |4\rangle$ may be labelled by their quantum numbers n_1, n_2, n_3, n_4. In the previous Sections of this Chapter, the carriers have all been assumed to reside in their respective ground state subbands, so that $n_1 = n_2 = n_3 = n_4 = 1$. However, it is possible for carriers to reside in higher lying confined subbands of the QW (subbands with quantum numbers greater than 1). The expressions for the Auger rates will be different from those derived earlier in this Chapter if one (or more) of the initial or final states lies in a higher subband since the matrix element and the activation energy of the Auger process will change. It should be realised that not all intersubband transitions are allowed, because the matrix element for the Auger transition can vanish due to symmetry. There is a selection rule that if $\Delta n = n_1 + n_2 - n_3 - n_4$ is odd, then the transition is forbidden. This selection rule disagrees with that proposed by Dutta [23], but is in agreement with that found by Smith [3], [7]. Dutta quotes a selection rule $\Delta n = 0$, which would forbid Auger transitions such as that shown in Figure (2.8), but this is the result of the unsatisfactory manner in which the matrix element is treated. Dutta assumes that the QW is narrow and the z-component of the Coulomb interaction may be neglected, which results in the misleading selection rule.

If the confined state wavevectors are assumed to be integer multiples of π/L, then the matrix element for the Auger process with general values of n_1, n_2, n_3, n_4 may be shown to be proportional to J, where

$$J = \int_{-\infty}^{\infty} \frac{s^2 A n_1 n_2 n_3 n_4}{(N_+^2 - s^2)(N_-^2 - s^2)(M_+^2 - s^2)(M_-^2 - s^2)(s^2 + (\kappa_o L/\pi)^2)} ds \quad (2.66)$$

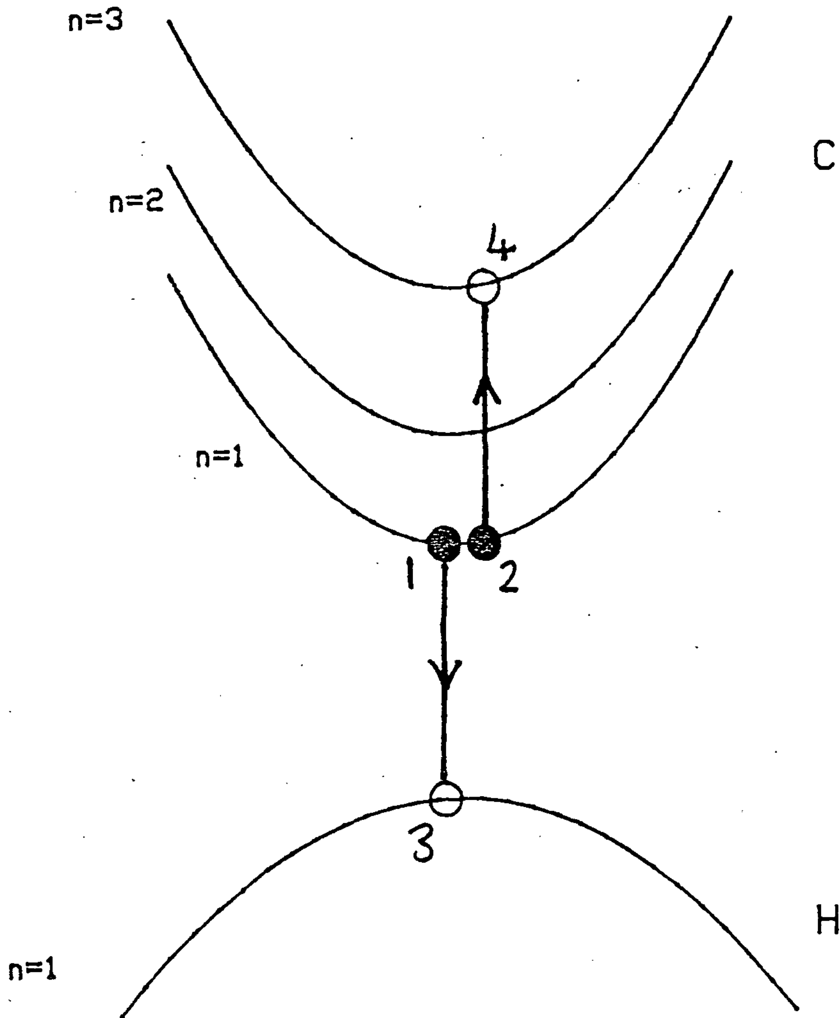

Figure (2.8) - An illustration of the reduction in activation energy that can occur for a QW CHCC Auger transition in which the excited state lies in a higher subband. In the figure, $n_1 = n_2 = n_3 = 1$ and $n_4 = 3$, corresponding to an activation energy of approximately zero.

where

$$N_+ = n_1 + n_3 \tag{2.67}$$

$$N_- = n_1 - n_3 \tag{2.68}$$

$$M_+ = n_2 + n_4 \tag{2.69}$$

$$M_- = n_2 - n_4 \tag{2.70}$$

and $A = \sin^2(\pi s/2)$ if N_+ is even, and $A = \cos^2(\pi s/2)$ if N_+ is odd.

From expression (2.66), processes which have $n_1 = n_3$ and $n_2 = n_4$ are expected to be favourably weighted, since in these cases both N_- and M_- are zero. This has also been found and commented upon by Takeshima [24].

The other effect that is of importance when higher subbands are involved in the transition is the change that can occur in the activation energy of the Auger process. An example of this is shown in figure (2.8) for the CHCC Auger process. In that figure, states $|1\rangle, |2\rangle, |3\rangle$ are in their respective ground state subbands whereas state $|4\rangle$ is in a subband that has $n_4 = 3$. This transition is allowed by our selection rule, and, in Figure (2.8), the subband energies are such that the Auger transition is vertical, corresponding to zero activation energy. Clearly, if such a situation could occur in practice, then the rate of that particular Auger transition would be enhanced.

In general, if the excited Auger carrier (state $|4\rangle$ in the CHCC process, and state $|2\rangle$ in the CHSH process) is in a subband with the highest possible quantum number, then the activation energy may be considerably reduced.

2.5 QW BOUND-UNBOUND AUGER PROCESSES

The previous Sections of this Chapter have assumed that the excited Auger particle makes a transition to one of the confined states of the QW. However transitions to unbound states of the well are also possible. To understand the nature of these unbound states, it is useful to split up the energy, E of a state in the following way.

$$E = E_{\perp} + E_{\parallel} \tag{2.71}$$

Where $E_{\perp}$ is the energy due to confinement in the QW, and $E_{\parallel}$ is the kinetic energy associated with motion parallel to the QW interfaces. For the excited Auger particle to reside in one of the confined states of the well, $E_{\perp}$ must correspond to one of the confined state energy levels of the QW. However, there also exists a continuum of states that have $E_{\perp}$ greater than the the barrier height of the confining well. These are the so-called unbound states of the QW.

Some possible bound-unbound Auger transitions are illustrated in Figure (2.9). To calculate the bound-unbound Auger rate, it is only necessary to note that the process is exactly the same as the bound-bound Auger process, except that the final state lies in a subband that forms part of the unbound state continuum. Hence, integration of an expression of the same form as the bound-bound Auger rate, weighted with the appropriate density of states, over all the continuum of unbound states will yield the bound-unbound Auger rate. In this Section, the only bound-unbound process that will be considered is the one where all states apart from the state of the final excited Auger carrier are in the respective ground state subbands, and the excited carrier is

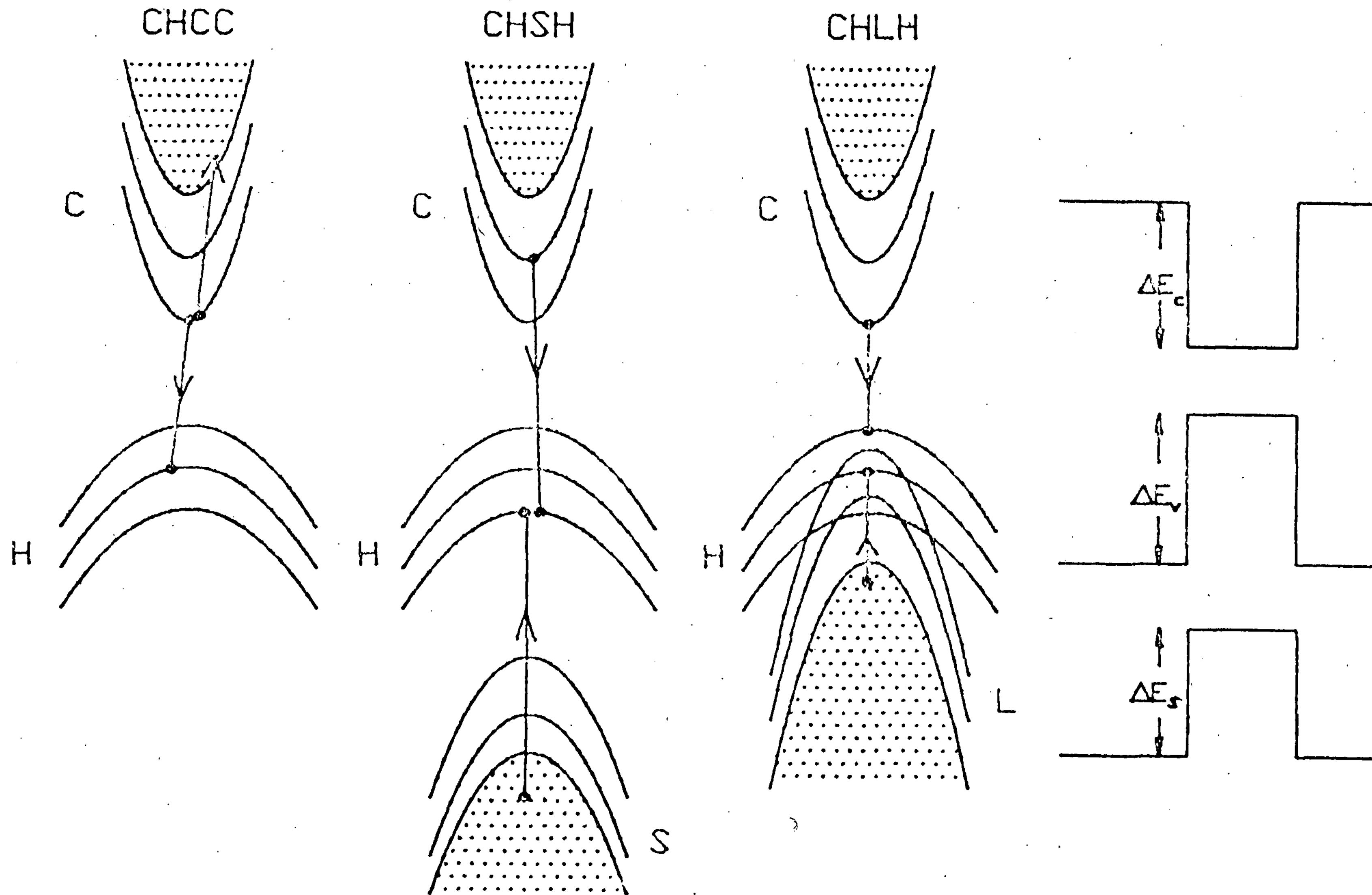

Figure (2.9) - Possible bound-unbound Auger processes in a QW. The shaded area indicates the continuum of unbound subbands.

unbound. Earlier work [3] has shown that this is the only significant bound-unbound Auger process for CHCC in a QW. It is also worth remarking that the matrix element for the bound-unbound Auger process is altered because the QW unbound state wavefunctions are essentially different from the bound state wavefunctions. For the bound-bound calculation, the wavefunction of the bound states was assumed to be zero outside the well, and this is not the case for the unbound wavefunctions. For the unbound wavefunctions, sinusoidal expressions are used both inside and outside the well, and suitable matching conditions are imposed at the QW interfaces, as discussed by Smith [3].

If the bound-bound Auger rate as a function of $E_{\perp}$ is written as $R(E_{\perp})$, then the bound-unbound rate may be written as

$$R_{\text{unbound}} = \int_{\Delta E}^{\infty} R(E)\sqrt{(\frac{2m^*}{\hbar^2})}\{\frac{l}{2\pi\sqrt{E-\Delta E}}\}dE \qquad (2.72)$$

where $2l$ = total system width = width of well and barrier regions, ΔE is the barrier height, and m^* is the effective mass of the unbound carrier. The terms in the integral in equation (2.72) that weight $R(E)$ arise because of the one-dimensional density of states of unbound subbands. In addition a factor of $\frac{1}{4}$ has been included, to take account of the fact that at any particular energy there will be two types of unbound states, one with even parity and one with odd parity. Only one of these states can be involved in an Auger transition if the other states are in specified confined subbands, and this introduces a factor of $\frac{1}{2}$, and the other factor of $\frac{1}{2}$ comes from noting that spin is included at the end of the calculation. It is worth noting that l will not appear in the final expression for the bound-unbound rate because the unbound wavefunctions are normalised with respect to l, and will contribute a factor of l^{-1} to $R(E)$.

Smith et al [7] have evaluated the Auger recombination rate for the QW bound-unbound CHCC process, with the unbound carrier being state $|4\rangle$, with

the remaining states occupying their respective ground state subbands. The conclusion reached in that work was that the bound-unbound CHCC Auger process was only significant at small QW widths ($\leq$ 100 Å) in 1.3 μm InGaAsP/InP QW lasers, and was unimportant in the same alloy system with a composition chosen to produce optical emission at 1.55μm.

The physical reason for the potential importance of the bound-unbound Auger process in QWs is the fact that, for one of the continuum of unbound subbands, the activation energy of the Auger process will be zero in the systems that are of interest in this thesis. For Auger transitions involving subbands close to the zero activation energy, the rate will be enhanced, although the matrix element of the transitions will also affect the rate. Numerical results of the bound-unbound Auger processes in which all bound states are in the ground state subbands, and the final excited Auger carrier is unbound, will be presented for the CHCC, CHSH and CHLH Auger processes in Chapter Four. In the remainder of this Chapter the bound-unbound Auger QW calculation for the CHSH process is discussed in more detail.

For the CHSH process, the bound-unbound QW Auger recombination rate may be written as

$$R_{\mathrm{unbound}} = \int_{\Delta E_S}^{\infty} R(E)\sqrt{(\frac{2m_S}{\hbar^2})}\{\frac{l}{2\pi\sqrt{E-\Delta E_S}}\}dE \qquad (2.73)$$

where m_S is the effective mass for carriers in spin split off subbands, and ΔE_S is the spin split off discontinuity of the QW.

For the case where all the bound carriers are in their respective ground state subbands, the QW wavefunctions may be written as

For $|z| \leq L/2$

$$\phi_{\text{bound}} = \sqrt{\frac{V_{\text{cell}}}{A}}\sqrt{\frac{2}{L}}U_{\underline{\kappa}}(\underline{r})\cos(\frac{\pi z}{L})\exp(i\underline{\kappa}.\underline{\rho}) \tag{2.74a}$$

For $|z| \geq L/2$

$$\phi_{\text{bound}} = 0 \tag{2.74b}$$

For $|z| \leq L/2$

$$\phi_{\text{unbound}} = \sqrt{\frac{V_{\text{cell}}}{Al}}a_1\cos(K_u z)U_{\underline{\kappa}}(\underline{r})\exp(i\underline{\kappa}.\underline{\rho}) \tag{2.75a}$$

For $|z| \geq L/2$

$$\phi_{\text{unbound}} = \sqrt{\frac{V_{\text{cell}}}{Al}}a_2\cos(K'_u z + \delta)U_{\underline{\kappa}}(\underline{\rho})\exp(i\underline{\kappa}.\underline{\rho}) \tag{2.75b}$$

Where a_1 and a_2 are coefficients found by matching the two different forms of ϕ_{unbound} at the QW edge. The wavevector of the unbound state in the well, K_u, is found from the relation

$$\frac{\hbar^2 K_u^2}{2m_S} = E_\perp \tag{2.76}$$

where energies are measured downwards into the spin-split off subbands. By using these wavefunctions, the direct matrix element, M_D, may be evaluated giving

$$|M_D|^2 = \pi^2(\frac{e^2}{\epsilon})^2\frac{1}{A^3}(\frac{2}{L})^3(\frac{1}{l})\frac{|M_{CH}|^2|M_{HS}|^2}{\kappa_o^2}\delta(\underline{\kappa})|V(\underline{\kappa}_o, K_u)|^2 \tag{2.77}$$

With $V(\underline{\kappa}_o, K_u) = I_1 + I_2$, where

$$I_1 = \int_{-L/2}^{L/2}\int_{-L/2}^{z_1}\exp(\kappa_o(z_2 - z_1))\cos^2(\frac{\pi z_1}{L})\cos(\frac{\pi z_2}{L})a_1\cos(K_u z_2)dz_1 dz_2 \tag{2.78}$$

$$I_2 = \int_{-L/2}^{L/2} \int_{z_1}^{L/2} \exp(\kappa_o(z_1 - z_2)) \cos^2(\frac{\pi z_1}{L}) \cos(\frac{\pi z_2}{L}) a_1 \cos(K_u z_2) dz_1 dz_2 \tag{2.79}$$

The integral defining $V(\kappa_o, K_u)$ can be performed analytically, although the calculation is tedious.

The expression for $|M_D|^2$ in equation (2.77) may now be inserted into Fermi's Golden Rule. The statistical factor, P, also required for the Golden Rule, may be derived in the same way as in Section 2.2.1. In fact, the calculation proceeds in exactly the same way as for the bound-bound QW CHSH Auger calculation except that the $E - \underline{\kappa}_{\|}$ relation for the carrier in the spin split-off band is now

$$E_2 = -\Delta_{QW} - \mu_S \alpha \underline{\kappa}_2^2 - E_\perp \tag{2.80}$$

The bound-bound Auger rate corresponding to this value of $E_\perp$ is thus

$$R(E_\perp) = \{\exp[\beta(F_c - F_v)]\} |V(\kappa_o, K_u)|^2 \exp(-\beta E_\perp) \frac{|M_{CH}|^2 |M_{HS}|^2}{\kappa_o^2 L^4 l} BS \tag{2.82}$$

with

$$B = \frac{\eta e^4}{8\pi^3 \epsilon^2 \hbar} \frac{a_S}{\mu_S^2 \mu_H (2 + \mu_H)} \frac{(k_B T)^2}{\alpha^3} \exp[-\beta(\Delta_{QW} + F_v)] \tag{2.83}$$

$$a_S = \mu_S - \frac{\mu_H}{(2 + \mu_H)} \tag{2.84}$$

and $S = \exp(-\beta \mu_S \Delta E / a_S)$ if $\Delta E \geq 0$, and for the case where $\Delta E \leq 0$, we find that $S = (1 - (\beta \mu_S \Delta E / a_S))$.

Also, $\Delta E = E_{QW} - \Delta_{QW} - E_{\perp}$. Hence, the expression for the bound-unbound QW CHSH Auger rate is

$$R_{\text{unbound}} = \sqrt{\frac{2m_S}{\hbar^2}} \frac{1}{L^4} B\{\exp[-\beta(F_c - F_v)] - 1\} J \tag{2.85}$$

J arises from the integration over the continuum of unbound subbands and is

$$J = \int_{\Delta E_S}^{\infty} S \frac{|M_{CH}|^2 |M_{HS}|^2 |V(\kappa_o, K_u)|^2}{\kappa_o^2 \sqrt{E_\perp - \Delta E_S}} \exp(-\beta E_\perp) dE_\perp \tag{2.86}$$

Unfortunately, in deriving equation (2.85), a number of approximations have been necessary. It has been assumed that it is still valid, as in the derivation of the bound-bound rate, to remove the slowly varying matrix elements from the phase space integral and evaluate it at the appropriate threshold wavevector transfer. However, as discussed in Section 2.3, this is only a good approximation if $(E_{QW} - \Delta_{QW}) \gg k_B T$. Here it must be recognised that in deriving the bound-unbound QW Auger rate, the parameter of interest is not $(E_{QW} - \Delta_{QW})$ but $(E_{QW} - \Delta_{QW} - E_\perp)$ and this can certainly equal zero, and become negative, when the final integration over the continuum of unbound states is performed.

This problem has been addressed in detail by Smith [3], and, although the statistical factor is no longer highly peaked if $\Delta E = (E_{QW} - \Delta_{QW} - E_\perp) \leq 0$, the results Smith obtained by removing the matrix element and evaluating it at an appropriate wavevector, were very close to the results of a full numerical calculation that was also performed [3]. This suggests that the approximation discussed above will not introduce significant errors into the calculation of the QW bound-unbound Auger rate. Expression (2.85) has been used to carry out numerical calculations of the QW CHSH bound-unbound Auger rates in the InGaAsP/InP QW system (assuming that all the bound states are the respective ground states). A similar analysis to that presented above has also

been carried out for the CHLH and CHCC bound-unbound QW Auger rates, with the bound states being ground states of the QW. Although the CHCC bound-unbound QW Auger rate has been examined by Smith, the calculation was worth repeating to check for consistent results. The numerical results and their physical interpretation will be presented in Chapter Four. However, it is perhaps worth stating at this point that the numerical results for the CHCC bound-unbound QW Auger rates are in good agreement with the work of Smith [3].

2.6 SUMMARY OF CHAPTER TWO

The work of Smith et al [3],[7] has been extended in order to calculate rates for the bound-bound CHSH QW Auger process. The expression for the rate that has been derived, may, by a suitable change of parameters, also be used to obtain expressions for the rates of the bound-bound CHCC, CHLH, CLSL, CLLL, CHHH QW Auger processes. Using this procedure, the result obtained for the bound-bound CHCC QW Auger rate involving all carriers in their respective ground state subbands was found to agree exactly with a previous result reported by Smith et al [16]. The description of the analytic work in this Chapter has concentrated on the case where all the carriers reside in their ground state subbands. However, the inclusion of intersubband transitions involving states in higher confined subbands is straightforward. In fact the calculation of QW Auger rates involving intersubband transitions is very similar to that for the ground state QW Auger rate, and the modifications needed to evaluate the intersubband transition rates were discussed in Section 2.4. The total QW

Auger bound-bound rate has been obtained by a summation over *all* possible intersubband transitions. However, physically, it is to be expected that the QW Auger process in which all the states are in the respective ground state subbands of the QW will dominate, since those subbands will be preferentially occupied by carriers, and this is found in the numerical results of Chaper Four.

Concerning the relative sizes of Auger rates in QWs and the bulk, it was found that, if the ground state QW Auger rate is the most important contribution to the total QW rate, and if the threshold carrier densities in the bulk and the QW are the same, then the Auger rates in a QW are about the same as those in the bulk (assuming the same material parameters, such as effective masses and bandgaps etc.). This indicates that significant improvements in radiative efficiency are not expected for QWs unless threshold carrier densities are significantly reduced compared to those in the bulk [25].

Finally, we discussed how the results for bound-bound QW Auger recombination could be used to calculate the bound-unbound QW Auger rates. Algebraic expressions for the bound-unbound QW CHSH Auger rate were given, and their use to calculate numerical estimates of this contribution to the total Auger rate will be described in Chapter Four.

REFERENCES FOR CHAPTER TWO

[1] J. Batey and S.L. Wright, J.Appl.Phys, 59, (1986), 200.

[2] R. Chin, N. Holonyak,Jr., S.W. Kirchoefer, R.M. Kolbas and E.A. Rezek, Appl. Phys. Lett., 34, (1979), 862.

[3] C. Smith, PhD thesis, Durham University, 1985 (unpublished).

[4] L.C. Chiu and A. Yariv, IEEE J. Quant. Electron., QE-18, (1982), 1406.

[5] L.I. Schiff, Quantum Mechanics, 3rd Edition (published by McGraw-Hill).

[6] M.G. Burt, Elect. Lett., 19, (1983), 210.

[7] C. Smith, R.A. Abram & M.G. Burt, Superlatt. Microstruct., 1,(1985),119.

[8] A. Haug, J.Phys.C:Solid State Phys., 16, (1983), 4159.

[9] P.T. Landsberg, 'Electron Collision Effects in Semiconductors', Boulder Series of Lectures in Theoretical Physics, 8*A*, (1965).

[10] B.K. Ridley, 'Quantum Processes in Semiconductors', Clarendon Press (1982).

[11] A.R. Beattie and P.T. Landsberg, Proc.Roy.Soc., *A*249, (1959), 16.

[12] M.G. Burt, J.Phys.C:Solid State Phys., 14, (1981), 3269.

[13] A. Haug and W. Ekardt, Solid State Comm., 17, (1975), 267.

[14] M. Takeshima, Phys.Rev.B26, (1982), 3192.

[15] D. Yevick and W. Bardyszewski, IEEE J.Quant.Elect., QE-23, (1987), 168.

[16] C. Smith, R.A. Abram and M.G. Burt, J.Phys.C:Solid State Phys., 17, (1984), L571.

[17] A. Haug, D. Kerkhoff & W. Lochmann, Phys.Stat.Sol.(b), 89,(1978),357.

[18] A. Sugimura, IEEE J.Quant.Elect., QE-17, (1981), 627.

[19] L.V. Keldysh, Sov.Phys.JETP, 37, (1960), 509.

[20] C.L. Anderson and C.R. Crowell, Phys.Rev.B5, (1972), 2267.

[21] R.I. Taylor, R.A. Abram, M.G. Burt and C. Smith, IEE Proc. 132 Part J (Optoelect.), (1985), 364.

[22] C. Smith, R.A. Abram and M.G. Burt, Elect. Lett., 20, (1984), 893.

[23] N.K. Dutta, J.Appl.Phys, 54, (1983), 1236.

[24] M. Takeshima, Phys.Rev.B31, (1985), 992.

[25] M.G. Burt and R.I. Taylor, Elect.Lett.,21, (1985), 733.

CHAPTER THREE

THE CHSH AUGER RECOMBINATION RATE IN A QUANTUM WELL WIRE

INTRODUCTION

In this chapter, the calculation of the CHSH bound-bound Auger recombination rate in a quantum well wire (QWW) is described. The derivation of an expression for the CHSH Auger rate also enables us to evaluate the rates of the CHCC, CHLH, CLSL, and CHHH Auger processes in an analogous way to that described in Chapter Two. A comparison of bound-bound Auger rates in QWs and QWWs is presented.

3.1 THE QUANTUM WELL WIRE

Recent advances in MBE and MOCVD have enabled the fabrication of quantum well wires (structures that confine carriers in two perpendicular directions) [1]. Theoretical investigations have suggested that quantum well wire lasers will exhibit improved gain spectra [2] compared to quantum well lasers, and also, in the absence of non-radiative recombination, the temperature sensitivity of a QWW laser can be improved over that for the QW (i.e. the temperature sensitivity parameter T_o has been predicted to be larger for a QWW than the value for a QW) [3]. However, as non-radiative recombination is thought to be significant in the conventional long wavelength lasers used as sources in optical fibre communications systems (and, as shown in Chapter Two, significant also in QWs), it is important to estimate the non-radiative recombination rate in a QWW.

The QWW is assumed to have a square cross section (of width L), and is assumed to be long, with length X. (see Figure (3.1)). For simplicity, the potential discontinuities ΔE_c, and ΔE_v are taken to be infinite, so that the energy levels of the QWW are straightforward to calculate. If the potential discontinuites were taken to be finite, Schrödinger's equation would not be seperable for the wire geometry considered in this Chapter. One consequence of assuming infinite potential discontinuities is the exclusion of any bound-unbound Auger processes. To examine these, it is necessary to model the QWW as a cylindrical wire, with finite band offsets. The cylindrical symmetry enables the matching of the wavefunctions inside and outside the wire to be carried out without difficulty. Theoretical work on such a system has been performed [4].

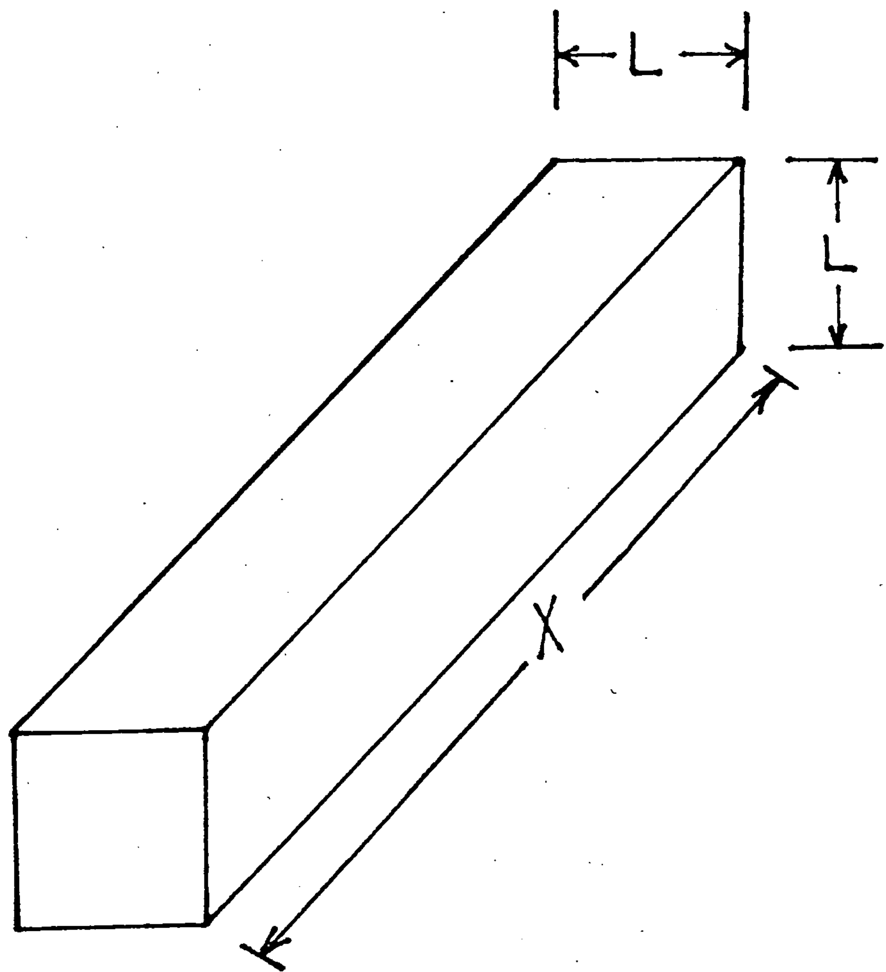

Figure (3.1) - Schematic diagram of a quantum well wire (QWW).

However, the essential physics of the bound-bound QWW Auger rate is not dependent on the cross-sectional shape of the wire.

The carriers in the QWW are free to move in the axial direction, and, as for the QW, subbands will be formed for each confined energy level in the well. The subband dispersion relations are assumed to be parabolic, with carriers in higher subbands having the same effective masses as those associated with their respective ground state subbands. Since the band offsets are assumed to be infinite, the energy levels of the confined states of the QWW are

$$E_{s,t} = \frac{\pi^2 \hbar^2}{2m^* L^2}(s^2 + t^2) \tag{3.1}$$

where m^* is the appropriate effective mass for carriers in the well. Two quantum numbers, s, and t, are required to specify a confined energy level of a QWW, and so there are many more possible intersubband Auger transitions than for the QW case.

A study of Auger recombination in a quasi-one-dimensional structure semiconductor has been carried out by Takeshima [5] but the approach he has used to calculate transition rates tends to obscure the physics of the process. The approach used in this work, which is summarised in [6], uses first order time dependent perturbation theory (Fermi's Golden Rule) to derive a relatively simple expression for the CHSH QWW Auger rate for bound-bound transitions.

3.2 CALCULATION OF THE CHSH QUANTUM WELL WIRE AUGER RATE

The starting point for the QWW Auger rate calculation is Fermi's Golden Rule, which gives the rate per unit volume, R, as

$$R = \frac{1}{XL^2}\frac{2\pi}{\hbar}\sum P|\langle\Psi_i|H_I|\Psi_f\rangle|^2\delta(E) \tag{3.2}$$

Where X is the length of the QWW, L is the confinement length of the (square cross section) wire, P is the statistical factor, Ψ_i is the wavefunction of the initial state, and Ψ_f is the wavefunction of the final state. H_I is the perturbation due to the electron-electron interaction. The statistical factor, P is calculated in exactly the same way as in Section 2.2.1. Thus, assuming Boltzmann statistics, we have

$$P = \{\exp[\beta(F_c - F_v)] - 1\}\exp[\beta(E_2 - F_v)] \tag{3.3}$$

However, it must be remembered that the calculation of the quasi-Fermi levels for the QWW is not the same as for the QW because the QWW has a different density of states. In an ideal QWW with parabolic bands, the density of states for the confined carriers, $g(E)$ is given by

$$g(E) = \frac{X}{\pi}\sqrt{\frac{2m^*}{\hbar^2}}\sum_{i=1}^{N}(E - E_i)^{-\frac{1}{2}}\theta(E - E_i) \tag{3.4}$$

See figure (3.2). In equation (3.4) there are N confined energy levels in the well with energies $E_1, \ldots, E_N$. For a QWW with an infinite square well potential, N

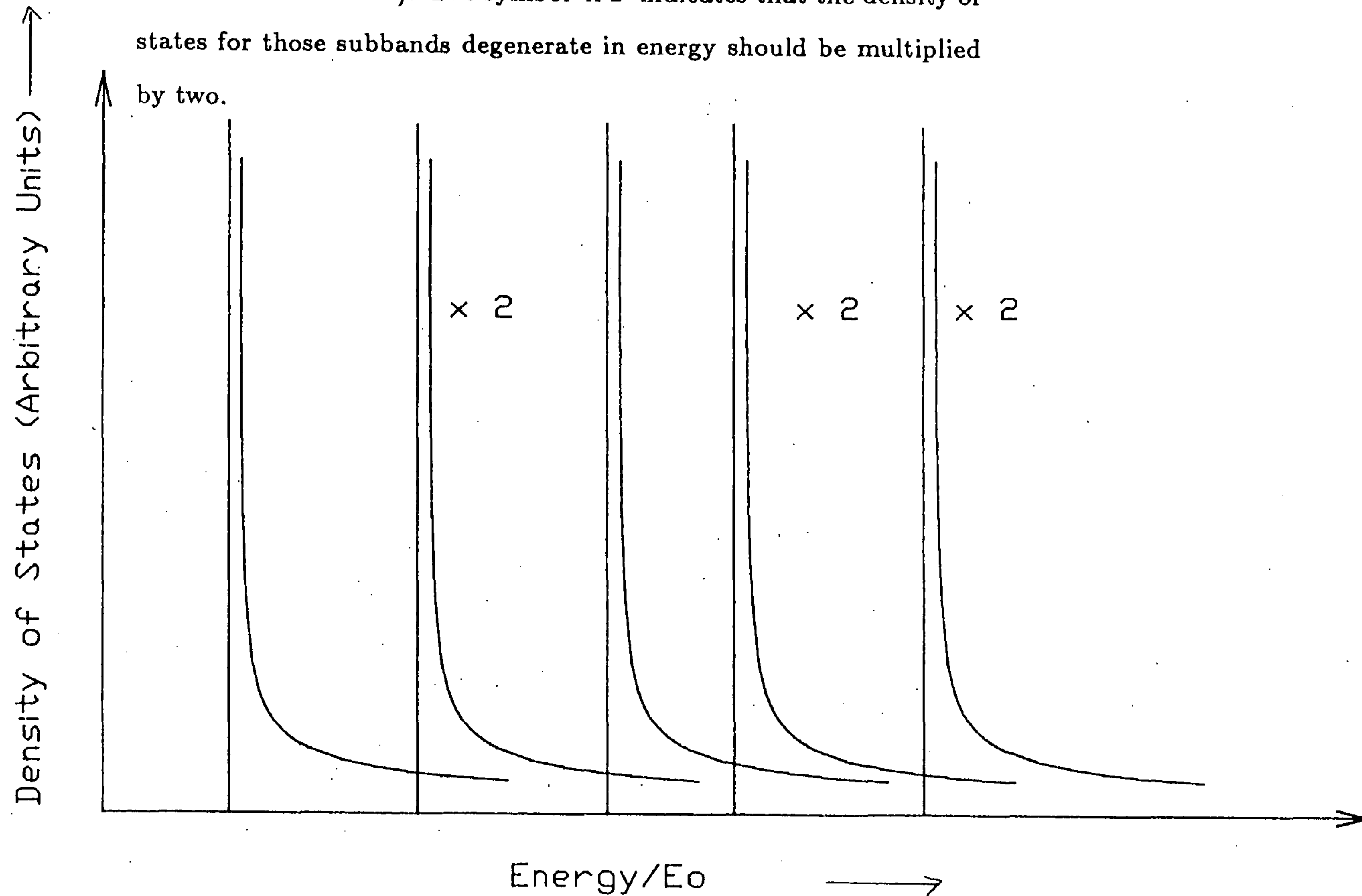

Figure (3.2) - The density of states for an ideal QWW, assuming parabolic subbands. $E_o = \pi^2\hbar^2/2m^*L^2$ (with m^* being the effective mass of the subbands). The symbol 'x 2' indicates that the density of states for those subbands degenerate in energy should be multiplied by two.

would be infinite. Hence if n electrons (n being the carrier density) are injected into the conduction band of the QWW then

$$n = \frac{1}{\pi L^2}\sqrt{\frac{2m_C}{\hbar^2}}\sum_{i=1}^{N}\int_{E_i}^{\infty}\frac{dE}{\sqrt{E-E_i}[\exp(\beta(E-F_c))+\lambda]} \tag{3.5}$$

Where $\lambda = 1$ if Fermi-Dirac statistics are used, and $\lambda = 0$ if Boltzmann statistics are used. Expression (3.5) may be simplified to

$$n = \frac{1}{\pi L^2}\sqrt{\frac{2m_C k_B T}{\hbar^2}}\sum_{i=1}^{N}\int_{0}^{\infty}\frac{dx}{\sqrt{x}[A\exp(x)+\lambda]} \tag{3.6}$$

where $A = \exp(\beta(E_i - F_c))$. A similar, albeit more complicated, expression may be written for the injected hole density. Equation (3.6), and the corresponding equation for the holes, may be solved numerically for F_c and F_v if n and p are specified. Once the quasi-Fermi levels have been calculated, the number of carriers in any particular subband may be calculated.

The arguments of Section 2.2.2, that enabled us to write the matrix element, M $(= \langle\Psi_i|H_I|\Psi_f\rangle)$ as

$$|M|^2 = (2 + 2\delta_{n1,n2})|M_D|^2 \tag{3.7}$$

may also be used for the QWW case, except that for the QWW we must write

$$|M|^2 = (2 + 2\delta_{n1y,n2y}\delta_{n1z,n2z})|M_D|^2 \tag{3.8}$$

Hence, as for the QW, it is only necessary to calculate the matrix element for the case where the carriers have opposite spins that are seperately conserved during the Auger transition. The matrix element, M_D, will be different from that for the QW since the extra degree of confinement in the QWW means that

the wavefunctions of the recombining carriers in the QWW are different from those in the QW.

It is still useful to use the analysis of Chapter Two, which enabled us to write the matrix element as

$$M_D = (\frac{e^2}{\epsilon})\frac{1}{(2\pi)^3}\int \frac{I_{3,1}(\underline{q})I_{4,2}(-\underline{q})}{\underline{q}^2}d\underline{q} \tag{3.9}$$

with

$$I_{m,n}(\underline{q}) = \int \phi_m^*(\underline{r})\phi_n(\underline{r})\exp(i\underline{q}.\underline{r})d\underline{r} \tag{3.10}$$

We now proceed to calculate the QWW CHSH Auger transition rate for the case where all the carriers reside in their ground state subbands. The case where the carriers are in states with general values for the quantum numbers will be discussed later in the chapter.

For carriers in the ground state subbands of a QWW with infinitely high barriers, the wavefunctions may be written as

$$\phi(\underline{r}) = \frac{2}{L}\sqrt{\frac{V_{cell}}{X}}\sin(\frac{\pi y}{L})\sin(\frac{\pi z}{L})\exp(i\kappa x)U_{\underline{\kappa}}(\underline{r}) \tag{3.11}$$

If $0 \leq y \leq L$ and $0 \leq z \leq L$. If y and z are outside this range then $\phi(\underline{r}) = 0$. Using equation (3.11), the evaluation of $I_{m,n}(\underline{q})$ can proceed.

$$I_{m,n}(\underline{q}) = \frac{8\pi}{XL^2}M_{m,n}\delta(\kappa_n - \kappa_m + q_x)K(q_y)K(q_z) \tag{3.12}$$

With

$$K(q) = \int_0^L \sin^2(\frac{\pi y}{L})\exp(iqy)dy \tag{3.13}$$

In equation (3.12), as stated previously, the carriers have been assumed to reside in their respective ground state subbands. After some algebra, the direct matrix element, M_D, may be written as

$$M_D = (\frac{128}{\pi})^2 \frac{1}{(2\pi)^3} (\frac{e^2}{\epsilon}) \frac{1}{X^2} M_{CH} M_{HS} \delta(\kappa) J \tag{3.14}$$

With $\kappa = \kappa_1 + \kappa_2 - \kappa_3 - \kappa_4$, also, J is given by

$$J = \int_{-\infty}^{\infty} \int_{-\infty}^{\infty} \frac{\sin^2(\pi s/2) \sin^2(\pi t/2) ds dt}{s^2 t^2 (s^2-4)^2 (t^2-4)^2 (s^2+t^2+(\kappa_o L/\pi))^2} \tag{3.15}$$

If $(\kappa_o L)$ is large, the double integral can be approximated by the product of two identical integrals, and it is possible to write

$$J = [\frac{\pi}{\kappa_o L}]^2 [\frac{3\pi^2}{64}]^2 S_{QWW}(\kappa_o L) \tag{3.16}$$

Where $S_{QWW}(\kappa_o L) \rightarrow 1$ as $\kappa_o L \rightarrow \infty$. The variation of $S^2(y)$ as a function of y is shown in figure (3.3). The final expression for $|M_D|^2$ thus simplifies to

$$|M_D|^2 = (\frac{81\pi}{8})[\frac{e^2}{\epsilon}]^2 \frac{|M_{CH}|^2 |M_{HS}|^2}{\kappa_o^4 L^4} \frac{1}{X^3} \delta(\kappa_1+\kappa_2-\kappa_3-\kappa_4) S_{QWW}^2(\kappa_o L) \tag{3.17}$$

Fermi's Golden Rule is now used to evaluate the Auger transition rate

$$R = \frac{1}{XL^2} \frac{2\pi}{\hbar} \sum P |\langle \Psi_i | H_I | \Psi_f \rangle|^2 \delta(E) \tag{3.18}$$

By converting the summation over all possible initial and final states into an integration over κ-space, we obtain

Figure (3.3) - Graph of $S^2_{QWW}(y)$ as a function of y.

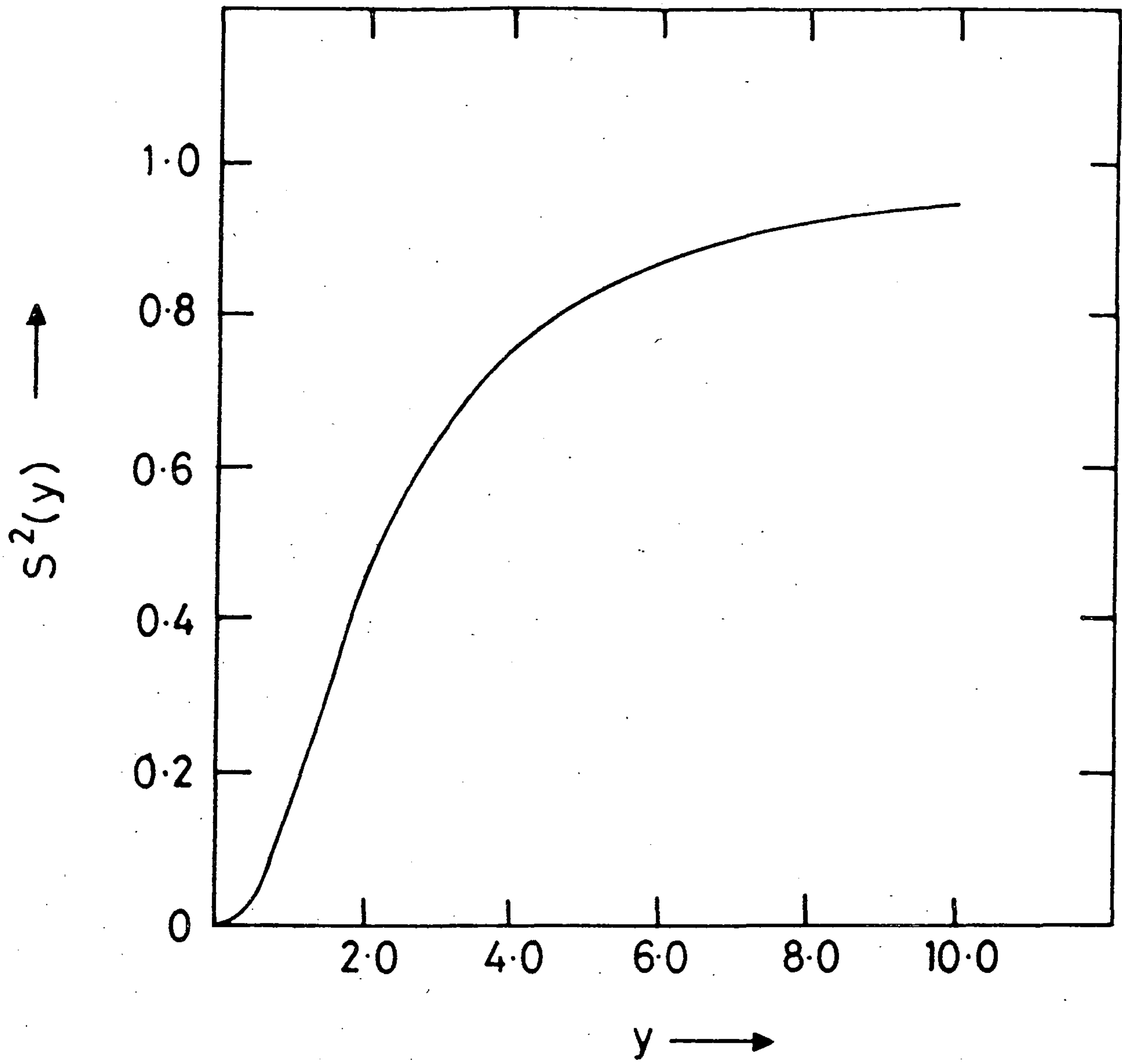

$$R = \frac{1}{XL^2}(\frac{2\pi}{\hbar})[\frac{X}{2\pi}]^4 \int\int\int\int P|M_D|^2\delta(E)\delta(\kappa)d\kappa_1 d\kappa_2 d\kappa_3 d\kappa_4 \qquad (3.19)$$

By assuming that the statistical factor is highly peaked for wavevectors in the vicinity of those corresponding to the threshold configuration, (see discussion in section (2.3)), the slowly varying matrix element can be removed from the integrand and may be evaluated at the threshold wavevector transfer (κ_o).

The expression for the CHSH QWW Auger rate for the case where all the participating carriers reside in their respective ground state subbands is (omitting the summation over all possible spin configurations)

$$R = \frac{81}{64\pi^2}(\frac{e^4}{\epsilon^2\hbar})\exp(\beta(F_c - F_v))\exp(-\beta(\Delta_{QWW}+F_v))\frac{|M_{CH}|^2|M_{HS}|^2}{\kappa_o^4 L^6}S_{QWW}^2(\kappa_o L)Q \qquad (3.20)$$

With

$$Q = \int\int\int\int \exp(-\beta\mu_S\alpha\kappa_2^2)\delta(\kappa)\delta(E)d\kappa_1 d\kappa_2 d\kappa_3 d\kappa_4 \qquad (3.21)$$

The subband dispersion relations in the x direction have been taken to be of the same functional form as those in Chapter Two. The κ-space integral (for $\Delta E_{QWW} = E_{QWW} - \Delta E_{QWW} \geq 0$) is

$$Q = \sqrt{\frac{\pi^3(k_B T)}{\alpha^3\mu_H(\mu_H+2)\mu_S}}\mathrm{erfc}(\sqrt{\frac{\beta\mu_S\Delta E_{QWW}}{a_S}}) \qquad (3.22)$$

where the symbols have their usual meanings. If $\beta\mu_S\Delta E_{QWW}/a_S \geq 3$, which is typically the case for III-V materials at room temperature, equation (3.22) may be rewritten as

$$Q = \frac{\pi(k_BT)}{\alpha^{\frac{3}{2}}\Delta E_{QWW}^{\frac{1}{2}}}\sqrt{\frac{a_S}{\mu_S^2\mu_H(2+\mu_H)}}\exp(\frac{-\beta\mu_S\Delta E_{QWW}}{a_S}) \tag{3.23}$$

where the relation $\mathrm{erfc}(x) = \exp(-x^2)/(\pi\sqrt{x})$ has been used for large values of x. (See Appendix Three for a proof of this). Hence, the final expression for the CHSH QWW Auger rate, for carriers residing in their ground state subbands is (omitting the summation over the spins)

$$R = \frac{81}{64\pi}(\frac{e^4}{\epsilon^2\hbar})S\exp(\beta(F_c-F_v))\exp(-\beta(\Delta_{QWW}+F_v))\exp(-\beta\mu_S\Delta E_{QWW}/a_S) \tag{3.24}$$

where S is

$$S = \frac{|M_{CH}|^2|M_{HS}|^2}{\kappa_o^4L^6}\sqrt{\frac{a_S}{\mu_S^2\mu_H(2+\mu_H)}}S_{QWW}^2(\kappa_oL)\frac{k_BT}{\alpha^{\frac{3}{2}}\Delta E_{QWW}^{\frac{1}{2}}} \tag{3.25}$$

and all the other symbols have their usual meanings (see Chapter Two). Comparison of the QW and the QWW CHSH Auger rates, assuming all material parameters are the same (i.e. same carrier effective masses, ΔE_{QW} equal to ΔE_{QWW}, same threshold carrier densities, etc), leads to

$$\frac{R_{QWW}}{R_{QW}} \approx \frac{9}{4\sqrt{\pi}}\frac{2m_H+m_C}{2m_H+m_C-m_S}[\frac{k_BT}{E_a}]^{\frac{1}{2}} \tag{3.26}$$

It has been assumed that the well width, L, is large enough for the wide well limit approximation to be valid (i.e. $S_{QW}(\kappa_oL)$, and $S_{QWW}(\kappa_oL)$ both close to the values they have for asymptotically large values of κ_oL), but narrow

enough so that the large majority of the carriers reside in their ground state subbands. E_a is the activation energy of the QW CHSH ground state Auger process, as defined in Chapter Two.

Expressions for the CHCC, CHLH, CLSL, CHHH, etc, Auger transition rates may be written down by following a similar procedure to that described in Chapter Two.

The magnitude of the activation energy for typical III-V materials of interest in optoelectronic engineering (at room temperature), is of the order of a few times k_BT, and so the QWW Auger transition rates will be of the same order of magnitude as the QW rates if the carrier densities required for threshold are the same in the two cases.

3.3 QWW AUGER RATES FOR GENERAL INTERSUBBAND TRANSITIONS

The last section dealt with the problem of the QWW CHSH Auger recombination rate for the case where all the carriers were assumed to reside in their respective ground state subbands. If one (or more) of the carriers resides in a higher lying QWW subband, then the activation energy of that particular Auger process, and the matrix element for the transition will be modified.

The definition of the activation energy for the QWW CHSH Auger process for carriers remaining in their ground state subbands is

$$E_a = \frac{m_S}{2m_H + m_C - m_S} \Delta E_{QWW} \tag{3.27}$$

For a general intersubband transition, the activation energy is proportional to ΔE_{QWW}, where ΔE_{QWW} is the wavevector independent part of $(E_1 + E_2 - E_3 - E_4)$. As in the case of the QW (see Chapter Two), for the CHCC process, state $|4\rangle$ should be in the highest possible subband to reduce the activation energy substantially. For the CHSH process, it is carrier $|2\rangle$ that is required to be in the highest possible subband for a substantial reduction in the activation energy for the Auger transition.

The matrix element for the Auger transition, M_D, also has an influence on the Auger rate. Consider the quantum numbers of the initial and final states to be $(n_{1y}, n_{1z}), (n_{2y}, n_{2z}), (n_{3y}, n_{3z}), (n_{4y}, n_{4z})$, and define numbers N and M by

$$n_{1y} + n_{2y} - n_{3y} - n_{4y} = N \tag{3.28a}$$

$$n_{1z} + n_{2z} - n_{3z} - n_{4z} = M \tag{3.28b}$$

Then if N and M are both odd that particular intersubband transition is forbidden by symmetry. This selection rule is not restricted to the case of a QWW with identical confinement lengths in the y and z directions.

For the QWW CHSH Auger process involving carriers in their respective ground state subbands, the matrix element was shown to be proportional to J where

$$J = \int_{-\infty}^{\infty}\int_{-\infty}^{\infty} \frac{\sin^2(\pi s/2)\sin^2(\pi t/2)dsdt}{s^2t^2(s^2-4)^2(t^2-4)^2(s^2+t^2+(\kappa_o L/\pi)^2)} \tag{3.29}$$

However, for a general intersubband transition, the matrix element is more complicated, and is proportional to K, with

$$K = \int_{-\infty}^{\infty}\int_{-\infty}^{\infty} \frac{s^2 t^2 PABdsdt}{S_1 S_2(s^2+t^2+(\kappa_o L/\pi)^2)} \tag{3.30}$$

where $P = \prod_{i=1,4} n_{iy} n_{iz}$, and $S_1 = \prod_{i=1,4}(s^2 - p_i^2)$, $S_2 = \prod_{i=1,4}(t^2 - q_i^2)$ in which $p_1 = n_{1y} - n_{3y}$, $p_2 = n_{1y} + n_{3y}$, $p_3 = n_{2y} - n_{4y}$, and $p_4 = n_{2y} + n_{4y}$. Similar expressions hold for the q_i, except it is the z components of the quantum numbers that are involved. $A = \sin^2(\pi s/2)$ if $(n_{1y} - n_{3y})$ is even, otherwise $A = \cos^2(\pi s/2)$. Similarly, $B = \sin^2(\pi t/2)$ if $(n_{1z} - n_{3z})$ is even, otherwise $B = \cos^2(\pi t/2)$.

From equation (3.30), it can be seen that Auger transitions involving carriers in states that have $n_{1y} = n_{3y}$, $n_{2y} = n_{4y}$, $n_{1z} = n_{3z}$, and $n_{2z} = n_{4z}$, will have an enhanced matrix element. This has also been found in the work of Takeshima [5].

Numerical results for QWW bound-bound Auger transition rates for various, important, intersubband transitions will be presented in Chapter Four.

3.4 THE DIRECTIONAL DEPENDENCE OF THE QWW AUGER RATE

In equation (3.24) the QWW CHSH Auger rate (for the case where all the carriers resided in their respective ground state subbands) was found to be dependent on $|M_{CH}|^2|M_{HS}|^2$ (i.e. proportional to the product of the squares of the conduction-heavy hole and heavy hole-spin split off overlap integrals). This dependence of the Auger rate on the overlap integrals has led to suggestions that the Auger rate should be strongly dependent on the direction of the QWW axis [5], (i.e. dependent upon the direction in which the carriers are free).

This conclusion was reached because the overlap integrals in bulk semiconductors have a strong dependence on the directions of the wavevectors of the states. For example, the CH overlap as a function of θ (the angle that the heavy hole wavevector makes with the z axis in the xz plane) changes dramatically as θ varies from 0 to $\pi/4$, [7], [8], [9], (see Figure (3.4), which has been reproduced from reference [7]).

However, the calculation shown in Figure (3.4) assumed that the wavevectors of the heavy hole and the conduction band carriers were parallel (in fact, the wavevector of the conduction band carrier was taken to to be zero). If the wavevectors are not parallel, the CH overlap depends strongly on ϕ, where ϕ is the angle between the heavy hole wavevector and the conduction band wavevector (see Figure (3.5)). For the QWW, it has been assumed throughout the calculation that the threshold condition of parallel wavevectors dominated

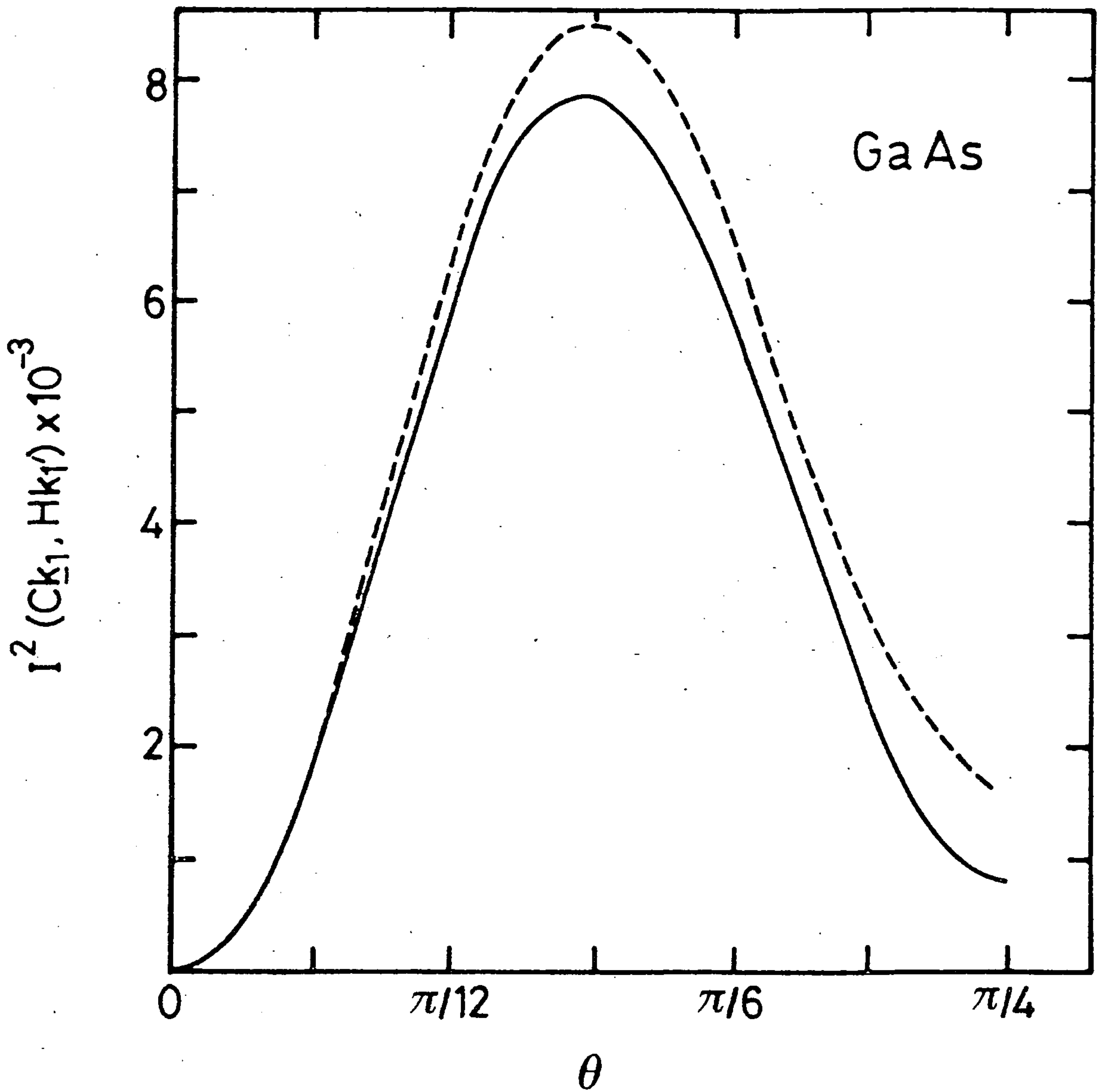

Angle Between k_1' and 100 in 001 Plane

Figure (3.4) - Graph of $M_{CH}(= |I_{CH}|^2)$ versus θ, the angle that the heavy hole wavevector makes with the z axis in the xz plane. The conduction band wavevector has been taken as zero, and the heavy hole wavevector is $0.2(2\pi/a)$ (with a the lattice constant). The full curve is from a 15 band $\underline{k}.\underline{p}$ calculation, and the dotted curve is from a non-local pseudopotential calculation. Figure taken from [7].

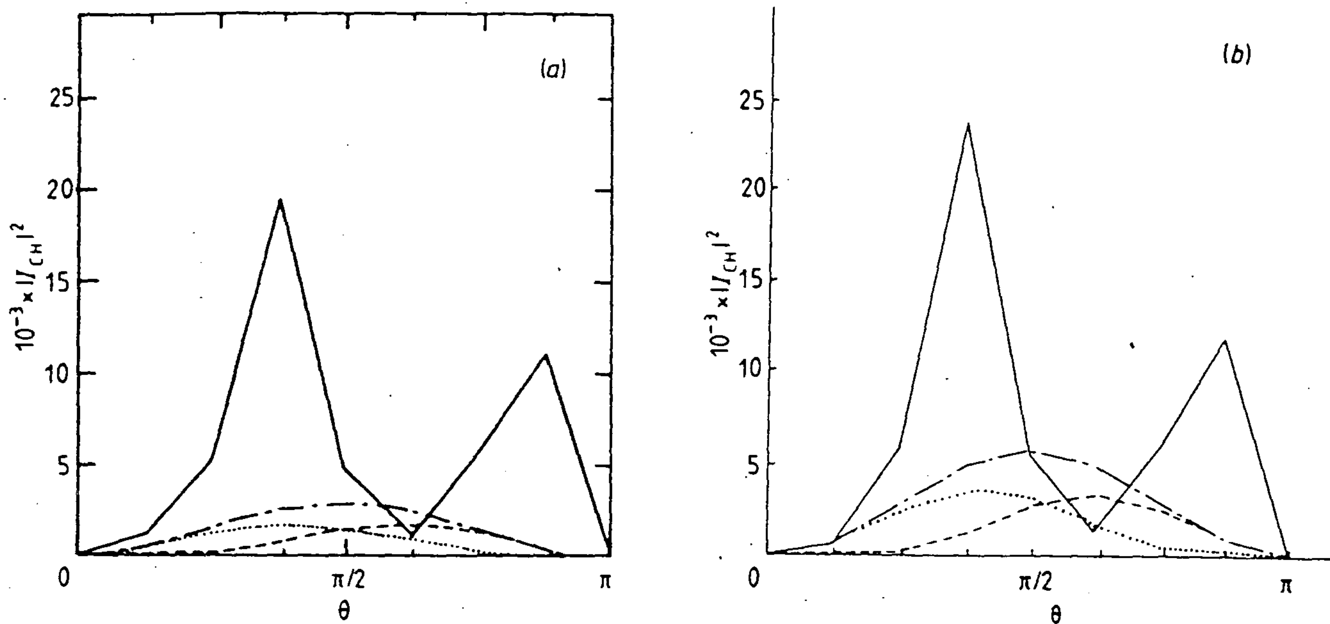

Figure 3. $|I_{CH}|^2$ as defined in equation (27) as a function of θ, the angle between the heavy-hole and conduction band wavevectors. Conduction band wavevector, $\boldsymbol{k}_C$, along the z axis. Heavy-hole band wavevector, $\boldsymbol{k}_H$, in the xz plane. $\boldsymbol{k}_C = 0.015(2\pi/a)$, $\boldsymbol{k}_H = 0.15\,(2\pi/a)$. Full curve, 15-band $\boldsymbol{k}\cdot\boldsymbol{p}$ results; chain curve, Kane four-band results, equation (33); broken curve, Kane four-band results for the equal 'spin indices', equation (32*a*); dotted curve, Kane four-band results for different 'spin indices', equation (32*b*). (*a*) GaAs; (*b*) InP.

Figure (3.5) - Results for the conduction - heavy hole overlap integrals for non-parallel wavevectors (taken from reference [7]).

the contribution to the κ-space integral. However, because of confinement in the y and z directions, there is an uncertainty of $2\pi/L$ in the transverse wavevector. For a wire with L=150 Å we find that $2\pi/L = 0.049\text{Å}^{-1}$, and $\kappa_o = 0.091\text{Å}^{-1}$ (for typical material parameters). The uncertainty in the transverse wavevector means that the wavevectors of the heavy hole and conduction band carriers cannot be assumed to be parallel. This is likely to blur out any marked directional dependence of Auger rates in a QWW, which may at first sight have been expected. A preliminary investigation into this blurring mechanism has been carried out by Kelsall[10].

3.5 SUMMARY OF CHAPTER THREE

The transition rate for the bound-bound CHSH Auger process in a quantum well wire (QWW) has been calculated algebraically with the assumptions of isotropic, parabolic subbands and Boltzmann statistics with quasi-Fermi levels. Transition rates for the CHCC, CHLH, CLSL, CLLL and CHHH Auger processes may be obtained from the CHSH result by using the procedure outlined in Chapter Two.

The QWW was assumed to have a square cross-section, and the potential wells were assumed to be infinitely deep.

It was found that, if the Auger process involving ground state subbands only gave the dominant contribution to the total QWW Auger rate, then the Auger rate in the QWW was approximately the same as the corresponding rate in the QW (assuming room temperature and equal threshold carrier densities).

REFERENCES FOR CHAPTER THREE

[1] P.M. Petroff, A.C. Gossard, R.A. Logan, W. Wiegmann, Appl.Phys.Lett., 41, (1982), 635.

[2] M. Asada, Y. Miyamoto, Y. Suematsu, Jap.J.Appl.Phys., 24, (1985), L95.

[3] Y. Arakawa, H. Sakaki, Appl.Phys.Lett., 40, (1982), 939.

[4] R.W. Kelsall, unpublished work (1986).

[5] M. Takeshima, Phys.Rev.B 31, (1985), 992.

[6] R.I. Taylor, R.W. Kelsall, R.A. Abram, Surf.Sci., 174, (1986), 169.

[7] M.G. Burt, S. Brand, C. Smith, R.A. Abram, J.Phys.C:Solid State Phys., 17, (1984), 6385.

[8] C. Smith, PhD thesis, Durham University, (1985) (unpublished).

[9] M.G. Burt, C. Smith, J.Phys.C:Solid State Phys., 17, (1984), L47.

[10] R.W. Kelsall, private communication.

CHAPTER FOUR

NUMERICAL ESTIMATES OF AUGER TRANSITION RATES IN InGaAsP/InP QUANTUM WELLS AND QUANTUM WELL WIRES

INTRODUCTION

In Chapters Two and Three, expressions for CHSH Auger transition rates in QWs and QWWs were presented. In this Chapter, those expressions are used to estimate Auger transition rates in 1.3μm and 1.55μm InGaAsP/InP quantum wells and quantum well wires. However to apply the theory it is first necessary to find the energy levels of the confined states of the QW or QWW, and then use these to calculate the conduction and valence band quasi-Fermi levels. In addition to explaining how the calculations are performed, the various methods used in previous work for including Bloch function overlap integrals in the Auger calculations are discussed. Numerical results for Auger transition rates in QWs (both bound-bound and bound-unbound) for all the important Auger processes (CHCC, CHSH, CHLH) are presented, and bound-bound results are presented for the QWW. A comparison with previous work is made.

4.1 NUMERICAL ESTIMATES OF BOUND-BOUND AUGER TRANSITION RATES IN InGaAsP/InP QUANTUM WELLS

In optoelectronic telecommunications systems, the two most important wavelengths are 1.3μm and 1.55μm, since these correspond to the zero of dispersion and the minimum of attenuation respectively in silica-based optical fibres. In practice, this means that if an InGaAsP/InP quantum well laser were used as a source for such a system, it would be designed to emit at one of these wavelengths. Thus, in the results that will be presented, the QW bandgap is kept constant at an energy corresponding to one or other of the two wavelengths. This is achieved by altering the alloy composition of the InGaAsP (the well material) at each well width to ensure that the sum of the alloy bandgap and the conduction and heavy hole ground state confinement energies equals one or other of the energies corresponding to wavelengths of 1.3μm or 1.55μm.

The parameters used in the calculation are as follows: For lattice matching of $In_{1-x}Ga_xAs_yP_{1-y}$ to InP

$$x = \frac{0.4526y}{1 - 0.031y} \tag{4.1}$$

The energy gap, E_g, and spin-orbit splitting, Δ, are given in electron volts by

$$E_g = 1.35 - 0.72y + 0.12y^2 \tag{4.2}$$

$$\Delta = 0.11 + 0.31y - 0.09y^2 \tag{4.3}$$

and the following expressions for the carrier effective masses are used

$$\frac{m_C}{m_o} = 0.08 - 0.039y \tag{4.4}$$

$$\frac{m_H}{m_o} = (1-y)(0.79x + 0.45(1-x)) + y(0.45x + 0.4(1-x)) \tag{4.5}$$

$$\frac{m_L}{m_o} = (1-y)(0.14x + 0.12(1-x)) + y(0.082x + 0.026(1-x)) \tag{4.6}$$

$$\frac{m_S}{m_o} = 0.14 \tag{4.7}$$

where m_C, m_H, m_L, and m_S are the carrier effective masses for the conduction, heavy hole, light hole and spin-split off bands respectively and m_o is the free electron mass. In addition to the above parameters, the relative permittivity, ϵ, which is required in the expression for the Auger transition rate, is given by

$$\epsilon = (1-y)(8.4x + 9.8(1-x)) + y(13.1x + 12.2(1-x)) \tag{4.8}$$

With the above parameters (taken from [1]), and using a band offset ratio $\Delta E_c : \Delta E_v$ of 2:1 [2], the energies of confined states in the quantum well may be calculated using a finite square well model [3]. The QW bandgap is then constrained to be either 0.80 eV (1.55μm) or 0.95 eV (1.3μm) and the remaining confined state energy levels are evaluated.

Once the energy levels are known the conduction and valence band quasi-Fermi levels can be determined. If n is the total number of electrons per unit volume injected into the QW, then, assuming isotropic, parabolic subbands, the conduction band quasi-Fermi level is obtained by solving the integral equation

$$n = \frac{m_C k_B T}{\pi \hbar^2 L} \sum_{i=1}^{N} \int_0^\infty \frac{dx}{A \exp(x) + \lambda} \tag{4.9}$$

with $A = \exp(\beta(E_i - F_c))$, and N is the number of confined states in the conduction band quantum well, with energies $E_1, \ldots, E_N$. Note that the continuum of states above the top of the quantum well should also be included in the calculation of the quasi-Fermi levels. However, for the InGaAsP/InP QW system, the size of the confining barrier is such that these states have a negligible effect on the quasi-Fermi level positions. In equation (4.9), $\lambda = 1$ if Fermi-Dirac statistics are assumed, whereas $\lambda = 0$ for Boltzmann statistics. In both cases, the integration can be achieved analytically to give

$$n = \frac{m_C k_B T}{\pi \hbar^2 L} \sum_{i=1}^{N} \log[\exp(\beta(F_c^{FD} - E_i)) + 1] \tag{4.10}$$

for Fermi-Dirac statistics, and

$$n = \frac{m_C k_B T}{\pi \hbar^2 L} \sum_{i=1}^{N} \exp(\beta(F_c^{B} - E_i)) \tag{4.11}$$

for Boltzmann statistics. Similar expressions may be written down for the holes except they are slightly more complicated because of the presence of light, heavy and spin-split off holes. Equations (4.10) and (4.11) and the corresponding equations for the injected hole density, p, can be solved numerically for the conduction and valence band quasi-Fermi levels if n and p are specified. Once the quasi-Fermi levels are known the number of carriers in any particular subband may be evaluated. The variation of the conduction and valence band quasi-Fermi levels with well width is illustrated in Figure (4.1) (for various values for the injected carrier density) for the 1.3 μm InGaAsP/InP QW. The quasi-Fermi levels were calculated using both Boltzmann and Fermi-Dirac statistics. Figure (4.2) gives similar results for the 1.55 μm InGaAsP/InP QW.

Figure (4.1) - (a) Conduction band quasi-Fermi levels and (b) valence band quasi-Fermi levels as a function of well width for varying injected carrier densities for a 1.3μm InGaAsP/InP QW. In (a), the zero of energy was taken as the bottom of the conduction band QW, with energies being negative in the bandgap. For (b), the zero of energy was taken as the top of the valence band QW, with energies being negative in the gap. Full lines are values using Boltzmann statistics, and the dashed lines are values using Fermi-Dirac statistics (Temperature is 300K).

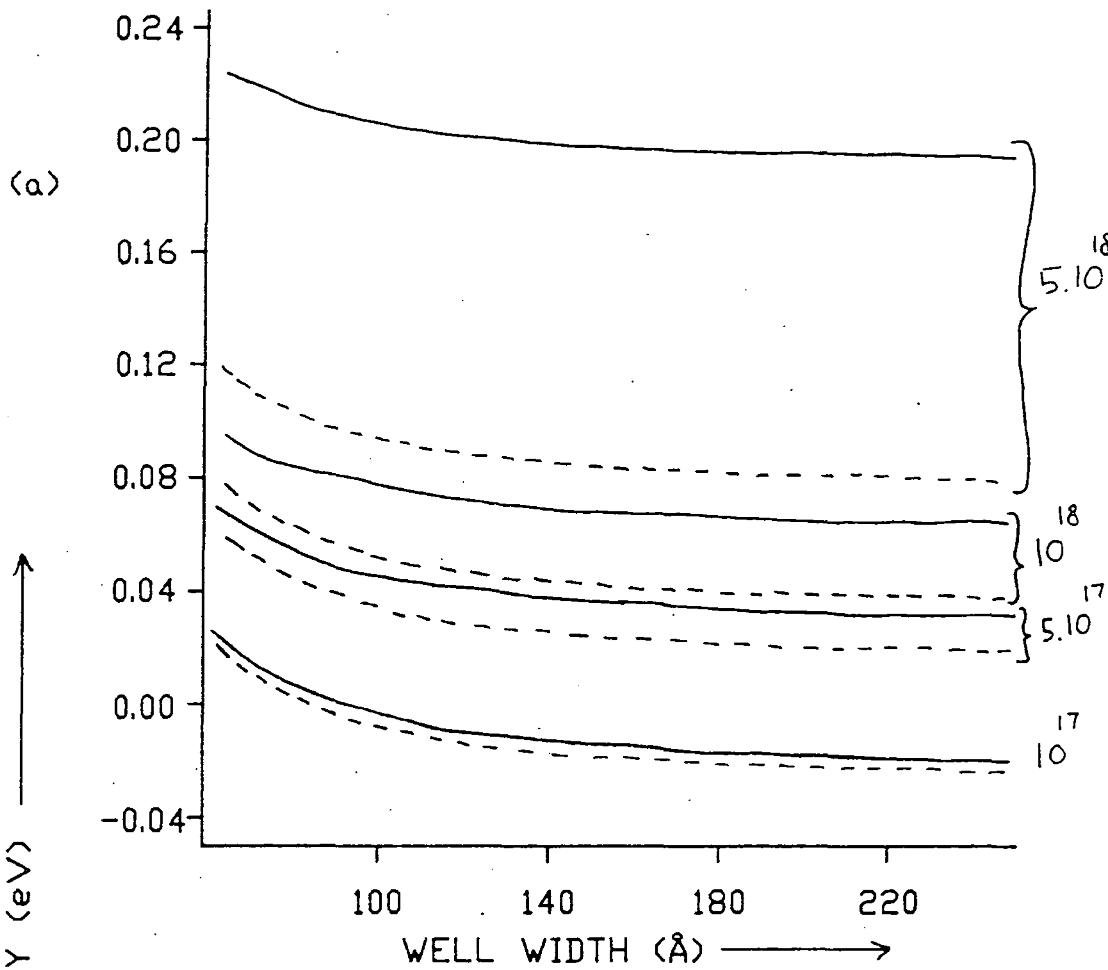
(a)
0.24
0.20
0.16
0.12
0.08
0.04
0.00
-0.04
100
140
180
220
WELL WIDTH (Å)
ENERGY (eV)
5.10 18
10 18
5.10 17
10 17

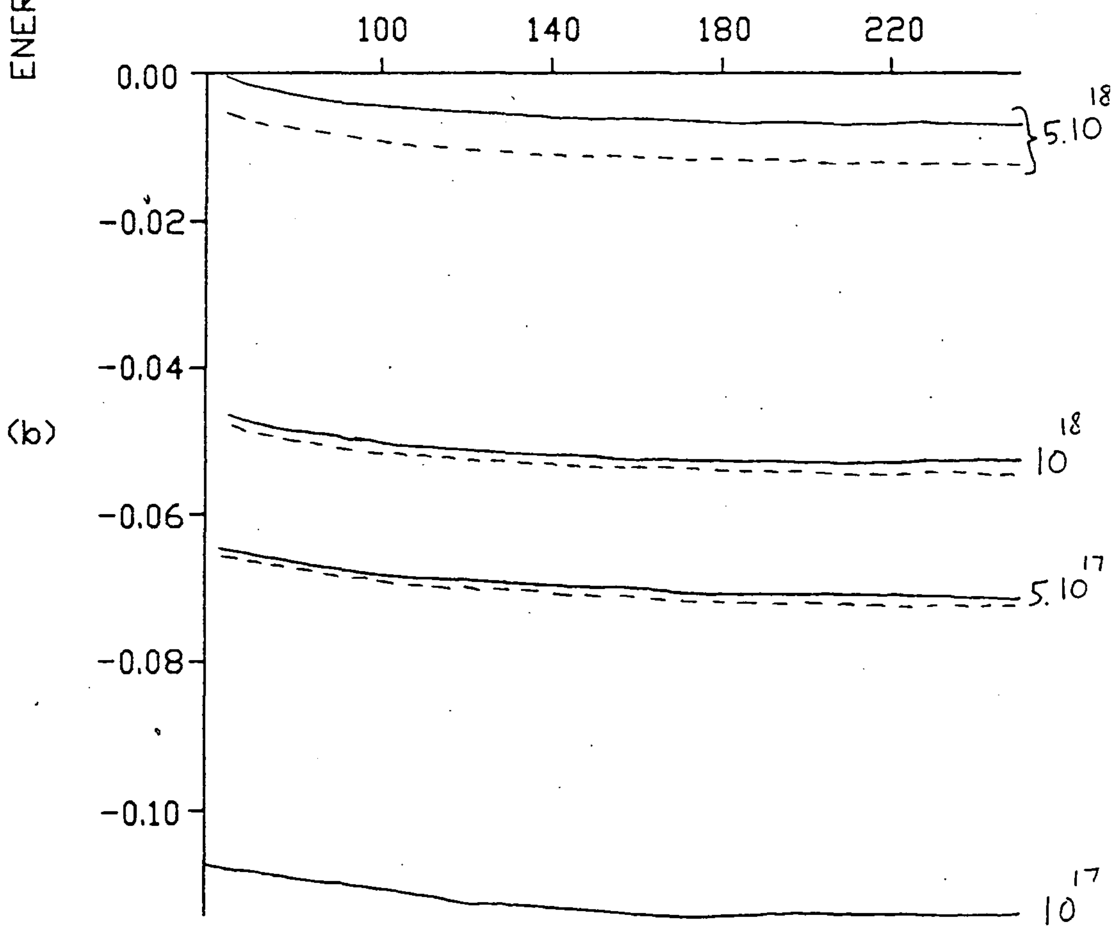
(b)
100
140
180
220
0.00
-0.02
-0.04
-0.06
-0.08
-0.10
5.10 18
10 18
5.10 17
10 17

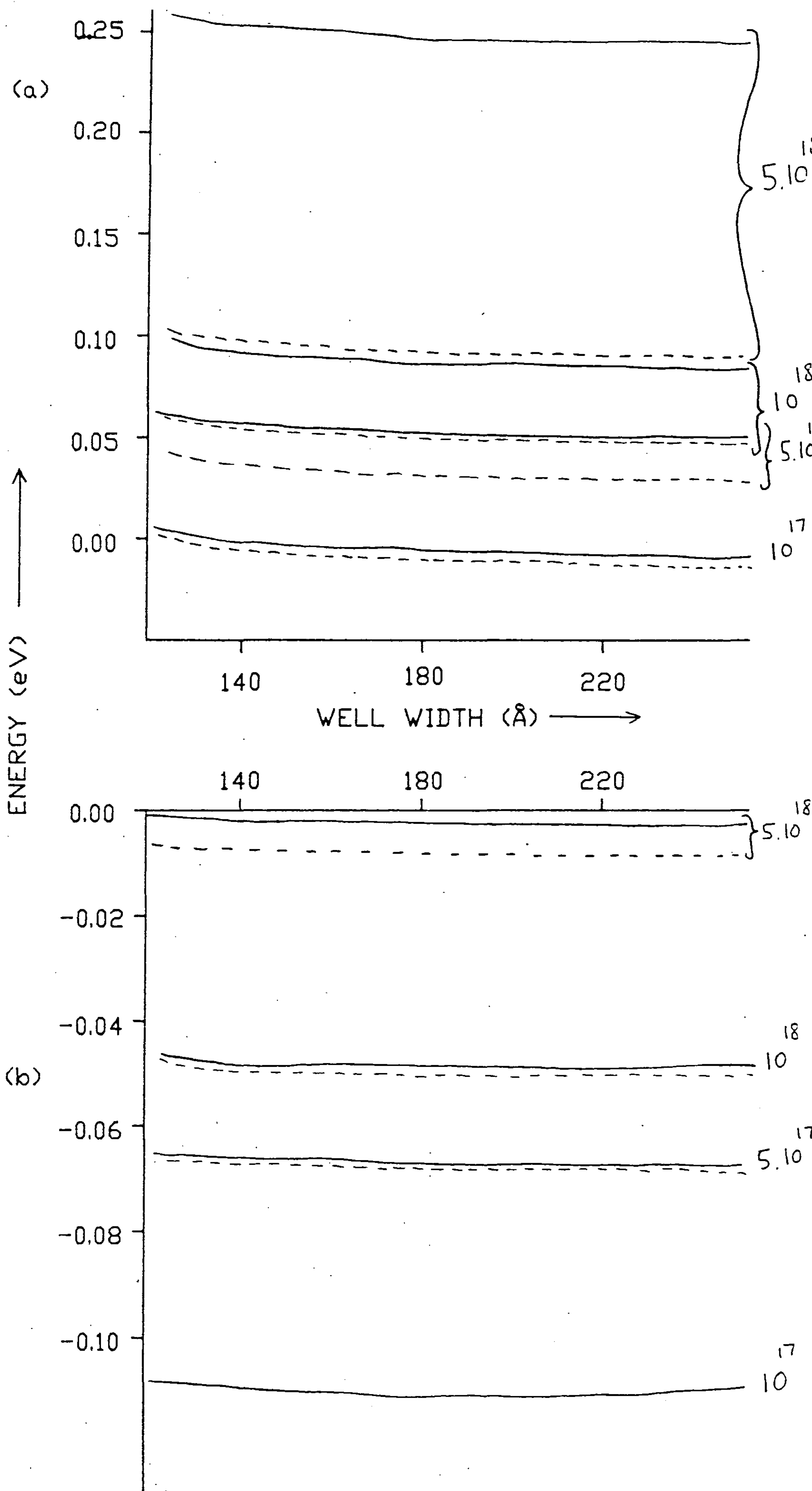

Figure (4.2) - Same as Figure (4.1) but for the 1.55μm InGaAsP/InP QW.

The figures show that, for the valence band quasi-Fermi level, Boltzmann and Fermi-Dirac statistics are in good agreement at room temperature for carrier densities of the order of 10^{18} cm^{-3} This is further illustrated in Figures (4.3) and (4.4), where the number of carriers in the valence subbands have been calculated as a function of well width (the calculations being performed with both Boltzmann and Fermi-Dirac statistics) for the 1.3 μm and 1.55 μm InGaAsP/InP QWs respectively.

The agreement between Boltzmann and Fermi-Dirac statistics is not, however, as good for the conduction band quasi-Fermi levels, for carrier densities of the order of 10^{18} cm^{-3} at 300 K (see Figures (4.5) and (4.6)). Although the agreement between the two types of statistics is not very good for the conduction subbands (for typical carrier densities of interest for lasers at room temperature), the effect of using Fermi-Dirac statistics in the calculation of Auger transition rates is discussed in Chapter Five, and it is concluded that Boltzmann-based calculations of such rates will only be in error by 20 or 30 percent. This conclusion is in agreement with the results of Haug [4] and, in Chapter Five, some physical justification is given for why Boltzmann statistics can be used at carrier densities of the order of 10^{18} cm^{-3}. The conduction and valence band quasi-Fermi levels from the Boltzmann calculations are used in the evaluation of the Auger transition rates (refer to the relevant expressions presented in Chapter Two).

The remaining material parameters required for the calculation of the Auger transition rates are found from equations (4.1) to (4.8), and the threshold wavevector transfer is determined from equation (2.50).

The only other quantities required for the calculation of the Auger transition rates are the overlap integrals of the Bloch periodic parts of the carrier wavefunctions, as described in Chapter Two. In the initial calculations of

Figure (4.3) - Hole densities as a function of well width in a 1.3μm InGaAsP/InP QW. The injected carrier density is $10^{18}cm^{-3}$, and the temperature is 300K. (a) shows the lowest three heavy hole subbands and (b) shows the lowest three light hole subbands. Full lines are Boltzmann results and dashed lines are Fermi-Dirac results.

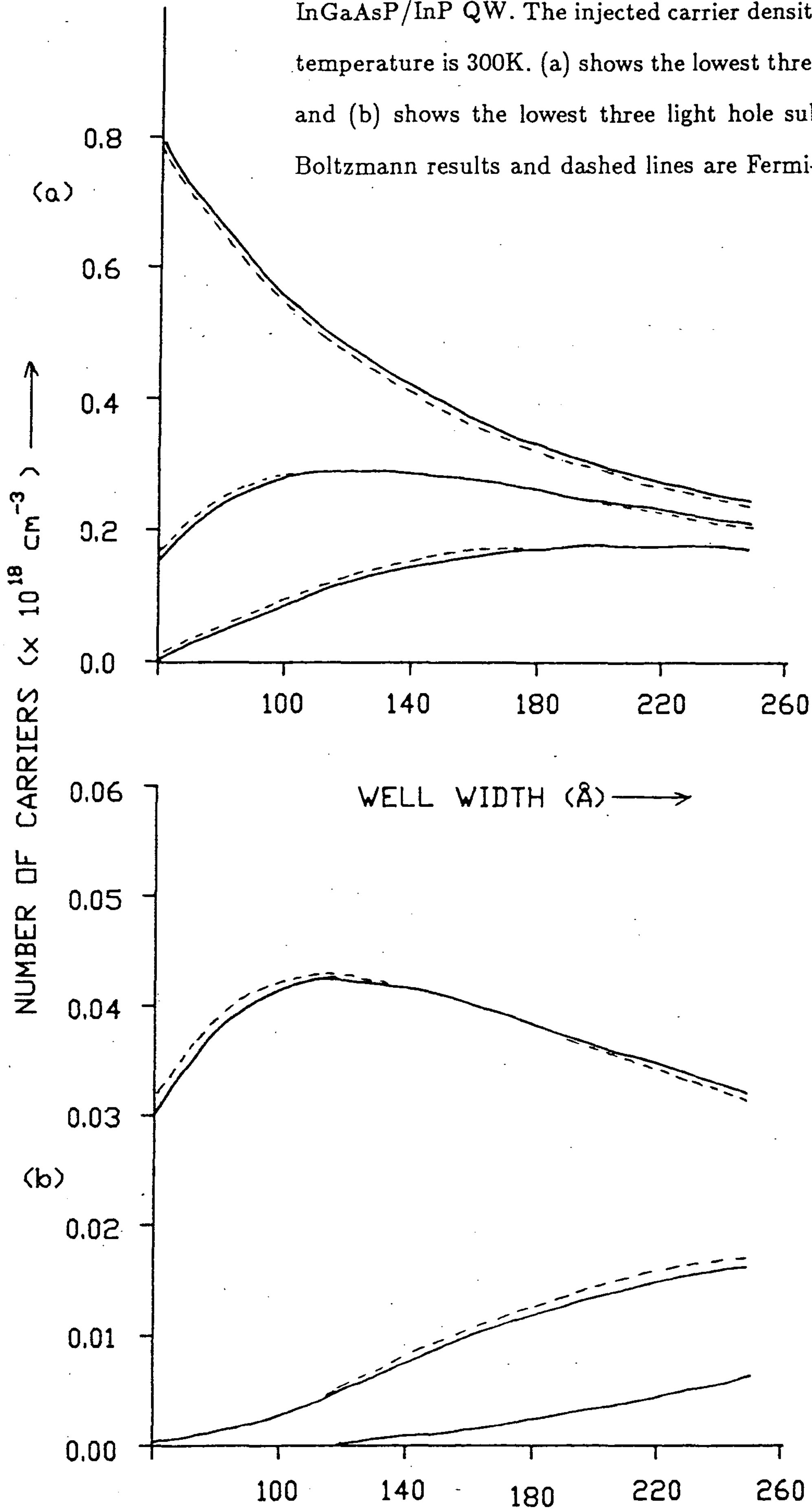

Figure (4.4) - Same as Figure (4.3) but for the 1.55μm InGaAsP/InP Qw.

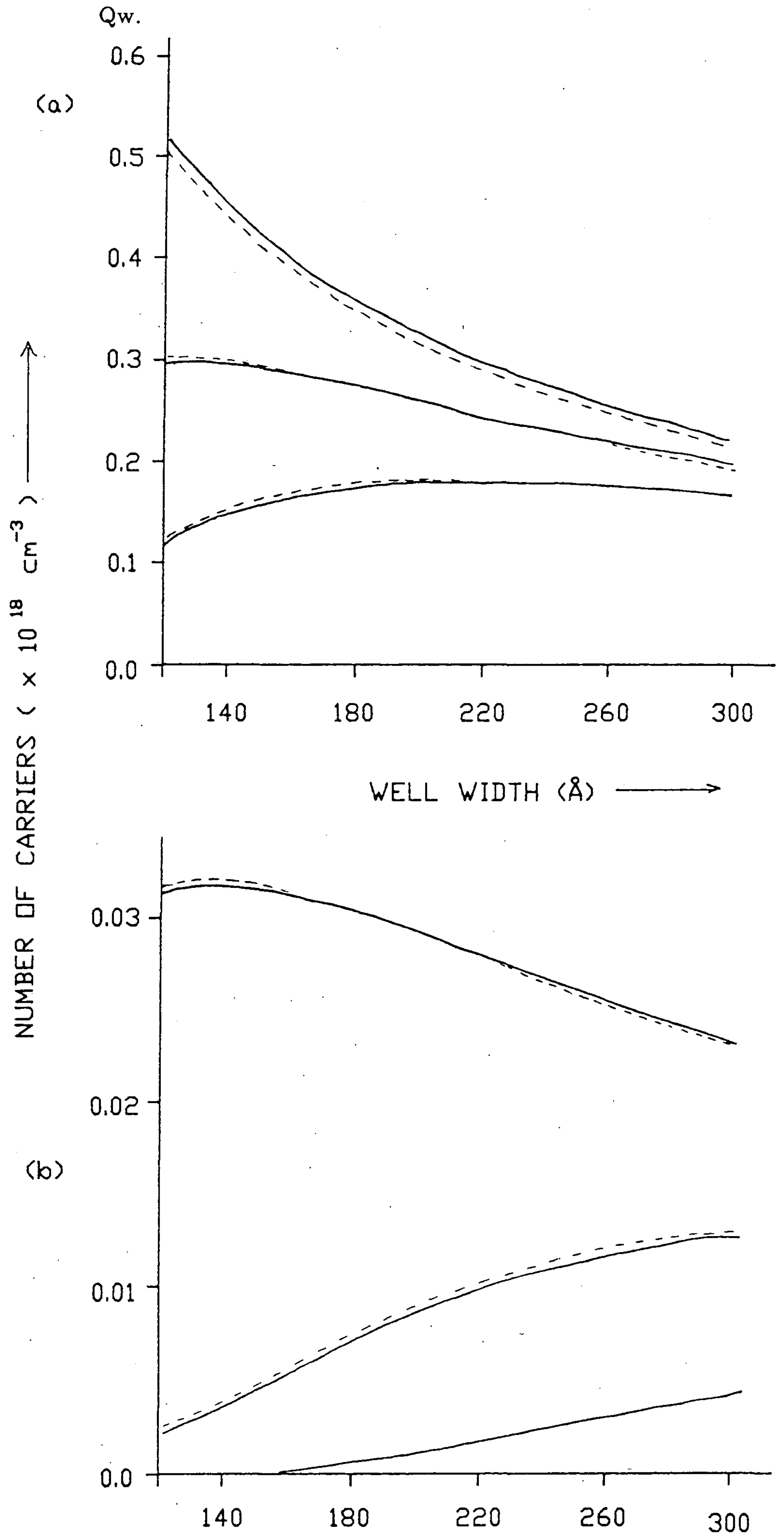

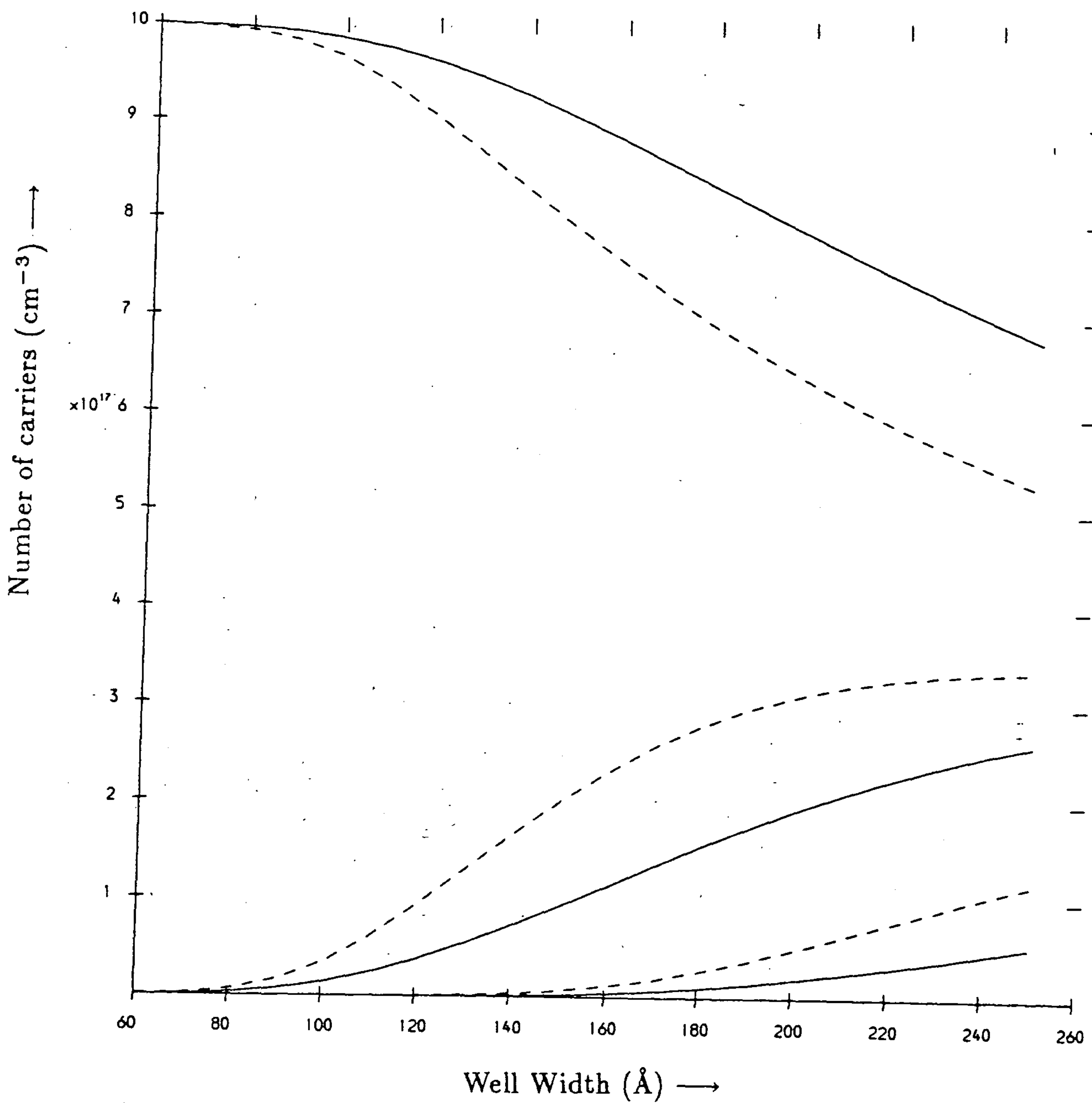

Figure (4.5) - Electron densities as a function of well width in a $1.3\mu m$ InGaAsP/InP QW. The injected carrier density is $10^{18}cm^{-3}$ and the temperature is 300K. The lowest three conduction subbands are shown, with full lines indicating Boltzmann results and dashed lines indicating Fermi-Dirac results.

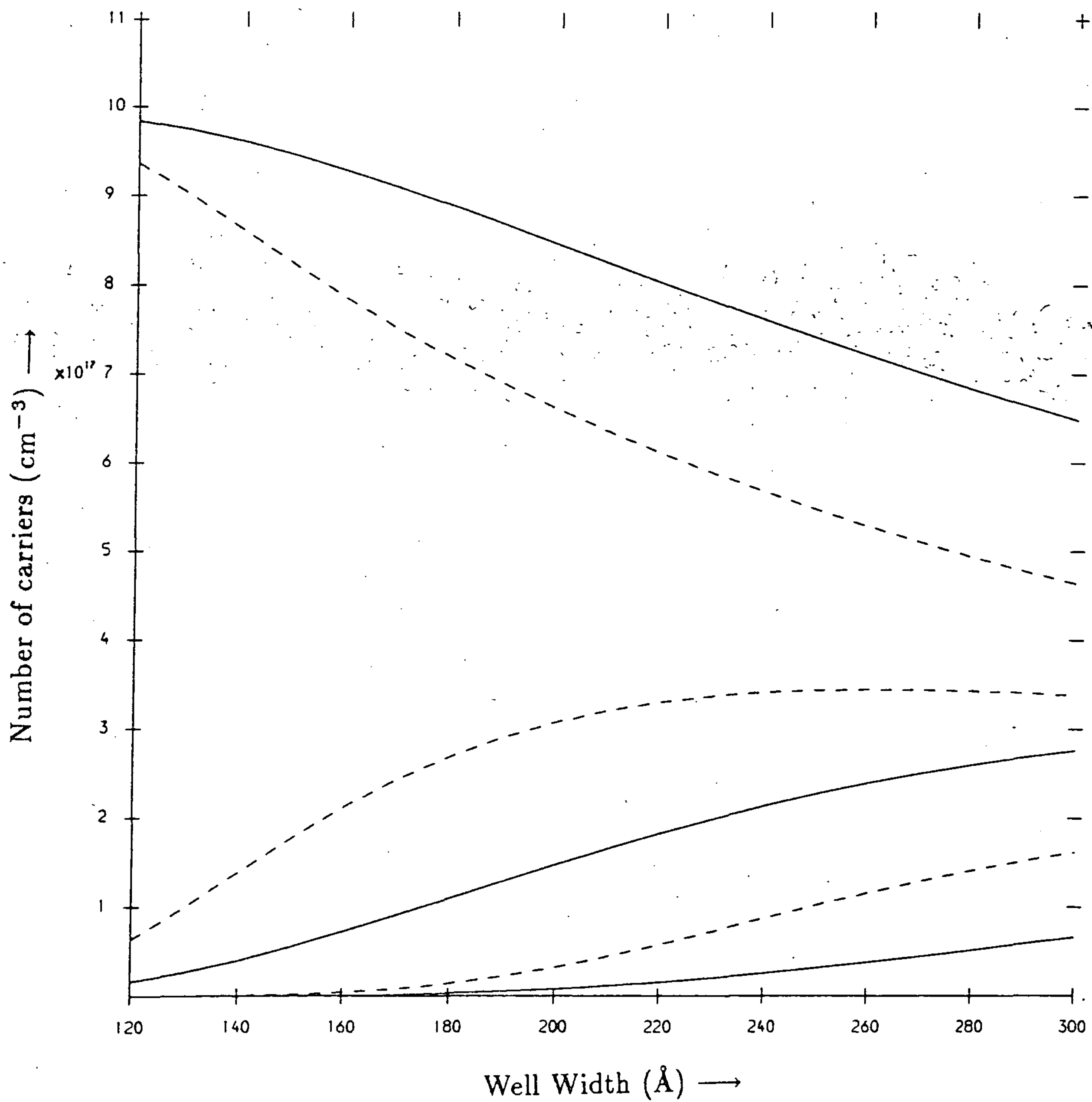

Figure (4.6) - Same as Figure (4.5) but for the 1.55μm InGaAsP/InP QW.

Auger transition rates in bulk semiconductors [5], the overlap integral between the conduction and heavy hole bands was estimated from a one-dimensional Kronig-Penney model [6], [7]. Later calculations of overlap integrals [8], [9], made use of effective mass sum rules derived from $\underline{k}.\underline{p}$ perturbation theory. Certain terms in the sum rule were assumed to dominate and approximate expressions for the overlap integrals were derived. The expressions for the overlap integrals given by Beattie and Smith [9] were calculated in this way, and will henceforth be referred to as 'conventional' estimates of overlap integrals. Such conventional estimates of the overlap integrals were used by Smith [10], and by Smith et al [11] in their calculations of CHCC Auger transition rates in InGaAsP/InP QWs. Calculations using conventional estimates for the overlap integrals predict Auger coefficients of between 10^{-27} and 10^{-28} cm^6s^{-1}.

Recently, it has been shown that the use of the conduction band effective mass sum rule [9] to calculate the overlap integral between the conduction band and the heavy hole band yields estimates that are approximately two orders of magnitude too large [10], [12], [13]. The reason for such a large discrepancy is that the terms which were assumed to dominate in the effective mass sum rules are, in fact, relatively unimportant [12]. Burt et al [13] have recently recalculated overlap integrals between the conduction and heavy hole bands using two different methods. The first method was a full-zone 15-band $\underline{k}.\underline{p}$ calculation, and the second method used non-local pseudopotentials to calculate the overlap integrals. The two seperate calculations yielded results for the conduction band - heavy hole band overlap integral that were in very good agreement, but the results were at least an order of magnitude smaller than conventional estimates.

For the conduction band - heavy hole band overlap integral, it is a good approximation [10], [12], [13], [14], to write

$$|M_{CH}|^2 = \beta(\underline{k}_3 - \underline{k}_1)^2 \tag{4.12}$$

where $\underline{k}_3$ is the heavy hole wavevector, and $\underline{k}_1$ is the conduction band wavevector, and the two wavevectors are taken to be antiparallel (corresponding to the threshold configuration in an Auger process). If the wavevectors are in units of $(2\pi/a)$, where a is the lattice constant of the semiconductor, then $\beta \approx 0.247$ for GaAs [10] when the wavevectors are directed midway between the [001] and [101] directions (the direction in which the CH overlap is maximum [13]). No explicit calculations of overlap integrals for the quaternary system InGaAsP have been reported, and throughout this Chapter results for GaAs overlap integrals are used (the only difference being that the lattice constant is taken to be that of InP), since there is little difference between the overlap integrals for different III-V materials [15].

So far, only the overlap integral between the conduction and heavy hole bands has been discussed. For calculations of CHLH and CHSH Auger transition rates, overlap integrals between the light hole and heavy hole bands (the LH overlap), and between the heavy hole and spin split off bands (the SH overlap) are required. The full-zone 15-band $\underline{k}.\underline{p}$ method and the non-local pseudopotential method described above have been used to calculate LH and SH overlaps. Very recently [16], results in close agreement with these two methods have been reproduced using a Kane four band model [17], with higher bands included using perturbation theory. The LH and SH overlaps used in the numerical results of this Chapter have been taken from this latter method.

Taking overlap integrals from calculations for bulk semiconductors and applying them to the QW is an approximation. The QW overlap integrals will be larger, since the uncertainty of at least $2\pi/L$ in the wavevector associated with the confinement direction means that the wavevectors of the carriers involved

in the Auger transition cannot be assumed parallel. As seen from the results of [13], when overlap integrals between the conduction and heavy hole band are calculated for carriers with non-parallel wavevectors, the values are increased over the results for carriers with parallel wavevectors. Another way of seeing that use of the overlap integrals above will underestimate the Auger rate is to consider the effect of the QW potential in mixing the bands. For example, the ground state heavy hole subband in a QW will have some light hole character. Thus a carrier that is confined to that subband, but is free to move in a plane parallel to the interface, cannot simply be described by a Bloch periodic function that is purely heavy hole like.

Unfortunately, no information is available on overlap integrals in QWs, and so, as in other calculations [10], [11], [19], bulk values are used, with the improvement that the bulk values are better estimates than 'conventional' values used in [10], [11], [19]. For the reasons given above results obtained using the bulk values are likely to underestimate the Auger transition rates in QWs.

Figures (4.7) and (4.8) show the bound-bound CHCC QW Auger transition rate as a function of well width for the 1.3 μm and 1.55 μm InGaAsP/InP QWs respectively (the threshold wavevectors are assumed to lie in a direction midway between the [001] and [101] directions so as to maximise the overlap integral between conduction and heavy hole bands). The number of carriers injected into the QW has been taken to be 10^{18}cm^{-3}. Note that all the results presented in this Chapter have been calculated assuming a temperature of 300K. In addition to the calculation that was described in Chapter Two, where all the confined state wavevectors were assumed to be integer multiples of π/L, a further calculation has also been performed in which the realistic confined state wavevectors (from a finite square well model) and the evanescent parts of the carrier wavefunctions have been included. However, as can be seen from

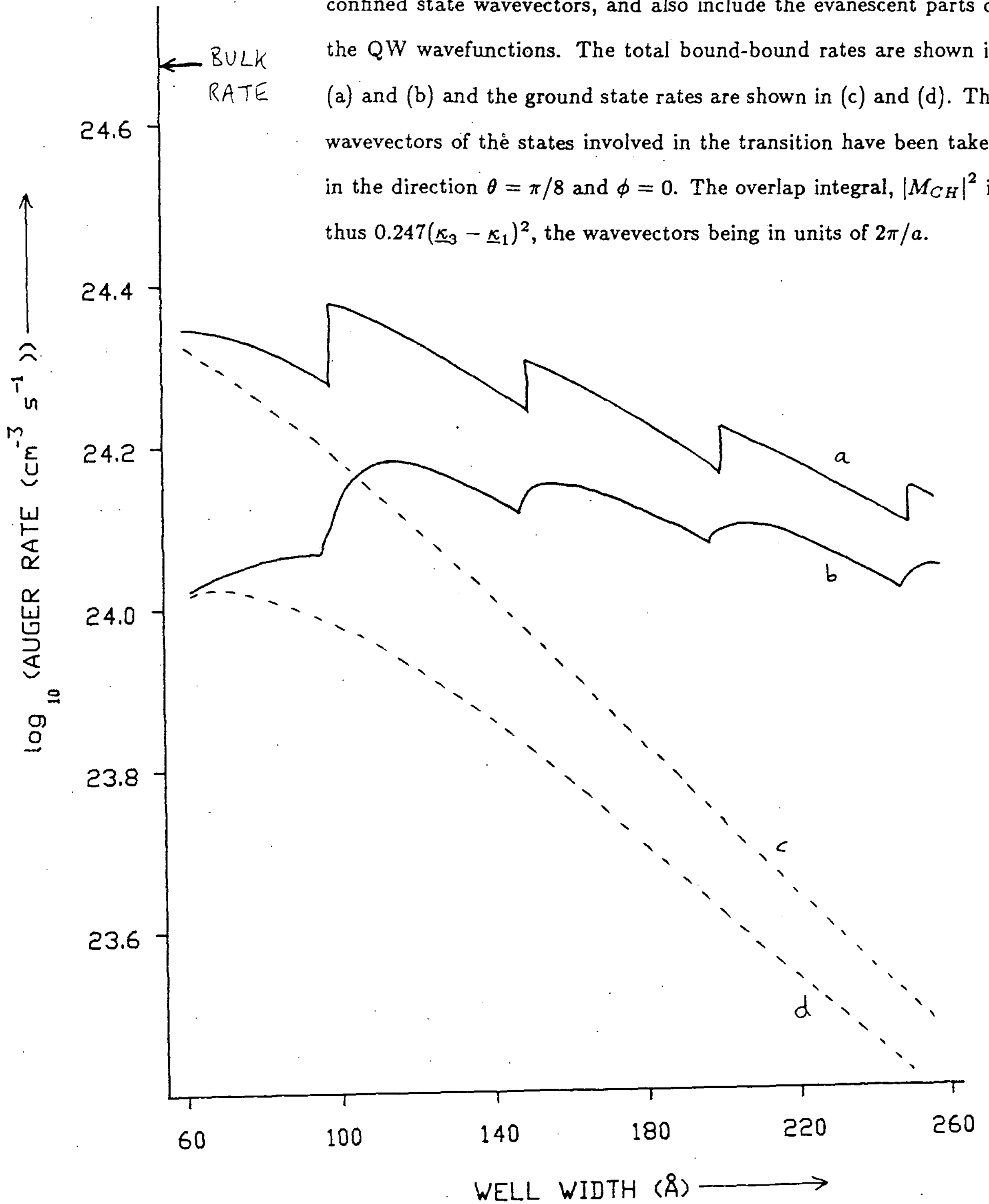

Figure (4.7) - Graph showing the variation of the QW CHCC bound-bound Auger rate as a function of well width for a 1.3μm InGaAsP/InP QW. The temperature is 300K and the injected carrier density is 10^{18}cm^{-3}. Curves (a) and (c) assume confined state wavevectors that are integer multiples of π/L, whereas curves (b) and (d) use realistic confined state wavevectors, and also include the evanescent parts of the QW wavefunctions. The total bound-bound rates are shown in (a) and (b) and the ground state rates are shown in (c) and (d). The wavevectors of the states involved in the transition have been taken in the direction $\theta = \pi/8$ and $\phi = 0$. The overlap integral, $|M_{CH}|^2$ is thus $0.247(\underline{\kappa}_3 - \underline{\kappa}_1)^2$, the wavevectors being in units of $2\pi/a$.

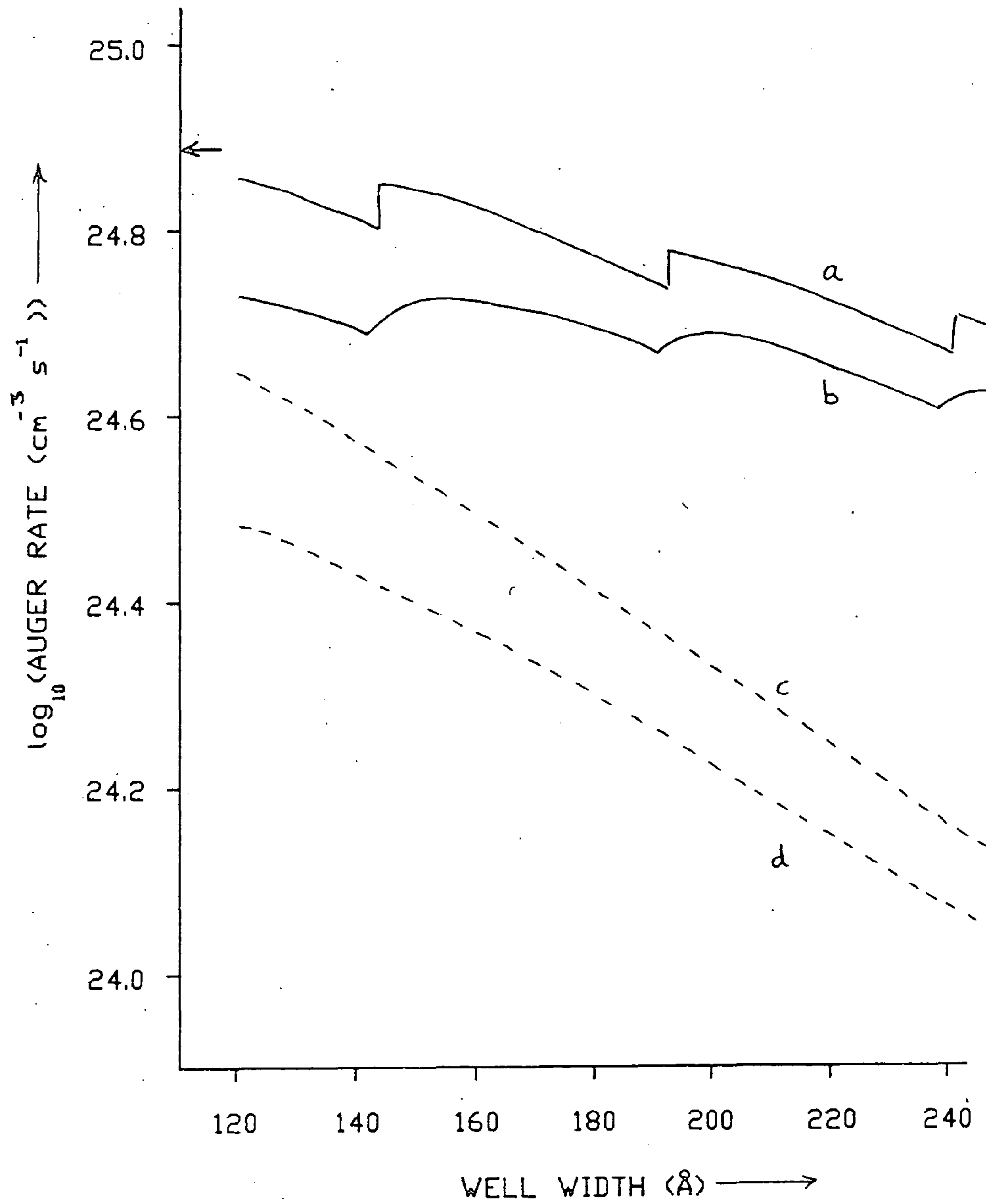

Figure (4.8) - Same as Figure (4.7) but for the 1.55μm InGaAsP/InP QW.

the figures, the more sophisticated calculation does not significantly change the results (i.e. the results are of the same order of magnitude). Also shown is the bulk Auger rate for the corresponding material parameters (i.e. bulk band gap equal to QW bandgap etc) and the same injected carrier density. The total QW CHCC bound-bound Auger transition rate is within a factor of two of the bulk rate, as expected from the discussions of Chapter Two.

The total bound-bound CHCC QW Auger rate has a 'saw tooth' appearance, the jumps in the rate occurring at well widths corresponding to a new conduction band level being confined. A similar type of behaviour was found by Smith [10]. The ground state CHCC QW Auger rate decreases by about a factor of ten over the range of well widths shown, due to less carriers occupying the ground state subbands of the QW at wider well widths.
The approximate Auger coefficients are

$$C^{QW}_{CHCC}(1.3\mu m) \approx 0.2 \text{ x } 10^{-29}\text{cm}^6\text{s}^{-1} \tag{4.13}$$

$$C^{QW}_{CHCC}(1.5\mu m) \approx 0.6 \text{ x } 10^{-29}\text{cm}^6\text{s}^{-1} \tag{4.14}$$

Now we consider the CHSH bound-bound QW Auger rate. Some calculations of CHSH Auger transition rates in InGaAsP/InP quantum wells have been reported [19], [20]. In reference [19] Dutta claims that the CHCC and CHSH Auger processes are about the same order of magnitude. However, with band offsets of $\Delta E_c : \Delta E_v = 2:1$, it can be seen from Figure (4.9) that the material parameters of the InGaAsP/InP QW are such that there is no spin-split off well in the InGaAsP/InP QW. This suggests that there are no bound-bound CHSH Auger transitions and that only bound-unbound processes will contribute to the CHSH rate (the bound states being in the conduction and heavy hole bands,

Figure (4.9) - The energies of the band edges of $1.3\mu m$ and $1.55\mu m$ InGaAsP/InP QWs, assuming $\Delta E_c : \Delta E_v = 2:1$.

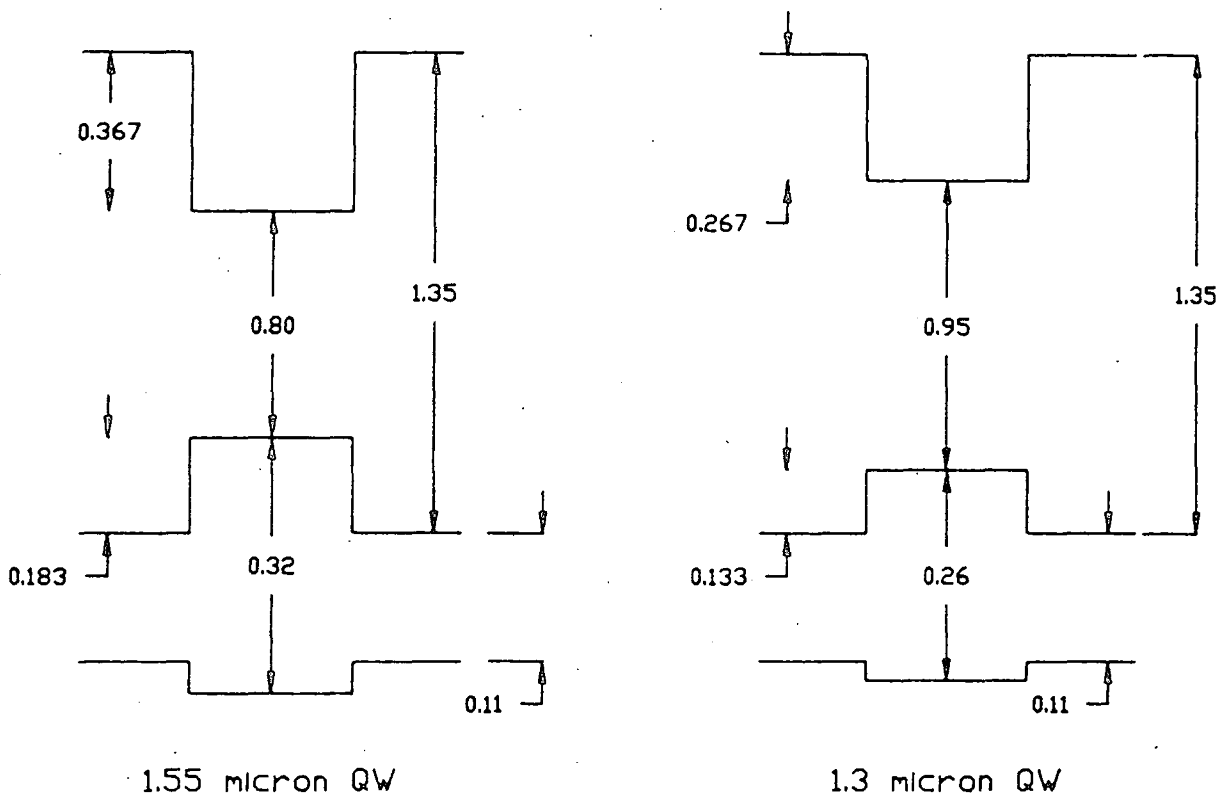

the unbound state being in the spin split off band). However, the earlier calculations mentioned above [19], [20] do not consider bound-unbound transitions, assuming only bound-bound transitions occur, and, in addition, the calculations assume that the confined state wavevectors are integer multiples of π/L. In view of these approximations, the earlier calculations should be treated with caution. If the band offsets were significantly different from the 2:1 ratio used throughout this thesis, then it is possible for a spin-split off well to be formed, and then bound-bound Auger transitions would be allowed. However, with the band offsets used here any CHSH Auger transition rate will arise from bound-unbound processes, which will be considered in the next Section.

Finally, the bound-bound CHLH QW Auger transition rate in InGaAsP/InP QWs is examined. The form of the conduction band - heavy hole band overlap integral given in equation (4.12) is used, and the light hole - heavy hole overlap integral has been calculated using the Kane four band model with higher bands included from perturbation theory [16]. The CH and LH overlaps are calculated assuming that the wavevectors of the carriers taking part in the Auger transition lie in a direction with $\theta = \pi/6$ and $\phi = 0$ (where spherical polar coordinates have been used). This direction is midway between the angles that maximise the CH overlap ($\theta = \pi/8$) and the LH overlap ($\theta = \pi/4$). Figure (4.10) illustrates the variation of the CHLH QW Auger rate with quantum well width for the 1.3μm InGaAsP QW, and figure (4.11) shows the results for the 1.55μm QW. The number of carriers injected into the QW has, again, been taken to be 10^{18}cm^{-3}. A 'saw-tooth' appearance was found, similar to the CHCC QW results, and the well widths at which the jumps occur correspond to well widths when new subbands become bound by the light hole QW. The actual magnitude of the CHLH QW Auger rate is approximately two orders of magnitude lower than the corresponding results for the CHCC process. This is

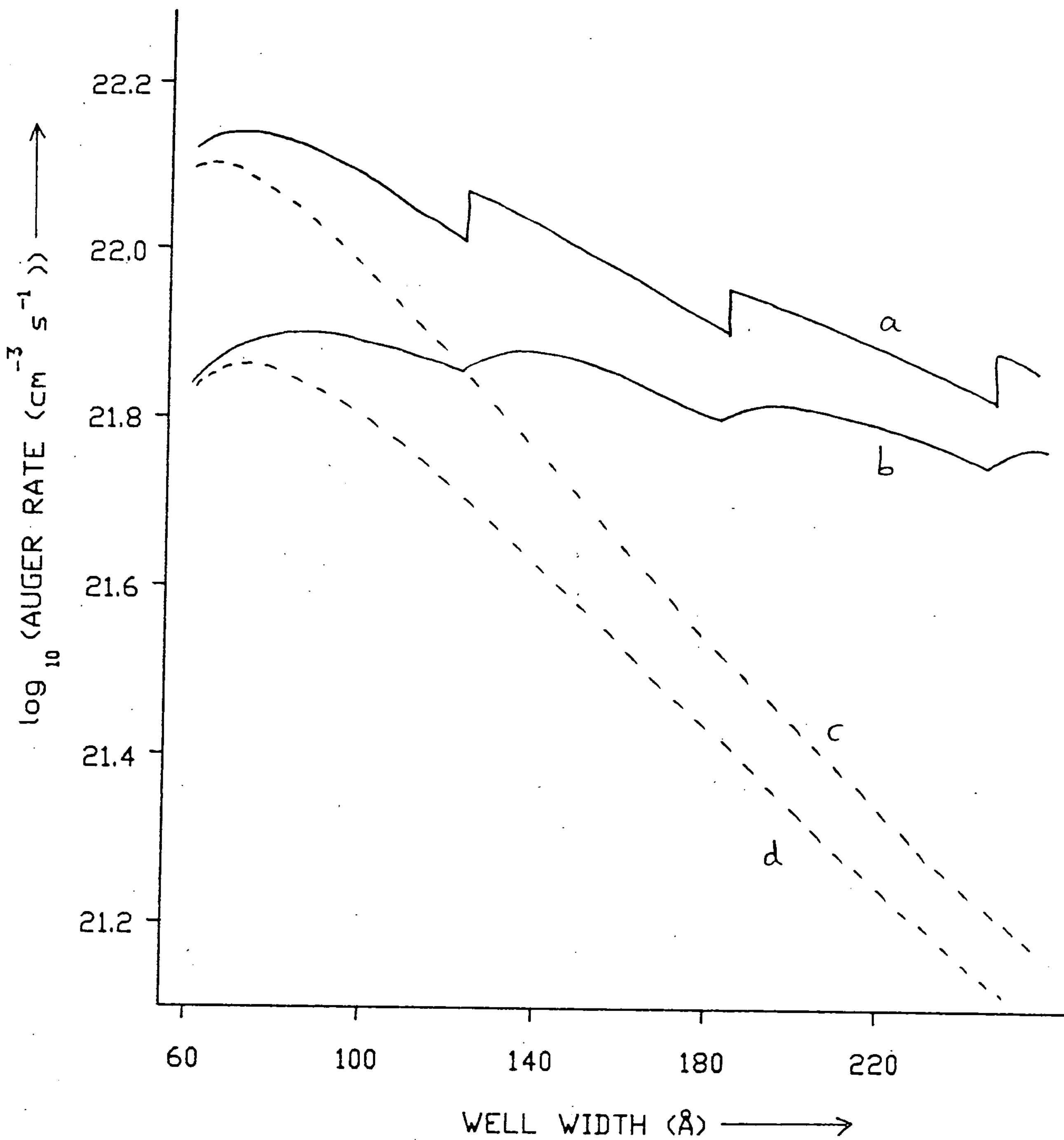

Figure (4.10) - Graph showing the variation of the QW CHLH bound-bound Auger rate as a function of well width for a 1.3μm InGaAsP/InP QW. The injected carrier density is 10^{18}cm^{-3} and the temperature is 300K. Curves (a) and (c) assume confined state wavevectors that are integer multiples of π/L, whereas curves (b) and (d) use realistic values for the confined state wavevectors and also include the evanescent parts of the QW wavefunctions. The total bound-bound rate is shown in curves (a) and (b) and the ground state rates are shown in (c) and (d). The wavevectors of the states have been taken in the direction $\theta = \pi/6$ and $\phi = 0$, and are given by $|M_{CH}|^2 = 0.176\Delta\kappa^2$ and $|M_{LH}|^2 = 0.1658\Delta\kappa - 7.335\Delta\kappa^2 + 99.96\Delta\kappa^3 - 230.6\Delta\kappa^4$ with $(\Delta\kappa = (\underline{\kappa}_3 - \underline{\kappa}_1))$. These values have been taken from the work of Scharoch [16].

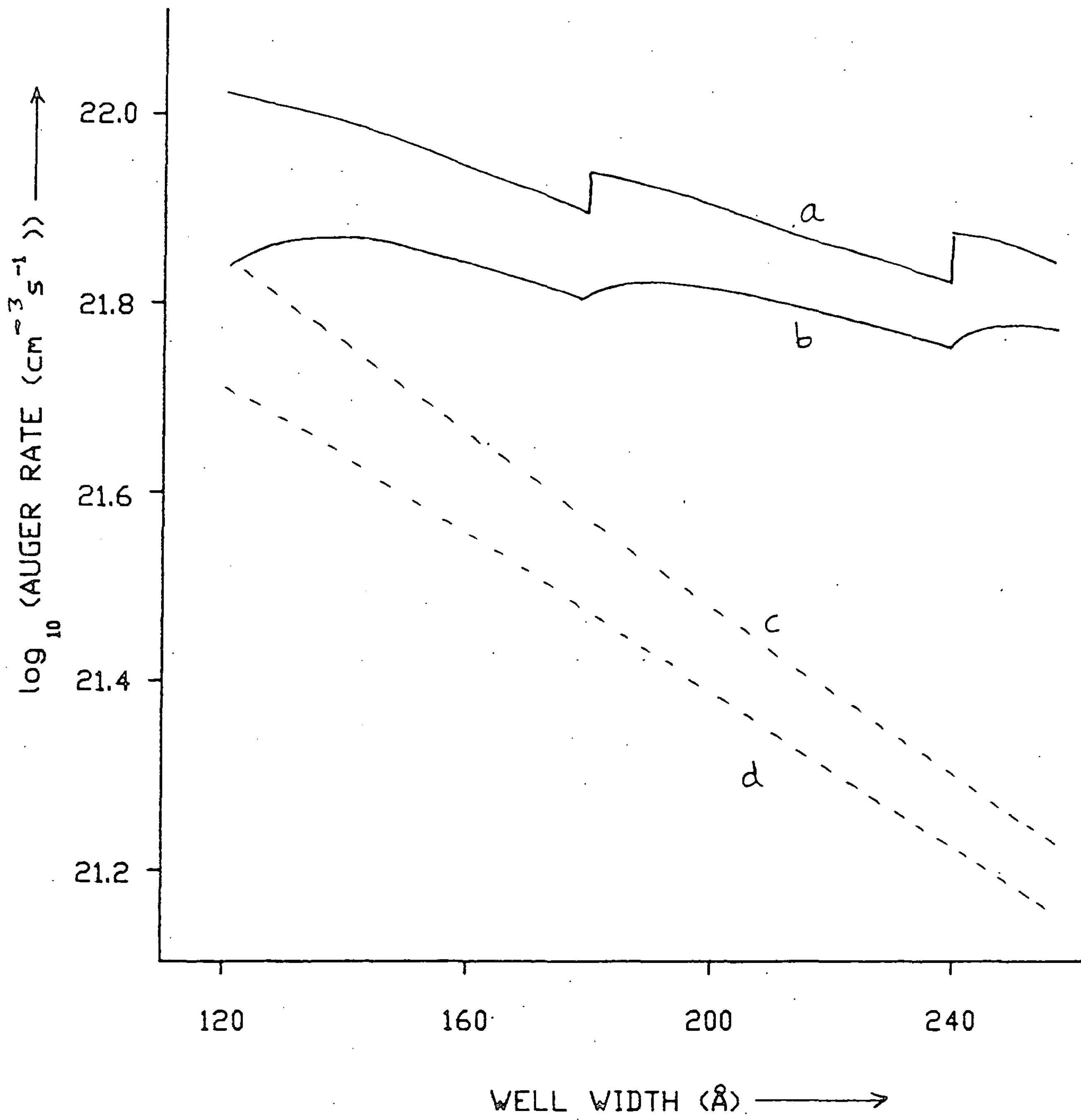

Figure (4.11) - Same as Figure (4.10) but for the 1.55μm InGaAsP/InP QW.

because the LH overlap is small (on the basis of the simplest Kane four band model, the overlap would be zero for the threshold configuration of parallel carrier wavevectors).

The absolute magnitude for the CHLH QW Auger rate is approximately three times less than the corresponding bulk Auger transition rates.

4.2 NUMERICAL ESTIMATES OF BOUND-UNBOUND AUGER TRANSITION RATES IN QWs

In the previous section, numerical estimates of bound-bound QW Auger transition rates were presented for InGaAsP/InP QWs. It was pointed out that some Auger processes that are considered important in bulk semiconductors (such as the CHSH process) do not have a bound-bound contribution in the QW because of the absence of a spin-split off well. Hence, any contribution to the CHSH process in a QW must arise from bound-unbound processes. The expressions derived in Chapter Two for bound-unbound QW Auger rates (where all bound states are assumed to be in ground state subbands) are applied to the CHCC, CHLH, and CHSH Auger processes. Smith [10], [11], has already studied the CHCC bound-unbound Auger process, and concluded that the bound-unbound contribution is only important at small well widths. The calculation that we present here can be checked by comparing the results that are obtained for the CHCC bound-unbound Auger process with those of Smith. As will be seen later, the two calculations are in good agreement. The results of Smith [10] were calculated using 'conventional' overlap integral estimates, but the improved overlap integral estimates discussed in the last section have been included here.

In Figure (4.12) the QW CHCC bound-unbound Auger rate as a function of QW width is shown for the 1.3μm InGaAsP/InP QW (with all the bound states being in ground state subbands). On the same figure the ground state bound-bound process (calculated with the assumption that confined state wavevectors are integer multiples of π/L) has been shown. Figure (4.13) presents the same

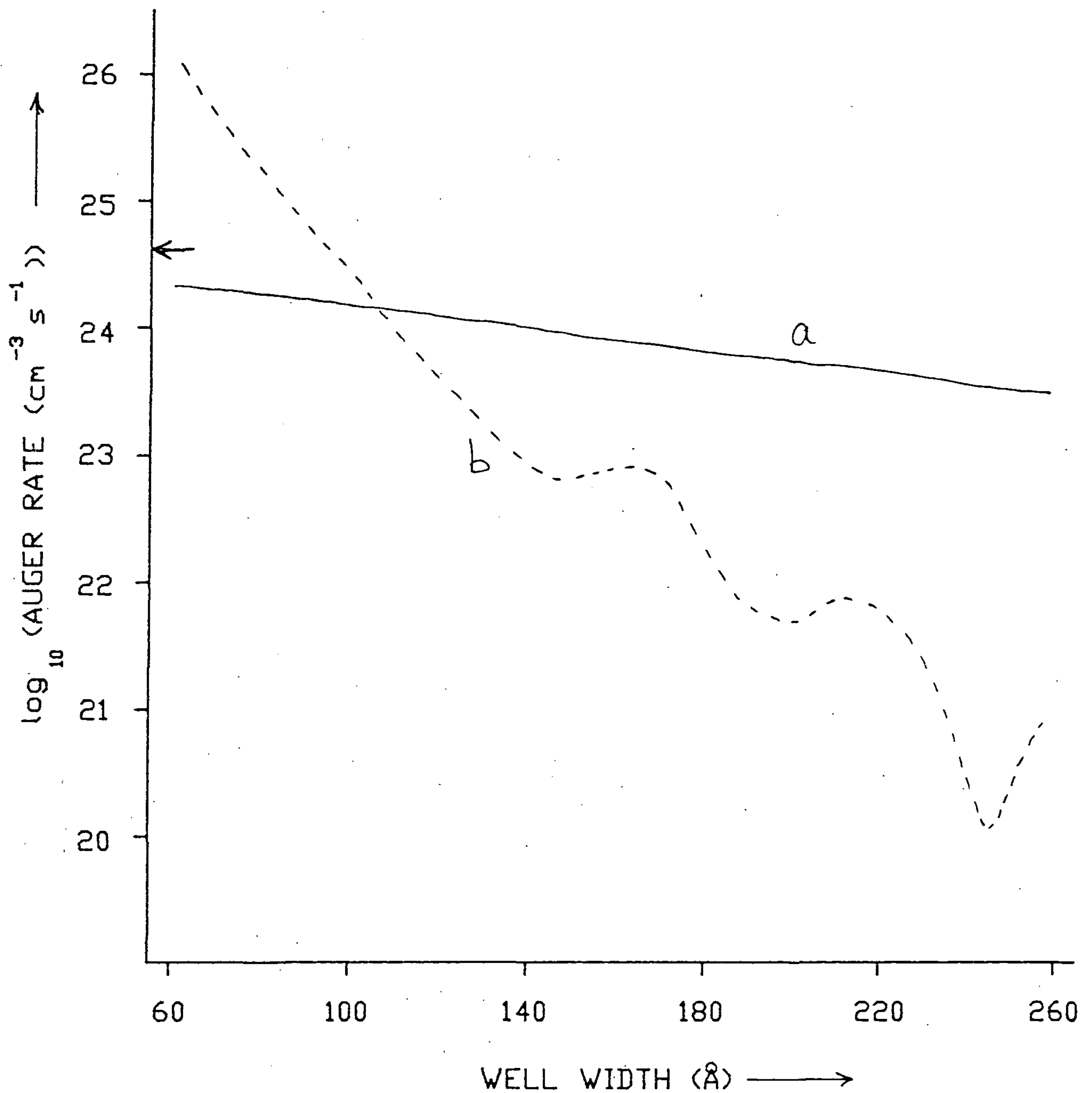

Figure (4.12) - Graph showing the variation with well width of (a) the ground state bound-bound CHCC Auger rate, and (b) the CHCC bound-unbound rate (with all the bound states being ground states) for a 1.3μm InGaAsP/InP QW. All the confined state wavevectors have been taken to be integer multiples of π/L, and the overlap integrals, temperature and injected carrier densities are the same as those

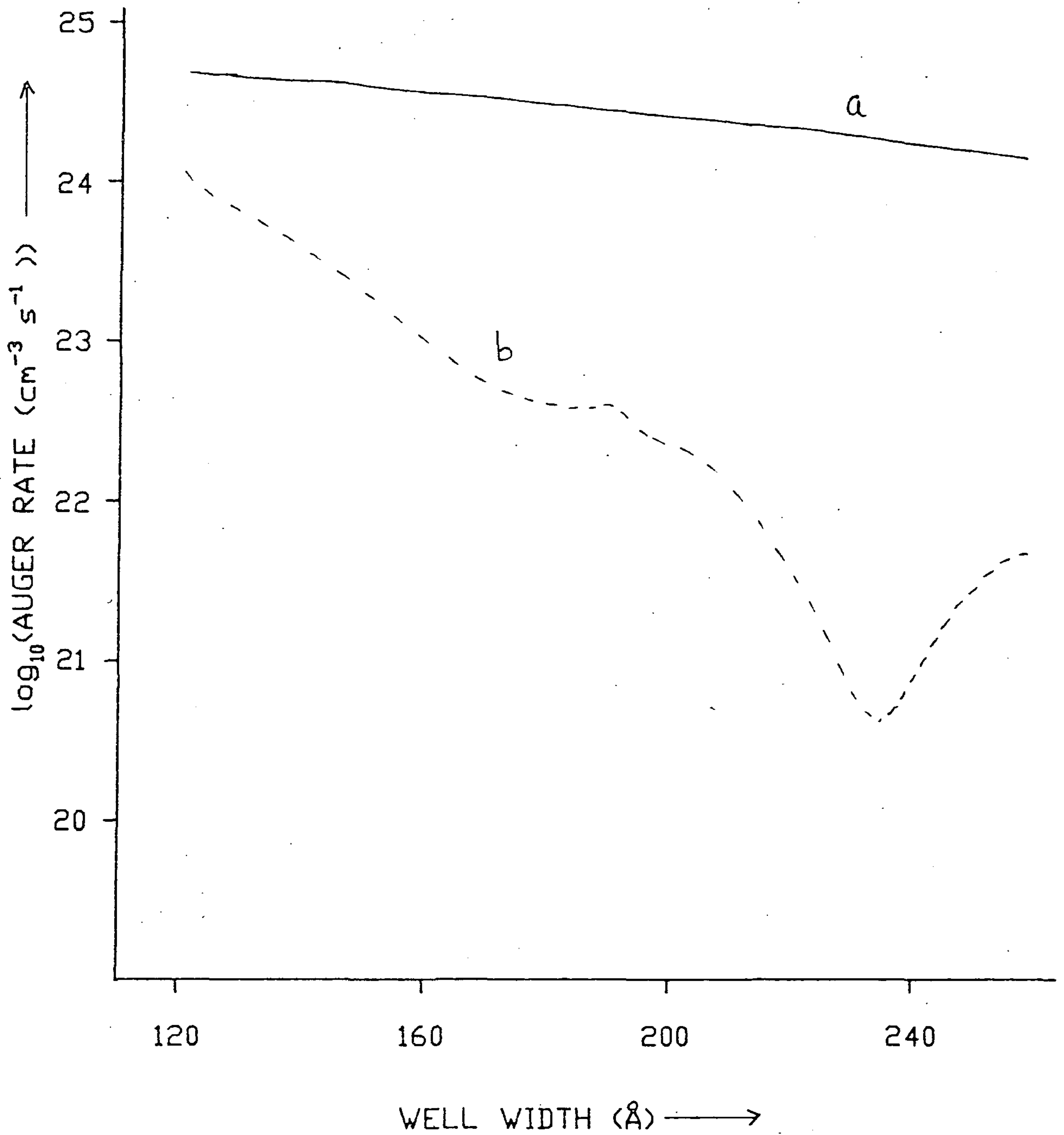

Figure (4.13) - Same as Figure (4.12) but for the 1.55μm InGaAsP/InP QW.

results for the 1.55μm InGaAsP/InP QW. For the 1.3μm QW, the bound-unbound process is dominant at small well widths (at those well widths virtually all the electrons are in the ground state subband, and this justifies the neglect of bound-unbound Auger processes involving bound states in higher subbands). Oscillations in the rate similar to those found by Smith [10] are observed. The bound-unbound Auger rate in the 1.55μm QW is not important compared to the bound-bound rate, as found by Smith [10]. The oscillations in the curves for the CHCC bound-unbound QW Auger rates can be explained by assuming that the main contribution to the recombination rate arises from transitions of the excited electrons to the continuum states close in energy to the final state corresponding to an activation energy, ΔE, of zero. If the well width takes a value such that the unbound wavevector of the final state is $(2n+1)\pi/L$, with $n = 1, 2, \ldots$ (i.e. a whole number of wavelengths just fit into the well) the matrix element for the transition corresponding to an activation energy of zero will vanish. If the $\Delta E = 0$ transition corresponds to an unbound final state wavevector k, then

$$\frac{\hbar^2 k^2}{2m_C} = E_c^0 + V_c \tag{4.15}$$

where V_c is the conduction band offset, and E_c^0 is the final state energy (measured from the top of the QW) corresponding to $\Delta E = 0$. This may be rewritten as

$$\frac{\hbar^2 k^2}{2m_C} = \Delta E^0 \tag{4.16}$$

with ΔE^0 corresponding to ΔE for the ground state bound-bound Auger transition. Substituting $k = (2n+1)\pi/L$ into equation (4.16), gives the QW widths where minima in the CHCC Auger bound-unbound transition are expected

$$L = (2n+1)\pi\sqrt{\frac{\hbar^2}{2m_C\Delta E^0}} \tag{4.17}$$

Substituting the appropriate values for the parameters of the 1.3μm QW laser gives

$$L = (2n+1) \text{ x } 26.3\text{Å} \tag{4.18}$$

which is in good agreement with the observed minima of Figure (4.11).

Unfortunately, the same analysis cannot be applied to the CHSH or CHLH bound-unbound Auger transitions, because the $\Delta E = 0$ transition that is assumed to dominate the CHCC bound-unbound rate gives zero contribution for the CHSH and CHLH processes, due to the overlap integrals involving the valence band states. The CHLH QW bound-unbound Auger rates are shown in Figure (4.14) for the 1.3μm laser and in Figure (4.15) for the 1.55μm laser. Figures (4.16) and (4.17) show the corresponding results for the CHSH bound-unbound processes. In both cases, the rates are significantly lower than the CHCC Auger rates, and, are thus expected to be correspondingly less important in determining the total QW Auger rate.

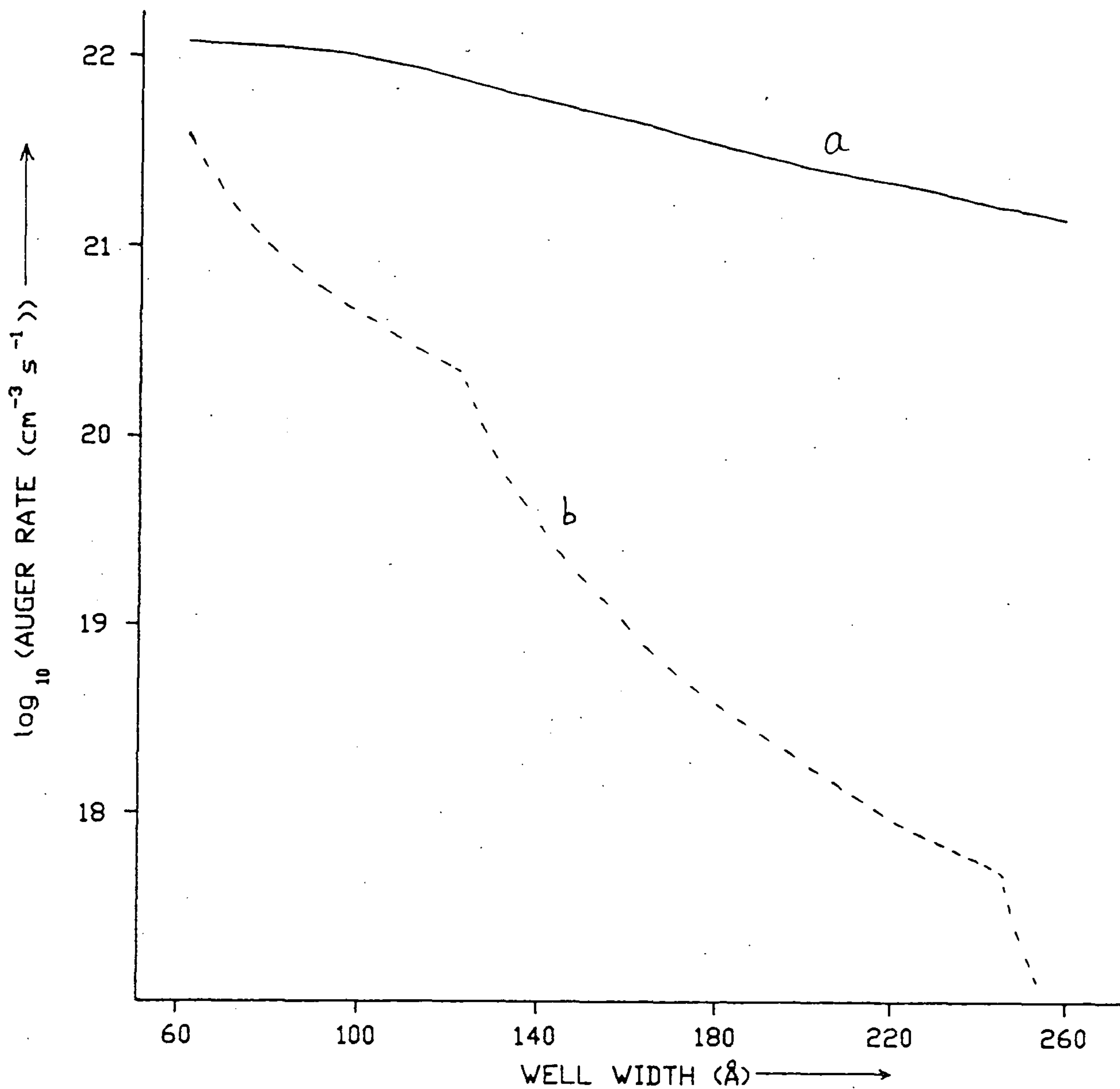

Figure (4.14) - Graph showing the variation with well width of (a) the ground state bound-bound CHLH Auger rate, and (b) the CHLH bound-unbound rate (all bound states being in the ground state) for the 1.3μm InGaAsP/InP QW. The confined state wavevectors are assumed to be integer multiples of π/L, and the overlap integrals, temperature, and injected carrier density are the same as those used in Figure (4.10).

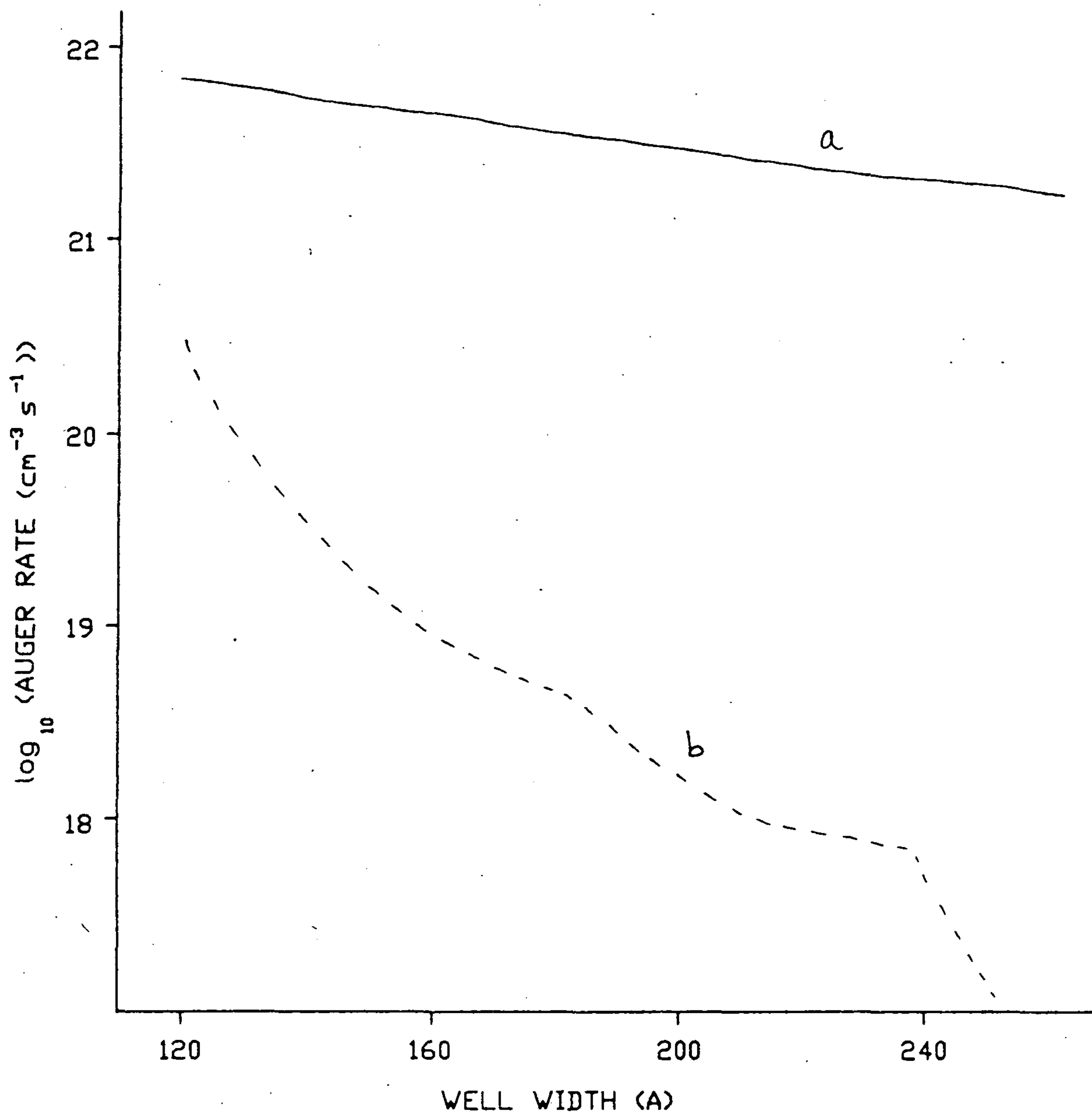

Figure (4.15) - Same as Figure (4.14) but for the 1.55μm InGaAsP/InP QW.

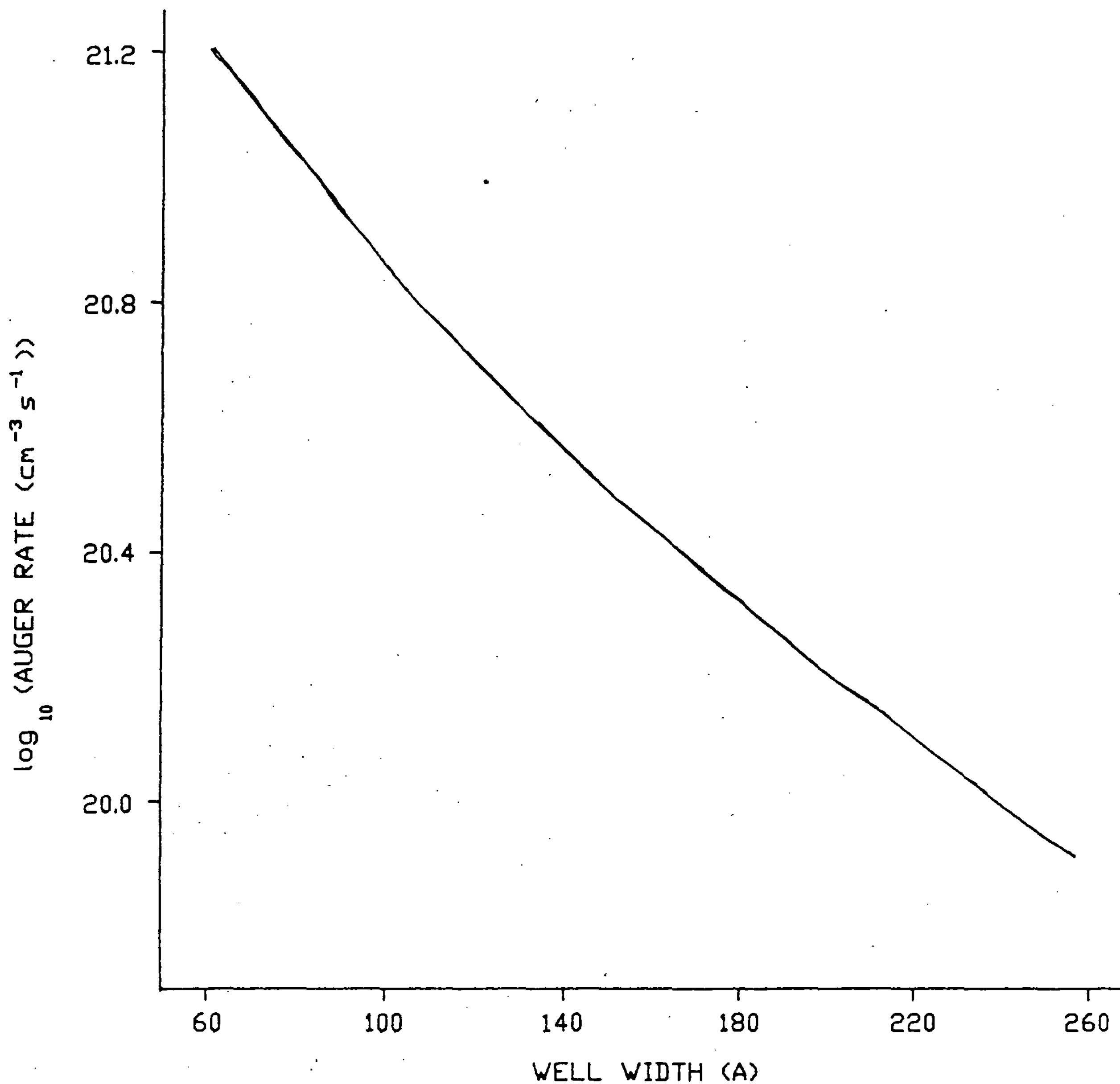

Figure (4.16) - Graph showing the variation with well width of the CHSH bound-unbound Auger rate (all bound states being in the ground state) for a 1.3μm InGaAsP/InP QW. The overlap integrals used are :

$|M_{CH}|^2 = 0.176\Delta k^2$, with

$\Delta k = \underline{k}_3 - \underline{k}_1$, and

$|M_{SH}|^2 = -0.01064\Delta k + 0.67\Delta k^2 - 5.637\Delta k^3 + 13.30\Delta k^4$

These values are appropriate when the wavevectors are parallel to the direction $\theta = \pi/6$ and $\phi = 0$. The temperature is 300K and the injected carrier density is 10^{18}cm^{-3}.

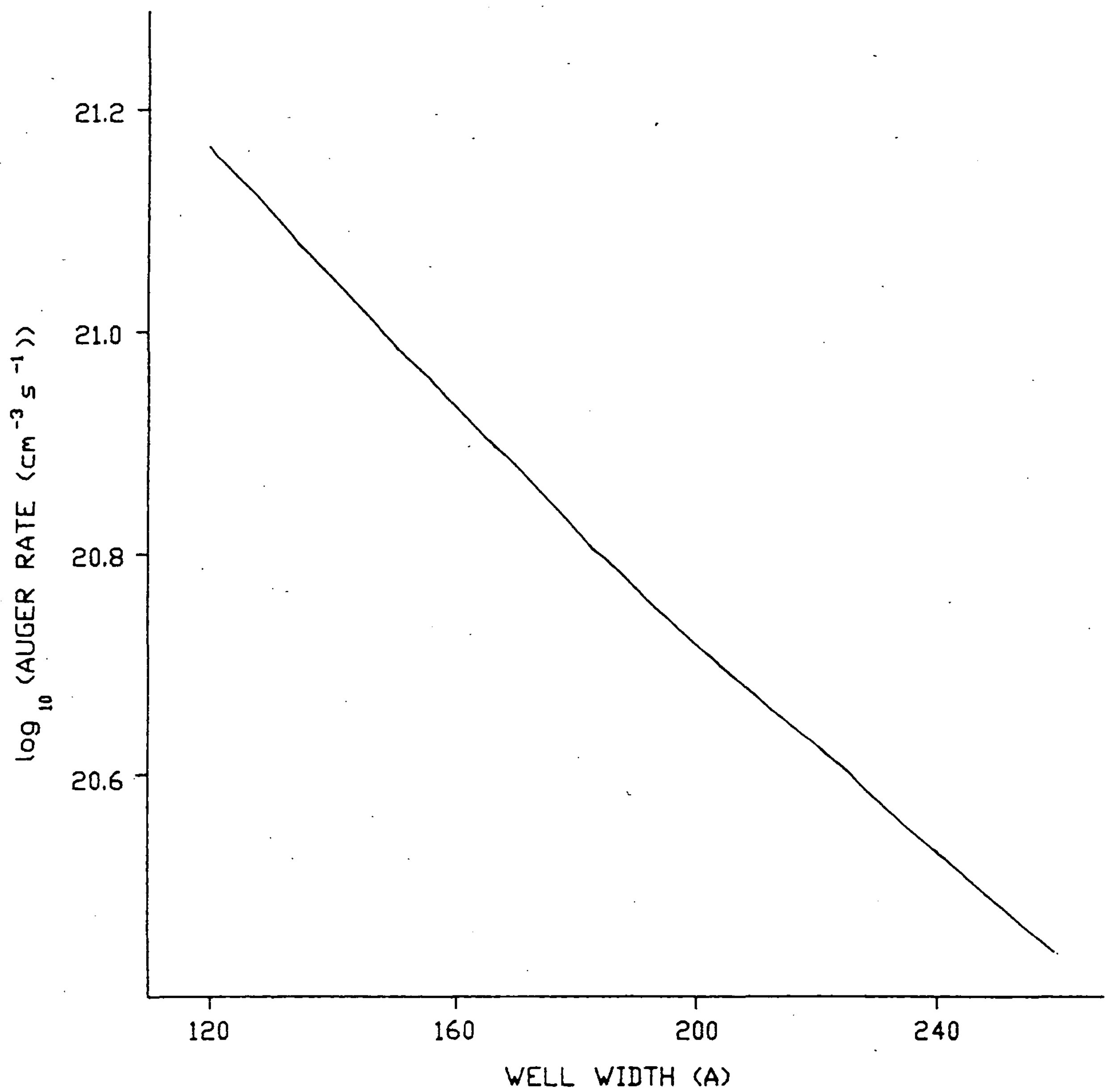

Figure(4.17) - Same as Figure (4.16) but for the 1.55μm InGaAsP/InP QW.

4.3 COMPARISON OF THEORETICAL AND EXPERIMENTAL RESULTS ON AUGER TRANSITION RATES IN InGaAsP/InP QUANTUM WELLS

In Section 4.2, numerical estimates of Auger transition rates in InGaAsP/InP quantum wells (based on the model described in Chapter Two) were presented. The results indicate that the most important Auger process is the CHCC transition. For the 1.3μm InGaAsP/InP QW at small well widths (less than about 100 Å) the bound-unbound Auger process was more important than the bound-bound transitions, but at wider well widths, the CHCC QW Auger rate was dominated by the contribution from bound-bound transitions. For the 1.55μm InGaAsP/InP QW, the CHCC bound-bound process was dominant for all widths. It was also observed that the QW Auger rates were of the same order of magnitude as the corresponding bulk rates.

Sermage et al [21] have reported Auger coefficients of 2.6 x 10^{-29}cm^{6}s^{-1} for bulk 1.3μm InGaAsP. An experimental study by Su et al [22] reported both radiative and Auger recombination rates for p-type 1.3μm InGaAsP diode lasers. That work was mainly concerned with doped samples, but an upper bound of 3 x 10^{-29}cm^{6}s^{-1} was given for the total Auger coefficient in undoped 1.3μm InGaAsP samples.

No values for Auger coefficients in InGaAsP/InP QWs have been reported, although expermental information is available for InGaAs/InAlAs multiple quantum wells (MQWs) [23]. The Auger coefficient in the InGaAs/InAlAs MQW was found to be 6 x10^{-29}cm^{6}s^{-1}, whereas the value for bulk InGaAs was reported in the same work to be 7 x10^{-29}cm^{6}s^{-1}. This appears to be the only experimental work that examines both QW and bulk rates and compares

the two and suggests that Auger coefficients for the bulk and QW system are within 20 percent of each other.

The experimental results for the InGaAs/InAlAs MQW system are encouraging since they indicate that QW and bulk Auger coefficients are of the same order of magnitude which is in agreement with the theoretical predictions of Chapter Two. Thus, the values for the Auger coefficients given for the InGaAsP/InP QWs (equations (4.13) and (4.14)) should be similar to bulk Auger coefficients for InGaAsP with corresponding material parameters (e.g. bulk bandgap equal to QW bandgap). The values for the Auger coefficients of $1.3\mu m$ InGaAsP reported in the experiments referred to above [21], [22], are approximately a factor of ten higher than the theoretical results presented in this Chapter. This contrasts with previous predictions based on conventional overlap integrals which gave Auger coefficients ten times too high [10], [11], [19]. The numerical results for recombination rates presented in this Chapter appear to be factor of ten too small, but they are expected to be underestimates since the overlap integrals are taken from bulk calculations as discussed in Section 4.1.

4.4 NUMERICAL RESULTS FOR BOUND-BOUND AUGER TRANSITIONS IN InGaAsP/InP QWWs

The expressions derived in Chapter Three for the bound-bound Auger transition rates in quantum well wires (QWW) are applied, in this Section, to InGaAsP/InP QWWs, the QWW bandgap being kept constant at an energy corresponding to a lasing wavelength of $1.3\mu m$. Two quantum numbers are needed to describe a particular subband, and in Figure (4.18) the dominant contributions to the bound-bound CHCC QWW Auger transition rate are shown ($10^{18} cm^{-3}$ carriers having been assumed to be injected into the QWW). In Figure (4.19) the results from the QW bound-bound CHCC calculation are shown for comparison, and it is seen that the Auger recombination rates are within a factor of two at small well widths. The QWW ground state rate falls more rapidly with well width than the corresponding QW rate because the carrier concentration in the ground state subbands of a QWW decreases faster. The CHCC process is the dominant Auger process in the QWW, the rate of the CHLH process is about two orders of magnitude lower.

The results presented here for QWW CHCC bound-bound Auger rates differ from those in [24]. In [24], the quasi-Fermi levels were calculated using Fermi-Dirac statistics, but used in the expressions derived in Chapter Three, that assume quasi-Fermi levels from Boltzmann calculations. In Figures (4.18) and (4.19) Boltzmann statistics have been used throughout which is a more consistent and accurate procedure, and so the results presented here are an improvement over those of [24]. Overlap integrals from bulk calculations have

Figure(4.18) - Graph showing contributions to the QWW CHCC bound-bound Auger rate for a 1.3μm InGaAsP/InP QWW. The temperature, overlap integrals and injected carrier density are the same as those used in Figure (4.7), and the wire axis is in a direction midway between the [001] and the [101] directions.

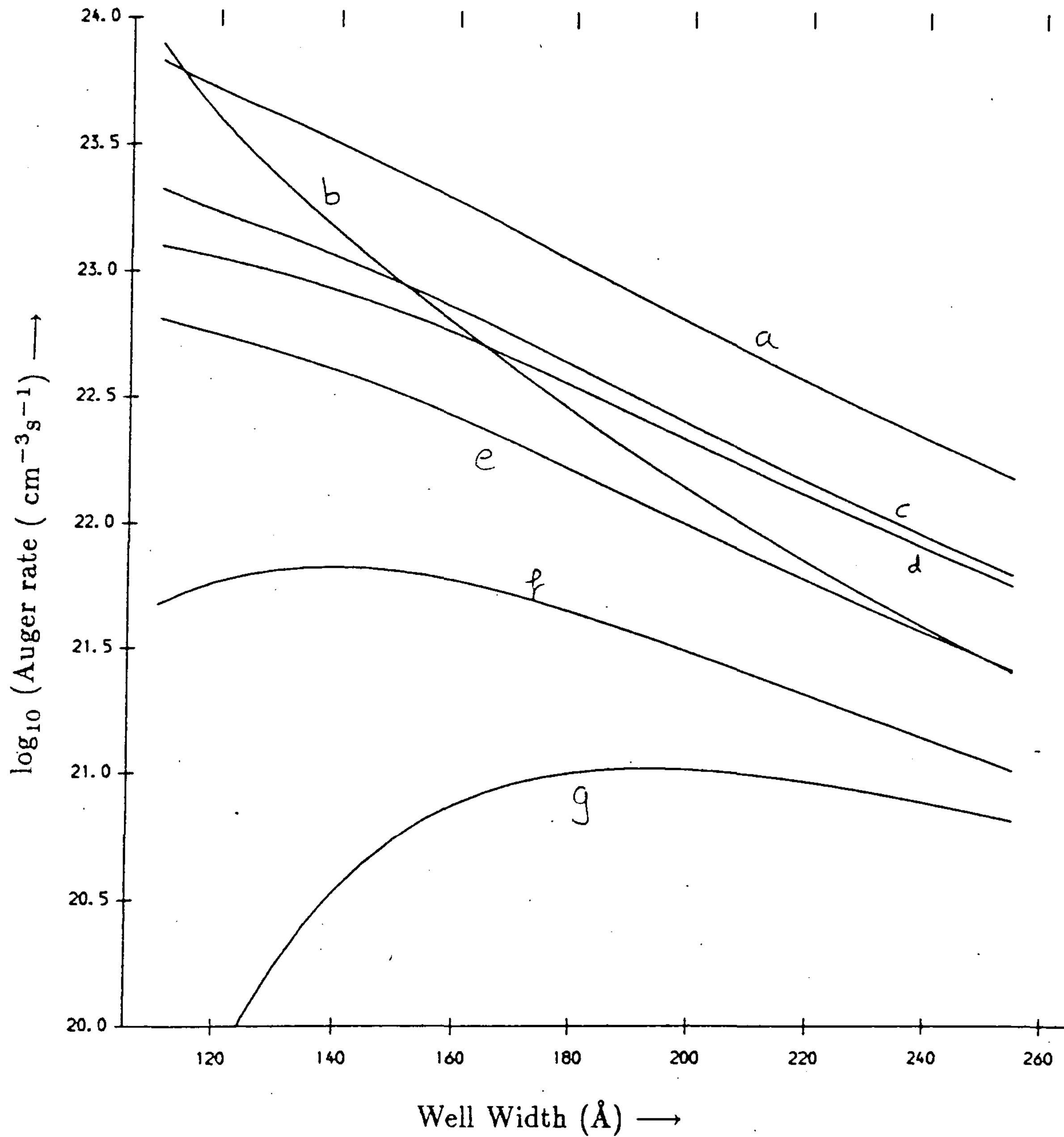

QUANTUM NUMBERS

	$\|1\rangle$	$\|2\rangle$	$\|3\rangle$	$\|4\rangle$
a	1,1	1,1	1,1	1,1
b	1,1	1,1	1,1	1,3
c	1,1	1,1	1,2	1,2
d	1,1	1,1	2,2	2,2
e	1,1	1,1	1,3	1,1
f	1,1	1,1	3,3	1,1
g	1,2	1,1	1,1	1,1

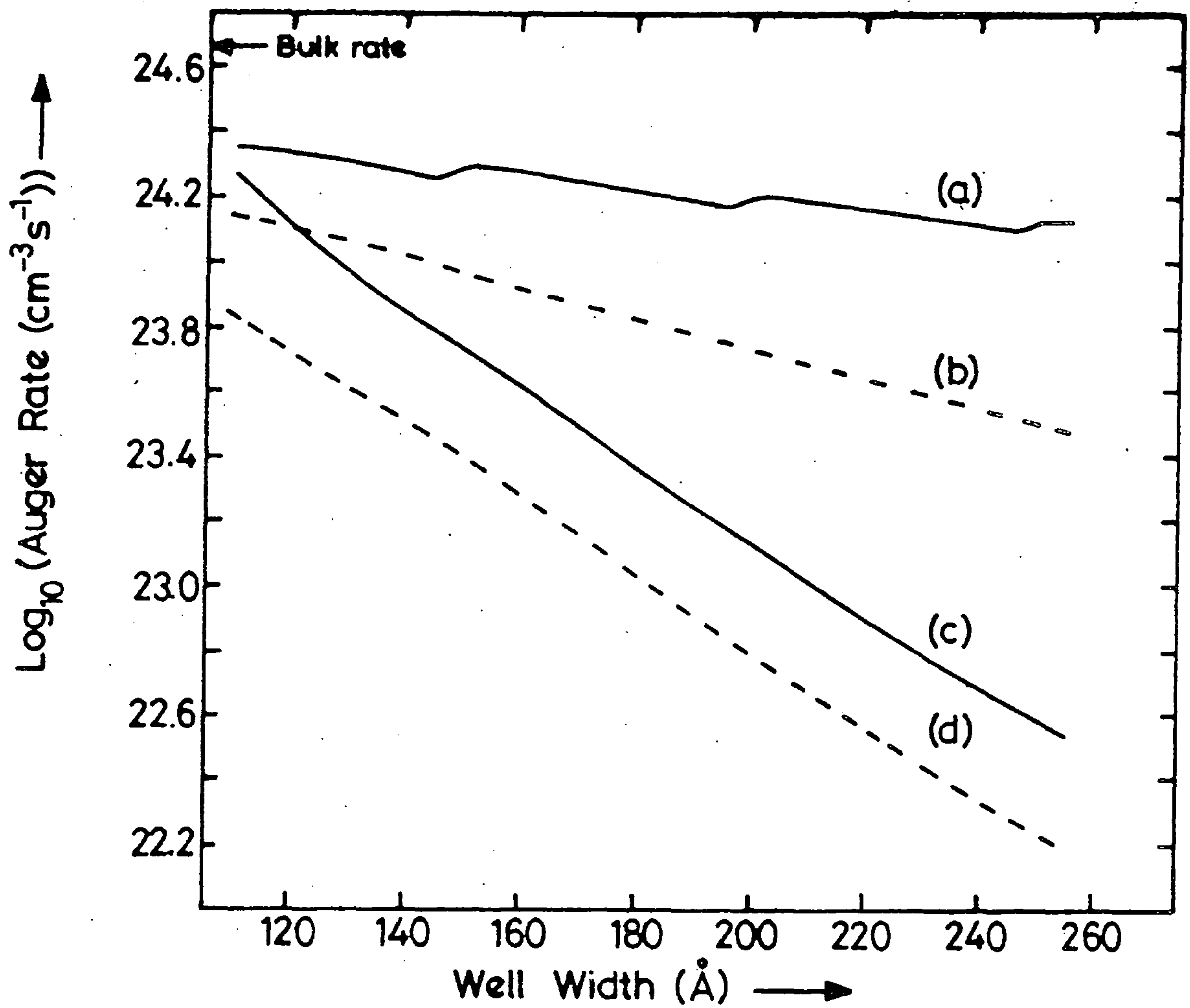

Figure (4.19) - Graph comparing the CHCC Auger rates in 1.3μm InGaAsP/InP QWs, QWWs, and in 1.3μm InGaAsP. The confined state wavevectors have been taken to be integer multiples of π/L, and the temperature, overlap integrals and injected carrier density are taken to be the same as those used in Figure (4.7). Curves (a) and (b) are results for the QW, whilst (c) and (d) are for the QWW. The full lines represent total bound-bound rates and the dashed lines represent ground state bound-bound rates.

been used, and so the results are expected to be underestimates of the recombination rates, for the same reasons as for the QW, as discussed in Section 4.1.

4.5 SUMMARY OF CHAPTER FOUR

Numerical estimates of Auger transition rates in InGaAsP/InP QWs and QWWs have been presented, using the algebraic expressions of Chapter Two and Three. Realistic overlap integrals were included in the calculations and it was found that the CHCC Auger process was the most important one in in InGaAsP/InP QWs and QWWs. The use of realistic confined state wavevectors, and the inclusion of the evanescent parts of the confined state wavefunctions gave results that were only about 50% smaller than calculations which neglected the evanescent parts of the confined state wavefunction (and which also assumed confined state wavevectors that were integer multiples of π/L).

The bound-unbound CHCC Auger rates in 1.3 and 1.55μm InGaAsP/InP QWs were found to be in good agreement with the results of Smith [10], [11]. Results were also presented for the bound-unbound CHSH and CHLH Auger rates.

Numerical estimates of the Auger coefficient were found to be a factor of ten too small, in comparison with experimental data, and possible reasons for such a discrepancy were discussed. Experimental work on Auger recombination in long-wavelength bulk and QW InGaAsP systems was briefly reviewed. Numerical estimates of CHCC Auger transition rates in 1.3μm InGaAsP/InP QWWs were also presented.

The temperature dependence of the Auger coefficient in InGaAsP/InP QWs was not investigated since insufficient information was available concerning the temperature variation of InGaAsP material parameters. It is perhaps worth noting, however, that Haug [25] has used the theoretical work of Chapter Two (and [26]) to investigate the temperature dependence of the Auger coefficient in GaSb/AlSb QWs.

REFERENCES FOR CHAPTER FOUR

[1] N.K. Dutta and R.J. Nelson, J.Appl.Phys., 53, (1982), 74.

[2] R. Chin, N. Holonyak, Jr., S.W. Kirchoefer, R.M. Kolbas and E.A. Rezek, Appl.Phys.Lett, 34, (1979), 862.

[3] L.I. Schiff, Quantum Mechanics, (Third edition, McGraw-Hill, 1968).

[4] A. Haug, J.Phys.C:Solid State Phys., 16, (1983), 4159.

[5] A.R. Beattie and P.T. Landsberg, Proc.Roy.Soc., *A249*, (1959), 16.

[6] R de L. Kronig and W.G. Penney, Proc.Roy.Soc., *A130*, (1931), 499.

[7] A.R. Beattie and P.T. Landsberg, Proc.Roy.Soc., *A285*, (1960), 486.

[8] E. Antoncik and P.T. Landsberg, Proc.Roy.Soc., 82, (1963), 337.

[9] A.R. Beattie and G. Smith, Phys.Stat.Sol., 19, (1967), 577.

[10] C. Smith, PhD thesis, Durham University, 1985, unpublished.

[11] C. Smith, R.A. Abram and M.G. Burt, Superlattices and Microstructures, 1, (1985), 119.

[12] M.G. Burt and C. Smith, J.Phys.C:Solid State Phys., 17, (1984), L47.

[13] M.G. Burt, S. Brand, C. Smith and R.A. Abram, J.Phys.C:Solid State Phys., 17, (1984), 6385.

[14] S. Brand, M.G. Burt, C. Smith and R.A. Abram, Proc. 17th Int. Conf. Phys. Semicond., San Francisco, (1984), page 1013.

[15] S. Brand, private communication (1987).

[16] P. Scharoch, private communication (1987).

[17] E.O. Kane, J.Phys.Chem.Solids, 1, (1957), 249.

[18] A. Haug, D. Kerkhoff & W. Lochmann, Phys.Stat.Sol.(b), 89,(1978),357.

[19] N.K. Dutta, J.Appl.Phys., 54, (1983), 1236.

[20] A. Sugimura, Appl.Phys.Lett., 42, (1983), 17.

[21] B. Sermage, J.L. Benchimol and J.P. Heritage, J.Lumin., 31,(1984),500.

[22] B. Sermage, D.S. Chemla, D. Sivco & A.Y. Cho, Physica, 134*B*,(1985),417.

[23] C.B. Su, J. Schlafer, J. Manning & R. Olshansky, Elect.Lett., 18,(1982),595.

[24] R.I. Taylor, R.W. Kelsall and R.A. Abram, Surf.Sci., 174, (1986), 169.

[25] A. Haug, J.Phys.C:Solid State Phys., 20, (1987), 1293.

[26] R.I. Taylor, R.A. Abram, M.G. Burt and C. Smith, IEE Proc. 132 Part J (Optoelect.), (1985), 364.

CHAPTER FIVE

THE EFFECTS OF NON-PARABOLIC BANDSTRUCTURE AND FERMI-DIRAC STATISTICS ON AUGER RATES

INTRODUCTION

In Chapter Two, expressions for Auger transition rates in quantum wells were presented, the calculations having been carried out with the assumptions of isotropic, parabolic subbands, and the approximation of Boltzmann statistics with quasi-Fermi levels. In Chapter Four, these expressions were used to calculate numerical estimates of Auger rates in QWs with the above assumptions. The purpose of this chapter is to discuss the assumptions in more detail, and to examine their validity.

The use of Boltzmann statistics with quasi-Fermi levels appears at first sight to be a drastic simplification considering that we are examining semiconductor lasers. In fact, it is not difficult to justify the approximation for the valence band, since the hole quasi-Fermi level lies in the QW bandgap due to the large heavy hole mass. However, the conduction band quasi-Fermi level lies above the first conduction subband at relevant carrier concentrations and so the use of Boltzmann statistics is less easy to justify. Haug [1], however, has shown that, for bulk GaSb at room temperature, the use of Boltzmann statistics is valid up to carrier densities of $10^{19}\mathrm{cm}^{-3}$. In this chapter, Haug's method, [1], has been extended to include QW systems, and it will be shown

how a simple correction factor can be used to incorporate Fermi-Dirac statistics into the Boltzmann-based Auger calculations of Chapter Two.

The assumption of using parabolic subbands is likely to be unrealistic for a CHCC Auger transition since the excited state is of the order of an energy gap above the conduction subband edge. In an extreme case, the realistic bandstructure could 'bend over' in $\underline{\kappa}$-space before the simultaneous conservation of energy and crystal momentum could be achieved. If this were the case, a CHCC Auger process involving the ground state conduction subband would not be allowed. This is a possibility that could not be predicted from a model based on the assumption of parabolic subbands.

In this chapter, a brief review will be given of work incorporating realistic electronic structure in Auger transition rate calculations. Then, a new method for the incorporation of non-parabolicity effects will be presented, which can be applied to bulk, QW, or QWW systems.

5.1 EFFECTS OF NON-PARABOLICITY ON CHCC QW AUGER TRANSITION RATES

The effect of subband non-parabolicity on QW Auger transition rates has not been studied in any great detail by other workers. Dutta [2] attempted a crude estimate of the effect of non-parabolicity - his result for the QW CHCC Auger rate (derived assuming isotropic, parabolic subbands) was used, with the assumption that the excited carrier had a larger effective mass than the band edge carriers. However, the effects of the subband dispersion were not included in the $\underline{\kappa}$-space integral, and so the estimate must be regarded as an

'order of magnitude' estimate only. Dutta assumed that the excited state had an effective mass twice that of the carriers at the subband edge, and found that the QW CHCC Auger rate was reduced by two orders of magnitude for an InGaAsP/InP QW.

A great deal more research has been carried out into the effects of realistic electronic structure on bulk Auger transition rates. For the CHCC bulk Auger process, Haug [1] has taken into account the effects of realistic bandstructure in the region of the excited state, and also for the heavy hole, but made the approximation that the initial states in the conduction band were at the zone centre, which greatly simplified the evaluation of the Auger transition rate. The method used by Haug [1] employs a graphical technique for determining the wavevectors for the threshold configuration, and uses realistic bandstructure from an empirical non-local pseudopotential calculation of Chelikowsky and Cohen [3]. Using this technique, Haug has shown that, at room temperature, the CHCC Auger coefficient of bulk InGaAsP is reduced by about four orders of magnitude [4] compared to the result obtained from a calculation employing parabolic bands (note that Haug's model [1] retained the assumption of band isotropy, but recently some progress has been made to relax this assumption [5], [6]). Haug also evaluated the CHSH and phonon assisted CHCC and CHSH Auger coefficients, but found that the values of these coefficients were much closer to the respective parabolic results. This confirms the (implicit) assumption of the Introduction to this chapter that non-parabolicity effects are likely to be most important for the direct CHCC Auger process.

Another attempt to include realistic bandstructure into Auger calculations was undertaken by Beattie and Smith [7] for the bulk CHLH Auger rate. In their calculation all states apart from the excited state were assumed to be in parabolic bands, whereas the carrier in the excited state was assumed to

have an energy dependent effective mass. The important difference between the work of [7] and that of Dutta [2] is the inclusion of the energy dependent effective mass in the $\underline{\kappa}$ -space integral, in contrast to Dutta's work. The method used by Beattie and Smith [7] has also been adopted by Sugimura [8].

In addition to the above methods, which attempt to incorporate realistic dispersion relations into analytical calculations for Auger transition rates, there are also some completely numerical approaches. For example, Bardyszewski and Yevick [9] have examined the compositional dependence of the Auger coefficient for QWs of InGaAsP lattice matched to InP. Their treatment is entirely numerical, utilizing a Monte Carlo method of integration, and includes Fermi Dirac statistics and non-parabolic conduction bands (through use of the Kane model). Unfortunately, no comment is made on how their results would change if parabolic bands and Boltzmann statistics (with quasi-Fermi levels) were used.

It is also worth mentioning the recent attempts of Beattie [10] to calculate numerically bulk Auger recombination rates using Fermi-Dirac statistics, four band $\underline{k}.\underline{p}$ wavefunctions and bandstructure for all carriers, and also including the accurate matrix element (with improved overlap integral estimates) in the $\underline{\kappa}$-space integral. A judicious change of the variables by Beattie enabled him to carry out an efficient numerical estimate of the bulk Auger transition rate. However, the method has only been applied to InSb, and not, so far, to any of the materials of interest in this thesis.

In the next section, a new method will be presented for the incorporation of realistic electronic structure in Auger calculations. The method is suitable for applying to bulk, QW and QWW systems, although the explicit calculations will only be carried out for QWs. The method makes the assumption that all carriers (apart from the one in the excited state) can be accurately described by parabolic dispersion relations. The carrier in the excited state has a realistic

dispersion relation taken from a non-local pseudopotential calculation [11]. Numerical calculations are then presented, based on the new method, that show (in agreement with other work [1], [2], [4]) that the CHCC Auger coefficient is significantly reduced in bulk semiconductors. In wide bandgap materials such as GaAs, the direct CHCC bulk Auger process involving the lowest conduction band only is found to be impossible.

5.2 EFFECTS OF SUBBAND NON-PARABOLICITY ON QW AUGER TRANSITION RATES

Realistic in-plane subband dispersion relations are required in order to calculate the effects of non-parabolicity on QW Auger transition rates. Recently local pseudopotential calculations [12] have been carried out to study in-plane dispersion relations for AlAs/GaAs superlattices, and a typical result of this work is shown in Figure (5.1). Although the calculations in [12] were performed for short period superlattices, it is possible to use the same method to look at wider superlattices, and by making the barrier width large, QW properties may be examined. However, the general features of the in-plane dispersion relations for the QW conduction subbands are expected to be the similar to those in Figure (5.1). For a QW, at $\underline{\kappa}_{\|} = (0,0)$, the subband energies will coincide with the confined energy levels of a one dimensional square well, and, as $|\underline{\kappa}_{\|}|$ increases, the dispersion relations should exhibit a maximum, similar to the bulk conduction band dispersion relations. Further details of the method used for calculating the electronic properties of superlattices and QWs are presented in Chapter Six, and results from the calculations are reported in Chapter Seven.

We now study the effects of subband non-parabolicity on the CHCC QW Auger transition rate for the case where all the carriers reside in the respective ground state subbands of the QW. Since the carrier in the excited state is approximately a bandgap from the conduction subband edge, it is necessary to use realistic bandstructure to describe the dispersion relations for that carrier. However, the other carriers are in states that are considerably closer to the Γ point, and these carriers are assumed to have parabolic dispersion relations. It is worth noting that the analysis that we are about to present is not just

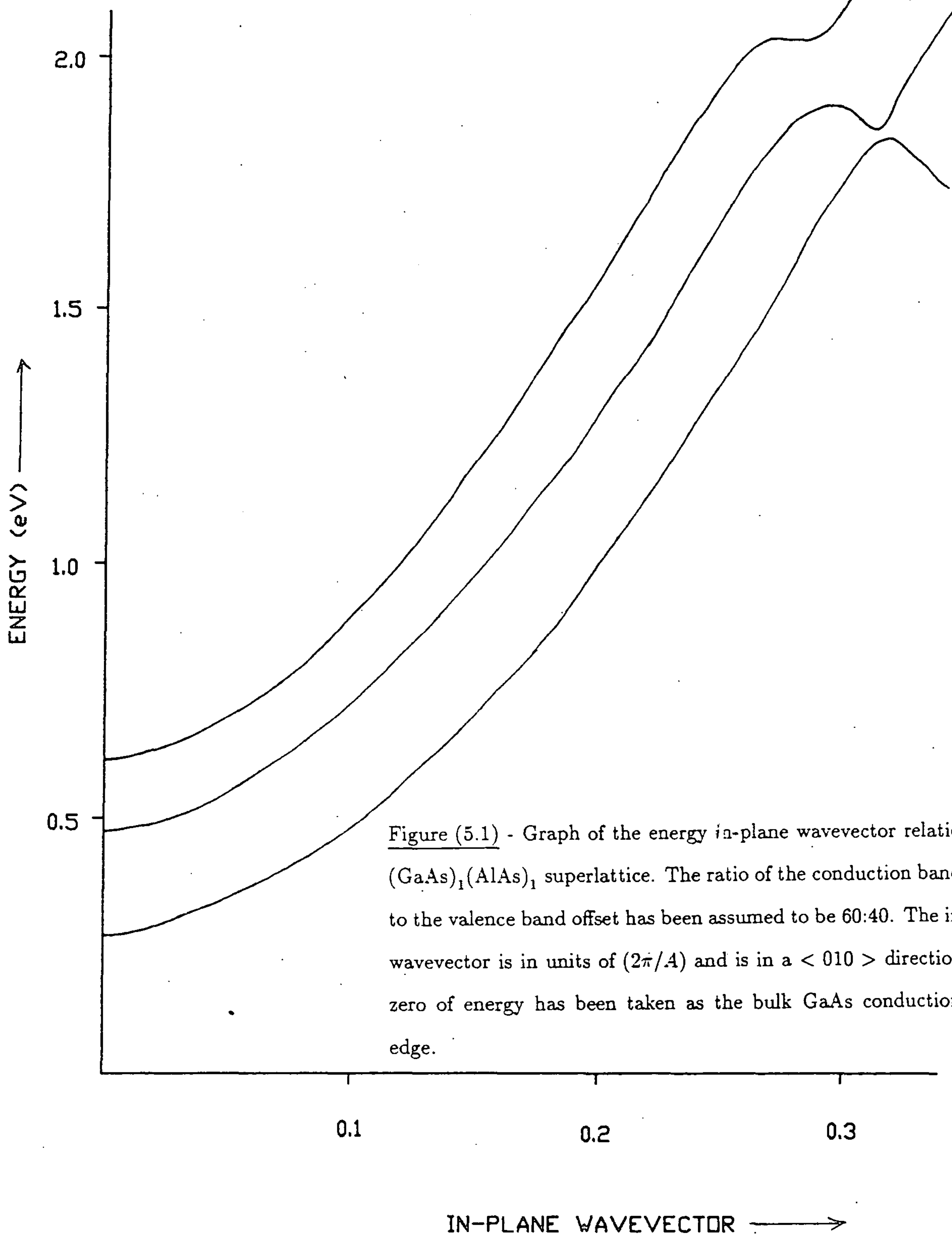

Figure (5.1) - Graph of the energy in-plane wavevector relation of a $(GaAs)_1(AlAs)_1$ superlattice. The ratio of the conduction band offset to the valence band offset has been assumed to be 60:40. The in plane wavevector is in units of $(2\pi/A)$ and is in a $< 010 >$ direction. The zero of energy has been taken as the bulk GaAs conduction band edge.

restricted to the CHCC process, but may be applied to other Auger processes, such as CHSH using the same technique of describing the carrier in the excited state by realistic bandstructure.

As in Chapter Two, the $E - \underline{\kappa}$ dispersion relations may be written as

$$E_1 = \alpha \underline{\kappa}_1^2 \tag{5.1a}$$

$$E_2 = \alpha \underline{\kappa}_2^2 \tag{5.1b}$$

$$E_3 = -E_{QW} - \mu_H \alpha \underline{\kappa}_3^2 \tag{5.1c}$$

$$E_4 = \alpha \underline{\kappa}_4^2 + R(\underline{\kappa}_4) \tag{5.1d}$$

With $\alpha = \hbar^2/(2m_C)$ and $\mu_H = m_C/m_H$. The function $R(\underline{\kappa})$ thus represents the effect of non-parabolicity for the excited state. Although a realistic dispersion relation is used for state $|4\rangle$, the assumption of isotropic energy bands is still used.

By using the above dispersion relations, the ground state QW CHCC Auger transition rate may be calculated in a similar way to that described in Chapter Two (and reference [13]). It is found that the Auger rate is proportional to Q, where

$$Q = \int (az^2 + \frac{R(z) - E_{QW}}{\alpha}) z \exp(-\beta(\alpha z^2 + R(z)))dz \tag{5.2}$$

The range of integration is determined by the condition

$$az^2 + \frac{R(z) - E_{QW}}{\alpha} \geq 0 \tag{5.3}$$

with $a = (1 + \mu_H)/(1 + 2\mu_H)$. For the case of parabolic bands, $R(z)$ is equal to zero, and the result of Chapter Two can be recovered. To understand the physical basis of equations (5.2) and (5.3), first imagine that the semiconductor

has infinitely heavy holes, so that $a = 1$. Then expression (5.3) means that the $\underline{\kappa}$-space integral has to be evaluated for wavevectors, z, satisfying

$$\alpha z^2 + R(z) \geq E_{QW} \tag{5.4}$$

Thus, for the case of infinitely heavy holes, we have to draw a horizontal line across the bandstructure corresponding to an energy E_{QW} above the conduction subband edge, and integrate in $\underline{\kappa}$- space between the wavevectors where the bandstructure lies above that line as illustrated in Figure (5.2). If the bandstructure always lies below the line, then it means that the Auger process will be forbidden, by the requirements of the simultaneous conservation of energy and crystal momentum.

For real semiconductors, the holes are not infinitely heavy, and so the curve that intersects with a horizontal line drawn E_{QW} above the subband edge is not the actual bandstructure curve, since a factor of a multiplies the quadratic term in the $E-\underline{\kappa}$ relation. This factor arises from the fact that energy and momentum have to be conserved in an Auger transition. Obviously, the condition given by equation (5.3) predicts that the ground state QW CHCC Auger process will be less probable if

(i) E_{QW} is large.

(ii) $a = (1 + \mu_H)/(1 + 2\mu_H)$ is smaller than one, i.e. μ_H is greater than zero.

(iii) If the height of the maximum in the conduction band (E_m in Figure (5.2)) is small.

It is instructive to follow through the working for the case where $R(z) = -Cz^4$, i.e. the next term in the expansion of the $E - \underline{\kappa}$ relation is used. This is done in Appendix Four.

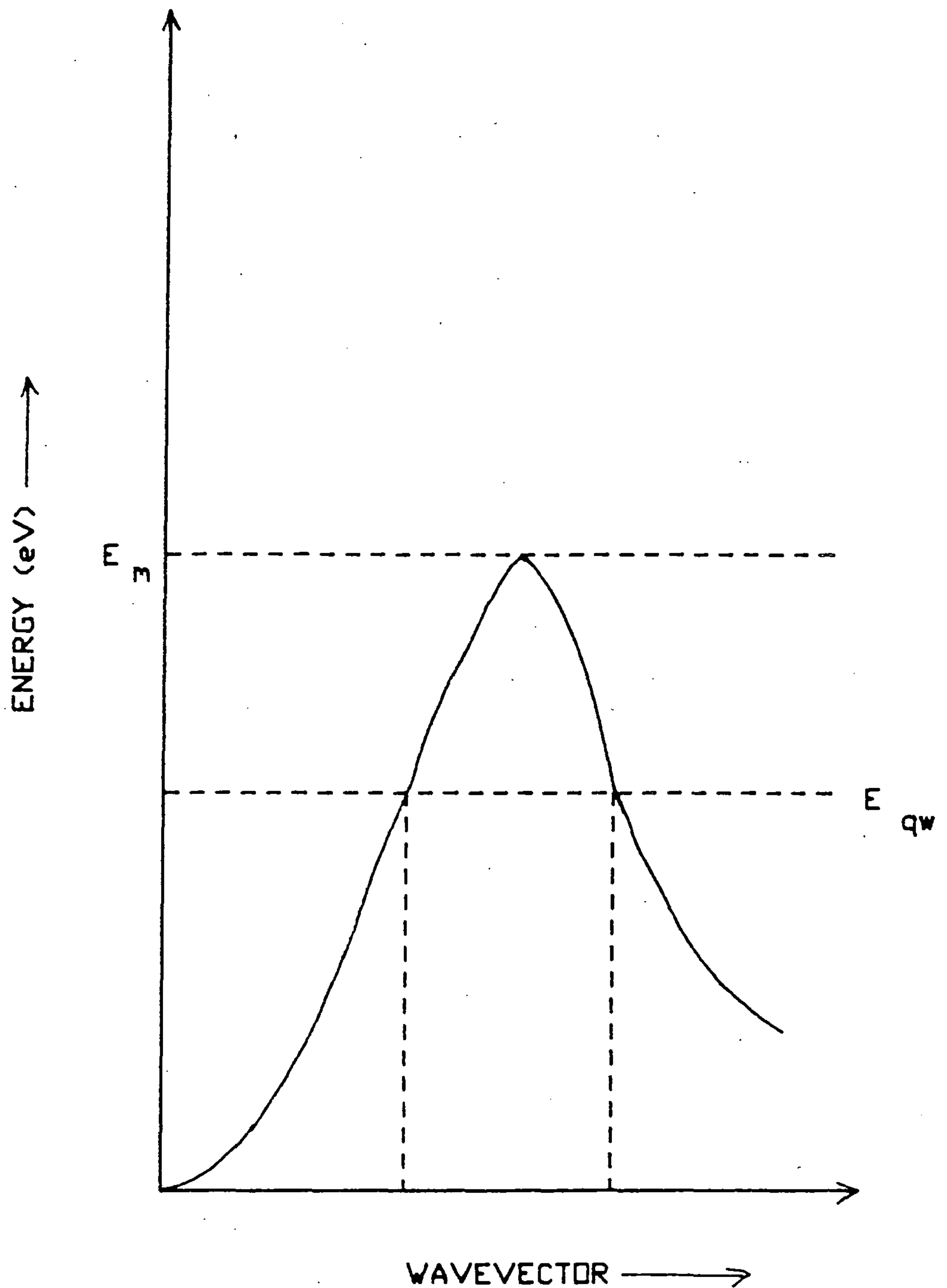

Figure (5.2) - Schematic diagram to illustrate the conditions under which a QW CHCC Auger process may occur (assuming a semiconductor that has $a = (1+\mu)/(1+2\mu) = 1$).

(i) If $E_m > E_{QW}$, then the direct CHCC Auger process involving the lowest conduction subband only can occur.

(ii) If $E_m < E_{QW}$, then the direct Auger process involving the lowest conduction subband only cannot occur.

It is also instructive to examine the ratio of the ground state QW CHCC Auger transition rates calculated both with and without the inclusion of non-parabolicity. The ratio, Y is given by :

$$Y = \frac{R_{QW}^{CHCC}(non-par)}{R_{QW}^{CHCC}(par)} \tag{5.5}$$

$$Y = \frac{\exp(2\beta F_c^{np})}{\exp(2\beta F_c^{p})} \frac{I_{QW}^2(\kappa_o^{np})}{I_{QW}^2(\kappa_o^{p})} J \tag{5.6}$$

$$J = \frac{F(a, E_{QW}, R(z))}{F(a, E_{QW}, 0)} \tag{5.7}$$

$$F(a, E_{QW}, R(z)) = \int_{zl}^{zu} (az^2 + \frac{R(z) - E_{QW}}{\alpha}) z \exp(-\beta(\alpha z^2 + R(z))) \tag{5.8}$$

With zu, zl being upper and lower roots of $\alpha z^2 + R(z) - E_{QW} = 0$. In equation (5.6), the exponential factors take account of the possible different values of the quasi-Fermi levels due to the modified $E - \underline{\kappa}$ relation. However, this is not expected to be very important since the quasi-Fermi levels are primarily determined by the bandstructure close to the Brillouin zone centre unless carrier densities are extremely high. There is also a term which is the ratio of the modulus squared of the matrix element. This term is needed because the threshold wavevector transfer calculated using non-parabolic dispersion relations ($\underline{\kappa}_o^{np}$) is different from that calculated on the basis of parabolic bands ($\underline{\kappa}_o^{p}$). The last term, J, is simply the ratio of the $\underline{\kappa}$-space integrals with and without subband non-parabolicity.

Note that, although this Chapter has carried through an explicit calculation of the effects of non-parabolicity on QW Auger transition rates, the same method as used here can also be used to examine the effects of non-parabolicity

on bulk and QWW Auger transition rates. The ratio of the $\underline{\kappa}$-space integrals will, of course, be different for the bulk and the QWW, and the values of the quasi- Fermi levels and the matrix elements will also differ from the QW values. For the bulk, the $\underline{\kappa}$-space integral ratio is

$$J_{BULK} = \frac{G(a, E_G, R(z))}{G(a, E_G, 0)} \tag{5.9}$$

where

$$G(a, E_G, R(z)) = \int_{zl}^{zu} [az^2 + \frac{R(z) - E_G}{\alpha}]^2 z^2 \exp(-\beta(\alpha z^2 + R(z)))dz \tag{5.10}$$

And, for the QWW, we have

$$J_{QWW} = \frac{H(a, E_{QWW}, R(z))}{H(a, E_{QWW}, 0)} \tag{5.11}$$

where

$$H(a, E_{QWW}, R(z)) = \int_{zl}^{zu} \exp(-\beta(\alpha z^2 + R(z)))dz \tag{5.12}$$

In fact, the theory presented is well suited to the case of the QWW, since the assumption of isotropic energy bands is automatically valid for the QWW.

The method for treating the effects of non-parabolicity on Auger transition rates that has been presented above has some definite advantages over that proposed by Haug [1]. However, as will be seen in the next section, the numerical results obtained using the two methods are very similar. The advantages over Haug's method are :

(i) The assumption of infinitely heavy holes is not made in our method.

(ii) Our method can be readily generalised to both bulk and QWW systems, although the explicit calculations in this chapter have been for the QW.

(iii) Haug's graphical technique is likely to produce inaccuracies unless the bandstructures are very accurately known, since his technique involves finding the intersection of two curves, whereas our method involves finding the intersection of a curve and a horizontal line.

(iv) Our method pinpoints the physical factors that will decrease CHCC Auger recombination rates. Namely, large bandgap, small band maxima, and large values of μ_H. The first two were also noted by Haug, but the neglect of μ_H for the conduction band edge electrons in his method meant that the latter condition was not noted by Haug.

However, we must also note that Haug's method has some advantages over that presented here.

(i) Haug [1] uses realistic bandstructure for both the excited state and for the heavy hole state in the CHCC process.

(ii) In addition to examining direct Auger processes, Haug also studies phonon-assisted Auger processes with realistic bands.

Finally we should once again emphasise that although the calculations in this chapter have been carried out explicitly for the CHCC Auger process, the same method can be used for CHSH, CHLH etc, where the carrier in the excited state is described with a realistic dispersion relation, and the other carriers are assumed to be in parabolic bands.

5.3 NUMERICAL ESTIMATES OF THE EFFECT OF NON-PARABOLICITY ON AUGER TRANSITION RATES

Haug [1] has estimated the effects of non-parabolicity of the bandstructure on Auger transition rates in bulk GaAs and GaSb, and also for InGaAsP [4]. However, the calculation for the latter material is crude, due to the difficulty of calculating the alloy bandstructure from that of the constituent binaries.

The method presented in the previous section may be used to make the estimates for the same materials as Haug so that comparison of the two methods can be carried out.

At 300K, the value of the bandgap of GaSb used by Haug is 0.7 eV. Haug then considers direct CHCC Auger processes, using bulk GaSb bandstructure in the Δ direction. The wavevector of the carrier in the excited state was found to be $0.16(2\pi/a)$ (a being the lattice constant of GaSb), and the CHCC Auger coefficient, C_n was found to be related to the CHCC Auger coefficient evaluated using parabolic bands, C_n^p, by

$$C_n = 0.026 C_n^p \tag{5.13}$$

For GaAs, Haug found that the CHCC Auger process involving the lowest conduction band only was impossible, a result that is consistent with the work of Pearsall et al [14]. In that work, a study of impact ionisation using realistic bandstructure was undertaken, and for GaAs it was found that the initiating electron in the impact ionisation process has to be in a state in the second conduction band (see Figure (5.3)).

The cases considered by Haug [1] are now examined using the method outlined in the previous section. An expression for the ratio of Auger transition

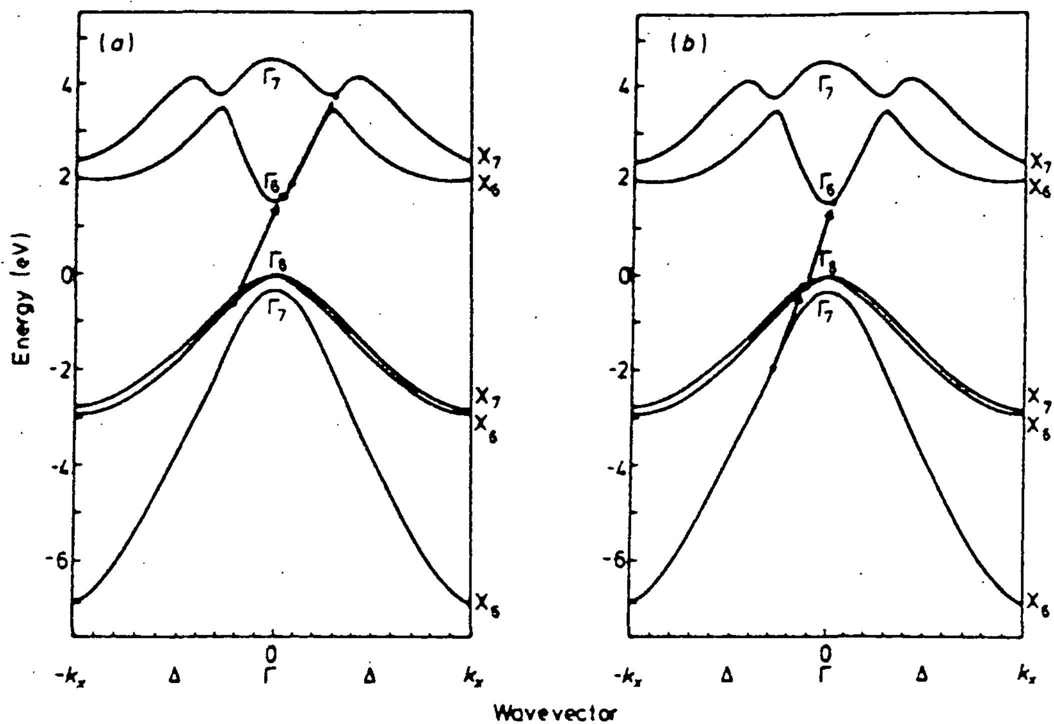

Figure 2. Lowest-energy impact ionization transitions in GaAs in the ⟨100⟩ direction. The band-structure diagram is drawn in an extended representation showing both $+k_x$ and $-k_x$ directions: (*a*) electron initiated; (*b*) hole initiated.

Figure (5.3) - Figure taken from the work of Pearsall et al [14], illustrating that the initiating electron in an impact ionisation process in GaAs has to be in the second conduction band.

rates calculated using non-parabolic and parabolic bandstructure was presented in the last section

$$Y = [\frac{\exp(2\beta F_c^{np})}{\exp(2\beta F_c^{p})}]\frac{I^2_{BULK}(\kappa_o^{np})}{I^2_{BULK}(\kappa_o^{p})}J_{BULK} \tag{5.14}$$

In the numerical work that follows, the assumption is made that the quasi-Fermi levels evaluated using non-parabolic and parabolic bands are the same. This assumption was also made in the work of Haug [1]. Thus the above equation simplifies to simply the ratio of the moduli of the matrix elements and the ratio of the $\underline{\kappa}$-space integrals, J_{BULK}. An expression for J_{BULK} was given in the previous Section.

In order to calculate the matrix element, we need to know the threshold wavevector of the carrier in the excited state. For the case of non-parabolic bands, this is found from the lower root of

$$a\alpha z^2 + R(z) - E_g = 0 \tag{5.15}$$

Where E_g is the bulk bandgap. Once the threshold wavevector of the carrier in the excited state has been found, the value of the threshold wavevector transfer,(κ_o^{np}), may be readily evaluated. Thus, to evaluate κ_o^{np}, an expression for $R(z)$ is required. Once the functional form of $R(z)$ is specified, the value of J_{BULK} can also be calculated.

The procedure for finding a functional form for $R(z)$ was as follows :

(1). Realistic non-local pseudopotential bandstructure calculations (with spin-orbit splitting) [11] were used to calculate the lowest conduction bands of GaAs and GaSb in the [100] direction. It is worth noting that local pseudopotential calculations [15] were found to overestimate the value of the height of the

conduction band maxima (E_m in Figure (5.2)), which could have led to discrepencies between our method and that of Haug's. Results of the non-local pseudopotential calculations are shown in Figures (5.4) and (5.5) respectively.

(2). A polynomial was then fitted to the bandstructure over a sufficiently large range of wavevectors. The quadratic term in the polynomial fit for the dispersion relation was then multiplied by $a(= (1+\mu_H)/(1+2\mu_H))$, which, typically has a value of about 0.88, and then the curve '$a\alpha z^2 + R(z)$' was studied. If the curve always lay below E_{QW}, then the CHCC Auger process involving the lowest conduction band only was forbidden. If the curve lay above E_{QW} for a range of wavevectors, then the ratio of the Auger transition rates using realistic dispersion relations and that calculated using parabolic bands could be estimated.

Figures (5.6) and (5.7) show the polynomial fits to the bandstructures of GaAs and GaSb in the [100] direction. Note that the fit only has to be accurate for wavevectors up to about $0.45(2\pi/a)$. It is also worth noting that on the basis of our model, the crystallographic direction which favours Auger recombination is the [100] direction since the height of the conduction band maximum is greatest in that direction, for typical III-V materials of interest, a point that has also been observed by Haug [1]. Once a polynomial fit to the realistic bandstructure has been obtained, it is possible to see whether the condition for Auger recombination is satisfied. This involves looking at equation (5.15)

$$a\alpha z^2 + R(z) \geq E_g \tag{5.16}$$

Polynomials have been fitted to the realistic bandstructures, and so a knowledge of the energy gap, E_g, and the parameter a can be used to see whether the

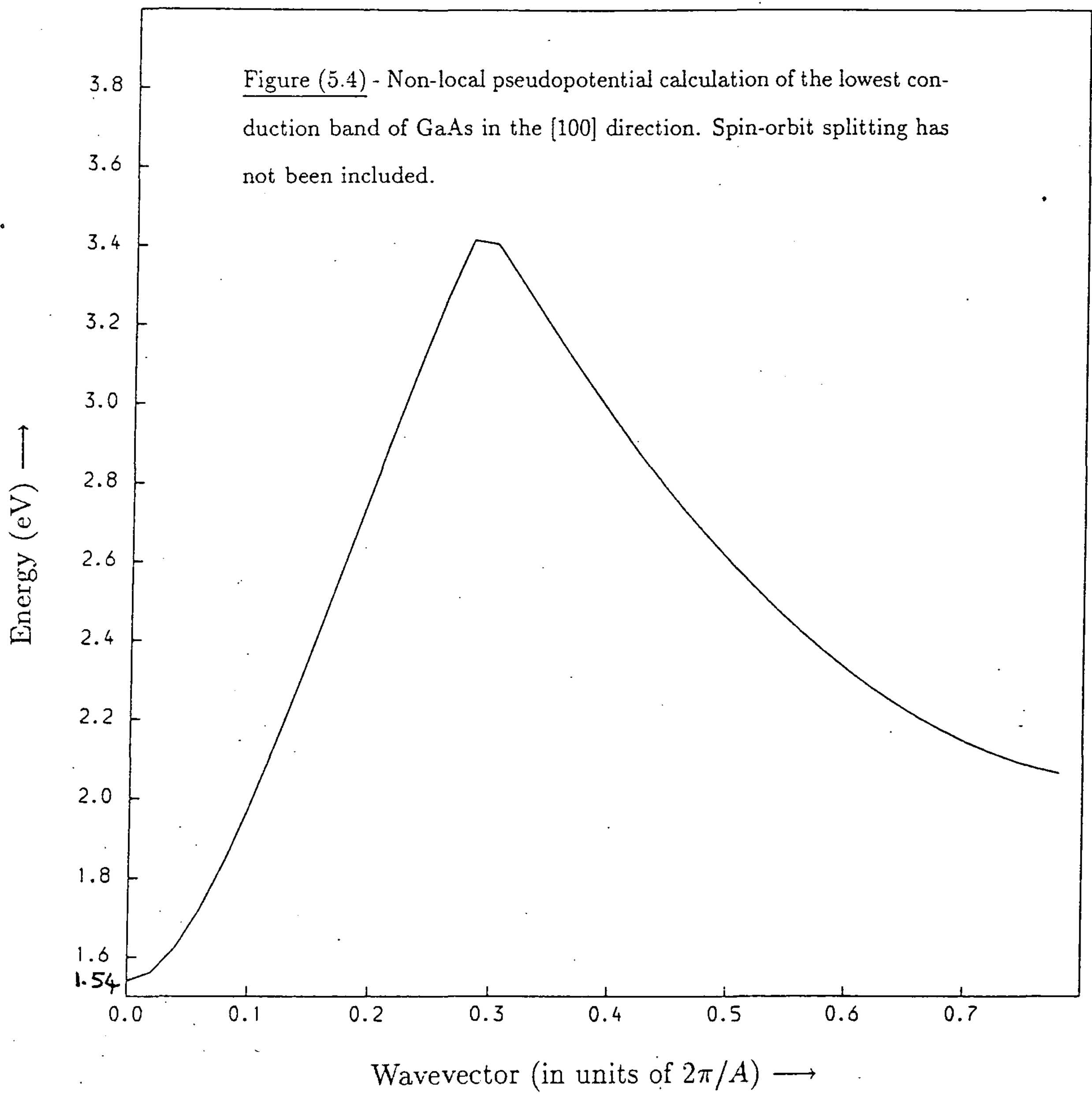

Figure (5.4) - Non-local pseudopotential calculation of the lowest conduction band of GaAs in the [100] direction. Spin-orbit splitting has not been included.

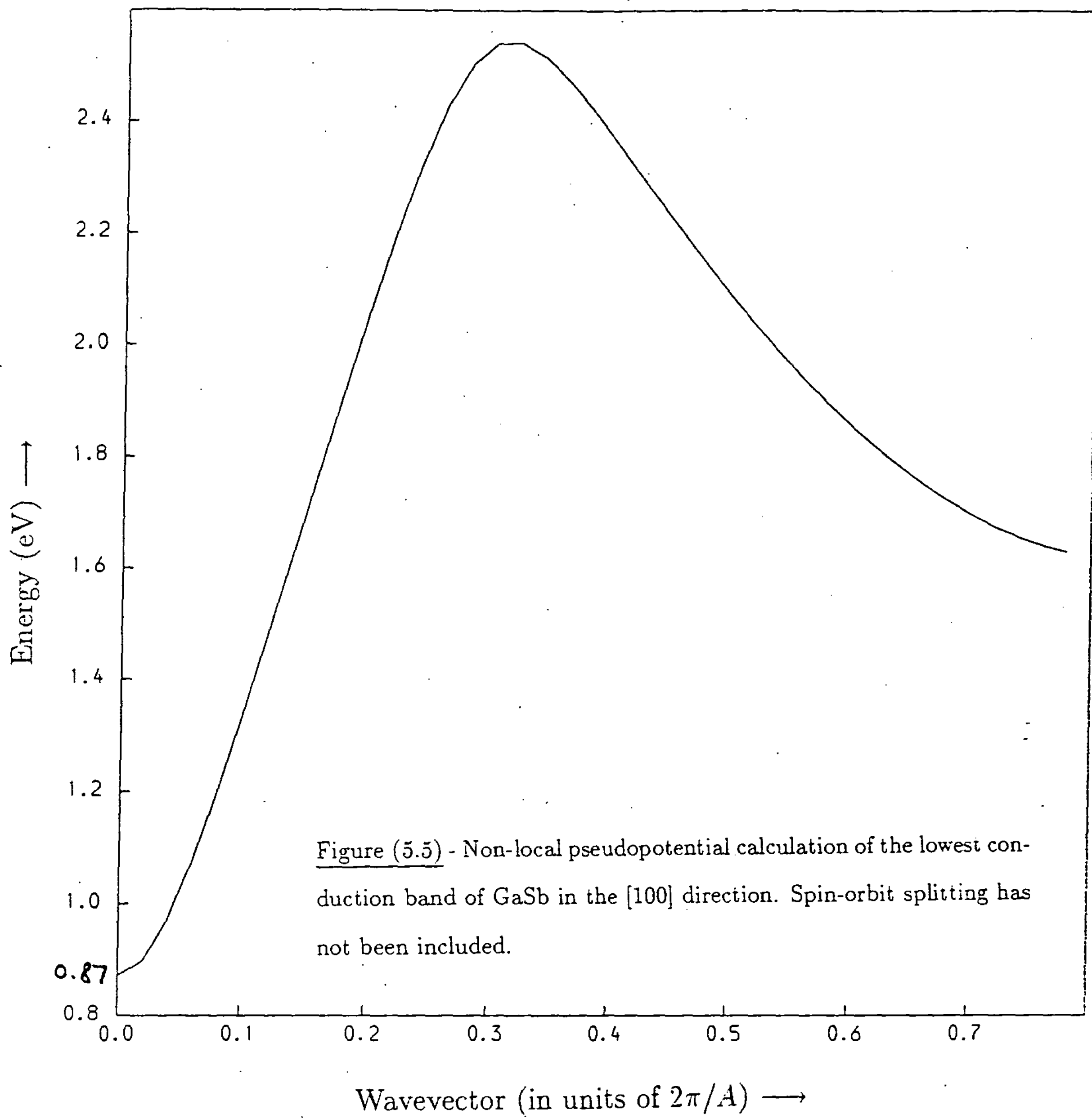

Figure (5.5) - Non-local pseudopotential calculation of the lowest conduction band of GaSb in the [100] direction. Spin-orbit splitting has not been included.

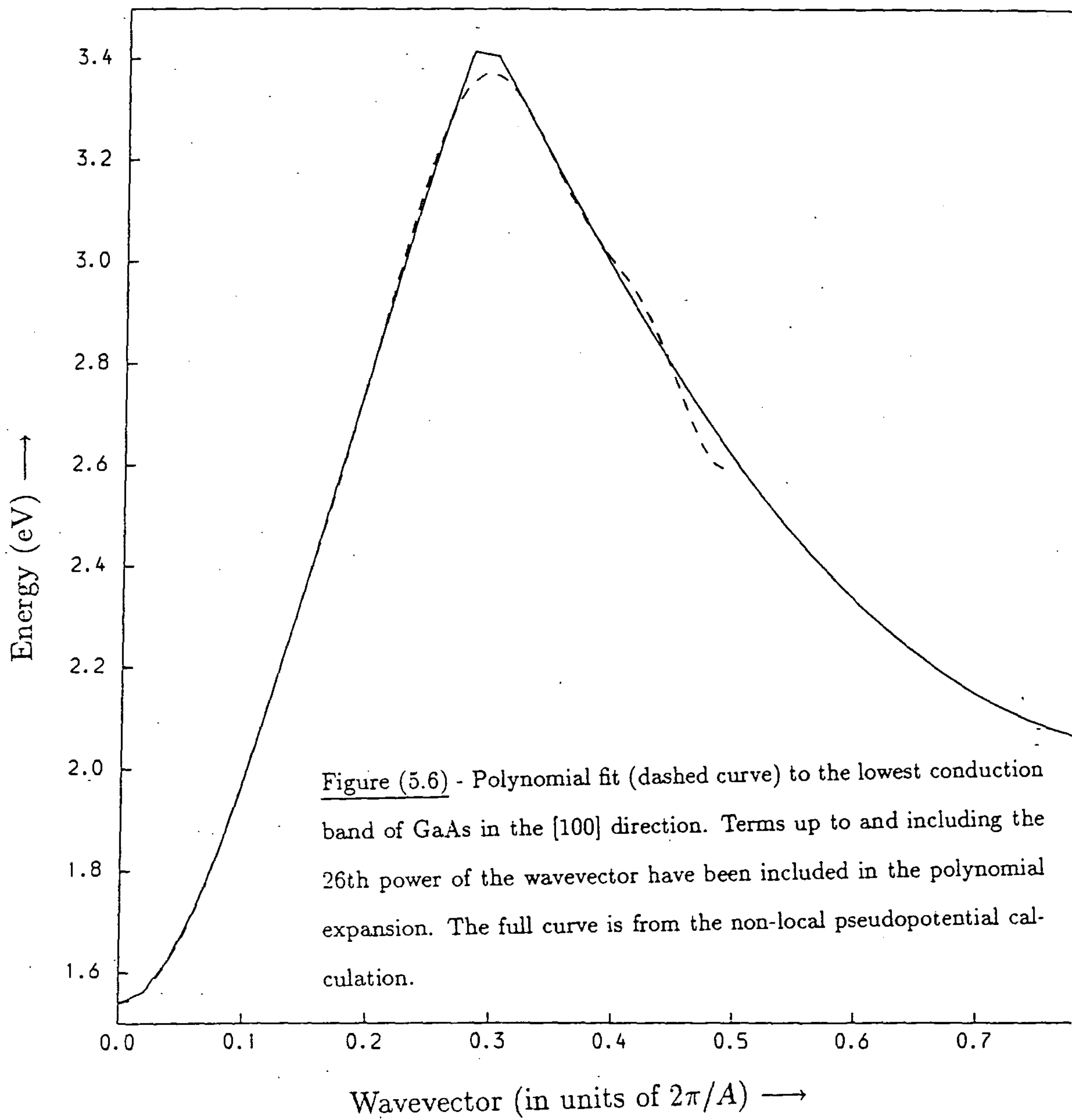

Figure (5.6) - Polynomial fit (dashed curve) to the lowest conduction band of GaAs in the [100] direction. Terms up to and including the 26th power of the wavevector have been included in the polynomial expansion. The full curve is from the non-local pseudopotential calculation.

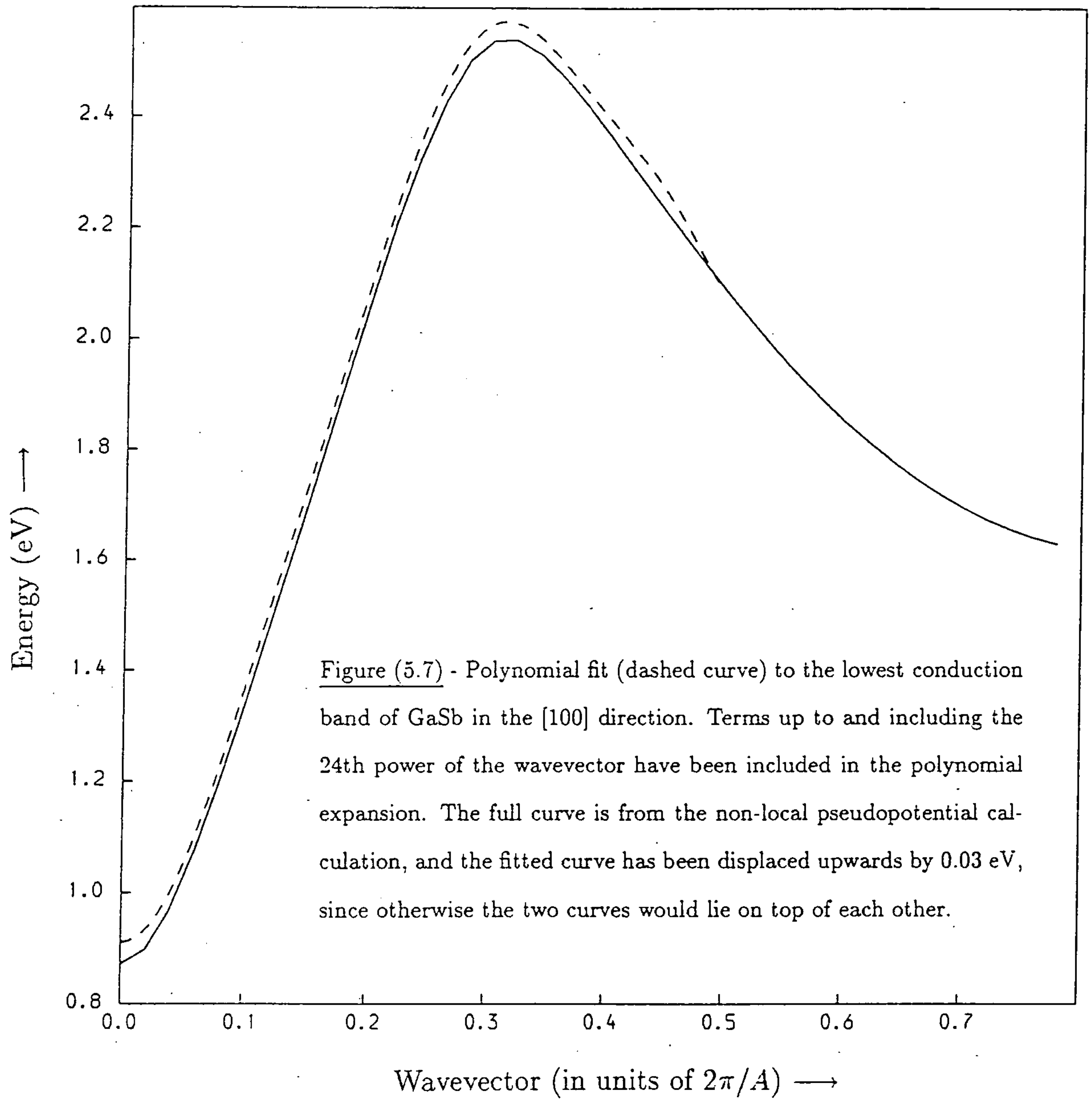

Figure (5.7) - Polynomial fit (dashed curve) to the lowest conduction band of GaSb in the [100] direction. Terms up to and including the 24th power of the wavevector have been included in the polynomial expansion. The full curve is from the non-local pseudopotential calculation, and the fitted curve has been displaced upwards by 0.03 eV, since otherwise the two curves would lie on top of each other.

simplest CHCC Auger process can occur in bulk GaAs and GaSb. The energy gaps of the two materials at 300 K are used, and it is assumed that the realistic bandstructures (which were evaluated at zero temperature) are valid at 300 K. Thus, we take $E_g(\text{GaAs}) = 1.4$ eV, and $E_g(\text{GaSb}) = 0.7$ eV.

In Figures (5.8) and (5.9), a graph of '$a\alpha z^2 + R(z)$' versus wavevector has been plotted for GaAs and GaSb respectively. The values of a have been calculated using effective masses taken from data books [16], although, since effective masses are not accurately known, it is worth treating a as a variable and letting it take values close to that predicted from [16]. Also, in Figures (5.8) and (5.9), a horizontal line corresponding to the appropriate value of E_g has been drawn. For CHCC Auger recombination to occur with only the lowest conduction band involved, the curve '$a\alpha z^2 + R(z)$' must lie above the horizontal line for some values of the wavevector. In Figure (5.8), for GaAs, this is found not to be the case.

Hence, for GaAs, we reach the same conclusion as that of Haug [1], that the direct CHCC Auger process involving the lowest conduction band only is impossible.

For GaSb, the direct CHCC Auger process can occur, as is clearly seen in Figure (5.9), and from equation (5.16), the wavevector of the carrier in the excited state is found to equal $0.157(2\pi/a)$, which agrees very well with the work of Haug, but is slightly larger than that predicted by Pearsall. The energy of the excited Auger particle relative to the conduction band edge is approximately 0.89 eV, which lies midway between the values proposed by Haug and Pearsall.

The ratio of the CHCC Auger transition rates in GaSb evaluated using realistic and parabolic dispersion relations may now be estimated. To do this, an expression for $I^2_{BULK}(\kappa)$ is needed. This is found to be

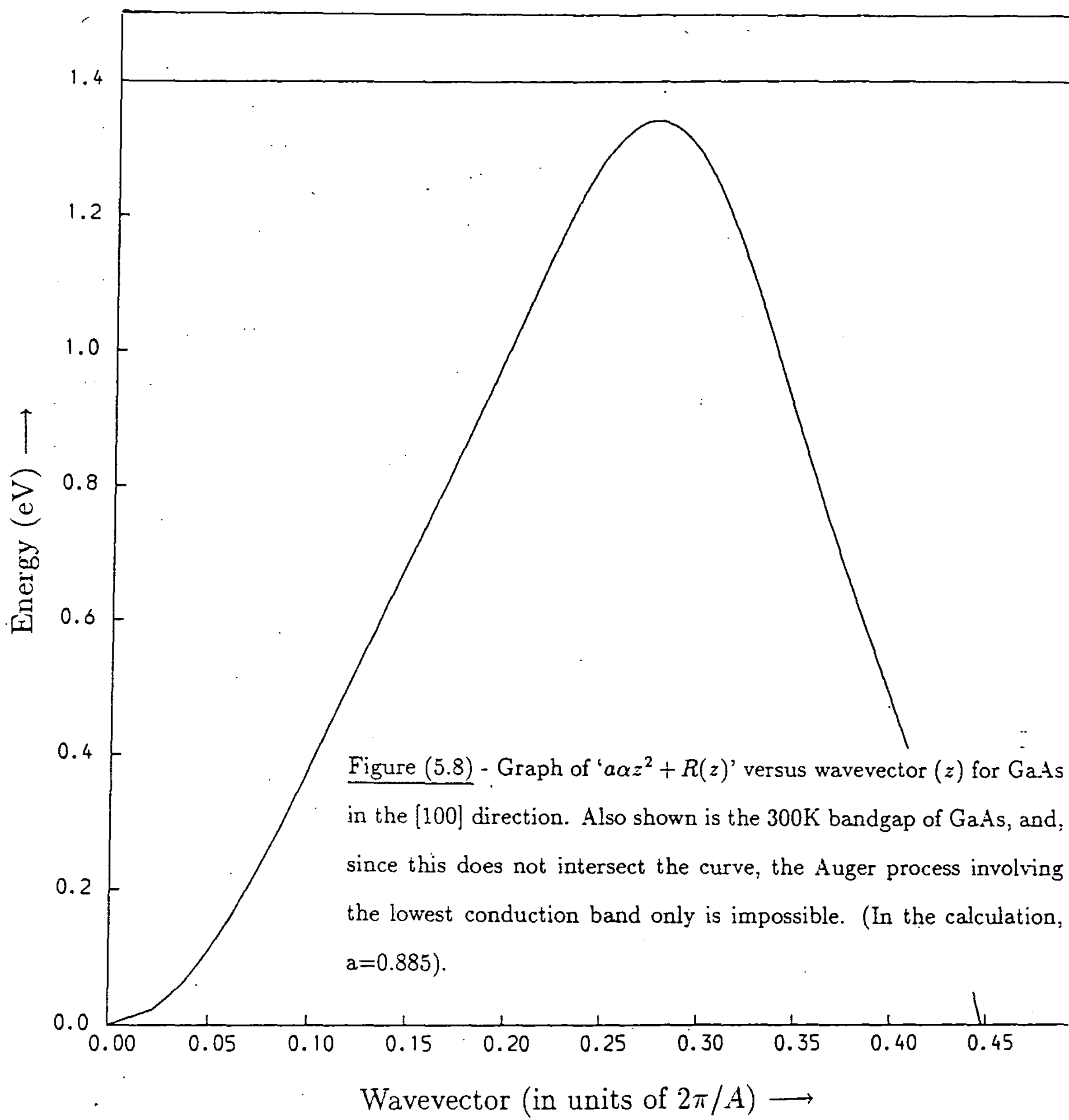

Figure (5.8) - Graph of '$a\alpha z^2 + R(z)$' versus wavevector (z) for GaAs in the [100] direction. Also shown is the 300K bandgap of GaAs, and, since this does not intersect the curve, the Auger process involving the lowest conduction band only is impossible. (In the calculation, a=0.885).

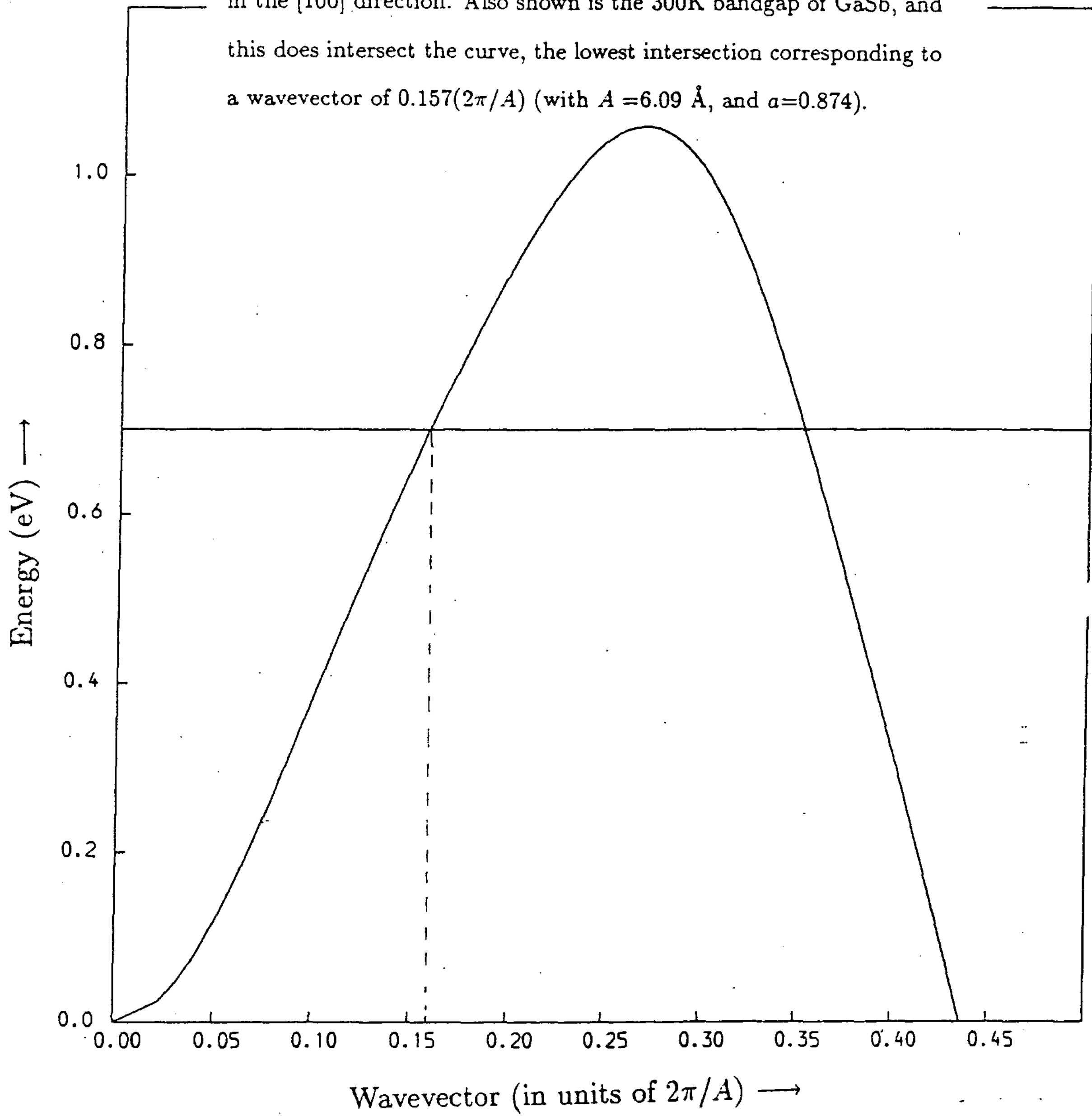

Figure (5.9) - Graph of '$a\alpha z^2 + R(z)$' versus wavevector (z) for GaSb in the [100] direction. Also shown is the 300K bandgap of GaSb, and this does intersect the curve, the lowest intersection corresponding to a wavevector of $0.157(2\pi/A)$ (with A =6.09 Å, and a=0.874).

$$I^2_{BULK}(\kappa) \propto \frac{|M_{CH}(\kappa)|^2 |M_{CC}(\kappa)|^2}{\kappa^4} \tag{5.17}$$

From the work of Burt et al, [17], we may write $|M_{CH}(\kappa)|^2 = C\kappa^2$, and also, for wavevectors in the region of the excited Auger particle, $|M_{CC}|^2 \approx 1$. Hence,

$$I^2_{BULK}(\kappa) \propto \frac{1}{\kappa^2} \tag{5.18}$$

Therefore,

$$Y = [\frac{\kappa_o^p}{\kappa_o^{np}}]^2 J_{BULK} \tag{5.19}$$

As discussed earlier, J_{BULK} is the ratio of the $\underline{\kappa}$- space integrals for the realistic and parabolic bandstructures respectively, and may be evaluated numerically once the functional form of $R(z)$ has been found from the polynomial fit. The ratio, J_{BULK}, has been evaluated for a range of values of a, to allow for any inaccuracies in published effective mass data, and values of J_{BULK} for different values of a are presented in Table (5.1). From Table (5.1), it may be concluded that the use of realistic bandstructure significantly reduces the CHCC Auger transition rate compared to the same rate evaluated with parabolic bands. We find that the CHCC Auger transition rate evaluated with realistic bandstructure is approximately an order of magnitude smaller than would have been expected from a calculation employing parabolic bands. This conclusion is in agreement with the work of Haug [1].

Table (5.1) - The threshold wavevectors, κ_o^p and κ_o^{np} are in units of $2\pi/A$ (where A=lattice constant of GaSb=6.09Å). The other symbols are as defined in the text.

TABLE (5.1)

a	K_o^p	K_o^{np}	J_{bulk}	Y
0.860	0.1019	0.1391	0.045	0.024
0.870	0.1025	0.1380	0.080	0.044
0.872	0.1026	0.1378	0.089	0.049
0.874	0.1027	0.1376	0.098	0.054
0.876	0.1029	0.1374	0.108	0.061
0.878	0.1030	0.1373	0.119	0.067
0.880	0.1031	0.1371	0.131	0.074
0.890	0.1037	0.1363	0.203	0.117

5.4 EFFECTS OF FERMI-DIRAC STATISTICS ON QW AUGER RATES

A typical III-V semiconductor laser will have a threshold carrier density in the region of $10^{18}cm^{-3}$. Such a value for the carrier density will give a conduction band quasi-Fermi level that lies above the ground state conduction subband of a QW. (The valence band quasi-Fermi level, in contrast, lies in the QW bandgap). Thus, it is necessary to examine the accuracy of Auger transition rate calculations employing Boltzmann statistics.

A number of studies have been undertaken to examine the effects of Fermi-Dirac statistics on bulk Auger recombination transition rates. Burt [18] examined CHSH Auger recombination in GaAlAsSb alloys at zero temperature, assuming a flat heavy hole band. The advantage of treating the system at zero temperature is that the Fermi-Dirac distribution functions become simple step functions. The conclusion from [18] was that the density dependence of the CHSH Auger rate was weaker in the degenerate case. For example, Burt claims that the CHSH Auger rate in GaAlAsSb varied as the injected carrier density raised to the power 7/3, whereas a non-degenerate calculation would predict a cubic dependence on carrier density.

Haug has also examined Auger recombination in degenerate semiconductors, both at zero temperature [19], and at finite temperatures [20]. Both calculations involved a number of simplifications, but also concluded that the carrier density dependence should be weaker for degenerate semiconductors than non-degenerate semiconductors. (Haug found an Auger rate proportional to np, with n the electron carrier density and p the hole density) Sugimura [21] included Fermi-Dirac statistics in calculations of bulk Auger transition rates in

GaSb and InSb at non-zero temperatures. The analytic expressions obtained were complicated, but reduced to the n^2p dependence in the non-degenerate limit. Unfortunately, Sugimura made no numerical comparison with Boltzmann statistics in that study. Later studies by Sugimura [8], [22], used an approximate expression for the statistical factor that is only valid when both quasi-Fermi levels are located at the band edges, a condition that Sugimura refers to as 'weak degeneracy', but a condition that is unlikely to be realised in practice. Beattie included Fermi-Dirac statistics in his numerical calculations of Auger transition rates [10] and concluded that 'the simple mass-action constant approach describes the lifetimes well at 80 K but somewhat less well at 300 K'. In that work, Beattie was referring to the CHCC and CHLH Auger processes in bulk InSb. Bardyszewski and Yevick [9] included Fermi-Dirac statistics (at non-zero temperatures) in their numerical calculations of Auger rates in bulk InGaAsP, but make no comment on how the results compare with those obtained by using Boltzmann statistics.

A recent, promising approach to the problem of Auger recombination with Fermi-Dirac statistics at finite temperatures is due to Haug [1]. The method used is physically appealing, produces results in analytic form, and also provides some insight into the reasons why Boltzmann statistics seem to provide reasonable estimates of Auger transition rates even at high carrier densities (e.g. Haug claims that Boltzmann statistics are valid in GaSb at carrier densities as high as 10^{19}cm^{-3}). In the original work [1], bulk Auger recombination was considered, but in the rest of this chapter, Haug's method will be applied to the case of QW systems.

5.5 THE USE OF FERMI-DIRAC STATISTICS FOR CALCULATING QW AUGER TRANSITION RATES

In this Section, the method employed by Haug [1] to study the effect of using Fermi-Dirac statistics on bulk Auger transition rates will be extended to QW systems. From Chapter Two, we have seen that the Auger transition rate may be written as

$$\text{Rate} \propto \int\int\int\int |M|^2 P\delta(\underline{\kappa})\delta(E)d\underline{\kappa}_1 d\underline{\kappa}_2 d\underline{\kappa}_3 d\underline{\kappa}_4 \tag{5.20}$$

With M being the matrix element for the transition and P the statistical factor. $E = E_1 + E_2 - E_3 - E_4$, and $\underline{\kappa} = \underline{\kappa}_1 + \underline{\kappa}_2 - \underline{\kappa}_3 - \underline{\kappa}_4$. The discussions in Chapter Two provided some physical justification for removing the slowly varying matrix element terms from the $\underline{\kappa}$-space integral and evaluating it for the wavevectors corresponding to the threshold configuration. In other words, equation (5.20) is rewritten as

$$\text{Rate} \propto |M(\underline{\kappa}_o)|^2 \int\int\int\int P\delta(\underline{\kappa})\delta(E)d\underline{\kappa}_1 d\underline{\kappa}_2 d\underline{\kappa}_3 d\underline{\kappa}_4 \tag{5.21}$$

In this section, the CHCC QW Auger transition will be examined. For the CHCC process, the statistical factor may be written as

$$P = [1 - \exp(\beta(F_v - F_c))] f_{c,n1}(\underline{\kappa}_1) f_{c,n2}(\underline{\kappa}_2) f_{v,n3}(\underline{\kappa}_3)(1 - f_{c,n4}(\underline{\kappa}_4)) \tag{5.22}$$

Since we wish to examine the effects of Fermi-Dirac statistics on the QW CHCC Auger transition rate, the full expression above for the statistical factor must be used in the $\underline{\kappa}$-space integral. Since the quasi-Fermi levels are constant for given carrier densities, then we are interested in Q, where

$$Q = \int\int\int\int f_{c,n1}(\underline{\kappa}_1) f_{c,n2}(\underline{\kappa}_2) f_{v,n3}(\underline{\kappa}_3)(1 - f_{c,n2}(\underline{\kappa}_4))\delta(\underline{\kappa})\delta(E) d\underline{\kappa}_1 d\underline{\kappa}_2 d\underline{\kappa}_3 d\underline{\kappa}_4 \tag{5.23}$$

In order to proceed further, assumptions must be made about the relative sizes of the wavevectors of the carriers involved in the Auger transition.

If parabolic bands are assumed for all the carriers, then, following the work of Beattie and Landsberg [23], the wavevectors and energies of the carriers for the threshold configuration for a CHCC QW Auger process can be shown to be

$$\underline{\kappa}_1 = \underline{\kappa}_2 = -\mu \underline{\kappa}_3 \tag{5.24}$$

$$\underline{\kappa}_4 = -(2\mu + 1)\underline{\kappa}_3 \tag{5.25}$$

$$\underline{\kappa}_4^2 = [\frac{2\mu + 1}{\mu + 1}](\frac{E_{QW}}{\alpha}) \tag{5.26}$$

with corresponding energies

$$E_1 = E_2 = E_{QW} + \frac{\mu^2}{(2\mu + 1)(\mu + 1)} E_{QW} \tag{5.27}$$

$$E_3 = -\mu\alpha\underline{\kappa}_3^2 = \frac{-\mu}{(2\mu + 1)(\mu + 1)} E_{QW} \tag{5.28}$$

$$E_4 = E_{QW} + [\frac{2\mu + 1}{\mu + 1}] E_{QW} \tag{5.29}$$

where the zero of energy has been taken to be the ground state heavy hole subband edge, and the ground state conduction subband edge has been taken as E_{QW}. Note that the above equations hold for the ground state QW CHCC Auger process only, and that is the only process that will be considered in this Section. For typical III-V semiconductors, μ (which equals m_C/m_H) is about 0.1. Hence, the wavevectors of carriers in states $|1\rangle$ and $|2\rangle$ are approximately

one-tenth of the wavevectors of carriers in states $|3\rangle$ and $|4\rangle$. Also, carriers in states $|1\rangle$ and $|2\rangle$ have energies that are very close to the conduction subband edge (i.e. only about one-hundredth of E_{QW} above the subband edge).

Although the values of the threshold wavevectors and energies will alter if realistic bandstructure is used, the general conclusions that carriers in states $|1\rangle$ and $|2\rangle$ are very close to the Γ point will be unaltered. The energy delta function requires that $E = 0$

$$E = E_1 + E_2 - E_3 - E_4 = E_{QW} + \epsilon_C(\underline{\kappa}_1) + \epsilon_C(\underline{\kappa}_2) + \epsilon_H(\underline{\kappa}_3) - \epsilon_C(\underline{\kappa}_4) \quad (5.30)$$

where the $\epsilon(\underline{\kappa})$ are the wavevector dependent parts of the carrier dispersion relations. Since carriers in states $|1\rangle$ and $|2\rangle$ are very close to the Γ point, Haug rewrote equation (5.30) as

$$E \approx E_{QW} + \epsilon_H(\underline{\kappa}_4) - \epsilon_C(\underline{\kappa}_4) \quad (5.31)$$

In other words, the energies of carriers in states $|1\rangle$ and $|2\rangle$ above the ground state conduction subband edge have been neglected, and the wavevector of the carrier in state $|3\rangle$ has been taken to equal that of the carrier in state $|4\rangle$. The above approximation, which Haug used in his calculation of the effects of realistic bandstructure and Fermi-Dirac statistics on bulk Auger recombination transition rates, greatly simplified the $\underline{\kappa}$-space integral. The same approximation also greatly simplifies the corresponding QW phase space integral.

$$Q = \int f_{c,n1}(\underline{\kappa}_1)d\underline{\kappa}_1 \int f_{c,n2}(\underline{\kappa}_2)d\underline{\kappa}_2 \int f_{v,n3}(\underline{\kappa}_4)(1 - f_{c,n4}(\underline{\kappa}_4))\delta(E')2\pi\kappa_4 d\kappa_4 \quad (5.32)$$

with $E' = E_{QW} + \epsilon_H(\underline{\kappa}_4) - \epsilon_C(\underline{\kappa}_4)$.

The above QW $\underline{\kappa}$-space integral has been written assuming general values for the quantum numbers of the states $|1\rangle$, $|2\rangle$, $|3\rangle$, and $|4\rangle$, but we shall only consider the case of $n1 = n2 = n3 = n4 = 1$. The integrations over $\underline{\kappa}_1$ and $\underline{\kappa}_2$ are straightforward, since

$$\int f_{c,m}(\underline{\kappa})d\underline{\kappa} = 2\pi^2 n_A \tag{5.33}$$

Where n_A is the number of carriers per unit area for the mth quantum well subband. Thus, for the ground state QW CHCC Auger process, the $\underline{\kappa}$- space integral becomes

$$Q = 4\pi^4 n_A^2 \int f_{v,1}(\underline{\kappa}_4)(1 - f_{c,1}(\underline{\kappa}_4))\delta(E_{QW} + \epsilon_H(\underline{\kappa}_4) - \epsilon_C(\underline{\kappa}_4))2\pi\kappa_4 d\kappa_4 \tag{5.34}$$

This final integration can be performed readily since the integrand contains a delta function. To evaluate the integral we note that

$$\delta(\phi(y)) = \sum_{i=1}^{N} \frac{\delta(y - y_i)}{|\phi'(y_i)|} \tag{5.35}$$

where y_i is one of the N roots of $\phi(y) = 0$. If κ_o is a root of

$$E' = E_{QW} + \epsilon_H(\kappa_o) - \epsilon_C(\kappa_o) = 0 \tag{5.36}$$

then, using equation (5.35), the final integration yields

$$Q = 4\pi^4 n_A^2 (2\pi\kappa_o) \frac{f_v(\kappa_o)(1 - f_c(\kappa_o))}{|\epsilon'_C(\kappa_o) - \epsilon'_H(\kappa_o)|} \tag{5.37}$$

It is worth noting that $|\underline{\kappa}_o|$ will be large since the equation $E' = 0$ will only be solved if $\epsilon_C(\kappa_o)$ is approximately equal to E_{QW}. Equation (5.37) predicts the dependence of the Auger transition rate on the distribution functions. However,

the approach used to obtain that result helps to provide physical insight into the reasons why Boltzmann statistics seem to provide reasonable estimates of Auger transition rates at carrier densities of $10^{18}\mathrm{cm}^{-3}$. The key to understanding this is the size of κ_o, this is large since it is the wavevector associated with a state in the conduction band about E_{QW} from the conduction subband edge. Thus in the distribution functions that appear in equation (5.37) it does not matter whether Boltzmann or Fermi-Dirac statistics are used, because the quasi-Fermi levels are close to the subband edges, and so the quantities $(\epsilon_C(\kappa_o) - F_c)$ and $(F_v - \epsilon_H(\kappa_o))$ are both large, and the two types of statistics are equivalent. This simple physical result is borne out by the numerical results presented by Haug [1] for Auger transitions in bulk GaSb, and has also been found for the QW in numerical work of the author.

Thus, the result of comparing Q_{FD} and Q_B (where Q_{FD} is the QW $\underline{\kappa}$-space integral calculated with Fermi-Dirac statistics, and Q_B is the corresponding quantity evaluated using Boltzmann statistics) is

$$\frac{Q_{FD}}{Q_B} = [\frac{n_{FD}}{n_B}]^2 \tag{5.38}$$

Where n_{FD} is the carrier density for the ground state conduction subband calculated using Fermi-Dirac statistics, and n_B is the corresponding carrier density evaluated with Boltzmann statistics.

Thus we may conclude that if CHCC QW Auger transition rates are calculated with the use of Boltzmann statistics, the effect of Fermi-Dirac statistics may be included by multiplying the Boltzmann based result for the transition rate by $(n_{FD}/n_B)^2$, where n_{FD} and n_B are the carrier densities defined above. For the ground state subband, $n_{FD} \leq n_B$, and so the correction factor for the ground state QW CHCC Auger process will be less than one. However, the size of the correction factor is close to one since there is not a large difference in

the ground state carrier densities calculated using Fermi-Dirac and Boltzmann statistics, as can be seen in Figures (4.5) and (4.6) for the 1.3μm and 1.55μm InGaAsP QW systems.

5.6 SUMMARY OF CHAPTER FIVE

Past studies of the effects of non-parabolic bandstructure on bulk Auger rates (which were briefly reviewed) suggest that the results obtained would differ considerably from the corresponding rates calculated with parabolic bands. A new method was described that enabled us to study the effects of non-parabolic bandstructure on Auger transition rates for the bulk, QW and QWW. To check that the method gave reliable results, numerical estimates of bulk Auger rates in GaAs and GaSb were obtained, using the realistic non-local pseudopotential bandstructure calculations of Chelikowsky and Cohen [3]. The numerical results were then compared with those of Haug [1], who had studied non-parabolicity effects in the same two systems. The two sets of results were found to be in good agreement. We found that, for bulk GaAs, the direct CHCC Auger process (involving the lowest conduction band only) was not possible, and for GaSb, the Auger coefficient of the simplest direct CHCC Auger process was reduced by at least an order of magnitude form the value obtained using parabolic bands. No numerical results were presented for the QW or the QWW because no realistic bandstructure was available for InGaAsP/InP QWs or QWWs at the relevant well widths. However, the effects of non-parabolicity are expected to be less important for the *total* QW Auger rate. The reason for this is that large contributions to the total rate arise from intersubband processes in which the excited carrier is in a higher subband, and these processes have a reduced activation energy. Thus, the excited carrier in the higher subband is closer to the Γ point (i.e. the transition is 'more vertical').

In addition to an examination of non-parabolicity on Auger rates, a brief review of the effects of using Fermi-Dirac statistics in Auger calculations was

given. A calculation of the Auger rate was then performed for the QW, in which Fermi-Dirac statistics were used. The method used was an extension of that of Haug [1] for bulk Auger calculations. The method gave an insight into the reasons why Boltzmann statistics seem to be valid for carrier densities of up to $10^{18}\mathrm{cm}^{-3}$. Also, a simple correction factor could be used to convert the QW Auger transition rate (obtained using Boltzmann statistics) into a rate that was valid for Fermi-Dirac statistics, although the two results only differed by 20-30%.

REFERENCES FOR CHAPTER FIVE

[1] A. Haug, J.Phys.C:Solid State Phys., 16, (1983), 4159.

[2] N.K. Dutta, J.Appl.Phys., 54, (1983), 1236.

[3] J.R. Chelikowsky and M.L. Cohen, Phys.Rev.B14, (1976), 556.

[4] A. Haug, Appl.Phys.Lett., 42, (1983), 512.

[5] M. Takeshima, Phys.Rev.B29, (1984), 1993.

[6] M. Combescot and R. Combescot, Solid State Comm., 61, (1987), 821.

[7] A.R. Beattie and G. Smith, Phys.Stat.Sol., 19, (1967), 577.

[8] A. Sugimura, IEEE J.Quant.Elect., QE-17, (1981), 627.

[9] W. Bardyszewski and D. Yevick, J.Appl.Phys., 58, (1985), 2713.

[10] A.R. Beattie, J.Phys.C:Solid State Phys., 18, (1985), 6501.

[11] The computer program used for the calculation of bulk, non-local pseudopotential bandstructure was provided by S. Brand, and uses the method described in reference [3].

[12] R.I. Taylor, M.G. Burt, and R.A. Abram, Superlattices and Microstructures, 3, (1987), 63.

[13] R.I. Taylor, R.A. Abram, M.G. Burt, and C. Smith, IEE Proc., 132, Part J (optoelect.), (1985), 364.

[14] T.P. Pearsall, R.E. Nahory, and J.R. Chelikowsky, Inst. Phys. Conf. Ser.No.33(b)., (1977), Chapter Six.

[15] M.L. Cohen and T.K. Bergstresser, Phys.Rev., 141, (1966), 789.

[16] Landolt-Börnstein Series, III-V Data Book, Volume 17(a), published by Springer-Verlag.

[17] M.G. Burt, S. Brand, C. Smith, and R.A. Abram, J.Phys.C:Solid State Phys., 17, (1984), 6385.

[18] M.G. Burt, J.Phys.C:Solid State Phys., 14, (1981), 3269.

[19] A. Haug, Proceedings of the 13th International Conference on the Physics of Semiconductors, Rome, 1976, page 1106.

[20] A. Haug, Solid State Comm., 21, (1978), 1281.

[21] A. Sugimura, J.Appl.Phys., 51, (1980), 4405.

[22] A. Sugimura, Appl.Phys.Lett., 39, (1981), 21.

[23] A.R. Beattie and P.T. Landsberg, Proc.Roy.Soc.A 249, (1959), 16.

CHAPTER SIX

ELECTRONIC BANDSTRUCTURE CALCULATIONS FOR SEMICONDUCTOR SUPERLATTICES : THEORY

INTRODUCTION

In Chapter Five, calculations of CHCC Auger transition rates for bulk semiconductors that included realistic bandstructure were shown to produce results that were significantly smaller than the corresponding rates calculated using parabolic bands. This is hardly surprising considering the excited carrier in the CHCC Auger transition lies approximately a bandgap above the conduction band edge. Presumably, inclusion of realistic subband structure for quantum wells would produce results for the QW Auger transition rates that would also differ from those calculated on the basis of a parabolic subband model.

However, whereas electronic bandstructure calculations are well developed for bulk semiconductors [1], [2], equivalent calculations for low-dimensional semiconductor structures (such as superlattices and quantum wells) are not so well developed. To calculate the electronic structure of superlattices (or any semiconductor system with interfaces between two different semiconductors), account must be taken of the evanescent states associated with the interface in addition to the more familiar propagating, Bloch states. Thus, the bandstructure for complex wavevector of the constituent semiconductors of the superlattice must be known. A method for calculating the bandstructure for complex wavevector of bulk semiconductors is described in this chapter. The

method uses a transfer matrix technique [3], [4], [5], based on an empirical local pseudopotential method [1].

The wavefunctions for complex wavevector of the bulk semiconductors making up the superlattice are used to construct the superlattice wavefunction. The superlattice wavefunction and its derivative are required to be continuous at the interface, and, in addition, the superlattice wavefunction must satisfy a superlattice Bloch condition. This latter condition enables a superlattice wavevector to be defined, and this wavevector may be calculated from the boundary conditions on the superlattice wavefunction. Information about the energy levels of a QW may be obtained from the superlattice calculation by simply letting the width of the barrier material tend to infinity. Details of the calculation are given in the remainder of this chapter, and, in Chapter Seven, results from the calculation are presented.

6.1 THE CALCULATION OF THE BANDSTRUCTURE FOR COMPLEX WAVEVECTOR FOR BULK SEMICONDUCTORS

In order to find the electronic structure of a semiconductor, Schrödinger's equation must be solved. In the one-electron approximation this is

$$\{\frac{-\hbar^2}{2m_o}\nabla^2 + V(\underline{r})\}\psi(\underline{r}) = E\psi(\underline{r}) \tag{6.1}$$

where m_o is the free electron mass, and $V(\underline{r})$ is the potential energy of the semiconductor. The wavefunction $\psi(\underline{r})$ varies relatively smoothly between the atoms of the semiconductor (and so can be described by a small number of Fourier coefficients) but is very rapidly varying inside the atomic cores (due to the deep, negative potential). Numerical difficulties are thus encountered if equation (6.1) is solved directly using a plane wave expansion, so a modified approach is preferable. Physically, the wavefunction of valence band states, $|\psi\rangle$, is expected to be smooth between the atoms, the smooth part of the wavefunction being described by some wavefunction $|\phi\rangle$, but $|\psi\rangle$ must also be orthogonal to the deep lying core states, denoted by $|\psi_C\rangle$. Both conditions may be achieved by writing

$$|\psi\rangle = |\phi\rangle - \sum_C |\psi_C\rangle\langle\psi_C|\phi\rangle \tag{6.2}$$

By inserting the above expression for $|\psi\rangle$ into equation (6.1), we obtain [6]

$$\{\frac{-\hbar^2}{2m_o}\nabla^2 + V(\underline{r}) + \sum_C (E - E_C)|\psi_C\rangle\langle\psi_C|\}|\phi\rangle = E|\phi\rangle \tag{6.3}$$

and this may be rewritten as

$$\{\frac{-\hbar^2}{2m_o}\nabla^2 + V_{ps}\}|\phi\rangle = E|\phi\rangle \tag{6.4}$$

Thus, equation (6.1) has been transformed into an equation with the *same* energy eigenvalue, but with a pseudowavefunction that is smooth (even inside the atomic core). The realistic potential has been replaced by a pseudopotential, V_{ps}, which is weak, in the sense that it has no bound core states. Physically, valence band wavefunctions are required to be orthogonal to the core states, and the resulting rapid oscillations of the wavefunction imply a large kinetic energy inside the core and it is this that approximately cancels out the large, negative potential energy of the core.

Equation (6.4) is much simpler to solve than equation (6.1) since only a small number of Fourier coefficients are required to describe the pseudopotential and thus the pseudowavefunction. In the empirical pseudopotential method, the pseudopotential form factors (which define the Fourier coefficients of V_{ps}) are chosen so that experimental information about semiconductor bandgaps is reproduced by solving equation (6.4).

In order to calculate the electronic bandstructure for complex wavevector we need to solve equation (6.4), which is conveniently rewritten as

$$\{-\nabla^2 + V\}\psi = E\psi \tag{6.5}$$

where V is the pseudopotential, the subscript *ps* having been dropped for notational convenience, ψ is the pseudowavefunction, and E is the energy eigenvalue (the units have been chosen so that $\hbar^2/2m_o$ is equal to unity).

Since information about evanescent waves is required in addition to information about Bloch waves, a semi-infinite semiconductor crystal is considered. The coordinate system used is $(\underline{r}, z)$, with z being the coordinate perpendicular

to the crystal surface, and $\underline{r}$ being the 2D component of position vector parallel to the crystal surface. The pseudopotential is periodic in $\underline{r}$, and so may be written as a two dimensional Fourier series

$$V(\underline{r}, z) = \sum_{\underline{g}} V_{\underline{g}}(z) \exp(i\underline{g}.\underline{r}) \tag{6.6}$$

where $\underline{g}$ is a reciprocal lattice vector associated with the surface lattice. By writing the pseudopotential as a Fourier series (equation (6.6)), i.e as a simple function of position, the assumption has been made that the crystal potential is a sum of local pseudopotentials. The extension of the pseudopotential method to include nonlocal correction terms has been thoroughly discussed in [7]. The solutions to Schrödinger's equation may be chosen to be simultaneous eigenstates of the translational symmetry operators in the $\underline{r}$ plane and so may be written as

$$\psi(\underline{r}, z) = \sum_{\underline{g}} \phi_{\underline{g}}(z) \exp(i(\underline{k} + \underline{g}).\underline{r}) \tag{6.7}$$

with $\underline{k}$ a 2D reduced wavevector.

Equations (6.6) and (6.7) may be substituted into (6.5) to give

$$\{\frac{-d^2}{dz^2} + (\underline{k} + \underline{g})^2 - E\}\phi_{\underline{g}}(z) = -\sum_{\underline{g}'} V_{\underline{g}-\underline{g}'}(z)\phi_{\underline{g}'}(z) \tag{6.8}$$

In this equation, E is the energy eigenvalue. The Fourier coefficients, $V_{\underline{g}}(z)$, of the potential may be generated using the pseudopotential form factors. Equation (6.8) can be solved numerically for $\phi_{\underline{g}}(z)$ and its derivative. The numerical solution can be checked by setting all the $V_{\underline{g}}(z)$ equal to zero, since then equation (6.8) may be solved algebraically.

For accurate wavefunctions, a large number of 2D reciprocal lattice vectors should be used in the Fourier expansion. However, as the number of $\underline{g}$'s is increased, the amount of computer time needed to solve (6.8) increases rapidly. The smallest number of $\underline{g}$'s used here for calculating dispersion relations of semiconductors in the [100] direction is 9, and the largest number used is 21.

The solutions, $\phi_{\underline{g}}(z)$ of (6.8) can be used to find the energy wavevector dispersion relation of the semiconductor as follows. Bloch's theorem states that there are a complete set of solutions to Schrödinger's equation with the property that

$$\Psi(\underline{R}+\underline{A}) = \exp(i\underline{K}.\underline{A})\Psi(\underline{R}) \tag{6.9}$$

where $\underline{A}$ is any lattice vector of the crystal. By writing $\underline{A} = (\underline{a}, l)$ and by expressing $\Psi(\underline{R})$ as a two-dimensional Fourier series, we find that

$$\phi_{\underline{g}}(z+l) = \phi_{\underline{g}}(z)\exp(ik_z l)\exp(-i\underline{g}.\underline{a}) \tag{6.10}$$

Thus, it is possible to write equation (6.10) for a particular value, z_o, of z.

$$\phi_{\underline{g}}(z_o+l) = \phi_{\underline{g}}(z_o)\exp(ik_z l)\exp(-i\underline{g}.\underline{a}) \tag{6.11a}$$

and also taking the derivative with respect to z of both sides of equation (6.10)

$$\frac{d\phi_{\underline{g}}}{dz}(z_o+l) = \frac{d\phi_{\underline{g}}}{dz}(z_o)\exp(ik_z l)\exp(-i\underline{g}.\underline{a}) \tag{6.11b}$$

where $\frac{d\phi_g}{dz}(z_o+l)$ denotes the z derivative of $\phi_{\underline{g}}$ evaluated at (z_o+l). $\phi_{\underline{g}}(z_o+l)$ and $\frac{d\phi_g}{dz}(z_o+l)$ will depend linearly on $\phi_{\underline{g}}(z_o)$ and $\frac{d\phi_g}{dz}(z_o)$ since they are solutions of a second order linear homogeneous differential equation. Hence, in addition to equations (6.11a) and (6.11b) we have

$$\phi_{\underline{g}}(z_o + l) = \sum_{\underline{g}'} M_{\underline{g},\underline{g}'}\phi_{\underline{g}'}(z_o) + \sum_{\underline{g}'} N_{\underline{g},\underline{g}'}\frac{d\phi_{\underline{g}'}}{dz}(z_o) \tag{6.12a}$$

$$\frac{d\phi_{\underline{g}'}}{dz}(z_o + l) = \sum_{\underline{g}'} P_{\underline{g},\underline{g}'}\phi_{\underline{g}'}(z_o) + \sum_{\underline{g}'} Q_{\underline{g},\underline{g}'}\frac{d\phi_{\underline{g}'}}{dz}(z_o) \tag{6.12b}$$

The matrices M, N, P, Q, are found by numerical integration of equation (6.8) from z_o to $(z_o + l)$ with appropriate initial conditions at $z = z_o$. Comparing equations (6.11a) and (6.11b) with the corresponding equations (6.12a) and (6.12b), we conclude that the allowed values of $\exp(ik_z l)$ are the eigenvalues of the matrix

$$\begin{pmatrix} \overline{M} & \overline{N} \\ \overline{P} & \overline{Q} \end{pmatrix}$$

with $\overline{M}_{\underline{g},\underline{g}'} = \exp(i\underline{g}.\underline{a})M_{\underline{g},\underline{g}'}$, etc. Thus, if $\underline{k}$, the component of wavevector parallel to the surface, and the energy, E are fixed, then the z-component of the wavevector may be calculated.

The method is similar to that used by Marsh and Inkson [8].

As an example of the above technique, the bandstructure for complex wavevector for GaAs (for k_z in the [100] direction) is presented in Figure (6.1).

One of the advantages of the method outlined above is that both real and *complex* values of k_z are calculated. The complex values of k_z correspond to the evanescent solutions of Schrödinger's equation and conventional electronic bandstructure calculations for bulk semiconductors ignore these states because the boundary conditions for the infinite bulk allow only propagating, Bloch, solutions. However, if the bulk solutions to Schrödinger's equation are to be used to construct a wavefunction near a semiconductor interface (such as for a QW or superlattice), the evanescent states must be included in the basis set. A comprehensive account of evanescent states has been given by Heine [9].

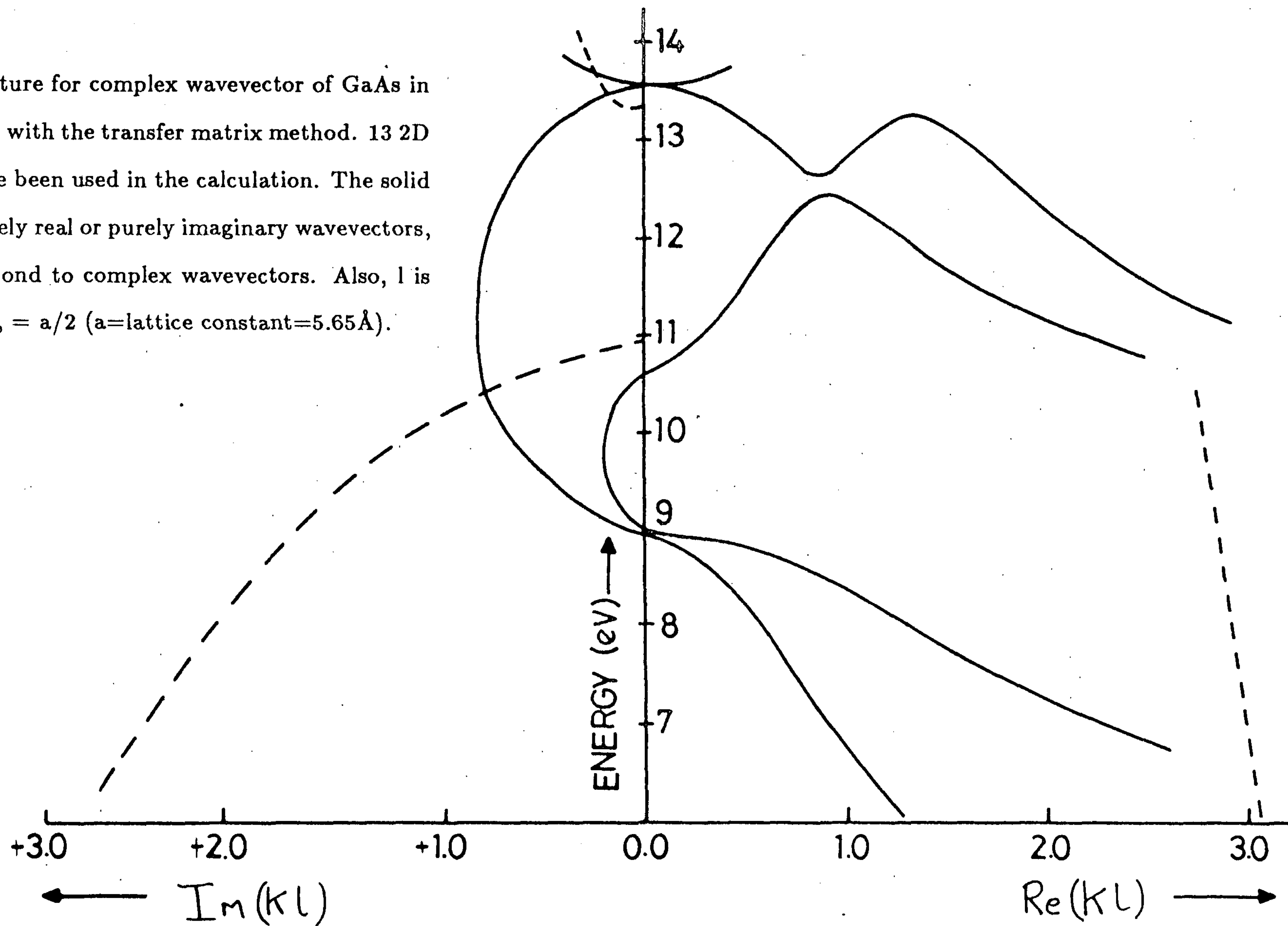

Figure (6.1) - The bandstructure for complex wavevector of GaAs in the [100] direction, calculated with the transfer matrix method. 13 2D reciprocal lattice vectors have been used in the calculation. The solid lines correspond to either purely real or purely imaginary wavevectors, and the dashed lines correspond to complex wavevectors. Also, l is the thickness of a monolayer, = a/2 (a=lattice constant=5.65Å).

By changing the pseudopotential form factors (for example,by using the data from [1]) the bandstructure for complex wavevector of other semiconductors may be readily calculated. Thus, for a superlattice bandstructure calculation, all the realistic solutions to Schrödinger's equation for both constituent semiconductor materials can be generated, and so the superlattice wavefunction can be constructed from a superposition of these solutions. By applying the relevant boundary conditions at the interfaces, as described in the next section, the relationship between superlattice wavevector and energy may be found.

6.2 THE CALCULATION OF SUPERLATTICE BANDSTRUCTURE

Consider a superlattice composed of semiconductors A and B (Figure (6.2)). The width of the A layer is L_A $(= N_A l)$, and that of the B layer is L_B $(= N_B l)$, with N_A, N_B being integers, and l is the thickness of a monolayer of material A (or B). Initially, the constituent semiconductors are assumed to have the same lattice constant. The superlattice wavefunction may be written as follows :

For $-L_A \leq z \leq 0$

$$\Psi_1 = \sum_n A_n \psi^n(\underline{R}, \underline{k}, E) \tag{6.13}$$

For $0 \leq z \leq L_B$

$$\Psi_2 = \sum_n B_n \phi^n(\underline{R}, \underline{k}, E) \tag{6.14}$$

For $L_B \leq z \leq (L_A + L_B)$

$$\Psi_3 = \sum_n C_n \psi^n(\underline{R}, \underline{k}, E) \tag{6.15}$$

where $\underline{k}$ is the wavevector parallel to the interfaces. $\underline{k}$ is the same either side of the interface since the superlattice has the same translational symmetry as its constituent semiconductors. ψ^n and ϕ^n are solutions to Schrödinger's equation for materials A and B at a given energy E. As in the previous Section, we write

$$\psi^n = \sum_{\underline{g}} \psi^n_{\underline{g}}(z) \exp(i(\underline{k} + \underline{g}).\underline{r}) \tag{6.16}$$

and

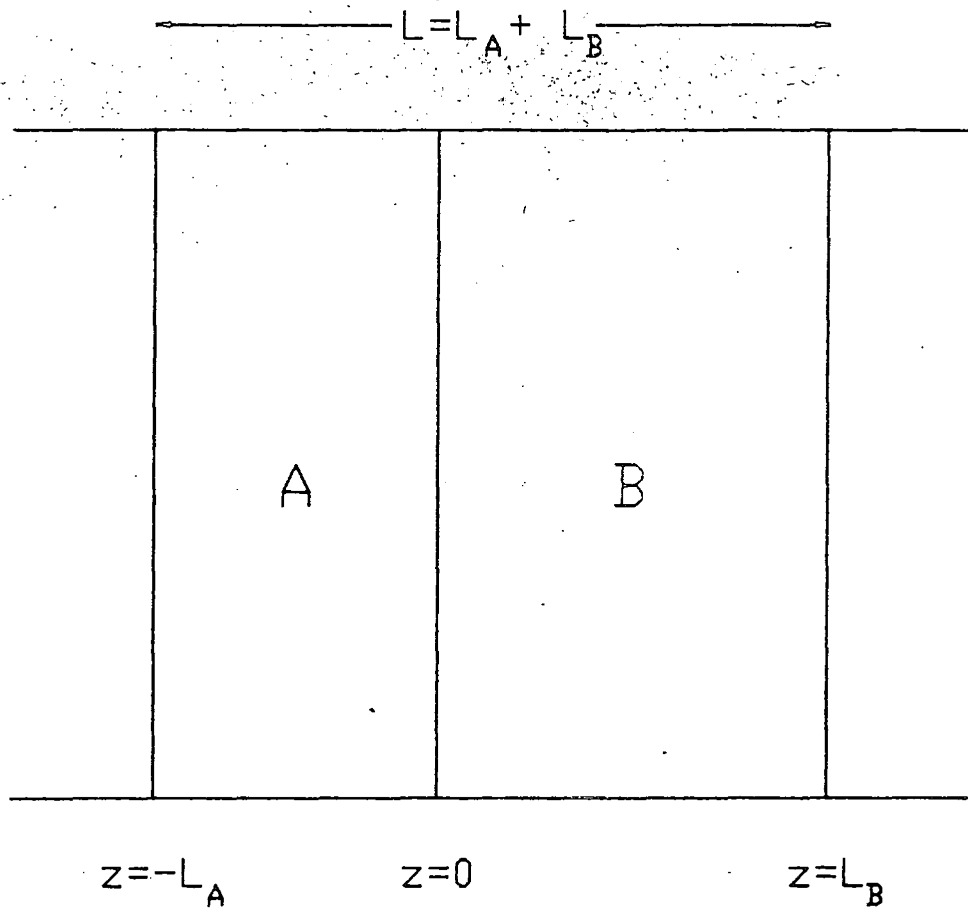

Figure (6.2) - Diagram showing part of the ...ABAB... superlattice close to z=0.

$$\phi^n = \sum_{\underline{g}} \phi^n_{\underline{g}}(z) \exp(i(\underline{k}+\underline{g}).\underline{r}) \tag{6.17}$$

The boundary conditions on the superlattice wavefunction are that the wavefunction and its derivative normal to the interface are equal on either side of an interface. Also, there is a superlattice Bloch condition associated with the superlattice periodicity. Thus, the boundary conditions are

$$\Psi_1(\underline{r}, 0) = \Psi_2(\underline{r}, 0) \tag{6.18}$$

$$\frac{d}{dz}\Psi_1(\underline{r}, 0) = \frac{d}{dz}\Psi_2(\underline{r}, 0) \tag{6.19}$$

$$\Psi_2(\underline{r}, L_B) = \Psi_3(\underline{r}, L_B) \tag{6.20}$$

$$\frac{d}{dz}\Psi_2(\underline{r}, L_B) = \frac{d}{dz}\Psi_3(\underline{r}, L_B) \tag{6.21}$$

and the superlattice Bloch condition is

$$\Psi_3(\underline{r}+\underline{\alpha}, z+L) = \exp(i\underline{k}.\underline{\alpha})\exp(iK_S L)\Psi_1(\underline{r}, z) \tag{6.22}$$

$$\frac{d}{dz}\Psi_3(\underline{r}+\underline{\alpha}, z+L) = \exp(i\underline{k}.\underline{\alpha})\exp(iK_S L)\frac{d}{dz}\Psi_1(\underline{r}, z) \tag{6.23}$$

Here, $(\underline{\alpha}, L)$ is a vector joining two identical atoms, where $\underline{\alpha}$ is the 2D vector in the plane parallel to the interfaces. L is the superlattice period, and K_S is called the superlattice wavevector. Equations (6.18-6.23) must be satisfied for *any* value of $\underline{r}$.

The boundary conditions, as written above, are not in a convenient form, because they are identities in the continuous variable $\underline{r}$. To circumvent this

problem one needs to expand the $\underline{r}$ dependence of (6.18) to (6.23) in terms of plane waves. If one then makes the approximation of truncating the number of plane waves in the expansion, a finite number of equations will be obtained.

The boundary conditions are thus re-expressed as

$$\sum_n A_n \psi^n_{\underline{g}}(0) = \sum_m B_m \phi^m_{\underline{g}}(0) \tag{6.24}$$

$$\sum_n A_n \frac{d}{dz} \psi^n_{\underline{g}}(0) = \sum_m B_m \frac{d}{dz} \phi^m_{\underline{g}}(0) \tag{6.25}$$

$$\sum_n B_n \phi^n_{\underline{g}}(L_B) = \sum_m C_m \psi^m_{\underline{g}}(L_B) \tag{6.26}$$

$$\sum_n B_n \frac{d}{dz} \phi^n_{\underline{g}}(L_B) = \sum_m C_m \frac{d}{dz} \psi^m_{\underline{g}}(L_B) \tag{6.27}$$

$$\sum_n C_n \psi^n_{\underline{g}}(L) \exp(i\underline{g}.\underline{\alpha}) = \exp(iK_S L) \sum_m A_m \psi^m_{\underline{g}}(0) \tag{6.28}$$

$$\sum_n C_n \frac{d}{dz} \psi^n_{\underline{g}}(L) \exp(i\underline{g}.\underline{\alpha}) = \exp(iK_S L) \sum_m A_m \frac{d}{dz} \psi^m_{\underline{g}}(0) \tag{6.29}$$

where the equations above have to hold for each $\underline{g}$ in the basis set. In equations (6.26-6.29), $\phi^n_{\underline{g}}(z)$, $\psi^n_{\underline{g}}(z)$ (and their derivatives) at non-zero values of z are required. In Section 6.1, equations (6.11a) and (6.11b) related the values of $\phi^n_{\underline{g}}(z)$ (and its derivative) at values of z separated by a monolayer and, using those equations, repeatedly if necessary, the values of $\phi^n_{\underline{g}}(z)$ (or $\psi^n_{\underline{g}}(z)$) and the derivative at any value of z may be related to the respective values at $z = 0$.

It is convenient to rewrite the boundary conditions in terms of a matrix eigenvalue problem. If the number of basis states is taken to be n, then there are

$2n$ solutions to equation (6.8) (because it is a 2nd order differential equation). Now define

$$M_1 = \begin{pmatrix} \psi^1_{\underline{g}_1}(0) & \dots & \psi^{2n}_{\underline{g}_1}(0) \\ \dots & \dots & \dots \\ \psi^1_{\underline{g}_n}(0) & \dots & \psi^{2n}_{\underline{g}_n}(0) \\ \frac{d}{dz}\psi^1_{\underline{g}_1}(0) & \dots & \frac{d}{dz}\psi^{2n}_{\underline{g}_1}(0) \\ \dots & \dots & \dots \\ \frac{d}{dz}\psi^1_{\underline{g}_n}(0) & \dots & \frac{d}{dz}\psi^{2n}_{\underline{g}_n}(0) \end{pmatrix} \tag{6.30}$$

A matrix M_2 is similarly defined for the $\phi^n_{\underline{g}}(0)$, and its derivative. The coefficients A_n, B_n and C_n are represented by column vectors A, B, and C, of dimensions 2n. In matrix form, equations (6.24) and (6.25) can be written as

$$M_1 A = M_2 B \tag{6.31}$$

In a similar way, equations (6.26) and (6.27) can be written as

$$M_3 B = M_4 C \tag{6.32}$$

with

$$M_3 = P^{N_B} M_2 K_B^{N_B} \tag{6.33}$$

and

$$M_4 = P^{N_B} M_1 K_A^{N_B} \tag{6.34}$$

where

$$P = \begin{pmatrix} G & 0 \\ 0 & G \end{pmatrix} \tag{6.35a}$$

$$G = \begin{pmatrix} \exp(i\underline{g}_1 . \underline{a}) & 0 & 0 & 0 \\ 0 & \ddots & 0 & 0 \\ 0 & 0 & \ddots & 0 \\ 0 & 0 & 0 & \exp(i\underline{g}_n . \underline{a}) \end{pmatrix} \qquad (6.35b)$$

and

$$K_A = \begin{pmatrix} \exp(ik_1^A l) & \dots & 0 \\ \vdots & \ddots & \vdots \\ 0 & \dots & \exp(ik_{2n}^A l) \end{pmatrix} \qquad (6.36)$$

The k_n^A appearing in equation (6.36) are the wavevectors from the solution of Schrödinger's equation for the bulk for material A. K_B is defined in a similar way to K_A. In equation (6.35) defining the matrix P, $(\underline{a}, l)$ is a lattice vector between atoms in adjacent monolayers.

Equations (6.31) and (6.32) yield

$$A = M_1^{-1} M_2 M_3^{-1} M_4 C \qquad (6.37)$$

However, the coefficients in the column vectors A and C are also related by the superlattice Bloch condition.

$$A = \exp(-iK_S L) K_A^{N_A + N_B} C \qquad (6.38)$$

Comparing equations (6.37) and (6.38), we conclude that $\exp(-iK_S L)$ (with K_S the superlattice wavevector) are eigenvalues of

$$K_A^{-(N_A + N_B)} M_1^{-1} M_2 M_3^{-1} M_4 \qquad (6.39)$$

Since the eigenvalues of a matrix are unaltered by a similarity transformation (i.e. a transformation of the form SAS^{-1}), then the allowed values of $\exp(-iK_S L)$ are eigenvalues of

$$M_1^{-1} M_2 K_B^{-N_B} M_2^{-1} M_1 K_A^{-N_A} \tag{6.40}$$

This result is true for any in-plane wavevector, $\underline{k}$. Expression (6.40) was derived from (6.39) by using the definitions for M_3 and M_4, and then using a similarity transformation (with $S = K_A^{(N_A+N_B)}$).

The superlattice wavevectors, K_S, are calculated from the eigenvalues of the matrix defined in (6.40). However, the eigenfunctions of the matrix in (6.40) do not immediately give the superlattice wavefunction, since, although eigenvalues are unaltered by a similarity transformation, the eigenvectors are altered. However, the superlattice wavefunction may be calculated from the eigenvectors of the matrix in (6.40) without difficulty.

Equation (6.40) shows the matrix which must be diagonalised to obtain the superlattice wavevector. M_1 and M_2 are matrices containing information about the bulk semiconductors A and B respectively. K_A and K_B are diagonal matrices, also containing information on the bulk materials, the matrix elements being of the form $\exp(i\lambda l)$, with λ a wavevector for the bulk (complex, in general). N_A and N_B are the numbers of monolayers of semiconductors A and B in the repeating unit of the superlattice.

The matrices are, in general, complex, and so diagonalisation of a complex, asymmetric square matrix is required. This was achieved by the use of a NAG library routine (routine F02AJF).

In order to calculate superlattice bandstructure, information about the band offsets at the interface between the two constituent semiconductors is required. For the GaAs/AlAs superlattice (or QW), experimental information is available about the band offsets (for example, see reference [10]). In our calculation, the zero of energy of the bulk semiconductor bandstructure (which is arbitrary) is altered accordingly so that the conduction and valence band

edges of the constituent materials of the superlattice are at appropriate energies to give offsets as close as possible to the experimental values.

Two types of calculation are possible for the superlattice :

(i) The in-plane wavevector may be fixed at a particular value (usually this is zero) and the energy-superlattice wavevector relationship can be studied. The increased periodicity of a superlattice compared to its constituent semiconductors leads to a smaller Brillouin zone for wavevectors corresponding to the direction normal to the layers and 'band-folding' effects can be examined.

(ii) The superlattice wavevector can be fixed at a particular value and the energy-in plane wavevector relationship may be studied. The information about the subband dispersion is useful for calculations of Auger rates, since it is the $E - \underline{k}$ relationship that is crucial in determining transition rates.

In summary, a method has been described for the calculation of the bandstructure for complex wavevector of bulk semiconductors. The bandstructure has then been used to generate the bandstructure for complex wavevector of a superlattice composed of two separate semiconductors. The method is flexible in that it allows specification of both well and barrier widths, band offsets, and even constituent materials (provided they are lattice matched). The method may also be extended to study strained layer superlattices, in which the constituent semiconductors have different lattice constants [11]. A brief summary of the work presented in this chapter can be found in reference [12].

In the next chapter, results for the $(GaAs)_n(AlAs)_m$ superlattice bandstructure obtained using the method outlined above will be presented. That particular system was chosen since the constituent materials are virtually lattice matched, information about the band offsets is extensive, and the system is also physically interesting since one of the constituent materials is an indirect gap semiconductor.

REFERENCES FOR CHAPTER SIX

[1] M.L. Cohen and T.K. Bergstresser, Phys.Rev., 141, (1966), 789.

[2] J.R. Chelikowsky and M.L. Cohen, Phys.Rev.B, 14, (1976), 556.

[3] M.G. Burt and J.C. Inkson, J.Phys.D:Appl. Phys., 9, (1976), 43.

[4] M.G. Burt, J.Phys.C:Solid State Phys., 13, (1980), 1825.

[5] J.B. Pendry, J.Phys.C:Solid State Phys., Ser. 2, 2, (1969), 2273.

[6] V. Heine, Solid State Physics, 24, (1970), 1.

[7] J.R. Chelikowsky and M.L. Cohen, Phys.Rev.B,14, (1976), 556.

[8] A.C. Marsh and J.C. Inkson, J.Phys.C:Solid State Phys., 17, (1984), 6561.

[9] V. Heine, Proc.Phys.Soc., 81, (1963), 300.

[10] J. Batey and S.L. Wright, J.Appl.Phys., 59, (1986), 200.

[11] D.T. Hughes and S. Brand, Proceedings of the 3rd International Conference on Modulated Semiconductor Structures, Montpellier, 1987, page 481.

[12] R.I. Taylor, M.G. Burt and R.A. Abram, Superlatt. and Microstruct., 3, (1987), 63.

CHAPTER SEVEN

THE ELECTRONIC STRUCTURE OF GaAs/AlAs SUPERLATTICES

INTRODUCTION

In this chapter, results for the electronic bandstructure of GaAs/AlAs superlattices (with interfaces normal to the [100] direction) will be presented, the method used being that described in Chapter Six. The GaAs/AlAs superlattice is a suitable system to study for the following reasons.

(i) The constituent materials have very similar lattice constants (the lattice mismatch is only about 0.1 %) and can be assumed to be lattice matched (with a lattice constant equal to 5.65 Å).

(ii) Experimental information is available for the band offsets at GaAs/AlAs interfaces (for a recent study, see [1]).

(iii) The pseudopotential form factors of both GaAs and AlAs can be found from the literature [2], [3]. Results presented in reference [4] for GaAs/AlAs superlattices used pseudopotential form factors taken from [2], but it has since been found that the values given by Gell et al [3] give better fits to experimental data.

(iv) AlAs is an indirect material, and recent calculations [3] show that, although the GaAs acts as a well for electrons close to the Γ point, it acts as a barrier

for electrons close to the X point. This leads to some interesting effects that will be discussed in more detail in this Chapter.

As far as this thesis is concerned, a more appropriate system to study would be the InGaAsP/InP QW, the energy-in plane wavevector relationship being crucial for accurate determination of Auger transition rates. However, the use of realistic bandstructure in Auger calculations is a major calculation in itself and also the calculation of the quaternary alloy bandstructure from that of its constituent binaries would lead to errors that are difficult to estimate.

Hence, the aim of this Chapter is to demonstrate that the method described in Chapter Six can be used to accurately determine the electronic structure of superlattices. Using the electronic bandstructure to calculate Auger transition rates, optical matrix elements, etc., are problems that must be left for future study.

One disadvantage of the method described in Chapter Six is that spin-orbit splitting is not included in the calculation, and so, in this chapter, the majority of results presented will be for the conduction bands. Spin-orbit splitting has been included in the superlattice bandstructure calculations of Brand et al [5], and also in calculations of quantum well energy levels by Brand and Hughes [6].

7.1 THE ENERGY-SUPERLATTICE WAVEVECTOR RELATION IN A GaAs/AlAs SUPERLATTICE

In Chapter Six, a method was described that enabled the calculation of the superlattice wavevector, given the energy and in-plane wavevector. In the calculations reported here the pseudopotential form factors for GaAs and AlAs have been taken from the work of Gell et al [3], and are given explicitly in Table (7.1). Using the above form factors, the bandstructures for complex wavevector (of GaAs and AlAs) have been calculated. In the calculations, equation (6.8) was solved, and this was done numerically, using a NAG routine (NAG routine D02BAF). An accuracy parameter, ACCU, had to be specified in the numerical routine, and a value of 1E-4 was found to be adequate, a value that has been used for all the results presented in this chapter. The number of 2D reciprocal lattice vectors used to describe the pseudowavefunction was 21 (corresponding to the projection of 51 reciprocal lattice vectors onto the (100) plane). With these parameters, the band gaps of GaAs and AlAs were found to have the values shown in Figure (7.1). In Figure (7.1), the band offsets assumed for the GaAs/AlAs interface are also shown. The offsets have been chosen so as to give the same energy separation between the lowest conduction states of GaAs and AlAs as that assumed by Gell et al [3]. This corresponds to ΔE_c being approximately 60 % of the difference of the direct energy gaps of AlAs and GaAs.

The effective mass of conduction electrons in GaAs (for motion in the [100] direction) at the Γ point was found to be $0.078m_o$ (m_o being the free electron mass), approximately 15 % higher than the experimental value [7].

Table (7.1) - Values of the pseudopotential form factors used in the calculations of bandstructure for complex wavevector of GaAs and AlAs. The values have been taken from reference [3].

TABLE 7.1

	AlAs	GaAs
VS3	-0.23074	-0.2396
VS8	0.02542	0.0126
VS11	0.07	0.06
VA3	0.0725	0.07
VA4	0.0625	0.05
VA11	-0.0075	0.01

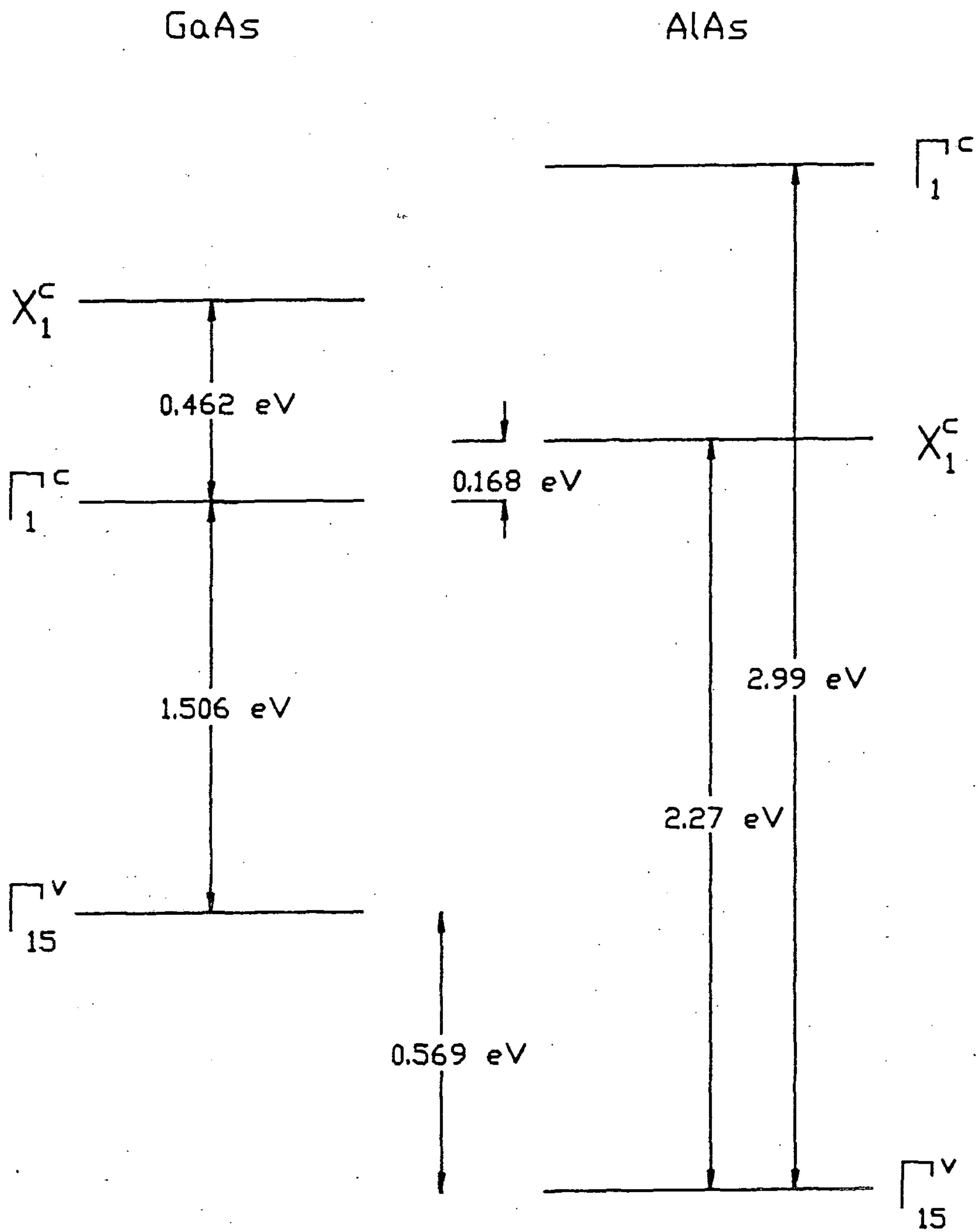

Figure (7.1) - The bandgaps and band offsets for the GaAs/AlAs system used throughout this Chapter.

The bandgaps of the principal symmetry points of AlAs and GaAs were found to be in good agreement with experiment [7] (see Table (7.2)).

Using the bandstructure for complex wavevector of GaAs and AlAs, and assuming band offsets for the GaAs/AlAs interface corresponding to the values of Figure (7.1), the energy-superlattice wavevector relationship was studied for the $(GaAs)_1(AlAs)_1$ superlattice, that is, alternate monolayers of GaAs and AlAs. The interfaces in the superlattice were assumed to be normal to the [100] direction. The results are shown in Figure (7.2), along with the energies corresponding to the high symmetry points of bulk GaAs and AlAs. The value of the in-plane wavevector (i.e. the wavevector parallel to the superlattice interfaces) was taken to be zero and the three lowest conduction subbands were all found to be direct, in agreement with the work of Gell et al [3]. However, the position of the lowest conduction band state was found to lie above the energy corresponding to the X point in AlAs, whereas Gell et al [3] found that the lowest conduction band state lay below that energy.

In Figure (7.3a), the energy-superlattice wavevector relationship for the conduction subbands of a $(GaAs)_2(AlAs)_2$ superlattice is shown, the in-plane wavevector again being taken as zero. The results are in qualitative agreement with those of Gell et al (e.g. see Figure (8)(b) of reference [3]), and also with those of Nakayama and Kammimura [8] and Nara [9]. In Figure (7.3b), the $(GaAs)_1(AlAs)_1$ superlattice (SL) bandstructure is shown 'folded over' into the Brillouin zone of the $(GaAs)_2(AlAs)_2$ SL. A good discussion of 'zone-folding' may be found in reference [10] and in this case, the basic idea is as follows. The period of the $(GaAs)_2(AlAs)_2$ SL is twice that of the $(GaAs)_1(AlAs)_1$ SL. Hence, the wavevector associated with the Brillouin zone edge in the [100] direction is $\pi/2a$ for the $(GaAs)_2(AlAs)_2$ SL (where a is the lattice constant of

TABLE (7.2)

GaAs		
	experiment	theory
$E(\Gamma_1^c) - E(\Gamma_{15}^v)$	1.520	1.506
$E(X_1^c) - E(\Gamma_1^c)$	0.467	0.462

AlAs		
	experiment	theory
$E(X_1^c) - E(\Gamma_{15}^v)$	2.230	2.270
$E(\Gamma_1^c) - E(\Gamma_{15}^v)$	3.130	2.990

Table (7.2) - Comparison of the bandgaps of GaAs and AlAs from the pseudopotential calculation with experimental values (the latter having been taken from [7]).

Figure (7.2) - The energy-superlattice wavevector relation for the conduction subbands of a $(GaAs)_1(AlAs)_1$ superlattice. The superlattice wavevector is (π/a), and the zero of energy has been taken to be the bulk GaAs conduction band edge.

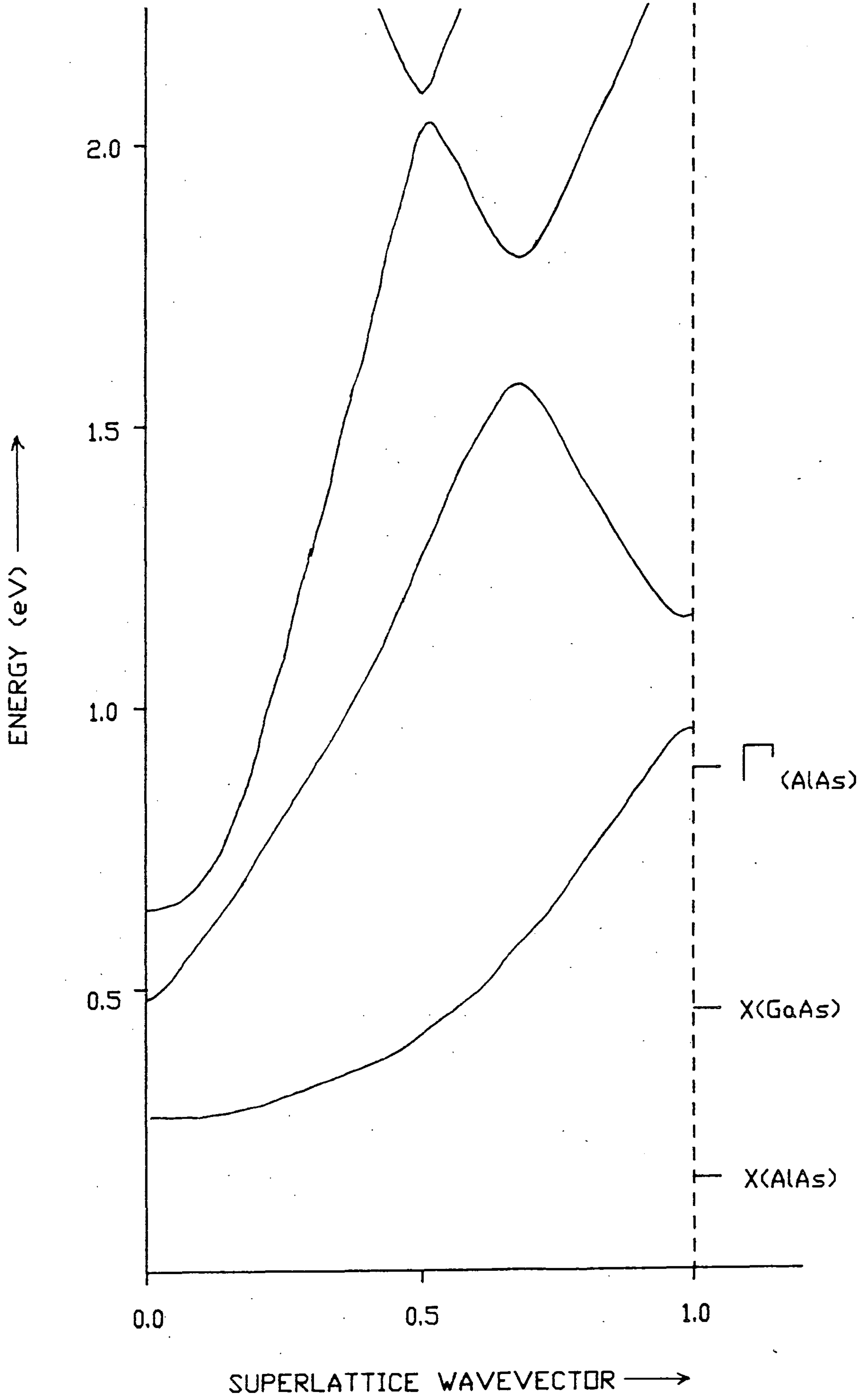

Figure (7.3) - (a) The energy-superlattice wavevector relation for the conduction subbands of a $(GaAs)_2(AlAs)_2$ superlattice. The superlattice wavevector is in units of $(\pi/2a)$, and the zero of energy is the bulk conduction band edge of GaAs.

(b) An illustration of the concept of 'band folding', where the energy-superlattice wavevector dispersion relation of the $(GaAs)_1(AlAs)_1$ superlattice has been redrawn fitted into the smaller Brillouin zone associated with the $(GaAs)_2(AlAs)_2$ superlattice.

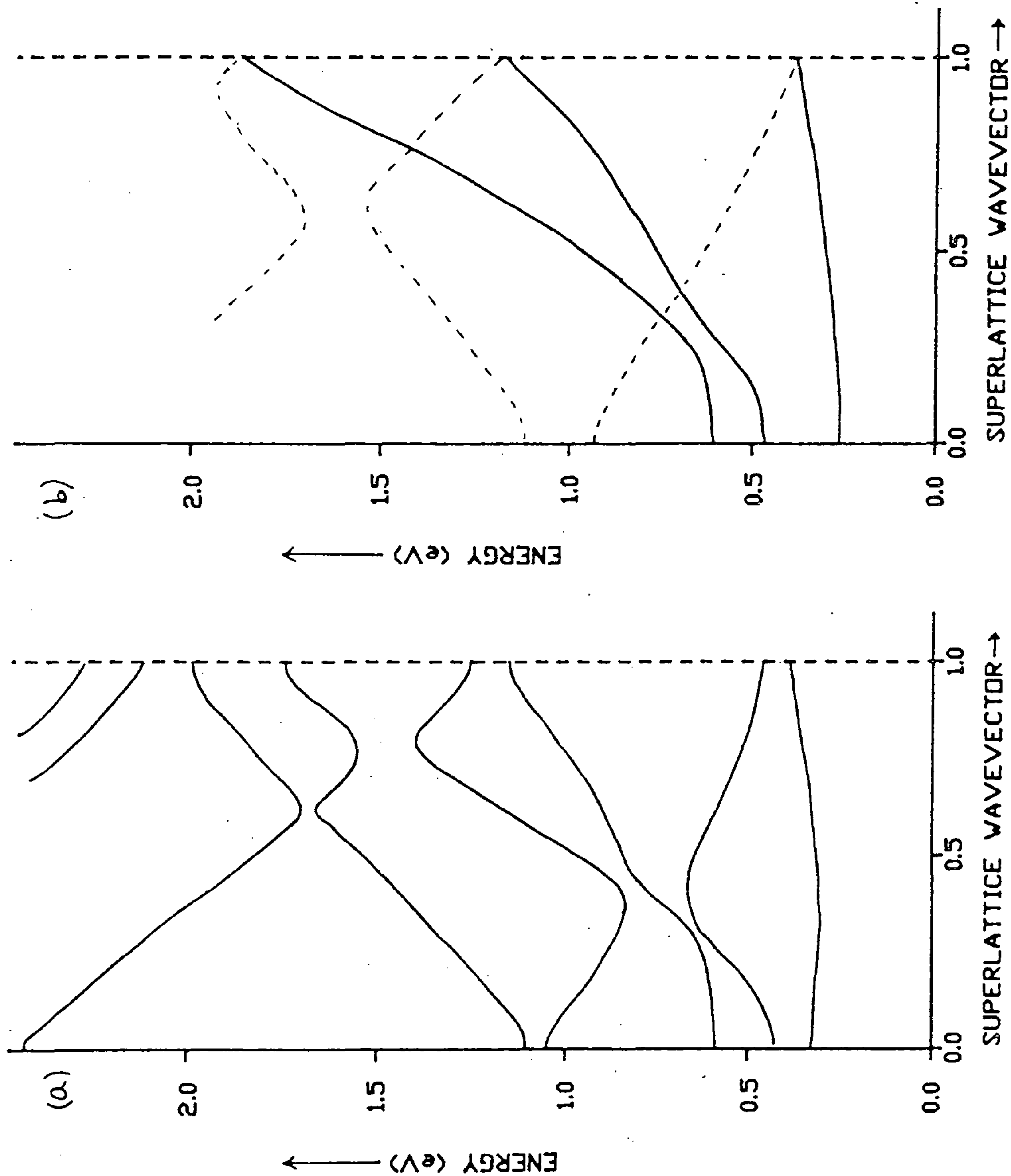

the constituent semiconductors). For the $(GaAs)_1(AlAs)_1$ SL, the corresponding wavevector is π/a. Hence, an approximation to the bandstructure of the $(GaAs)_2(AlAs)_2$ SL may be obtained by 'folding over' the $(GaAs)_1(AlAs)_1$ SL bandstructure about the line $K_S = \pi/2a$. This is done in Figure (7.3b), and, if account is taken of possible interactions caused by the 'folding over' (which will shift band edge energies, and cause anticrossing behaviour) then the qualitative form of the $(GaAs)_2(AlAs)_2$ SL bandstructure may be predicted.

In addition to plotting energy-superlattice wavevector dispersion relations, it is possible, by searching for superlattice states that have both $\underline{k}_{\parallel} = (0,0)$ and $K_S = 0.0$, to find the positions of the band edges in a $(GaAs)_n(AlAs)_m$ SL. In Figure (7.4), the lowest conduction band edge of a $(GaAs)_n(AlAs)_m$ is shown as a function of the AlAs concentration (=m/(m+n)). To interpret the results the concept of two separate quantum wells (QW) is useful, a QW for Γ states, with the well being in the GaAs, and a QW for the X states, with the well being in the AlAs. For GaAs-rich superlattices, the lowest conduction band state will be close to the bulk GaAs conduction band edge as the AlAs concentration of the SL approaches zero. As the AlAs concentration in the SL increases, the width of the GaAs layers decreases, and on a QW picture, the conduction band edge is expected to rise rapidly. For AlAs-rich superlattices, the lowest conduction band state will be close to the bulk AlAs conduction band edge as the molar AlAs concentration in the SL approaches one. As the AlAs concentration decreases, the lowest conduction band edge is expected to increase slowly because the width of the AlAs layers decreases. The increase in the conduction band edge for molar AlAs concentrations close to one is expected to be slower than the increase for molar AlAs concentrations close to zero because of the relative depths of the wells for the Γ electrons and for the X electrons. Figure (7.4) shows the results obtained for the position of

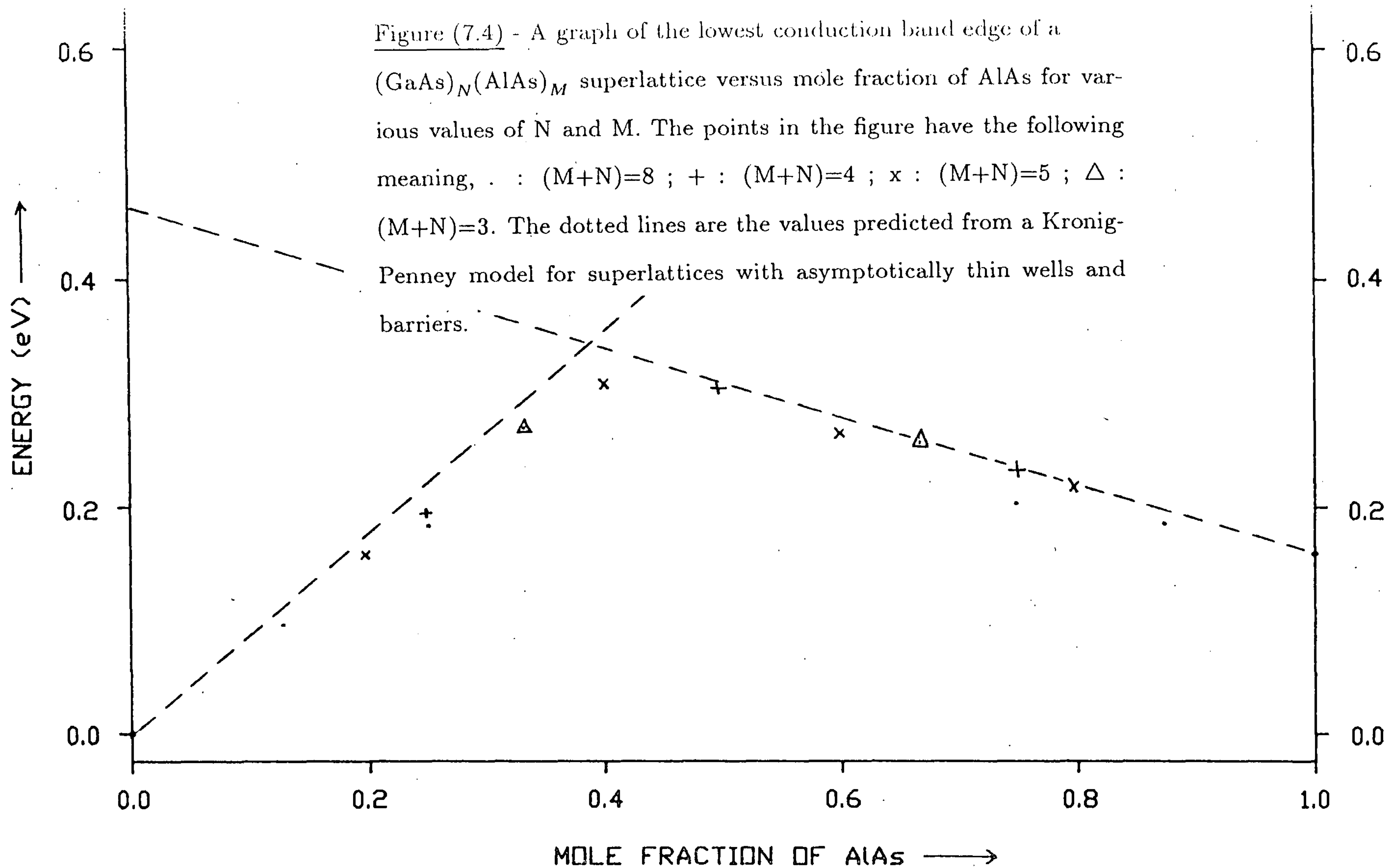

Figure (7.4) - A graph of the lowest conduction band edge of a $(GaAs)_N(AlAs)_M$ superlattice versus mole fraction of AlAs for various values of N and M. The points in the figure have the following meaning, . : (M+N)=8 ; + : (M+N)=4 ; x : (M+N)=5 ; △ : (M+N)=3. The dotted lines are the values predicted from a Kronig-Penney model for superlattices with asymptotically thin wells and barriers.

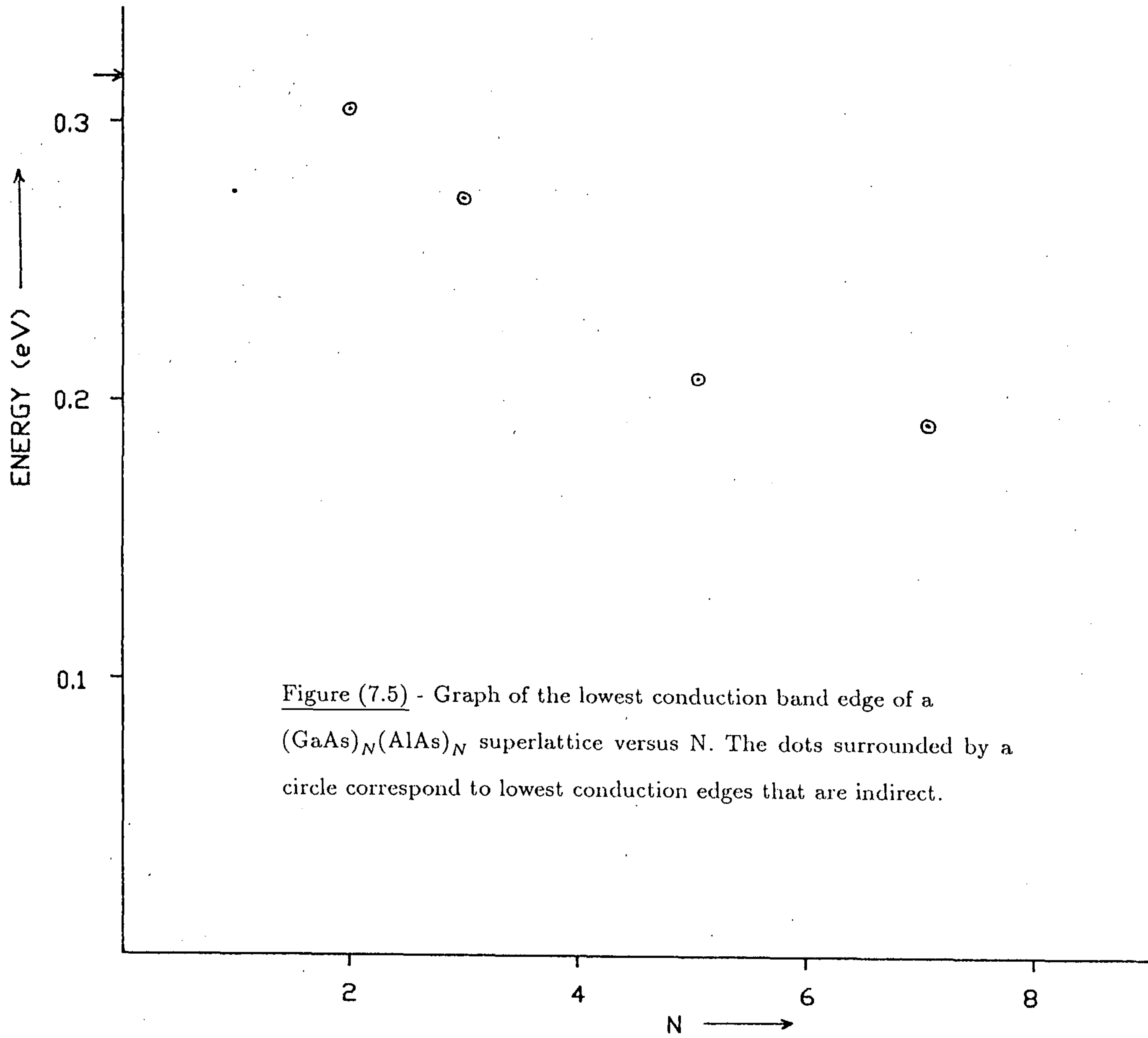

Figure (7.5) - Graph of the lowest conduction band edge of a $(GaAs)_N(AlAs)_N$ superlattice versus N. The dots surrounded by a circle correspond to lowest conduction edges that are indirect.

the lowest conduction band edge from the pseudopotential calculation. Also shown in the figure are two straight lines, one connecting the lowest conduction Γ states in GaAs and AlAs, the other connecting the two lowest conduction X states in GaAs and AlAs. A Kronig-Penney type dispersion relation (which may be derived from envelope function approximations [11]) predicts that, for asymptotically thin wells and barriers, the lowest conduction band state should lie on the lower of the two lines (a result that is true independent of any effective masses assumed for the well and barrier materials). As can be seen from Figure (7.4), the agreement between the full SL calculation and the simple prediction above is found to be best for short period superlattices, and becomes progressively worse as the period increases. For SLs that have the same AlAs concentration but different periods, the results of Figure (7.4) show that the SL with the larger period has the lowest conduction band edge, a result that can easily be understood on the basis of a QW model.

Figure (7.5) shows the lowest conduction band edge of a $(GaAs)_n(AlAs)_n$ SL as a function of n. The lowest conduction band edge of the $(GaAs)_1(AlAs)_1$ SL lies below that of the lowest conduction band edge of the $(GaAs)_2(AlAs)_2$ SL. Also, the $(GaAs)_1(AlAs)_1$ SL was found to be direct, whereas the other $(GaAs)_n(AlAs)_n$ SLs were found to be indirect (at least up to n=7, the maximum value of n used in this study). Both these last two results were also obtained by Gell et al [3]. The lowest conduction band edge of $(GaAs)_n(AlAs)_n$ SLs decreases rapidly as n varies from two to five, but then a plateau is reached for n between five and seven. Such a variation for the lowest conduction band edge with n would cause a plateau to be seen in the bandgap of $(GaAs)_n(AlAs)_n$ SLs for n between five and seven, as was found by Ishibashi et al [12] in their experimental work. Gell et al [3] also found a variation in the bandgap of $(GaAs)_n(AlAs)_n$ SLs with n that exhibited a plateau for n between about five

and ten. Gell [3] explained this by assuming that, in this range of n, the lowest conduction band state changed its character, from being an X-like state for low values of n, to being a Γ-like state for larger values of n. Certainly, for large values of n, the lowest conduction band state would be expected to lie below the X minimum of AlAs because the Γ minimum in GaAs (the bottom of the well) lies about 0.17 eV lower in energy.

7.2 THE ENERGY-IN PLANE WAVEVECTOR RELATIONSHIP FOR SHORT PERIOD GaAs/AlAs SUPERLATTICES

The method described in Chapter Six for the evaluation of the superlattice wavevector required the specification of both the energy *and* the in-plane wavevector. Alternatively, subband dispersion relations may be examined by plotting the $E - \underline{k}_{\|}$ relation whilst keeping the superlattice wavevector fixed at some constant value (taken to be zero throughout this section). As is clear from the Auger recombination calculations presented earlier in this thesis, the subband dispersion relations in a QW are crucially important if an accurate determination of transition rates is required. However, previous superlattice bandstructure calculations have, in general, concentrated on the energy-superlattice wavevector relationship. This could well be a consequence of the heavy computational demands of the determination of the $E - \underline{k}_{\|}$ relationship. One calculation of the subband dispersion relationship is that of Schulman and Chang [13], although the results that they present are for wider period superlattices than those considered here.

In Figure (7.6), the $E - \underline{k}_{\|}$ relationship for a $(GaAs)_1(AlAs)_1$ SL is shown for the lowest three conduction subbands (the superlattice wavevector is equal to zero). The same parameters (i.e. band offsets, number of 2D reciprocal lattice vectors in basis, etc.) as in Section 7.1 have been used, and $\underline{k}_{\|}$ has been taken to be of the form $(k_{\|}, 0)$. The same calculation has also been performed for the $(GaAs)_2(AlAs)_2$ SL (see Figure (7.7)). For planes parallel to the semiconductor interfaces of the superlattice, the original periodicity is retained, and so the wavevector corresponding to the Brillouin zone edge in the

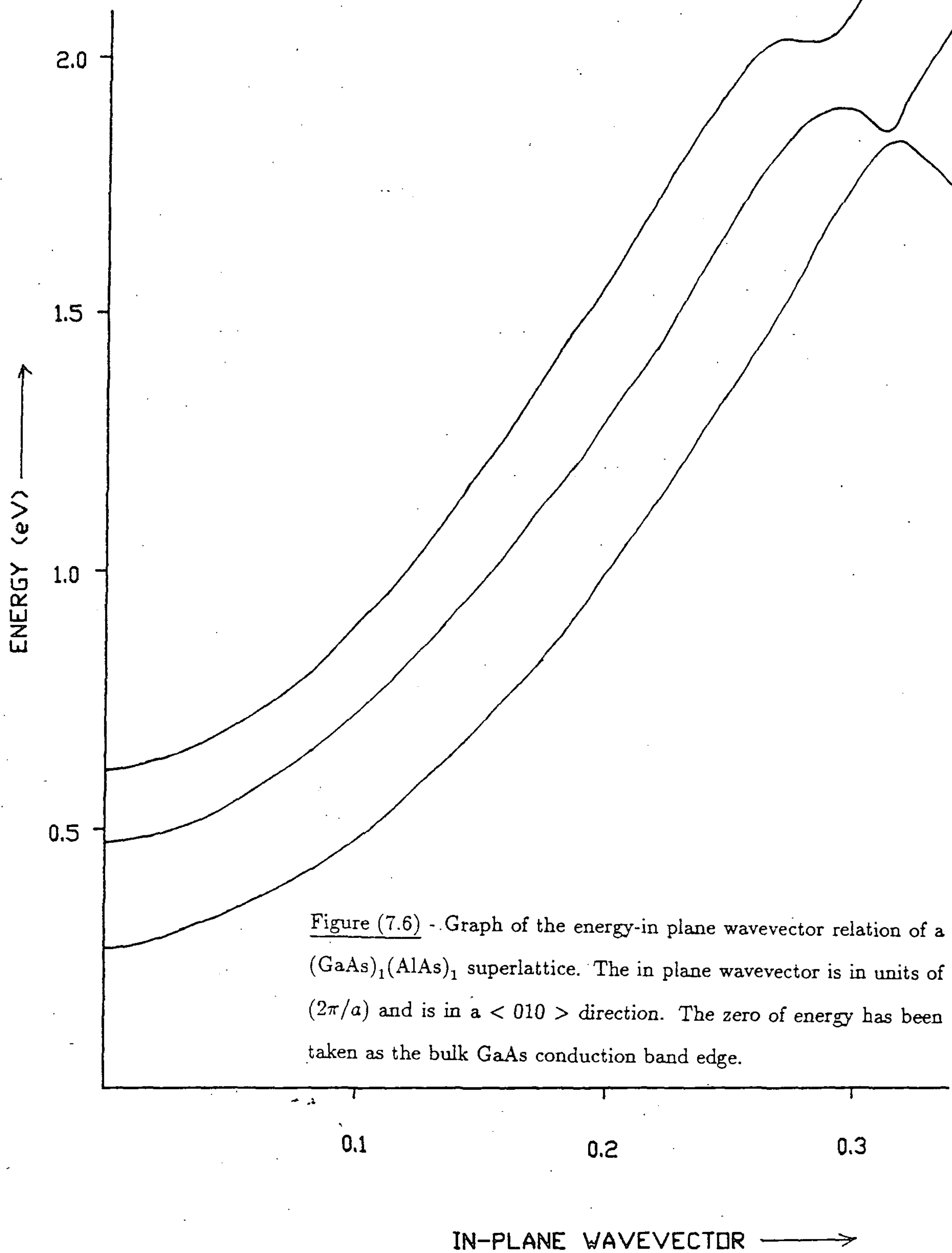

Figure (7.6) - Graph of the energy-in plane wavevector relation of a $(GaAs)_1(AlAs)_1$ superlattice. The in plane wavevector is in units of $(2\pi/a)$ and is in a $< 010 >$ direction. The zero of energy has been taken as the bulk GaAs conduction band edge.

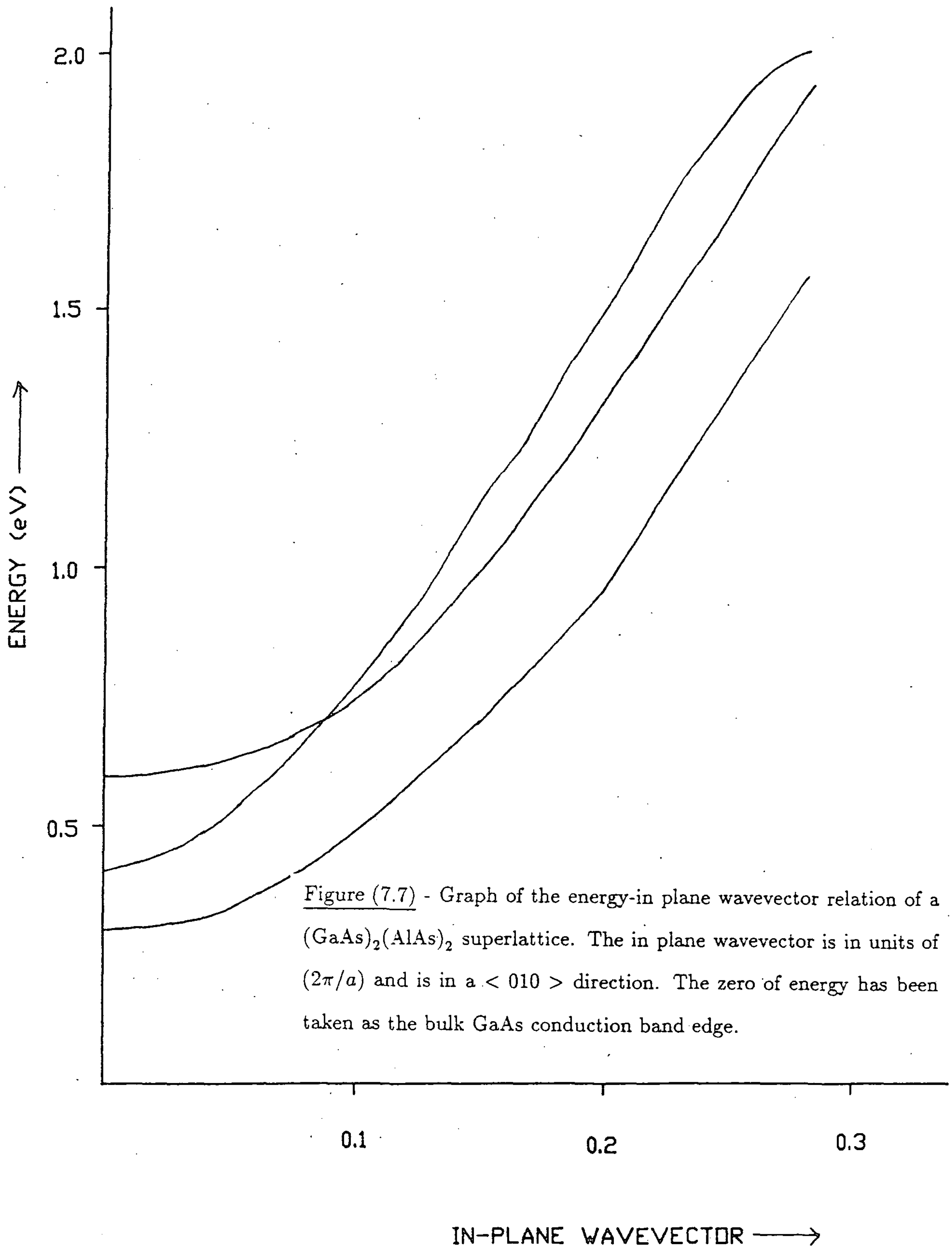

Figure (7.7) - Graph of the energy-in plane wavevector relation of a $(GaAs)_2(AlAs)_2$ superlattice. The in plane wavevector is in units of $(2\pi/a)$ and is in a < 010 > direction. The zero of energy has been taken as the bulk GaAs conduction band edge.

Δ direction is $2\pi/a$ (a being the lattice constant of the constituent semiconductors). Thus, no zone-folding effects are expected in the results of Figures (7.6) and (7.7). However, zone-folding does affect the $E - \underline{k}_{\|}$ relationship because extra states are found at the Γ point and these can mix when $k_{\|} \neq 0$. For the $(GaAs)_1(AlAs)_1$ SL, no structure is seen in the subbands until $k_{\|} \approx 0.3(2\pi/a)$. For the $(GaAs)_2(AlAs)_2$ SL, the 2nd conduction subband appears to cross the third conduction subband (within the accuracy of the numerical calculation no anticrossing behaviour was seen) at $k_{\|} \approx 0.1(2\pi/a)$, which has the implication that the second and third conduction subbands of the $(GaAs)_2(AlAs)_2$ SL have different symmetry, the degeneracy at $k_{\|} = 0.1(2\pi/a)$ being an *accidental* degeneracy.

7.3 SUMMARY

The electronic structure of the conduction subbands of various GaAs/AlAs superlattices has been presented. The principle aim has been to demonstrate that the method described in Chapter Six for the calculation of superlattice wavevectors (given the energy and in-plane wavevector) can be used to accurately determine the bandstructure of GaAs/AlAs superlattices. The energy-superlattice wavevector relationship for the $(GaAs)_2(AlAs)_2$ SL has been found to be in good agreement with previous calculations [3], [8], [9]. The concept of 'zone-folding' has been discussed and the relationship between the bandstructure of the $(GaAs)_1(AlAs)_1$ SL and the $(GaAs)_2(AlAs)_2$ SL has been emphasised.

In addition, the variation of the energy of the lowest conduction band edge in $(GaAs)_n(AlAs)_m$ SLs has been studied, for various values of n and m.

Results for the energy-in plane wavevector relation of conduction subbands in short-period GaAs/AlAs superlattices have also been presented, which, as far as the author is aware have not been presented elsewhere in the literature.

REFERENCES FOR CHAPTER SEVEN

[1] J. Batey and S.L. Wright, J.Appl.Phys., 59, (1986), 200.

[2] A. Baldereschi, E. Hess, K. Mashke, H. Neumann, K-R. Schulze and K. Unger, J.Phys.C:Solid State Phys., 10, (1977), 4709.

[3] M.A. Gell, D. Ninno, M. Jaros and D.C. Herbert, Phys.Rev.B34, (1986), 2416.

[4] R.I. Taylor, M.G. Burt and R.A. Abram, Superlatt. and Microstruct., 3, (1987), 63.

[5] S. Brand, S. Monaghan and P.P. Szydlik, Semicond.Sci.Technol., 2, (1987), 1236.

[6] S. Brand and D.T. Hughes, accepted for publication in Semicond. Sci. Technol., (1987).

[7] Landolt-Börnstein Series, III-V Data Book, Volume 17(a), published by Springer-Verlag Berlin (1982).

[8] T. Nakayama and H. Kammimura, J.Phys.Soc.Jpn., 54, (1985), 4726.

[9] S. Nara, Jap.J.Appl.Phys., 26, (1987), 690.

[10] 'Aspects of the Theory of Superlattices', J.N. Schulman and T.C. McGill, page 77 of 'Synthetic Modulated Structures', edited by L.L. Chang and B.C. Giessen (published by Academic Press, Inc., 1982).

[11] G. Bastard, Phys.Rev.B,24, (1981), 5693.

[12] A. Ishibashi, Y. Mori, M. Itabashi and N. Watanabe, J.Appl.Phys., 58, (1985), 2691.

[13] J.N. Schulman and T.C. McGill, Phys.Rev.B, 19, (1979), 6341.

APPENDIX ONE

Evaluation of the phase space integral
appearing in the calculation of the ground
state CHSH QW Auger rate

The method used in reference [A1.1] can be employed to evaluate the following phase space integral that is required in Section 2.3

$$J = \int\int\int\int \exp(-\beta\mu_S\alpha\underline{\kappa}_2^2)\delta(\underline{\kappa})\delta(E)d\underline{\kappa}_1 d\underline{\kappa}_2 d\underline{\kappa}_3 d\underline{\kappa}_4 \qquad (A1.1)$$

Where $\underline{\kappa} = \underline{\kappa}_1 + \underline{\kappa}_2 - \underline{\kappa}_3 - \underline{\kappa}_4$ and $\beta = (1/k_B T)$

$$E = E_1 + E_2 - E_3 - E_4 = E_{QW} - \Delta_{QW} + \alpha(\underline{\kappa}_1^2 - \mu_S\underline{\kappa}_2^2 + \mu_H(\underline{\kappa}_3^2 + \underline{\kappa}_4^2)) \quad (A1.2)$$

It is useful to change the variables

$$\underline{h} = \underline{\kappa}_3 + \underline{\kappa}_4 \qquad (A1.3)$$

$$\underline{j} = \underline{\kappa}_3 - \underline{\kappa}_4 \qquad (A1.4)$$

Thus, we obtain

$$J = \frac{1}{4\alpha}\int\int\int\int \exp(-\beta\mu_S\alpha\underline{\kappa}_2^2)\delta(\underline{h} - \underline{\kappa}_1 - \underline{\kappa}_2)\delta(E)d\underline{\kappa}_1 d\underline{\kappa}_2 d\underline{h} d\underline{j} \qquad (A1.5)$$

Integration over $\underline{h}$ and $\underline{j}$ leads to

$$J = \frac{\pi}{2\alpha\mu_H} \int\int \exp(-\beta\mu_S\alpha\underline{\kappa}_2^2) d\underline{\kappa}_1 d\underline{\kappa}_2 \tag{A1.6}$$

This last integral has to be evaluated under the condition that $j_o^2 \geq 0$ where

$$j_o^2 = \frac{2}{\mu_H}(\mu_S\underline{\kappa}_2^2 - \underline{\kappa}_1^2 - \frac{\Delta E}{\alpha}) - (\underline{\kappa}_1 + \underline{\kappa}_2)^2 \tag{A1.7}$$

and $\Delta E = E_{QW} - \Delta_{QW}$. A further change of variables is convenient

$$\underline{z}_1 = \underline{\kappa}_1 + \frac{\mu_H}{2+\mu_H}\underline{\kappa}_2 \tag{A1.8}$$

$$\underline{z}_2 = \underline{\kappa}_2 \tag{A1.9}$$

Which converts (A1.6) and (A1.7) into

$$J = \frac{\pi}{2\alpha\mu_H} \int\int \exp(-\beta\mu_S\alpha\underline{z}_2^2) d\underline{z}_1 d\underline{z}_2 \tag{A1.10}$$

$$j_o^2 = \frac{2}{\mu_H}(a_S\underline{z}_2^2 - (1 + \frac{\mu_H}{2})\underline{z}_1^2 - \frac{\Delta E}{\alpha}) \tag{A1.11}$$

Where

$$a_S = \mu_S - \frac{\mu_H}{2+\mu_H} \tag{A1.12}$$

Integration over $\underline{z}_1$ and $\underline{z}_2$ leads to the following result, if $\Delta E \geq 0$

$$J = \frac{\pi^3 (k_B T)^2 a_S}{\alpha^3 \mu_S^2 \mu_H (2+\mu_H)} \exp(-\frac{\mu_S \Delta E}{k_B T a_S}) \tag{A1.13}$$

This is the result that is used in Chapter Two for bound-bound Auger transitions. If carriers are in states that are in higher subbands, the same result holds, except that the value of ΔE will be different from that for the ground state case. If $\Delta E \leq 0$, a case that will arise when bound-unbound Auger transitions are considered, then the result of performing the integral (A1.10) is

$$J = \frac{\pi^3 (k_B T)^2 a_S}{\alpha^3 \mu_S^2 \mu_H (2 + \mu_H)} [1 - \frac{\mu_S \Delta E}{a_S k_B T}] \qquad (A1.14)$$

REFERENCES FOR APPENDIX ONE

[A1.1] R.I. Taylor, R.A. Abram, M.G. Burt, C. Smith, IEE Proc. 132 Part J (optoelect.), (1985), 364.

APPENDIX TWO

Calculation of $I(\underline{\kappa}_o)$

From equation (2.34), $I(\underline{\kappa}_o)$ is given by

$$I(\underline{\kappa}_o) = \int_{-\infty}^{\infty} \frac{\{3,1,q\}\{4,2,-q\}}{|\underline{\kappa}_o|^2 + q^2} dq \tag{A2.1}$$

Where

$$\{m,n,q\} = B^2 M_{m,n} [\frac{-4\pi^2}{L^2} \frac{\sin(qL/2)}{q(q^2 - 4\pi^2/L^2)}] \tag{A2.2}$$

With the $M_{m,n}$ defined in equation (2.33). The expression above is valid for the case where all carriers involved in the Auger transition reside in the respective ground state subbands of the QW. B is a normalisation factor associated with the z-part of the carrier wavefunctions.

$$B = \sqrt{\frac{2}{L}} \tag{A2.3}$$

Rewriting equation (A2.1), we have

$$\{m,n,q\} = \frac{M_{m,n}}{2} [2\frac{\sin x}{x} - \frac{\sin x}{x+\pi} - \frac{\sin x}{x-\pi}] \tag{A2.4}$$

Where $x = qL/2$. We also write $M_{3,1} = M_{CH}$ and $M_{4,2} = M_{HS}$

We thus have

$$I(\underline{\kappa}_o) = \frac{M_{CH} M_{HS}}{2L\kappa_o^2} \int_{-\infty}^{\infty} \frac{\kappa_o^2 L^2}{\kappa_o^2 L^2 + 4x^2} [2\frac{\sin x}{x} - \frac{\sin x}{x-\pi} - \frac{\sin x}{x+\pi}]^2 dx \tag{A2.5}$$

The last equation may be rewritten in the following form

$$I(\underline{\kappa}_o) = \frac{M_{CH}M_{HS}}{2L\kappa_o^2} S(\kappa_o L) \tag{A2.6}$$

With

$$S(y) = \int_{-\infty}^{\infty} \frac{y^2}{y^2+4x^2}[2\frac{\sin x}{x} - \frac{\sin x}{x-\pi} - \frac{\sin x}{x+\pi}]^2 dx \tag{A2.7}$$

This integral may be calculated using contour integration

$$S(y) = 4\pi + \frac{2\pi y^2}{y^2+4\pi^2} + (1-\exp(-y))\{\frac{6\pi y}{y^2+4\pi^2} + \frac{2\pi y(4\pi^2-y^2)}{(y^2+4\pi^2)^2} - \frac{4\pi}{y}\} \tag{A2.8}$$

In the extreme cases of (a) y tending towards infinity and (b) y tending towards zero, we can write

$$\lim_{y\to\infty} = 6\pi - \frac{8\pi^3}{y^2} + O(\frac{1}{y^3}) \tag{A2.9}$$

$$\lim_{y\to 0} = 2\pi y + O(y^2) \tag{A2.10}$$

See figure (A2.1) for a graph of $S(y)$ versus y.

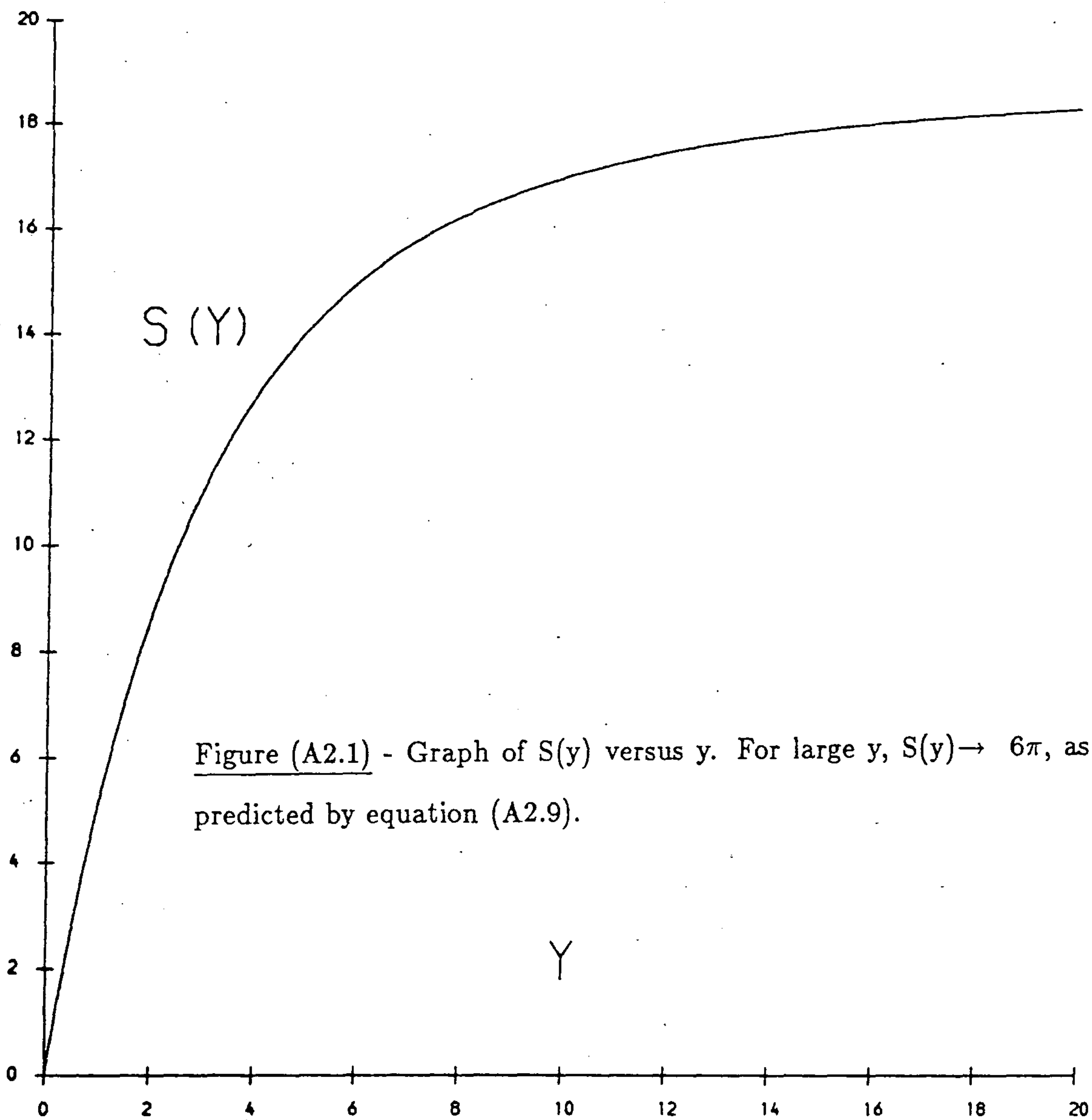

Figure (A2.1) - Graph of S(y) versus y. For large y, $S(y) \rightarrow 6\pi$, as predicted by equation (A2.9).

APPENDIX THREE

Erfc(x) at large values of x

We have

$$\mathrm{erfc}(x) = 1 - \mathrm{erf}(x) = \frac{2}{\sqrt{\pi}} \int_x^\infty \exp(-t^2)dt \qquad (A3.1)$$

This may be integrated by parts to give

$$\int_x^\infty \exp(-t^2)dt = \frac{\exp(-x^2)}{2x} - \int_x^\infty \frac{\exp(-t^2)}{2t^2}dt \qquad (A3.2)$$

Integrating by parts once more gives

$$\int_x^\infty \exp(-t^2)dt = \frac{\exp(-x^2)}{2x} - \frac{\exp(-x^2)}{4x^3} + O(\frac{\exp(-x^2)}{x^5}) \qquad (A3.3)$$

Hence the final result is :

$$\mathrm{erfc}(x) = \frac{\exp(-x^2)}{\sqrt{\pi}}[\frac{1}{x} - \frac{1}{2x^3} + O(\frac{1}{x^5})] \qquad (A3.4)$$

APPENDIX FOUR

Non-parabolicity effects on Auger rates : An example

The $E - \underline{\kappa}$ relation for the carrier in the excited state is taken to be of the form

$$E_4 = \alpha \underline{\kappa}_4^2 - C \underline{\kappa}_4^4 \qquad (A4.1)$$

so that in the notation of Chapter Five, $R(z) = -Cz^4$. Hence, for a QW CHCC Auger transition involving the ground state subbands only to occur, we must have (using the same notation as that of Chapter Five)

$$a\alpha z^2 - Cz^4 - E_{QW} \geq 0 \qquad (A4.2)$$

or

$$Cz^4 - a\alpha z^2 + E_{QW} \leq 0 \qquad (A4.3)$$

The phase space integral is performed over the range of z which lies between the roots of

$$Cz^4 - a\alpha z^2 + E_{QW} = 0 \qquad (A4.4)$$

The roots of the equation (A4.4), z_+, and z_-, are given by

$$z_\pm^2 = (\frac{\alpha a}{2C})[1 \pm \sqrt{1 - \frac{C}{C_m}}] \qquad (A4.5)$$

with

$$C_m = \frac{(\alpha a)^2}{4E_{QW}} \tag{A4.6}$$

Thus, for a QW CHCC Auger process to occur involving ground state subbands only we must have $C \leq C_m$, otherwise the two roots of equation (A4.4) would be complex. In terms of the graphical technique used in Chapter Five, the curve of $a\alpha z^2 - Cz^4$ always lies below E_{QW}. Physically, the non-parabolicity (effectively determined by C) must not be too big or the simultaneous conservation of energy and momentum will not be possible. The condition that $C \leq C_m$ for the CHCC Auger process to be possible illustrates the points raised in Chapter Five that the transition is more likely to be forbidden in materials that have large values of E_{QW}, and values of a less than one. We note that if we let $C \rightarrow 0$, the values of $z_{\pm}^2$ tend towards the parabolic values, as expected.

$$lim_{C\rightarrow 0} = (\frac{\alpha a}{2C})[1 \pm \sqrt{(1 - \frac{C}{C_m})}] = (\frac{\alpha a}{2C})[1 \pm (1 - \frac{C}{2C_m})] \tag{A4.7}$$

so we have

$$z_-^2 \rightarrow \frac{E_{QW}}{\alpha a} \tag{A4.8}$$

and

$$z_+^2 \rightarrow \infty \tag{A4.9}$$